

The Pennsylvania State University
The Graduate School
Department of Mechanical Engineering

**MODELING AND NUMERICAL SIMULATION OF INTERIOR BALLISTIC
PROCESSES IN A 120mm MORTAR SYSTEM**

A Dissertation in
Mechanical Engineering

by

Ragini Acharya

© 2009 Ragini Acharya

Submitted in Partial Fulfillment
of the Requirements
for the Degree of

Doctor of Philosophy

May 2009

The dissertation of Ragini Acharya was reviewed and approved* by the following:

Kenneth K. Kuo
Distinguished Professor of Mechanical Engineering
Dissertation Advisor
Chair of Committee

André L. Boehman
Professor of Fuel Science

Daniel C. Haworth
Professor of Mechanical Engineering

John H. Mahaffy
Professor of Nuclear Engineering

Richard A. Yetter
Professor of Mechanical Engineering

Karen A. Thole
Professor of Mechanical and Nuclear Engineering
Head of the Department of Mechanical Engineering

*Signatures are on file in the Graduate School

ABSTRACT

Numerical Simulation of interior ballistic processes in gun and mortar systems is a very difficult and interesting problem. The mathematical model for the physical processes in the mortar systems consists of a system of non-linear coupled partial differential equations, which also contain non-homogeneity in form of the source terms. This work includes the development of a three-dimensional mortar interior ballistic (3D-MIB) code for a 120mm mortar system and its stage-wise validation with multiple sets of experimental data. The 120mm mortar system consists of a flash tube contained within an ignition cartridge, tail-boom, fin region, charge increments containing granular propellants, and a projectile payload. The ignition cartridge discharges hot gas-phase products and unburned granular propellants into the mortar tube through vent-holes on its surface. In view of the complexity of interior ballistic processes in the mortar propulsion system, the overall problem was solved in a modular fashion, i.e., simulating each physical component of the mortar propulsion system separately. These modules were coupled together with appropriate initial and boundary conditions.

The ignition cartridge and mortar tube contain nitrocellulose-based ball propellants. Therefore, the gas dynamical processes in the 120mm mortar system are two-phase, which were simulated by considering both phases as an interpenetrating continuum. Mass and energy fluxes from the flash tube into the granular bed of ignition cartridge were determined from a semi-empirical technique. For the tail-boom section, a transient one-dimensional two-phase compressible flow solver based on method of characteristics was developed. The mathematical model for the interior ballistic processes

in the mortar tube posed an initial value problem with discontinuous initial conditions with the characteristics of the Riemann problem due to the discontinuity of the initial conditions. Therefore, the mortar tube model was solved by using a high-resolution Godunov-type shock-capturing approach was used where the discretization is done directly on the integral formulation of the conservation laws. A linearized approximate Riemann Solver was modified in this work for the two-phase flows to compute fully non-linear wave interactions and to directly provide upwinding properties in the scheme. An entropy fix based on Harten-Heyman method was used with van Leer flux limiter for total variation diminishing. The three dimensional effects were simulated by incorporating an unsplit multi-dimensional wave propagation method, which accounted for discontinuities traveling in both normal and oblique coordinate directions.

For each component, the predicted pressure-time traces showed significant pressure wave phenomena, which closely simulated the measured pressure-time traces obtained at PSU. The pressure-time traces at the breech-end of the mortar tube were obtained at Aberdeen Test Center with 0, 2, and 4 charge increments. The 3D-MIB code was also used to simulate the effect of flash tube vent-hole pattern on the pressure-wave phenomenon in the ignition cartridge. A comparison of the pressure difference between primer-end and projectile-end locations of the original and modified ignition cartridges with each other showed that the early-phase pressure-wave phenomenon can be significantly reduced with the modified pattern. The flow property distributions predicted by the 3D-MIB for 0, 2, and 4 charge increment cases as well the projectile dynamics predictions provided adequate validation of theory by experiments.

TABLE OF CONTENTS

LIST OF FIGURES	ix
LIST OF TABLES	xvii
ACKNOWLEDGEMENTS	xviii
Chapter 1 INTRODUCTION	1
1.1 Description of 120mm mortar system	1
1.1.1 Flash tube	2
1.1.2 Tail-boom section	3
1.1.3 Mortar tube section	5
1.2 Motivation	6
1.3 Specific objectives	8
1.4 General method of approach	9
1.5 Major advantages of theoretical/numerical work	13
1.6 Literature review	13
1.7 Survey of numerical methods	16
Chapter 2 IGNITION CARTRIDGE COMBUSTION SUB-MODEL	21
2.1 Introduction	21
2.2 Flash tube sub-model	23
2.2.1 Go/No-Go ignition criterion for primer	24
2.2.2 Black powder combustion	24
2.2.3 Gas-phase mass flow rate from the nth set of vent holes	25
2.2.4 Condensed-phase mass flow rate from the nth set of vent holes	26
2.2.5 Gas-phase energy flux and enthalpy from the nth set of vent holes	27
2.2.6 Condensed-phase energy flux from the nth set of vent holes	27
2.2.7 Rate of energy loss to the flash tube	28
2.2.8 Protective tube resistance	28
2.2.9 Calculated results from flash tube sub-model	29
2.3 Granular bed combustion sub-model	36
2.3.1 Method of approach	38
2.3.2 Basic assumptions	39
2.3.3 Governing equations	40
2.3.4 Equation of state in granular bed	44
2.3.5 Intragranular stress	45
2.3.6 Burning rate expression of ball propellants	46
2.3.7 Formulation of the heat equation	47
2.3.8 Method of characteristics formulation	50
2.3.9 Linearization of the characteristic equations	54
2.3.10 Validation of calculated results	56

2.4 Summary of the ignition cartridge sub-model	73
Chapter 3 APPLICATION OF IGNITION CARTRIDGE SUB-MODEL FOR PERFORMANCE IMPROVEMENT	74
3.1 Background.....	74
3.2 Effect of vent hole pattern modification on the flash tube	77
3.2.1 Calculated results.....	78
3.2.2 Discussion of vent-hole pattern analysis	95
3.3 Effect of pyrotechnic materials in the flash tube	96
3.3.1 Flash tube results	97
3.3.2 Ignition cartridge results.....	99
3.4 Summary.....	102
Chapter 4 FORMULATION OF MORTAR TUBE COMBUSTION SUB- MODEL	104
4.1 Assumptions	104
4.1.1 Governing equations for the mortar tube gas dynamics	105
4.2 Initial conditions	110
4.2.1 Initial condition for velocity	110
4.2.2 Initial condition for porosity.....	111
4.2.3 Initial condition for temperature and pressure.....	112
4.3 Boundary conditions.....	113
4.3.1 On ignition cartridge surface in the vent hole region	113
4.3.2 In the fin region	114
4.3.3 The z-direction boundary conditions.....	114
4.4 Summary of mortar tube sub-model	115
Chapter 5 FORMULATION OF PROJECTILE DYNAMICS SUB-MODEL.....	116
5.1 Basic assumptions.....	116
5.2 Net force and pressure distribution.....	117
5.3 Mesh generation with the moving projectile	119
5.4 Summary of projectile dynamics sub-model	121
Chapter 6 FINITE ELEMENT SOLUTION FOR MORTAR TUBE SUB- MODEL	122
6.1 Finite element model for two-phase governing equations.....	122
6.1.1 Galerkin method.....	123
6.1.2 Leap-Frog Taylor-Galerkin finite element scheme	124
6.1.3 Reduction of governing equations using LFTG method	125
6.1.4 Weight functions	127
6.1.5 Formulated finite element equations	128
6.1.6 The Ritz-Galerkin finite element models	129

6.1.7 Mesh generation	134
6.1.8 Computed results and discussions	139
6.2 Remarks on calculated results from mortar tube sub-model	154
Chapter 7 MORTAR TUBE SUB MODEL SOLUTION WITH TWO-PHASE APPROXIMATE RIEMANN SOLVER.....	155
7.1 General approach	156
7.2 Godunov methods	158
7.3 Issues with Godunov's method.....	161
7.4 Approximate Riemann solver: Roe-Pike method	162
7.4.1 Roe's method.....	170
7.4.2 Roe-Pike method	173
7.5 •Entropy condition and entropy fix	174
7.6 Flux limiter	176
7.7 Higher order correction.....	177
7.8 Three dimensional wave propagation.....	178
7.9 Runge-Kutta method.....	182
7.10 Boundary conditions.....	183
7.11 Calculated results and discussions.....	183
7.11.1 Exact solution versus calculated solution.....	184
7.11.2 Validation of calculated results by experimental data.....	186
7.12 Summary of mortar tube sub-model simulation	202
Chapter 8 CONCLUSIONS AND FUTURE WORK	203
8.1 Major contributions	205
8.2 Future work.....	207
Bibliography	208
Appendix A Formulation of Heat Equation for Ball Propellants	215
Appendix B Shape Functions.....	221
B.1 Master element	221
B.2 Lagrange polynomials.....	223
Appendix C Numerical Integration on the Master Element	226
Appendix D Hyperbolic Systems.....	229
D.1 Wave formation	232
D.2 Rankine-Hugoniot condition.....	234
D.3 Entropy condition	235

Appendix E Riemann Problem	237
----------------------------------	-----

LIST OF FIGURES

Figure 1-1: Cross-sectional view of the 120mm mortar projectile.	2
Figure 1-2: Cross-sectional view of the flash tube with 20 vent holes having a diameter of 0.165 cm.	3
Figure 1-3: Cross-sectional view of the granular bed of the ignition cartridge.	4
Figure 1-4: 120mm mortar cartridge family (from left to right): M934/M934A1 HE, M929 WP smoke, M930/M983 illumination, M931 practice [75].	5
Figure 1-5: Damaged fin-blade during the 120mm mortar firings.	6
Figure 1-6: Damaged fin-blade during the 120mm mortar firings (end-view).	7
Figure 1-7: Major building blocks of the 3D-MIB code.	11
Figure 1-8: Overall flow chart for the 3D-MIB code.	12
Figure 2-1: Cross-sectional view of the flash tube with 20 vent holes.	23
Figure 2-2: Photograph of the flash tube test setup (a) entire test rig and (b) zoomed-in portion of the instrumented flash tube [50].	31
Figure 2-3: Cross sectional drawing of the flash tube and axial locations of pressure transducers used in this study.	32
Figure 2-4: Recorded pressure-time traces from a flash tube test.	33
Figure 2-5: Deduced gas-phase mass flow rates-time traces from the flash tube using flash tube sub-model.	36
Figure 2-6: Cross-sectional view of the granular bed of the ignition cartridge.	37
Figure 2-7: Region of coated ball propellant particles in the vicinity of a flash-tube vent hole and temperature profile in a coated particle.	47
Figure 2-8: Characteristic curves at different locations.	52
Figure 2-9: Location of pressure transducers on the ignition cartridge.	58
Figure 2-10: Computed pressure-time traces for ignition cartridge at five port locations.	60
Figure 2-11: Measured pressure-time traces for ignition cartridge at five port locations.	60

Figure 2-12: Comparison of 5 experimental pressure-time traces with the calculated pressure-time traces at port 0 location ($x=0.11$ cm).	61
Figure 2-13: Comparison of 5 experimental pressure-time traces with the calculated pressure-time traces at port 1 location ($x=2.94$ cm).	61
Figure 2-14: Comparison of 5 experimental pressure-time traces with the calculated pressure-time traces at port 2 location ($x=5.86$ cm).	62
Figure 2-15: Comparison of 5 experimental pressure-time traces with the calculated pressure-time traces at port 3 location ($x=8.76$ cm).	62
Figure 2-16: Comparison of 5 experimental pressure-time traces with the calculated pressure-time traces at port 4 location ($x=8.78$ cm).	63
Figure 2-17: Comparison of 5 experimental pressure-time traces with the calculated pressure-time traces at port 5 location ($x=11.70$ cm).	63
Figure 2-18: Comparison of calculated pressure difference-time traces.	64
Figure 2-19: Comparison of experimental pressure difference-time traces with the calculated pressure difference-time traces for $\Delta P=P_5-P_0$	65
Figure 2-20: Comparison of experimental pressure difference-time traces with the calculated pressure difference-time traces for $\Delta P=P_4-P_1$	66
Figure 2-21: Comparison of gas velocity variation in the ignition cartridge at different axial locations.	67
Figure 2-22: Comparison of surface temperature increase of propellant grain in the ignition cartridge.	68
Figure 2-23: Comparison of gas temperature variation in the ignition cartridge at different axial locations.	70
Figure 2-24: Comparison of porosity variations in the ignition cartridge at different axial locations.	70
Figure 2-25: Comparison of particle velocity variation in the ignition cartridge at different axial locations.	71
Figure 2-26: Comparison of calculated and measured particle diameter in the ignition cartridge at different axial locations at the end of ballistic event (Test 1).	72

Figure 2-27: Comparison of calculated and measured particle diameter in the ignition cartridge at different axial locations at the end of ballistic event (Test 2).	72
Figure 3-1: Deduced gaseous mass flow rate vs. time traces from one of the P-t traces of five flash tube tests with the original vent-hole pattern (case 0).	79
Figure 3-2: Deduced gaseous mass flow rate vs. time traces from one of the P-t traces of five flash tube tests with modified vent-hole pattern (case 1).	80
Figure 3-3: Deduced gaseous mass flow rate vs. time traces from one of the P-t traces of five flash tube tests with modified vent-hole pattern (case 2).	82
Figure 3-4: Deduced gaseous mass flow rate vs. time traces from one of the P-t traces of five flash tube tests with modified vent-hole pattern (case 3).	83
Figure 3-5: Computed pressure-time traces for a M1020 ignition cartridge at various pressure-gage port locations with a modified flash-tube vent-hole pattern (case 1).	85
Figure 3-6: Computed pressure-time traces for M1020 ignition cartridge at five pressure-gage port locations with modified flash-tube vent-hole pattern (case 2).	85
Figure 3-7: Computed pressure-time traces for a M1020 ignition cartridge at five pressure-gage port locations with a modified flash-tube vent-hole pattern (case 3).	86
Figure 3-8: A comparison of predicted time variations of ΔP between projectile and primer ends in the granular for various flash-tube vent-hole patterns.	87
Figure 3-9: Deduced gaseous mass flow rate vs. time traces from one of the P-t traces of five flash tube tests with modified vent-hole pattern (final case).	88
Figure 3-10: Difference in deduced mass flow rate from flash tube with five BP pellets between projectile and primer-ends for various vent-hole designs.	89
Figure 3-11: Computed pressure-time traces for ignition cartridge at five pressure-gage port locations with a modified flash-tube vent-hole pattern (final case).	90
Figure 3-12: Comparison of numerical ΔP (P_4-P_1)-time traces and with modified ignition cartridge modified ignition cartridge [final modification].	91
Figure 3-13: Comparison of experimental and numerical ΔP ($P_{16}-P_1$)-time traces and ΔP ($P_{17}-P_0$)-time traces with modified ignition cartridge [final modification].	91

Figure 3-14: Comparison of experimental and numerical ΔP ($P_{17}-P_0$)-time traces with modified ignition cartridge [final modification].....	92
Figure 3-15: Narration of physical processes in the flash tube.....	93
Figure 3-16: Explanation of pressure-time traces behavior in final modification of the flash tube.....	93
Figure 3-17: Computed accumulated condensed-phase mass from flash tube at various ports (original design).	94
Figure 3-18: Computed accumulated condensed-phase mass from modified flash tube at various ports (final modification).	95
Figure 3-20: Deduced gaseous mass flow rate vs. time traces from the flash tube with MRBPS pellets.	99
Figure 3-21: Computed P-t traces in ignition cartridge using MRBPS pellets in the flash tube.....	101
Figure 4-1: Fin region of the 120mm mortar projectile.....	112
Figure 5-1: Pressure acting on a local projectile surface at angle α	118
Figure 5-2: Cartoon of a portion of projectile surface profile and control volumes attached to the surface.	119
Figure 5-3: Schematic of projectile motion and axial expansion of the gas-phase region near the base of the projectile in an earlier phase.....	120
Figure 5-4: Schematic of projectile motion and axial expansion of the gas-phase region near the base of the projectile at a later time.	120
Figure 6-1: Several types of elements and node locations.....	135
Figure 6-2: Hexahedral element with uniform distribution of ball propellants.	136
Figure 6-3: Finite element mesh generated in a section of mortar tube: (a) vent-hole region meshed, (b) vent-hole and conical regions meshed, (c) all regions meshed except fin-blade region, (d) all regions meshed.	138
Figure 6-4 A section of mortar tube region with finite element mesh.....	139
Figure 6-5: Computed mass flow rates from tail-boom into mortar tube at various axial locations.	140
Figure 6-6: Computed P-t traces in the mortar tube at various axial locations.....	141

Figure 6-7: Computed P-t traces in the vent-hole region of mortar tube at various axial locations.	142
Figure 6-8: Computed P-t traces in the projectile-payload region of mortar tube at various axial locations.	143
Figure 6-9: Computed P-t traces in the conical region of mortar tube at various axial locations.	144
Figure 6-10: Computed P-t traces in the fin-blade region of mortar tube at various axial locations.	145
Figure 6-11: Measured P-t traces of projectile firing (P~13,000 psig, rise time ~ 2.6 m).	145
Figure 6-12: Computed temperature-t traces in the mortar tube at various axial locations.	146
Figure 6-13: Computed temperature-t traces in the fin-blade region of mortar tube...	147
Figure 6-14: Computed particle surface temperature-t traces in the mortar tube at various axial locations.	148
Figure 6-15: Computed burn rate-t trace in the vent-hole region of the mortar tube at various axial locations.	149
Figure 6-16: Computed pressure contours in the mortar tube at the beginning of ballistic cycle.	150
Figure 6-17: Computed pressure contours in the mortar tube at various time instances.	151
Figure 6-18: Computed pressure contours in the mortar tube at various time instances.	152
Figure 6-19: Computed pressure contours in the mortar tube at various time instances.	153
Figure 7-1: Illustration of the initial data for the Riemann problem. At the initial time the data consists of two constant states separated by a discontinuity at $x = 0$	157
Figure 7-2: Piece-wise constant distribution of data at time level n [71].	159
Figure 7-3: Structure of Riemann problem solution for the x-split three dimensional Euler equations [71].	161

Figure 7-4: Illustration of the numerical phenomenon of spurious oscillations near high gradients [71].	176
Figure 7-5: Discretization of a three-dimensional Cartesian domain into finite volumes of volume $\Delta x \Delta y \Delta z$.	181
Figure 7-6: Comparison of exact density profile with calculated results at time 0.25 s.	185
Figure 7-7: Comparison of exact velocity profile with calculated results at time 0.25 s.	185
Figure 7-8: Schematic of instrumented mortar simulation and pressure transducer locations.	186
Figure 7-9: Calculated pressure variation in the mortar tube with projectile motion (with 0 charge increments).	188
Figure 7-10: Early phase pressure wave phenomena in the mortar tube before projectile motion (with 0 charge increments).	188
Figure 7-11: Calculated porosity variation in the mortar tube with projectile motion (with 0 charge increments).	189
Figure 7-12: Calculated axial gas-velocity variation in the mortar tube with projectile motion (with 0 charge increments).	189
Figure 7-13: Calculated axial particle velocity variation in the mortar tube with projectile motion (with 0 charge increments).	190
Figure 7-14: Calculated gas temperature variation in the mortar tube with projectile motion (with 0 charge increments).	190
Figure 7-15: Comparison of 3D-MIB predictions for pressure-time traces at 3 port locations along the mortar tube with measured data.	191
Figure 7-16: Comparison of 3D-MIB predictions for projectile dynamics with measured data for 0 charge increments loading.	191
Figure 7-17: Calculated pressure variation in the mortar tube with projectile motion (with 2 charge increments).	193
Figure 7-18: Early phase pressure wave phenomena in the mortar tube before projectile motion (with 2 charge increments).	193
Figure 7-19: Calculated porosity variation in the mortar tube with projectile motion (with 2 charge increments).	194

Figure 7-20: Calculated gas temperature variation in the mortar tube with projectile motion (with 2 charge increments).....	194
Figure 7-21: Calculated axial gas velocity variation in the mortar tube with projectile motion (with 2 charge increments).....	195
Figure 7-22: Calculated axial particle velocity variation in the mortar tube with projectile motion (with 2 charge increments).....	195
Figure 7-23: Comparison of 3D-MIB predictions for pressure-time traces at 3 port locations along the mortar tube with measured data for 2 charge increments loading.	196
Figure 7-24: Comparison of 3D-MIB predictions for projectile dynamics with measured data for 2 charge increments loading.	196
Figure 7-25: Calculated pressure variation in the mortar tube with projectile motion (with 4 charge increments).	198
Figure 7-26: Early phase pressure wave phenomena in the mortar tube before projectile motion (with 4 charge increments).	198
Figure 7-27: Calculated porosity variation in the mortar tube with projectile motion (with 4 charge increments).	199
Figure 7-28: Calculated gas temperature variation in the mortar tube with projectile motion (with 4 charge increments).	199
Figure 7-29: Calculated axial gas velocity variation in the mortar tube with projectile motion (with 4 charge increments).	200
Figure 7-30: Calculated axial particle velocity variation in the mortar tube with projectile motion (with 4 charge increments).	200
Figure 7-31: Comparison of 3D-MIB predictions for pressure-time traces at 3 port locations along the mortar tube with measured data for 4 charge increments loading.	201
Figure 7-32: Comparison of 3D-MIB predictions for projectile dynamics with measured data for 4 charge increments loading.	201
Figure B-1: Transformation of an actual element into a master element.	222
Figure D-1: Wave steepening in a convex , non-linear hyperbolic conservation law, (a) Initial condition, (b) Slopes of characteristic curves	233

Figure **E-1**: Structure of the solution of the Riemann problem on the $x-t$ plane for the one-dimensional time-dependent Euler equations [71].239

Figure **E-2**: Possible wave patterns in the solution of the Riemann problem: (a) left rarefaction, contact, right shock (b) left shock, contact, right rarefaction (c) left rarefaction, contact, right rarefaction (d) left shock, contact, right shock [71].240

LIST OF TABLES

Table 1-1 : Finite difference schemes for hyperbolic equations.....	19
Table 2-1 : Input parameters for the flash tube sub-model.....	35
Table 3-1 : Distribution of flash tube vent-hole sizes at various axial locations.....	78
Table 7-1 : Data for test problem with exact solution for the time-dependent, one dimensional Euler equations.....	184
Table 7-2 : Comparison of 3D-MIB calculations for the muzzle velocity with the IMS data.....	202
Table C-1 : Gauss-Legendre abscissae and weights.....	228

ACKNOWLEDGEMENTS

First of all, I would like to express profound appreciation and deep regards for my Ph.D. adviser, Prof. Kenneth K. Kuo. His vision, professional expertise, and continued guidance have greatly helped this research effort and have strongly affected my evolution as a researcher. He has given me excellent opportunities to refine my research potential and advance my professional credentials. I can not thank him enough. I would also like to thank Prof. André L. Boehman for his support and continued guidance from the beginning through the end of my stay at The Penn State University.

I would like to thank Profs. Richard A. Yetter, Daniel H. Haworth, and John C. Mahaffy for their time and effort in reviewing this work and serving on my doctoral committee. I would like to thank Mr. Randy Rand of U.S. Army/ARDEC and Mr. Jack Sacco of the Savit Corporation for supporting this technical work as a part of the overall task under a prime contract DAAE30-03-D-1008 through Savit Corporation. I would like to thank Dr. Jeffrey D. Moore, Mr. Peter J. Ferrara, and Dr. Eric Boyer for the experimental data, which is invaluable and which I have extensively used in this work. I want to thank my colleagues at the High Pressure Combustion Laboratory for doing great work and being an inspiration for excellence to me. I want to thank The Penn State University and Department of Mechanical and Nuclear Engineering for giving me this opportunity.

I want to acknowledge my friends for being supportive and fellow travelers in this journey. I want to especially thank my friend Mr. Kshitij V. Deshmukh for his support. Finally, I would like to thank my parents and my brother for having endless faith in me.

Chapter 1

INTRODUCTION

The central topic of interest in the proposed research is the modeling and simulation of flame spreading and combustion processes in a 120mm mortar system. Completed work presented here addresses the flame spreading, combustion, pressurization process, and wave propagation in some parts of the 120mm mortar system. The comprehensive modeling of the 120mm mortar system under realistic firing conditions involves several complex processes, which can be best described by two-phase processes, for both gas-phase and condensed-phase.

1.1 Description of 120mm mortar system

The 120mm mortar system is one of the three mortar systems that are currently used by the U.S. Army. The 120mm Mortar System provides close in and continuous indirect fire support to maneuver forces. It is capable of rapid response, which is critical since a mortar platoon must move frequently to avoid counter fire. This mortar is used by mechanized infantry, armor and cavalry units. The 120mm mortar system consists of many parts. The drawing of the cross-sectional view of the 120mm mortar projectile is shown in Fig. 1-1. There are several components in this mortar system; however, in this work, the 120mm mortar system is divided into three major parts; flash tube, tail boom, and mortar tube. These three major parts are described as following:

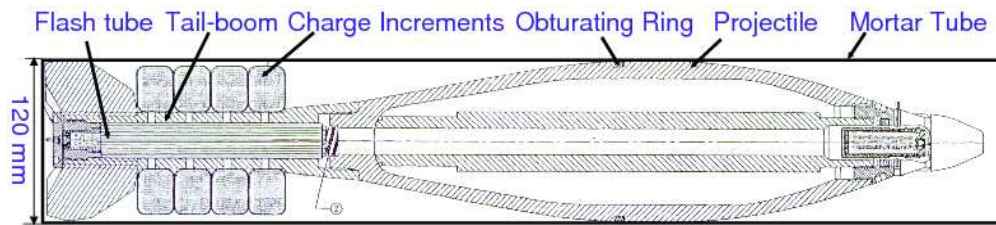


Figure 1-1: Cross-sectional view of the 120mm mortar projectile.

1.1.1 Flash tube

This is the innermost cylindrical portion, which is an assembly of a primer and igniter contained in a partially perforated cylindrical tube. The primer is located at one end known as the primer-end. Primer is a combustible material, which ignites upon impact provided that the energy of impact is above the threshold energy required for ignition. The threshold energy required for ignition is called initiation energy (E_{req}) and it is related to the striking velocity (V_{imp}) of impact. The impact is delivered by a device called firing pin, which hits the primer to ignite it. Next to the primer, five center perforated annular black powder pellets are located. The hot gases produced by the ignition of primer heat and subsequently ignite the black powdered pellets. The combustion products from the ignition of black powder pellets comprise of both gas-phase and condensed-phase products. There is an extended tube with 20 circular vent holes on its surface after the black powder pellets. This tube is empty and closed on the other end, which is called the projectile end. Both gas-phase and condensed-phase products of combustion from primer and black powder expand into this empty cylindrical

tube. These products of combustion are subsequently discharged from the flash tube through the 20 vent holes on the flash tube. A schematic diagram of flash tube assembly is shown in Fig. 1-2.

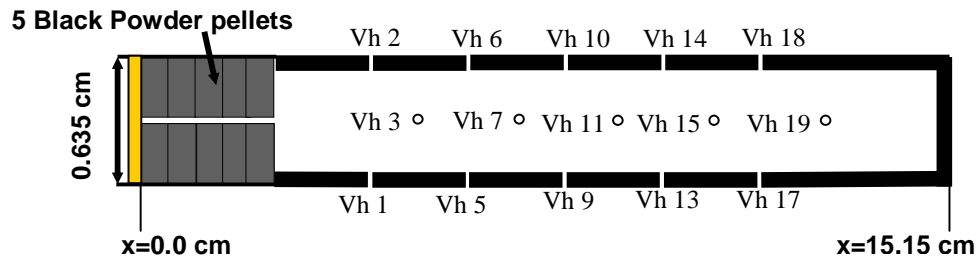


Figure 1-2: Cross-sectional view of the flash tube with 20 vent holes having a diameter of 0.165 cm.

1.1.2 Tail-boom section

The tail-boom section is the intermediate portion, which contains the flash tube assembly. The interior of the tail-boom section is cylindrical and contains closely packed ball propellants (referred as M48) in the annular region between flash tube and tail-boom. The surface of tail-boom section is perforated and it has 28 circular holes known as "vent holes." These vent holes are arranged in 8 rows around the middle exterior surface of the tail-boom section. Four such rows have 4 vent holes and the other four rows have 3 vent holes each. These rows are uniformly arranged on the middle exterior surface of the tail-boom section. There is a set of fins on the external surface of the tail-boom section on one end. This end is referred as the "primer end." These fins are used to aerodynamically stabilize the projectile flight through the airspace toward its target. The other end of the tail-boom section is referred as the "projectile end" and is conical in shape from the

outside. There are no vent holes in this part of the tail-boom section. The ball propellants in the tail-boom section are contained in a paper tube, which fits the tail-boom section from the inside and blocks the vent holes on the surface of tail boom till the pressure reaches a threshold rupture pressure. The tail-boom section receives the discharge of high-pressure and high-temperature combustion products from the flash tube. These combustion products contain both the gas-phase and condensed-phase species. These combustion products heat the ball propellants in the tail-boom section. The assembly of flash tube and tail-boom is also called the ignition cartridge or M1020 ignition cartridge. Each tail boom section has 28 vent holes. For the purpose of experimental pressure-time trace measurements, each tail boom section was drilled for 16 additional threaded holes so that pressure transducers could be mounted on the tail boom without affecting the discharge process from the original 28 vent holes. The tail-boom section and its components can be seen in Fig. 1-3.

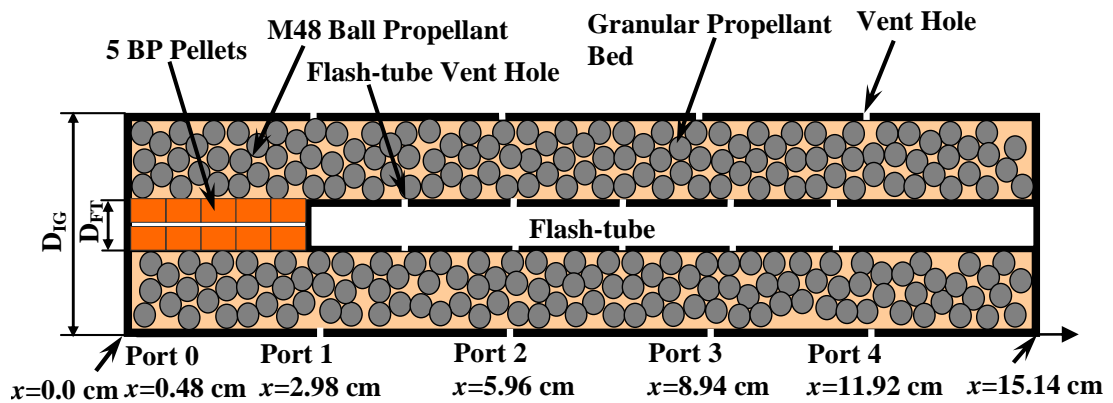


Figure 1-3: Cross-sectional view of the granular bed of the ignition cartridge.

1.1.3 Mortar tube section

The outermost portion of the 120mm mortar system is called mortar tube as shown in Fig. 1-1 and Fig. 1-4. The mortar tube section contains the ignition cartridge, horseshoe-shaped charge increments, and the projectile payload. There are four horseshoe-shaped propelling charges mounted outside of the tail-boom. These horseshoe-shaped charge increments are also filled with ball propellants. The mortar tube has a cylindrical shape from outside. The combustion products discharged from the tail-boom section heat the ball propellants in the horseshoe-shaped charge increments. The combustion of ball propellants in the charge increments results in pressurization in the mortar tube, which initiates the projectile motion and sustains projectile acceleration along the mortar tube. There is a sealing ring called the obturating ring between the mortar tube surface and projectile outer surface to minimize the leakage (called blow-by) of combustion products from the pressurized region in the mortar tube.



Figure 1-4: 120mm mortar cartridge family (from left to right): M934/M934A1 HE, M929 WP smoke, M930/M983 illumination, M931 practice [75].

1.2 Motivation

Simulation of the flame spreading and combustion processes in various parts of a 120mm mortar system under realistic firing conditions is imperative for design modifications and improvement of the system performance. The motivation for this work came through the firing experiments at the Picatinny Arsenal, in which mortar rounds did not cover the desired distance and some of them had damaged fin blades (*see* Fig. 1-5 and Fig. 1-6).

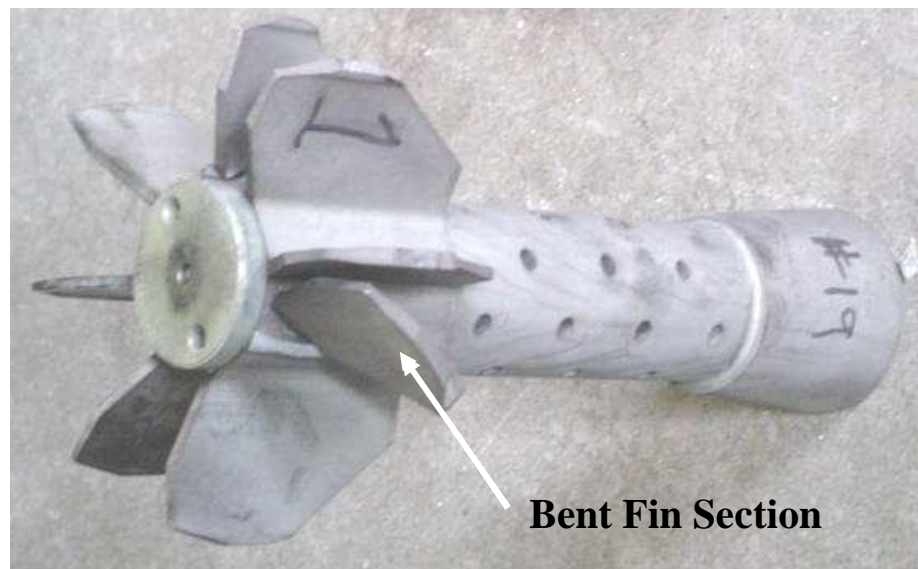


Figure 1-5: Damaged fin-blade during the 120mm mortar firings.

These instances provided the impetus for detailed modeling and stepwise experimental validation of the numerical predictions of the ballistic behavior of the ignition cartridge and propelling charges. The knowledge gained from the simulation of these processes can help to advance future improvements of the propulsion system to achieve increased safety for the operating personnel and greater reliability in the field. The numerical code can

add a new tool for designing, developing and supporting the production of mortar systems. The numerical code also enables cost effective design efforts by reducing costly live fire testing, characterizes combustion and pressurization processes in various components of the 120mm mortar system, and allows engineers to design mortar cartridges with improved performance to meet the needs of the future combat system and the future force. The model also assists evaluation of production issues through modeling and simulation of the effect of component variation on performance, potential cost savings proposals and other typical production questions. Therefore, it is beneficial to study the interior ballistics of the existing design.

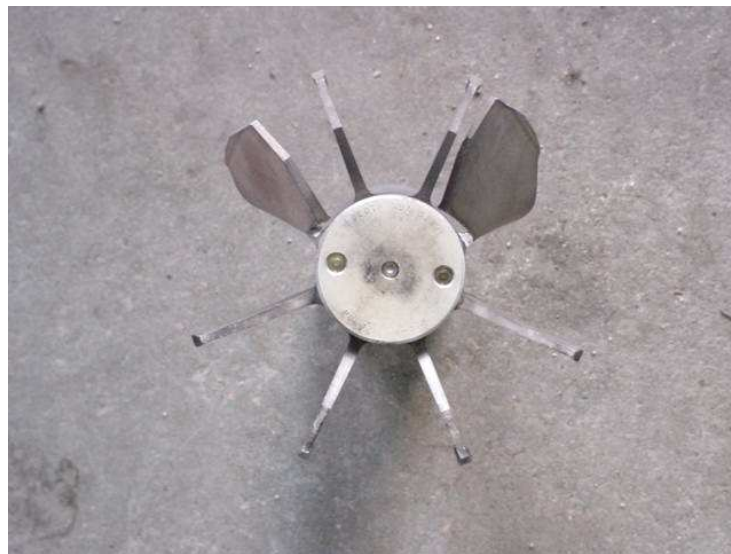


Figure 1-6: Damaged fin-blade during the 120mm mortar firings (end-view).

1.3 Specific objectives

The overall objective of this work was to develop a comprehensive theoretical model and an efficient numerical code to simulate the transient 3D interior ballistic processes of the 120mm mortar system. To achieve the above objective, major physical and chemical processes that need to be modeled and numerically simulated, are as following:

1. Simulation of rate of discharge of combustion products from flash tube to the granular bed in the tail-boom section.
2. Modeling and simulation of the burning behavior of granular propellants in the tail-boom section by two-phase processes, interaction of discharging jets of combustion products from flash tube section to the granular bed in tail-boom section.
3. Pressurization process, propagation of compression waves, rupture of the paper tube, discharge of both gas-phase and condensed-phase combustion products, and subsequent depressurization in the tail-boom.
4. Modeling and simulation of the interaction of the discharging jets of combustion products from the tail-boom section to the propelling charge increments in the mortar tube section to initiate combustion in the mortar tube.
5. Subsequent combustion of granular propellants in the free volume between projectile and mortar tube while the projectile is still stationary.

6. Advancement of the current theoretical model for describing the ignition and combustion processes in order to achieve better understanding of the detailed mechanism for performance improvement of a general mortar system.

All of the above steps were stepwise validated by experimental data.

1.4 General method of approach

In order to develop a comprehensive 3-dimensional mortar interior ballistics (3D-MIB) model and an efficient numerical code to simulate the interior ballistic processes of the 120mm mortar, various physical and chemical processes occurring in the mortar system must be considered. The mortar system consists of several parts including an ignition cartridge with a primer and a flash tube, propellant charge increments, the projectile body, and the mortar tube. To understand the ignition and combustion processes, the modeling and simulation of interior ballistic processes in the mortar system is performed in the following order.

1. An empirical flash tube sub-model for instantaneous energy and mass fluxes of the gas-phase and condensed-phase combustion products from the flash tube.
2. Mobile granular bed combustion sub-model based upon conservation equations of gas-phase and particle-phase, equation of state for gas in granular bed inside the tail boom, propellant burn rate, propellant surface temperature, and an intragranular stress relationship.
3. Sub-model to determine flame spreading rate instantaneous gas-phase and condense-phase properties along the granular bed inside the tail boom, including:

pressure, temperature, density, velocity, propellant burn rate, propellant surface temperature, intragranular stress, etc.

4. 3D combustion sub-model for propellant grains in the expanding free volume between projectile and mortar tube pressure distribution around the projectile.
5. A projectile dynamics sub-model to predict the projectile trajectory, including: projectile acceleration, velocity, and any undesirable combustion phenomena, in-bore p-t traces, effect of elevation angle, effect of design parameters, etc.
6. Integration of above sub models.
7. Model validation by experimental data up to the shot start.
8. Extending the theoretical model and numerical code to other mortar systems.

The major building blocks of the 3D-MIB code are shown in Fig. **1-7**. A detailed flow chart outlines the various steps in this work as shown in Fig. **1-8**.

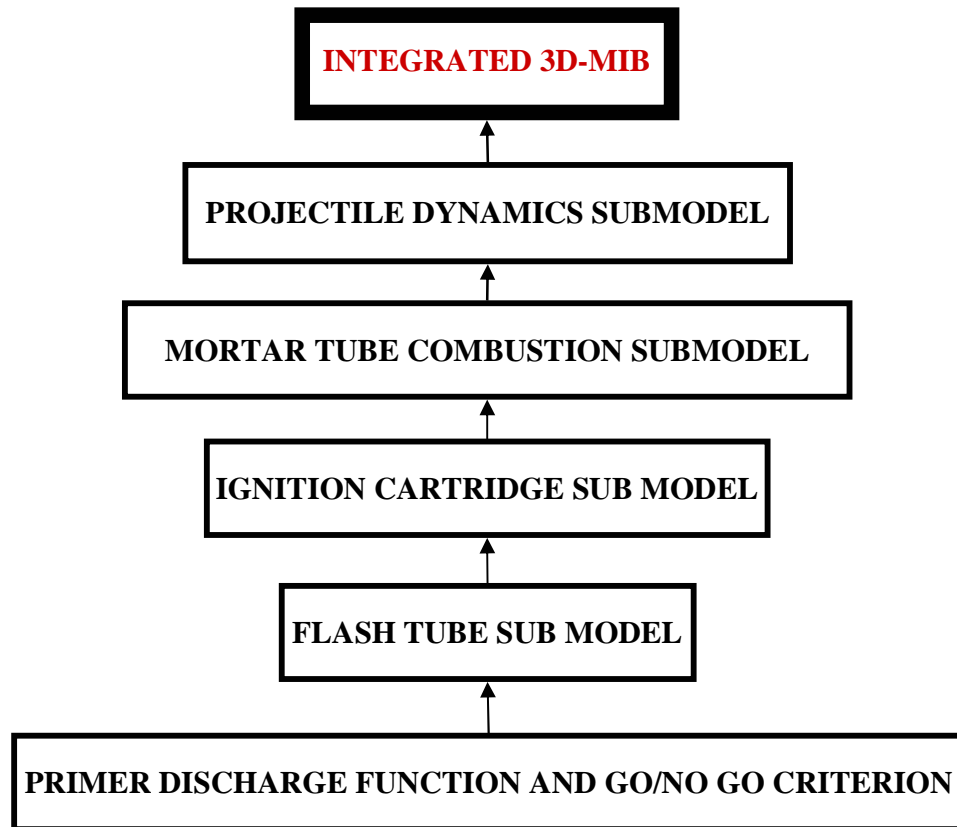


Figure 1-7: Major building blocks of the 3D-MIB code.

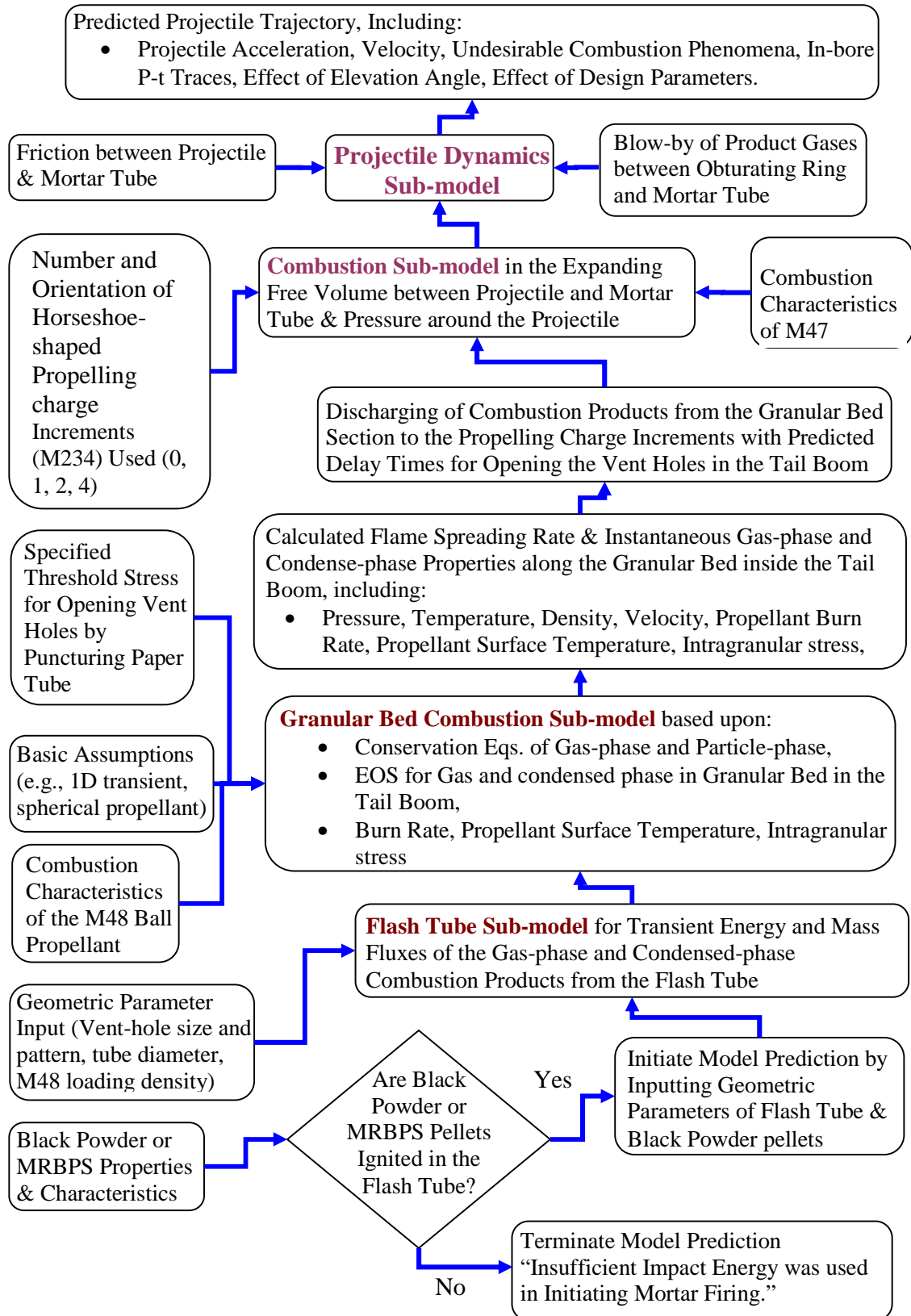


Figure 1-8: Overall flow chart for the 3D-MIB code.

1.5 Major advantages of theoretical/numerical work

Once validated, the 3D mortar interior ballistics (3D-MIB) code can be used to provide the guidance for design and performance improvements of the mortar projectile. For example, different primer material, flash tube geometry, pellets configurations, granular bed loading densities, vent-hole distributions can be studied to achieve increased reliability and higher performance. The numerical code can provide rigorous analysis and deeper understanding of the ballistic processes of the mortar system to proceed in the right direction for performance improvements. 3D-MIB code can provide predicted pressure-time traces and many other physical parameter variations at multiple axial locations. These physical parameter variations are useful for reducing the pressure-wave phenomena during the interior ballistic cycle in the mortar firing. The knowledge gained from the simulation of these processes can help to reduce the possibilities for fin-blade damage during operation in the field; thus, the code can help to achieve greater safety for the operating personnel with enhanced propulsion performance in the field. The 3D-MIB code can also be used as an analytical tool for studying any abnormal behavior of the mortar projectile during operation. The numerical simulation with the code can be used to partially replace the expensive experimental test runs.

1.6 Literature review

Traditionally, the multiphase flow modeling has been considered to be one of the most challenging problems of research in applied mathematics and computational fluid dynamics. There have been two major approaches to solve the two-phase flow problems

with one compressible phase and another incompressible phase. One approach is to treat the fluid phase as a continuum and the particulate second phase as single particles. This approach, which predicts the particle trajectories in the fluid phase as a result of forces acting on particles, is called the Lagrangian approach. This approach was used by Gough [18-23] for modeling of medium and large caliber gun systems with one-dimensional two-phase flows with area change. The interior ballistic computer code based on this approach is called XNOVAKTC (XKTC). This version of the code has chemical kinetics, tank gun features and end burning traveling charge increments. Other extensions include the modeling of single perforated monolithic charges, charges bonded to the tube or the projectile, and a ballistic control tube. The XKTC code was applied to the simulation of traveling charges with finite reaction zones. The Lagrangian approach used in the XKTC code was further extended to the two-dimensional and three-dimensional compressible flows to the development of next generation interior ballistic code known as NGEN3 [51-56]. This comprehensive code is developed by Army Research Laboratory (ARL) and it can be applied to simulate the interior ballistic processes in various systems including modularly packaged granular charges [51] [54], high-loading density (HLD) charges in which various solid propellant media are employed [55], and telescoped-ammunition propelling charge [56]. The NGEN3 code incorporates three-dimensional continuum equations along with auxiliary relations by treating gas-phase (i.e., air and gaseous combustion products) as continuous and solid propellants as discrete phase thereby using an Eulerian/Lagrangian approach to simulate the gun systems. Recently, Miura and Matsuo [46-48] have also used the Eulerian/Lagrangian type approach to perform two-dimensional axisymmetric calculations for the interior ballistic processes in an AGARD

gun and projectile motion through a long-slotted tubular gun. The AGARD (Advisory Group for Aerospace Research and Development) gun has been used as a standard test case to aid the development of UK internal ballistics codes for many years.

The other approach treats both solid-phase and gas-phase as continuum and appropriate conservation equations are solved for both phases. This approach is called the Eulerian approach. The Lagrangian approach has some advantages for solving those two-phase flows where the solid-phase experienced large accelerations. This approach is also useful in solving the two-phase consisting of poly-dispersed particle size distributions. The Eulerian approach has advantages in those cases where the concentrations of solid particles are high and the volume fraction of solid-phase could be a dominating flow parameter. The models based on Eulerian approach consists of governing equations for mass, momentum, and energy for both phase with the interfacial exchange terms between the two phase included in the source terms. Baer and Nunziato [3-4] were the first group to propose such models and those are generally referred to as B-N models. The B-N model has emerged as the most prominent multiphase flow model for simulating combustion of energetic materials such as explosives and propellants. The numerical algorithms to solve the Eulerian type model involves either solving the complete system, using the method of characteristics for example, or splitting the problem into a sequence of two sub-problems that included the solution to a transport equation followed by an ODE integration (to include the effect of algebraic source terms). Similar approaches have been adopted to solve the B-N equations as demonstrated by Bdzil et al. [5].

1.7 Survey of numerical methods

The governing equations for the two-phase compressible flows are almost always non-linear hyperbolic equations (*see* Appendix D). Numerically, it is generally accepted that the hyperbolic terms of the partial differential equations of the fluid flow are the terms that pose the most stringent requirements on the discretization techniques. Fortunately, the theory of hyperbolic systems is much more advanced than that for more complete mathematical models, such as the Navier-Stokes equations. There are two major numerical approaches to solve such equations, namely finite difference methods and finite volume methods. More recently, the finite element methods have also been to solve the governing equations of compressible flow.

The partial differential equations for any system represent a continuous physical problem. Numerical methods replace the continuous problem into a finite set of discrete values. This process is called discretization and it is accomplished by dividing the physical domain into a finite set of points or a finite number of volumes via a mesh or grid. In the finite difference approach, physical variables are calculated at each point in the physical domain and their derivatives are approximated by the differences between these points. In the finite volume approach, the physical quantities at each point in the mesh are calculated as an average over a finite volume. Averaging process indicates integration of physical quantities over a volume, which means that the finite volume approach is an integral approach. It is widely accepted that the non-linear hyperbolic equation may always consist of discontinuity and a numerical solution based on finite difference method may break down. In case of discontinuity, the derivatives of physical

quantities do not exist but it is always possible to perform integration over a discontinuous domain [58]. Thus, finite volume methods are more popular for solving such problems. Despite this, there have been some well known finite difference schemes to solve the problems in compressible flows.

A dimensionless parameter called Courant number; it is also known as the Courant-Friedrichs-Lewy number, or CFL number is used to determine the stability of any discretization method. Physically, the CFL number can be interpreted as the ratio of two speeds, namely the wave propagation speed in the partial differential equation in and the grid speed defined by the discretization of the domain. In case, there are more than one wave are present in the solution of the hyperbolic problem, the CFL number is calculated by using the maximum wave speed. The grid speed is defined as the ratio of spatial step and time step. Based on this definition, the CFL number is given by Eq. (1.1)

$$c \equiv \frac{\max(|\lambda_i|)}{\Delta x / \Delta t} \text{ where } \lambda_i \text{ is the wave propagation speed of the } i^{th} \text{ wave} \quad (\text{Eq. 1.1})$$

Courant, Isaacson and Rees [9] proposed a first order upwind method (also known as CIR scheme) to solve the hyperbolic PDEs. In this method, the spatial derivative is approximated by a first order Taylor series approximation. The Taylor series approximation to calculate derivative is explained in greater details in a book by Roache [58]. The term upwind (or upstream), refers to the fact that spatial differencing is performed using mesh points on the side from which information (wind) flows. The major disadvantage of this method is numerical dissipation, which results in heavy smearing at the discontinuities. Another first-order scheme is that of Lax and Friedrichs. The scheme is sometimes also called the Lax Method [32-36], or the scheme of Keller

and Lax. This does not require the differencing to be performed according to upwind directions. In this scheme, the physical variables in the time derivative are replaced by an average of these quantities at forward and backward points, thereby making this a second order accurate in space. However, the Lax and Friedrichs scheme is considered more diffusive than the CIR scheme. A scheme of historic as well as practical importance is that of Lax and Wendroff [37-38]. The basic Lax-Wendroff scheme is second-order accurate in both space and time. This scheme gives spurious oscillations in the numerical solution in the vicinity of sharp gradients, such as at discontinuities. Another second-order accurate scheme is the upwind method of Warming and Beam [78]. This scheme also gives oscillations in the vicinity of discontinuities. Yet another second order scheme is the Fromm scheme [14], which is also second order accurate in space. All second order schemes are dispersive in nature, which means that the results will suffer from oscillations. A short summary of all of the above-mentioned finite difference methods is shown in Table 1-1.

Due to the limitations of finite difference methods in problem with discontinuities like shock waves, finite volume methods are more often used. These methods are also called conservative methods because the partial differential equations are written in terms of conserved variables (like mass, momentum, and energy) and not in terms of primitive variables (like density, velocity, and pressure).

Table 1-1: Finite difference schemes for hyperbolic equations

<u>Numerical method</u>	<u>Explicit form</u>	<u>Accuracy</u>
Courant, Isaacson and Rees (CIR)	$u_i^{n+1} = u_i^n - c(u_i^n - u_{i-1}^n)$	First order in space and time
Lax and Friedrichs	$u_i^{n+1} = \frac{1}{2}(1+c)u_{i-1}^n + \frac{1}{2}(1-c)u_{i+1}^n$	Second order in space and first order in time
Lax-Wendroff	$u_i^{n+1} = \frac{1}{2}c(1+c)u_{i-1}^n + \frac{1}{2}(1-c^2)u_i^n - \frac{1}{2}c(1-c)u_{i+1}^n$	Second order in both space and time
Warming and Beam	$u_i^{n+1} = -\frac{1}{2}c(1-c)u_{i-2}^n + \frac{1}{2}(1-c)(2-c)u_i^n + c(2-c)u_{i-1}^n$	First order in space and time
Fromm	$u_i^{n+1} = -\frac{1}{4}c(1-c)u_{i-2}^n + \frac{1}{4}(5-c)cu_{i-1}^n + \frac{1}{4}(1-c)(4+c)u_i^n - \frac{1}{4}(1-c)cu_{i+1}^n$	First order in space and time

Godunov [15] first proposed a first order upwind scheme (an extension of the CIR scheme) for the equations of gas dynamic by solving a set of Riemann problems to obtain solution at a next time level. The Riemann problem is a fundamental problem in gas dynamics, which is described in extensive details in Appendix 5. Briefly, the Riemann problem arises in the conservation equations of gas dynamics if the initial data are prescribed as two semi-infinite states with a large jump at $x = 0$. The key observation is that if the approximation is viewed as a piecewise constant function, local Riemann problems are introduced at cell boundaries. However, the low accuracy and the complexity of this method meant that other methods were mostly used for a long time. The methods in use were typically based on modifications of simple first or second order schemes to improve the representation of discontinuities. There has been significant

improvement over the past several years in this area. A comprehensive literature review in this field is provided in chapter 7.

Chapter 2

IGNITION CARTRIDGE COMBUSTION SUB-MODEL

This chapter describes theoretical modeling, numerical technique, and results of numerical simulation of the interior ballistic processes in the ignition cartridge of a 120mm mortar system. The ignition cartridge consisted of a flash tube containing five black powder pellets and a tail-boom loaded with M48 granular propellant bed. The flash tube model solved ordinary differential equations and used experimental pressure-time traces to deduce the results; i.e., the discharge rates of gaseous and condensed-phase products, enthalpy, temperature, and velocity of the combustion products.

2.1 Introduction

The overall interior ballistic processes associated with the 120mm mortar ignition cartridge firing are extremely complicated. These processes include:

1. Initiation of primer function by firing pin impact;
2. Flame spreading over center-perforated black powder pellets;
3. Discharging of combustion products from the vent holes of the multi-perforated flash tube;
4. Heating the M48 ball propellants in the tail-boom section to ignition;
5. Flame spreading and combustion of ball propellants in the tail-boom section of the projectile;

6. Puncturing of the paper tube through the 28 vent holes of the tail boom section followed by discharge of propellant products.

It is intended that the above physical processes can be incorporated by coupling two different sub-models that are described below:

- Simulation of pressure and temperature traces in the flash tube (packed with black powder) using a generalized flow model.
- Simulation of pressure and temperature traces in the tail boom section (packed with ball propellants) using both generalized transient 1-D flow model.

The specific objectives of this chapter are:

- (i) Computation and analysis of the combustion and mass discharging processes in the flash tube;
- (ii) Simulation of interior ballistics processes in the granular bed with the original design of flash tube with black powder as the pyrotechnic material;
- (iii) Simulation and analysis of interior ballistics processes in the granular bed with the modified design of flash tube with vent-hole patterns and black powder as the pyrotechnic material;
- (iv) Comparison of the interior ballistic processes in the granular bed of M1020 ignition cartridge of the 120mm mortar system using Black Powder (BP), and Moisture Resistant Black Powder Substitute (MRBPS) as two different pyrotechnic materials.

2.2 Flash tube sub-model

The flash tube consists of an assembly of a primer and five black powder (BP) pellets contained in a partially perforated cylindrical tube. The primer is located near the BP pellets. The primer contains combustible pyrotechnic material, which ignites upon impact when the impact energy is above the threshold energy required for ignition. The hot products (both gas-phase and condensed-phase species) are generated from the primer heat and ignite the BP pellets. In the hollow cylindrical tube section following the BP pellets, there are twenty circular vent holes on the flash tube wall. This section is initially empty and it is closed by a steel pin on the other end, which is called the projectile end. Both gas-phase and condensed-phase products of combustion from primer and BP pellets expand into this empty cylindrical tube. These products are discharged from the flash tube through the twenty vent holes when a thin Mylar tape wrapped around the flash tube is ruptured locally. A schematic of flash tube assembly is shown in Fig. 2-1. The modeling of mass discharge process from the flash tube into the granular bed is described in following sections.

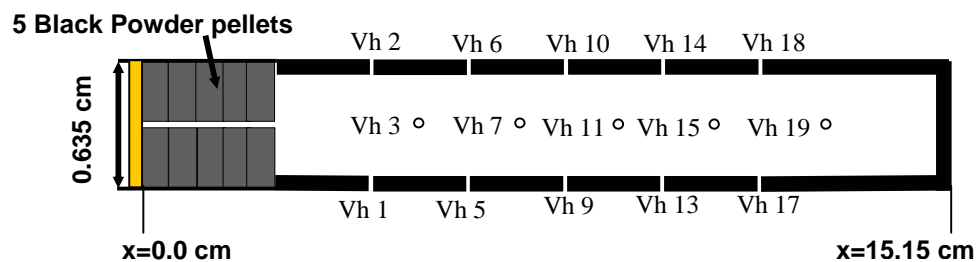


Figure 2-1: Cross-sectional view of the flash tube with 20 vent holes.

2.2.1 Go/No-Go ignition criterion for primer

The required initiation energy (E_{req}) in (in-oz) and striking velocity (V_{imp}) in (in/s) for Fed 150 primer were found to be related by the following equation by Boyer et al. [6].

$$E_{req} = \frac{aV_{imp}^2}{V_{imp}^2 - 2bg} \quad (\text{Eq. 2.1})$$

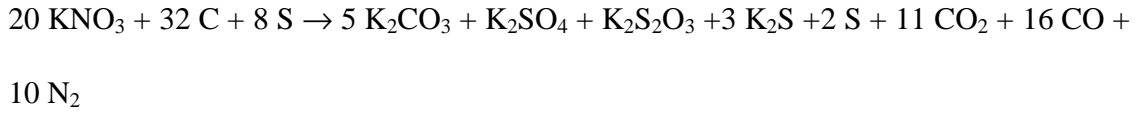
In Eq. (2.1), $a = 16.172$ in-oz, $b = 0.22405$ in and g (the gravitational acceleration) = $32.174 \text{ ft/s}^2 = 386.089 \text{ in/s}^2$. This equation can be regarded as the go/no-go criterion for successful ignition upon impact. In terms of the cgs units, the above equation can be written in the following form:

$$E_{req} = \frac{a^*V_{imp}^2}{V_{imp}^2 - 2b^*g} \quad (\text{Eq. 2.2})$$

In Eq. (2.2), the required initiation energy (E_{req}) in (cal) and striking velocity (V_{imp}) in (cm/s), $a^* = 0.02729$ cal, $b^* = 0.5691$ cm and g (the gravitational acceleration) = 980.665 cm/s^2 . At a given impact velocity, if the impact energy (E_{imp}) is greater than (E_{req}) ignition is considered to be successful.

2.2.2 Black powder combustion

The combustion reaction of black powder containing (a mixture of potassium nitrate, charcoal and sulfur) can be written as:



The combustion product has 43% of gaseous species and about 57% solid residues. This implies that the value of mass fraction of the condensed phase product (Ψ_c) is 0.57; i.e., $\Psi_c = 0.57$. The major flash tube output to be determined from empirical correlation includes the following:

2.2.3 Gas-phase mass flow rate from the nth set of vent holes

Gas-phase mass flow rate from a single vent hole of the nth set of vent holes on the flash tube can be calculated from the choked flow equation as shown by Eq. (2.3):

$$\dot{m}_{svhg,n}(t) = \Gamma(\gamma) \frac{P_n(t) A_{vh}}{\sqrt{RT_{g,n}(t)}} \quad (\text{Eq. 2.3})$$

where A_{vh} is the area of a single vent hole on the flash tube and it is given by Eq. (2.4).

$$A_{vh} = \pi d_{vh}^2 / 4 \quad (\text{Eq. 2.4})$$

The gaseous mass flow rate from the nth set of vent holes is related to $\dot{m}_{svhg,n}$ by

Eq. (2.5) as following:

$$\dot{m}_{vhg,n} = \dot{m}_{svhg,n} \times N_{vh,n} \quad (\text{Eq. 2.5})$$

In the above equation, $N_{vh,n}$ is the number of vent holes in the nth set of vent holes. The current flash tube design has 10 sets of vent holes along its length and each set has two

vent holes of the same size with a diameter of $d_{vh}=1.65$ mm. The function of $\Gamma(\gamma)$ is shown by Eq. (2.6):

$$\Gamma(\gamma) = \sqrt{\gamma} \left[\frac{2}{\gamma+1} \right]^{\frac{1}{2} \frac{\gamma+1}{\gamma-1}} \quad (\text{Eq. 2.6})$$

The combustion product of black powder is assumed to have $\gamma = 1.2$ and $R = 0.0598$ cal/(gm-K) = 250.2 J/(kg-K). The flame temperature was taken as 1,600 K before any thermocouple measurements. The pressure at nth vent hole was deduced from the experimental data of flash tube tests. Several pressure transducers were used for pressure measurement along the flash tube; including one near the end of the stainless steel pin (P_{pin}). In addition to P-t traces, it is possible to add ultra-fine thermocouple measurements at one or more intermediate locations. Therefore, for numerical calculations, the $P_n(t)$ and $T(t)$ traces are assumed to be known. In addition, the delay time for onset of mass and energy discharge from the nth vent hole ($t_{d,n}$) is considered known from the experimental data.

2.2.4 Condensed-phase mass flow rate from the nth set of vent holes

Condensed-phase mass flow rate from the nth set can be calculated from the total mass flow rate from the same set as shown by Eq. (2.7):

$$\dot{m}_{vhc,n}(t) = \Psi_c \dot{m}_{vht,n}(t) \quad (\text{Eq. 2.7})$$

where, $\dot{m}_{vhc,n}(t)$ is given by Eq. (2.8) as:

$$\dot{m}_{vht,n}(t) = \dot{m}_{vhg,n}(t) / [1 - \Psi_c] \quad (\text{Eq. 2.8})$$

2.2.5 Gas-phase energy flux and enthalpy from the nth set of vent holes

The energy flux and enthalpy of the discharging gaseous products from a vent hole of the nth set can be calculated as shown by Eq. (2.9):

$$\dot{H}_{vhg,n}''(t) = C_{pg} [T_{vhg,n}(t) - T_{amb}] \dot{m}_{svhg,n}(t) / A_{vh} \quad (\text{Eq. 2.9})$$

where $T_{vhg,n}(t)$ is the gas-phase temperature at the exit of the nth set of vent holes, and the relationship between $T_{vhg,n}(t)$ and $T_{g,n}(t)$ is given by Eq. (2.10):

$$\frac{T_{vhg,n}(t)}{T_{g,n}(t)} = \frac{2}{\gamma + 1} \quad (\text{Eq. 2.10})$$

The delay time for the energy flux of the nth vent hole is the same as that for the mass flow rate.

2.2.6 Condensed-phase energy flux from the nth set of vent holes

The energy flux and enthalpy of the discharging gaseous products from a vent hole of the nth set can be calculated by Eq. (2.11):

$$\dot{H}_{vhc,n}''(t) = C_{pc} [T_{vhc,n}(t) - T_{amb}] \dot{m}_{svhc,n}(t) / A_{vh} \quad (\text{Eq. 2.11})$$

where, $T_{vhg,n}(t)$ is the gas-phase temperature at the exit of the nth set of vent holes.

Again, the delay time for the energy flux of the nth vent hole is the same as that for the mass flow rate. It is reasonable to assume that

$$T_{c,n}(t) = T_{g,n}(t) \quad (\text{Eq. 2.12})$$

Before any reliable data is obtained for C_{pc} , it has been assumed that $C_{pc} = C_{pg}$.

2.2.7 Rate of energy loss to the flash tube

Due to the extremely rapid combustion and discharging event associated with the flash tube, it is assumed that the energy loss to the aluminum tube is negligible during the initial time. However, the heat transfer process from the ball propellant combustion will be included in the granular bed sub-model.

2.2.8 Protective tube resistance

The wall thickness of the plastic protective tube is very thin. Its resistance for penetration by hot combustion products of black powder is considered to be included in the delay times of vent holes on the flash tube. Therefore, no additional stress analysis is performed on this penetration process.

2.2.9 Calculated results from flash tube sub-model

The central objective of the flash tube sub-model is to calculate mass discharge rate of gaseous and condensed-phase products as a function of time and axial position. The flash tube has five segments of cylindrical center-perforated black powder pellets to generate combustion products as shown in Fig. 2-1, which are discharged through 20 vent holes along the surface of flash tube into the granular propellant bed at 10 different axial locations with vent holes alternate in their orientation. A separate experimental test set-up was used to obtain pressure-time traces from the flash tube at 5 different axial locations. A secure test apparatus was designed and fabricated to house the flash tube and its firing system. This was accomplished by mounting the flash tube between two stainless-steel stands on a test deck, as seen in Fig. 2-2.

A firing pin was installed inside of the test stand near the primer end of the flash tube to initiate the combustion process. This procedure was performed by a retracted rod, which held a heavy pendulum above the flash tube. The pendulum then swung from its initial position, impacting the firing pin with the same force used in the field. The impact of the pendulum on the firing pin provided the force necessary to compress the primer between the deformed primer cup and the anvil inside of the breech plug, initiating the impact-sensitive charge. The hot gases and particles generated from the percussion primer passed through the breech plug and into the flash tube, igniting the BP pellets loaded near in the primer end of the flash tube. The locations of each of the pressure transducer along with the cross section of the flash tube are shown in Fig. 2-3. In order to measure this fast combustion event, 5 PCB dynamic pressure transducers were installed

at pre-selected axial locations along the flash tube to measure the instantaneous chamber pressure at a sampling rate of 100,000 samples/s. These port locations started near the primer end and finished at the projectile end of the flash tube (P_1 to P_5). The pressure transducers were held in place by a clamp-mount assembly, which allowed for pressure measurements without hindering the discharging hot product gases through the vent holes. Generally, five pressure transducers were used simultaneously in any experiment owing to the limited space on the flash tube.

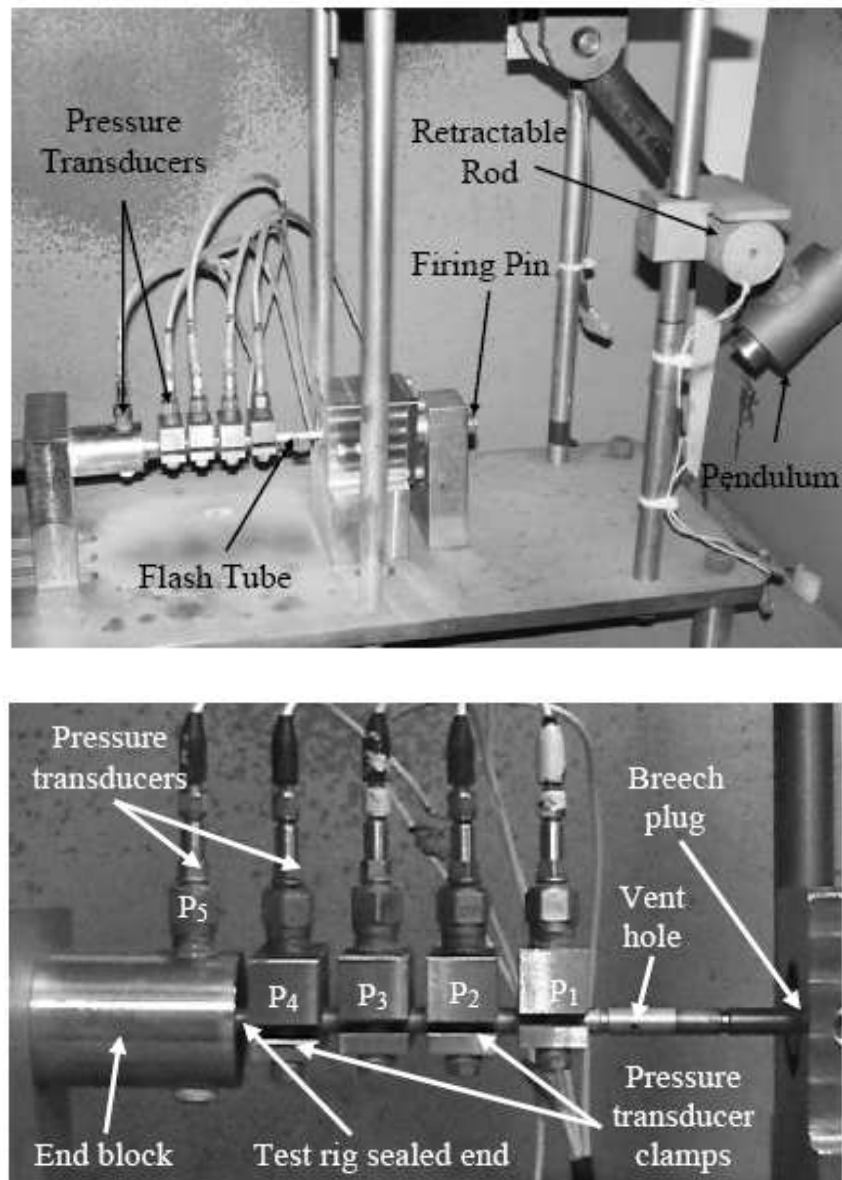


Figure 2-2: Photograph of the flash tube test setup (a) entire test rig and (b) zoomed-in portion of the instrumented flash tube [50].

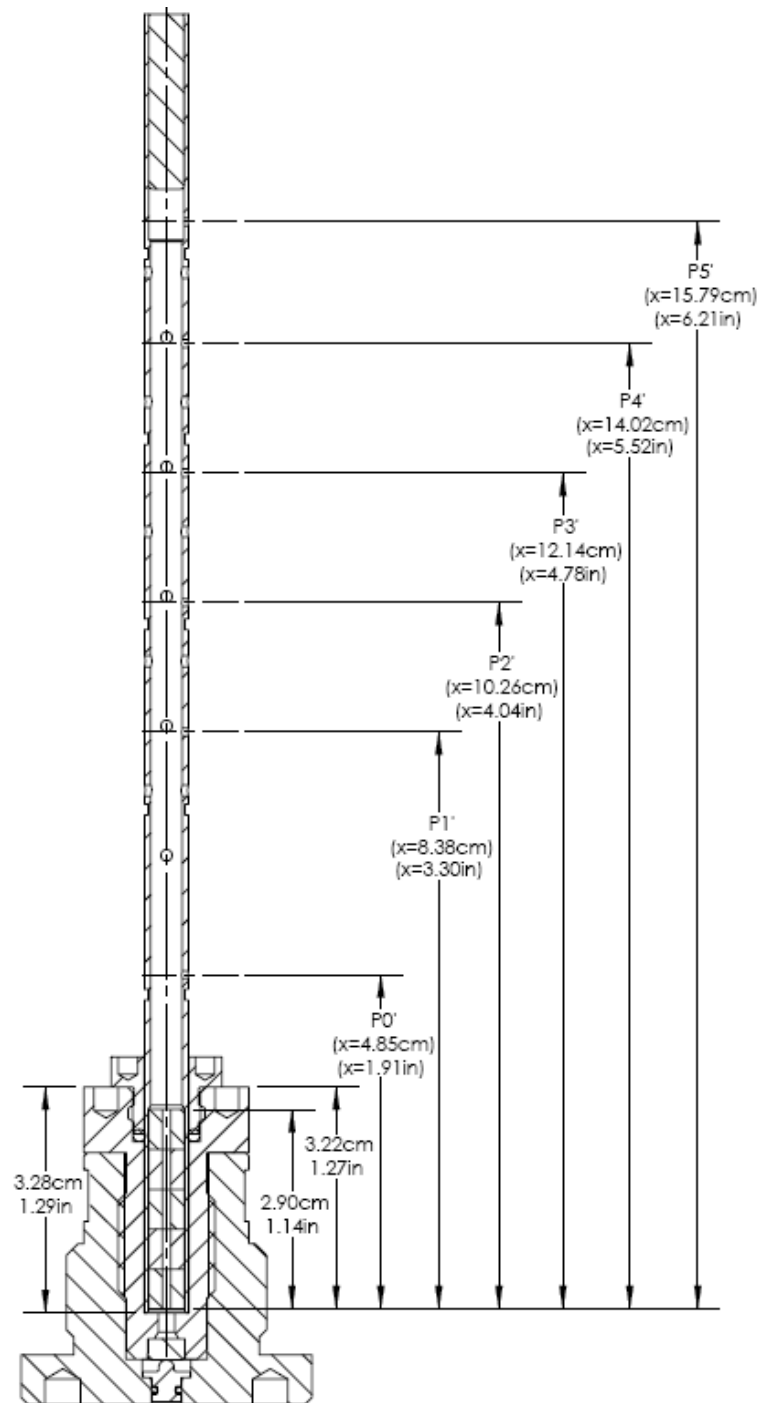


Figure 2-3: Cross sectional drawing of the flash tube and axial locations of pressure transducers used in this study.

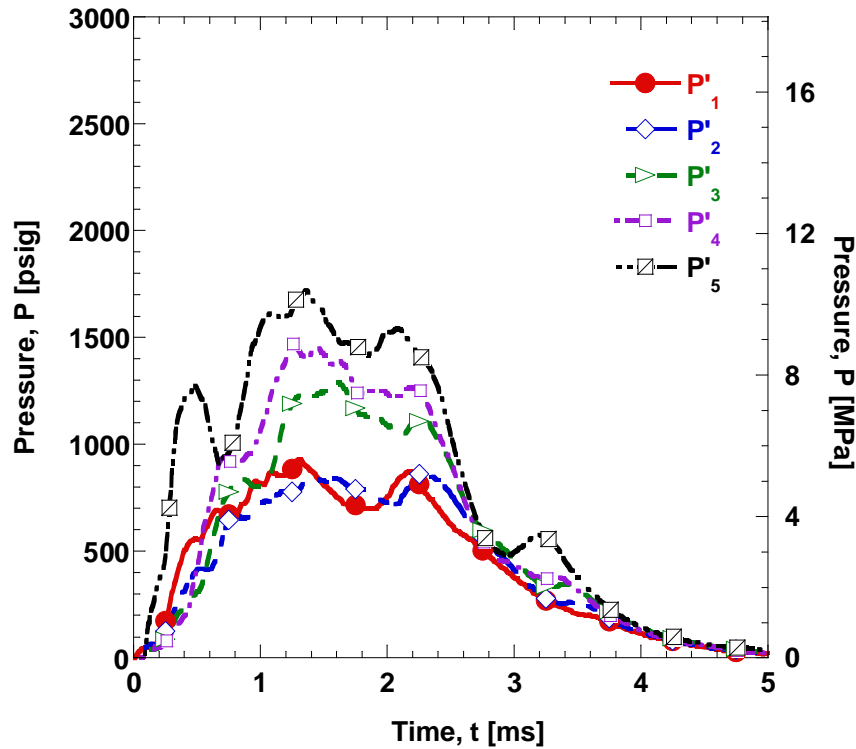


Figure 2-4: Recorded pressure-time traces from a flash tube test.

A typical pressure-time trace from the flash tube with 5 black powder pellets is shown in Fig. 2-4. It can be observed from this plot that the gauge P_1 sensed the initial rise in pressure earlier than other gauges, while gauge P_5 sensed the last increase in pressure, indicating presence of a strong axial pressure gradient that could have generated a pressure wave inside the flash tube. The gauge P_5 was observed to have the highest peak pressure level (between 1,700 and 2,700 psig over the tests conducted) and had the fastest pressure rise rate. The average time from ignition to depressurization of the flash tube for the baseline testing was around 2-3 ms. The order of first rise in pressure was chronological according to distance away from the primer ($P_1 \rightarrow P_5$).

In addition to the results shown in Fig. 2-4, four more tests were conducted and it was found that there was poor reproducibility among the baseline black powder tests. This characteristic is inherently associated with black powder pellets, even though these BP pellets used for all testing were from the same batch. The difference in peak pressures on average of these five tests between P_5 and P_1 was around $1,200 \pm 240$ psi. The overall average pressure at different axial locations also varied significantly. The average pressure at P_1 location for the five flash tube tests was 640 ± 47 psig, whereas the average pressure at P_5 location was $1,146 \pm 75$ psig for the test duration. The non-reproducibility of the baseline tests can be seen from the high standard deviation for peak pressures. This issue is discussed in greater details in sections 2.5-2.6. The measured pressure-time traces inside the flash tube were used to evaluate mass flow rate of gas-phase products through the vent holes using the flash tube sub-model. The physical parameters used in the flash tube sub-model are shown in Table 2-1.

The calculated mass flow rate-time traces from flash tube are shown in Fig. 2-5. Essentially, the deduced time variations of gaseous mass flow rates at various vent-hole locations are very similar to the pressure-time traces. All traces monotonically decay to zero around 4 ms. As shown in this figure, there is a significant difference in the mass flow rate-time traces at various axial locations. This implies the non-uniformity of gas-dynamic processes in the flash tube, which results in non-uniform discharge of combustion products in the granular bed. The mass flow rate is highest at the farthest axial location from the black powder pellets (gauge P_5 location) and lowest at the closest axial location (gauge P_1 location). This unusual behavior could be caused by the combined effect of (a) continuous compression of gaseous products generated from the

black powder and jammed at the far end of the stagnation zone of the flash tube, (b) discharging of combustion products through the vent holes on the surface of flash tube, and (c) heating of gaseous products due to wall friction as they travel along the tube.

In addition, there is a certain degree of non-repeatability in the pressure-time traces from the flash tube. A statistical analysis of these 5 baseline tests showed that the total mass flow rates varied as much as 15%, indicating poor reproducibility of BP pellets with the original M1020 flash tube design

Table 2-1: Input parameters for the flash tube sub-model

<u>Description</u>	<u>Input parameter</u>	<u>Value</u>	<u>Units</u>	<u>Source</u>
Density of Black Powder	ρ_{prop}	1677	kg/m ³	literature and calculation
Density of Condensed-phase Products	ρ_{cond}	1900	kg/m ³	assumed
Specific Heat Ratio	γ	1.2	-	assumed
Flame Temperature	T_f	923	K	measured
Initial Chamber Volume	V_c	3.4422×10^{-6}	m ³	calculation
Area of Throat (0.1321 cm diameter)	A_t	1.37014×10^{-6}	m ²	measurement
Molecular Weight of Product Gases	MW_g	33.526	kg/kmol	literature and calculation

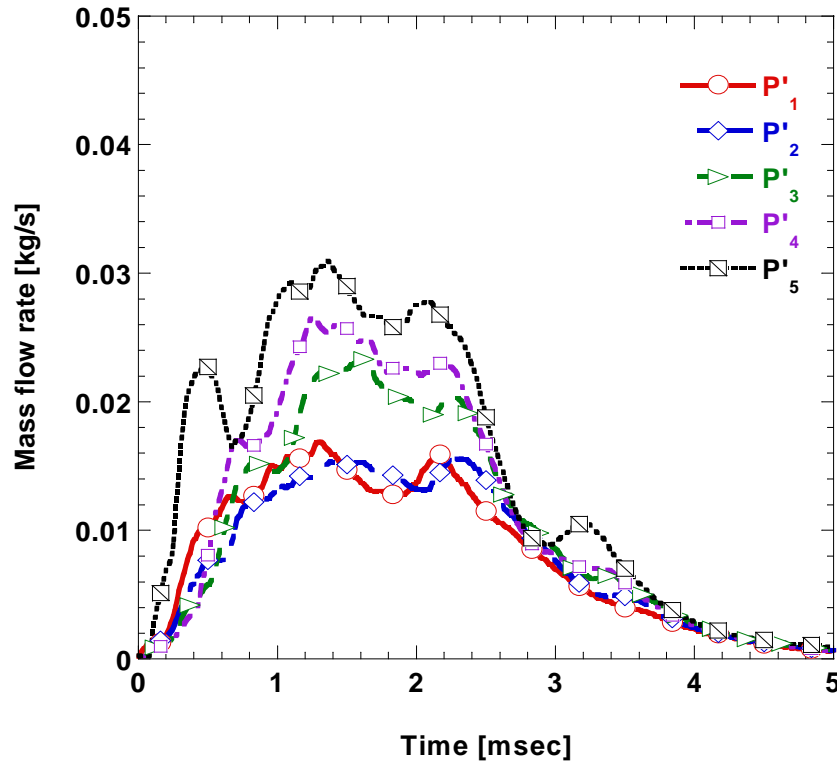


Figure 2-5: Deduced gas-phase mass flow rates-time traces from the flash tube using flash tube sub-model.

From a separate experimental characterization study of the flash tube discharging behavior, the measured pressure-time traces inside the flash tube were used to evaluate mass flow rate of gas-phase products through the vent holes by the empirical flash tube sub-model. These deduced mass flow rates at different axial locations are presented in Fig. 2-5.

2.3 Granular bed combustion sub-model

Prior to the solution of the complete problem, it is better to solve the problem without propellant charge increments loaded on the external surfaces of the tail boom.

Without being confined in the mortar tube, the combustion products generated from the ignition cartridge are discharged directly into the atmosphere. A schematic drawing of the longitudinal cross-sectional view of the ignition cartridge is shown in Fig. 2-6. In this design, the flash tube is initially loaded with five center-perforated cylindrical black powder pellets to generate combustion products, which flows into its cavity region and are partially discharged into the granular bed through 20 vent holes along the surface of flash tube. The existence of strong pressure waves in the combustion of ball propellants in the granular bed is believed to be caused mainly by the non-uniform discharge of both gas-phase and condensed-phase products from flash tube into the tail boom section of the projectile as shown in an experimental work performed by Kuo et al. [30]. Their test data obtained from 65° ignition cartridge testing provided useful information about the flame spreading and combustion processes inside the tail boom. These data were utilized for model validation in the present study.

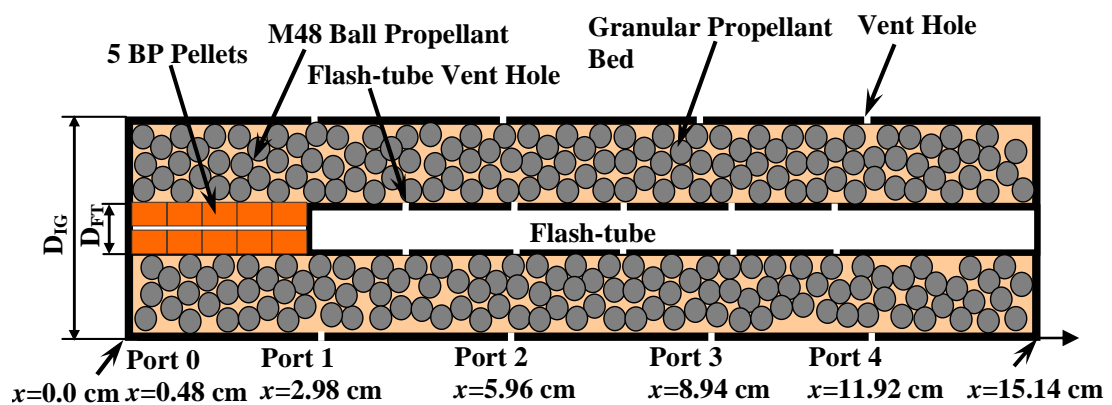


Figure 2-6: Cross-sectional view of the granular bed of the ignition cartridge.

2.3.1 Method of approach

In this sub-model, the governing equations for the granular bed combustion processes are simulated in an unsteady and pseudo one-dimensional form. These equations represent a system of hyperbolic partial differential equations. They are transformed into a system of ordinary differential equations using the method of characteristics [68]. For hyperbolic equations, the flow properties at each point in the flow field depend on those properties in a finite region of the upstream flow field, but are independent of the conditions at the next time step. Thus, marching-type numerical methods may be applied for obtaining the solutions of such flow fields. Method of characteristics is the most accurate marching-type method applicable to quasi-linear partial differential equations. The concept of characteristics may be introduced from several points of view (*see Appendix D for hyperbolic equations*):

1. From a physical point of view, a characteristic curve is defined as the path of propagation of a physical disturbance. For example, in a supersonic flow field, disturbances are propagated along the Mach lines of the flow. These Mach lines are generally known as Prandtl-Meyer waves.
2. From a purely heuristics point of view, a characteristic curve is defined as a curve along which the governing partial differential equations can be manipulated into total differential equations.
3. From a more rigorous mathematical point of view, a characteristic curve is a curve across which the derivatives of a physical property may be discontinuous, while the property itself remains continuous.

4. From a most rigorous mathematical point of view, a characteristic curve is defined as a curve along which the partial differential equations reduce to compatibility equations, which link the flow property changes along the characteristic curves. These compatibility equations can be solved algebraically.

The above concepts have been employed for developing the numerical procedure for solving the system of hyperbolic partial differential equations described in this report. The Noble-Abel equation of state for the gas-phase mixture was adopted in this formulation to account for the non-ideal behavior of the gas-phase. The eigenvalues and eigenvectors of the system of equations were determined from mathematical derivations. The eigenvalues were then used to form the characteristic equations of the system. Using characteristic equations and eigenvectors, the partial differential equations were transformed into ordinary differential equations. Finally, these ordinary differential equations were then discretized to form linear equations for numerical solution.

2.3.2 Basic assumptions

A number of basic assumptions, listed below, have been made in order to make the problem tractable during the theoretical study.

1. The ball propellant grains are assumed to be spherical in shape and they are uniformly distributed initially in the annular space between the flash tube and propellant container tube before the combustion event.
2. Due to the tightly packed initial condition and the relatively small volume between the flash tube and propellant container tube, the flow field in the

granular bed is considered to be independent of azimuthal angle (θ) and the radial distance (r) from the centerline. This implies that the two-phase flow is only a function of time (t) and axial position (x) in the tail boom section of the ignition cartridge.

3. The opening of any vent holes on the tail boom is caused by the mechanical shearing effect of the unsupported propellant container-tube wall instead of burning through by the hot combustion products.
4. It is assumed that the paper tube material does not participate in the overall combustion process since very small amount of energy release is associated with the combustion of propellant container tube.
5. The Noble-Abel dense gas law is assumed to be suitable for describing the non-ideal gas effect in the granular bed.
6. The intragranular stress relationship for WC 870 ball propellants can be applied to ball propellants in tail-boom section.
7. The flow resistance correlation for WC 870 ball propellants can also be applied to M48 (WC 816) ball propellants.

2.3.3 Governing equations

To determine the transient gas dynamic behavior of hot igniter gas and particle penetration, flame propagation, chamber pressurization and combustion processes in the granular propellant bed, the mass, momentum and energy equations for the gas phase and the mass and momentum equations for the solid phase are derived and expressed in a

quasi one-dimensional form. The gas-phase control volume is the void portion occupied by the gas-phase material, while the remaining portion occupied by the particles is considered the control volume for the particle-phase material. The overall cross-sectional area of the annular space is A and it remains unchanged. The specific surface area of the granular propellants is A_s , which represents the total exposed surface area of the propellant in the control volume per unit spatial volume. The value of A_s can be calculated from instantaneous values of particle radius r_p , and porosity or void fraction ϕ by Eq. (2.13):

$$A_s = \frac{3}{r_p} (1 - \phi_g) = \frac{3}{r_p} (1 - \phi) \quad (\text{Eq. 2.13})$$

The void fraction is defined by Eq. (2.14) as following:

$$\phi = \frac{\text{void volume}}{\text{total volume}} = 1 - \tilde{n} \left(\frac{4}{3} \pi r_p^3 \right) \quad (\text{Eq. 2.14})$$

The gas phase mass equation is by Eq. (2.15):

$$\begin{aligned} \frac{\partial(\phi\rho)}{\partial t} + \frac{1}{A} \frac{\partial(\phi\rho U_g A)}{\partial x} &= I_1 \\ I_1 &= A_{sb} \rho_p r_b + \dot{m}_{FTvhg} / V_{cv} - \dot{m}_{TBvhg} / V_{cv} \end{aligned} \quad (\text{Eq. 2.15})$$

In the above Eq. (2.15), A_{sb} is the specific surface area of the burning particles in the control volume which is given by Eq. (2.16), \dot{m}_{FTvhg} is the sum of gaseous mass flow rate from all associated vent holes from the flash tube into the control volume of the granular bed and $V_{cv} = A\Delta x$. The parameter \dot{m}_{TBvhg} is the sum of gaseous mass flow rate from all associated vent holes from the tail-boom section out of the control volume of the granular bed.

$$A_{sb}(t) = A_s \frac{\theta_0^o + \theta_{fs}^o (t - t_{ID})}{180} \quad (\text{Eq. 2.16})$$

In Eq. (2.16), θ_0^o represents the half angle of the exhaust jet coming out of the vent hole of the flash tube and θ_{fs}^o is the angular flame spreading rate in the propellant cup. The term on the numerator of Eq. (2.16) represents the half angle covering the instantaneous zone of the burning particles. The maximum value of the half angle is 180° . The propellant particle phase mass equation is Eq. (2.17) as following:

$$\begin{aligned} \frac{\partial[(1-\phi)\rho_p]}{\partial t} + \frac{1}{A} \frac{\partial[(1-\phi)\rho_p U_p A]}{\partial x} &= I_2 \\ I_2 &= -A_{sb}\rho_p r_b + \dot{m}_{FTVhc}/V_{cv} - \dot{m}_{TBVhc}/V_{cv} \end{aligned} \quad (\text{Eq. 2.17})$$

The gas phase momentum equation is Eq. (2.18) as following:

$$\begin{aligned} \frac{\partial(\phi\rho U_g)}{\partial t} + \frac{1}{A} \frac{\partial(\phi\rho U_g^2 A)}{\partial x} + \frac{1}{A} \frac{\partial(\phi P A)}{\partial x} &= I_3 \\ I_3 &= A_{sb}r_b\rho_p U_p - A_s D_t \end{aligned} \quad (\text{Eq. 2.18})$$

The particle-phase momentum equation is Eq. (2.19) as following:

$$\begin{aligned} \frac{\partial[(1-\phi)\rho_p U_p]}{\partial t} + \frac{1}{A} \frac{\partial[(1-\phi)\rho_p U_p^2 A]}{\partial x} - \frac{1}{A} \frac{\partial[(1-\phi)\tau_p A]}{\partial x} &= I_4 \\ I_4 &= -A_{sb}r_b\rho_p U_p + A_s D_t \end{aligned} \quad (\text{Eq. 2.19})$$

It is important to note that D_t is the total drag force between the gas and particle phases.

It is equal to the sum of the drag due to the presence of relative velocity between the gas and particle phases and the drag due to the porosity gradient as shown by Eq. (2.20):

$$D_t = D_v + D_p = D_v - \frac{P}{A_s} \frac{\partial\phi}{\partial x} \quad (\text{Eq. 2.20})$$

For the non-fluidized region, the correlation obtained by Kuo *et al.* [29] was used for D_v . For the fluidized region, the expression for D_v is deduced from Andersson's [1] expression, which is valid for porosities ranging from 0.45 to 1.0 and particle Reynolds number (Re_p) from 0.003 to 2,000. Although the Reynolds number range is not wide enough to cover the variation in the overall transient process, it is the best correlation available in the literature for spherical particles. For convective heat transfer calculations, Denton's [10] formula was used for the non-fluidized region. For fluidized regions, h_c was obtained from Rowe and Claxton's [67] correlation. The gas phase energy equation is Eq. (2.21) as following:

$$\begin{aligned} \frac{\partial(\rho\phi e)}{\partial t} + \frac{\partial(\rho\phi U_g e)}{\partial x} + \frac{\partial(P\phi U_g)}{\partial x} = I_5 \\ I_5 = \left(\dot{m}_{FTvhg} / V_{cv} \right) \left(h_{FTvhg} + \frac{V_{FTvhg}^2}{2} \right) - A_s h_t (T - T_{ps}) + A_{sb} r_b \rho_p \left(h_{chem} + \frac{U_p^2}{2} \right) \\ - \left(\dot{m}_{TBvhg} / V_{cv} \right) \left(h_{TBvhg} + \frac{V_{TBvhg}^2}{2} \right) - A_s D_v U_p \end{aligned} \quad (\text{Eq. 2.21})$$

In the above Eq. (2.21), h_{FTvhg} is the average enthalpy of discharging gases from all associated vent holes of the flash tube into a given control volume of the granular bed and $V_{FTvhg} = \sqrt{\gamma R T_{FTvhg,n}}$. The last term, associated with the sum of gaseous mass flow rate from all related vent holes of the tail-boom section out of the control volume of the granular bed $\left(\dot{m}_{TBvhg} \right)$, represents the outgoing total enthalpy to the mortar tube after the local propellant cup wall is ruptured.

It should be noted that the governing equations for the gas and particle phases are simplified by neglecting some terms. These higher-order neglected terms are: (a) the

viscous normal stress in the gas-phase momentum equation, (b) the shear force at the combustor wall for the particles in the particle momentum equation (this is justified since the contact surface area between the particles and chamber wall is small and also the initial porosity considered is high), (c) the gas-phase heat conduction term, (d) the work done by the viscous normal stress in the gas-phase energy equation, (e) the heat loss to the chamber wall in the extremely short transient combustion experiments, (f) the rate of pressure work for the dilatation of the gaseous control volume in the gas-phase energy equation, and (g) the rate of change of the total heat transfer coefficient in the calculation of propellant surface temperature. The relationship between the discharging solid particles and gases from the vent holes of the tail boom is considered to be similar to that from the flash tube; thus,

$$\dot{m}_{TBvhc}(t) = \dot{m}_{TBvhg}(t) \frac{1-\phi}{\phi} \quad (\text{Eq. 2.22})$$

2.3.4 Equation of state in granular bed

In addition to the above governing equations, the equations of state for gas-and particle-phases must be specified. The co-volume effect becomes important at high pressures, so the Noble-Abel dense gas law was used. It is shown in Eq. (2.23):

$$P \left(\frac{1}{\rho} - b \right) = RT \quad (\text{Eq. 2.23})$$

The solid-propellant particles are assumed to be incompressible. Therefore, the statement of a constant density for the solid-propellant particles serves as the equation of state for the particles, i.e., $\rho_p = \text{constant}$.

2.3.5 Intragranular stress

To complete the theoretical model it is necessary to specify several empirical correlations: the intragranular stress transmitted through the packed granular particles, the flow resistance due to the drag force between particle and gas phases, the convective heat transfer coefficient and the regression rates of the solid propellant particles. The following relation shown by Eq. (2.24) relates the intragranular stress to the speed of sound:

$$c^2 = \frac{1}{\rho_p} \frac{d[(1-\phi)\tau_p]}{d\phi} \quad (\text{Eq. 2.24})$$

Here c is the speed of sound in the aggregate of ball propellants. The speed of sound in solid propellant aggregate can also be expressed by Eq. (2.25):

$$c^2 = c_{ref}^2 \left(\frac{\phi_c}{\phi} \right)^2 \quad (\text{Eq. 2.25})$$

In the above Eq. (2.25), c_{ref} is the speed of sound in solid at critical porosity ϕ_c . The critical porosity is defined as the upper limit of void fraction above which the aggregate would be dispersed and no sound transmission can take place through the dispersed

particles. Therefore, when $\phi = \phi_c$, $c = c_{ref}$ and $\tau_p = 0$. The expression for intragranular stress can be written by Eq. (2.26):

$$\tau_p = \rho_p c_{ref}^2 \frac{\phi_c (\phi_c - \phi)}{\phi (1 - \phi)} \quad (\text{Eq. 2.26})$$

Differentiating Eq. (2.26) with respect to x , we get the following: Eq. (2.27)

$$\frac{\partial}{\partial x} [(1 - \phi) \tau_p] = \rho_p \left(\frac{c_{ref}^2 \phi_c^2}{\phi^2} \right) \frac{\partial \phi}{\partial x} = \rho_p c^2 \frac{\partial \phi}{\partial x} \quad (\text{Eq. 2.27})$$

This has been used in particle-phase momentum equation.

2.3.6 Burning rate expression of ball propellants

For burning rate calculations, the Lenoir and Robbillard [39] semi empirical burning rate law was adopted. This burning rate expression is shown by Eq. (2.28) as:

$$r_b = aP^n + K_e h_c \exp \left(- \frac{\beta r_b \rho_p}{\rho |U_g - U_p|} \right) \quad (\text{Eq. 2.28})$$

Here h_c is the local zero blowing convective heat transfer coefficient, K_e is the erosive-burning constant, and the β is erosive burning exponent. The rate of change in the particle radius is governed by the propellant burning rate given by Eq. (2.29):

$$\frac{dr_p}{dt} = -r_b \quad (\text{Eq. 2.29})$$

2.3.7 Formulation of the heat equation

It is proposed that the condensed phase mass coming from flash tube into the tail boom is deposited on the surface of ball propellants in form of a thin coating. This phenomenon has been confirmed by experiments at the High Pressure Combustion Laboratory through previous studies. These ball propellants are a fraction of all the ball propellants in the tail boom and these are located in the vicinity of vent holes on the flash tube as shown in Fig 2-7.

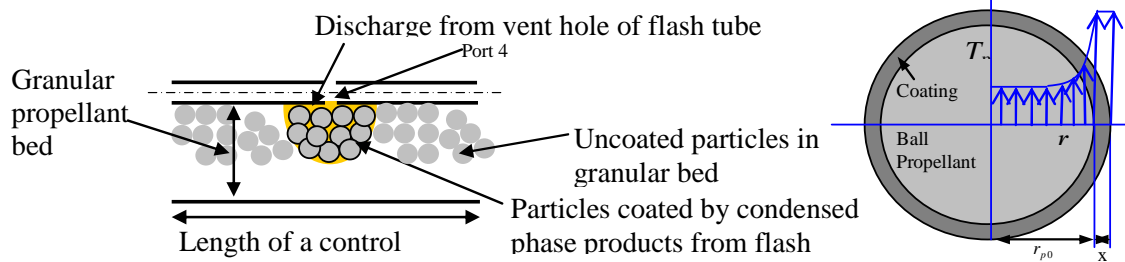


Figure 2-7: Region of coated ball propellant particles in the vicinity of a flash-tube vent hole and temperature profile in a coated particle.

There are both gas-phase and condensed-phase combustion products in the discharging jet from the vent holes of the flash tube. The gas-phase products can penetrate the granular bed in larger regions. However, the condensed-phase products have usually limited distance of penetration. The heat content in the condensed-phase products can have a very strong impact on the ignition process of the granular propellants, since they can directly deposit their energy onto the ball propellant surface during the coating process. Furthermore, the gas-phase products expand during the discharging process and a part of their thermal energy is converted into the kinetic energy during expansion. The condensed-phase products experience a very limited expansion

during the discharging process. Thus, their thermal energy is higher than that of gas-phase products. In view of these reasons, the conductive heat transfer from the thin coated layer of condensed phase to the ball propellant is the dominant heat-transfer mechanism to attain ignition for ball propellants in the granular bed. The temperature profile in the thin coated layer and the partially heated ball propellant is shown in Fig. 2-7(b). The solid propellant particle is referred to as region I. The thin condensed phase coating has a thickness and it is referred to as region II. The surface of propellant particle is the boundary of region I. In this case, only the surface temperature of propellant particle is of interest. In order to determine the surface temperature variation with time, the heat equation for the propellant particle in spherical coordinates is used as given by Eq. (2.30):

$$\frac{\partial}{\partial t}(\rho_p c_p T_p) = \frac{1}{r^2} \frac{\partial}{\partial r} \left(r^2 k_p \frac{\partial T_p}{\partial r} \right) \quad (\text{Eq. 2.30})$$

In the above equation, ρ_p is the mass density of propellant, c_p is the heat capacity of propellant, k_p is thermal conductivity of propellant and T_p is the temperature as a function of r and t . In order to solve the heat equation, the initial and boundary conditions given by Eq. (2.31) were used:

$$\begin{aligned} \text{IC: } T_p(t=0, r) &= T_0 \\ \text{BC: } \partial T_p(t, 0) / \partial r &= 0 \\ \partial T_p(t, r_{p0}) / \partial r &= \dot{q}_{\text{loss}, II}(t) / k_p = Z(t) \end{aligned} \quad (\text{Eq. 2.31})$$

In the above, $\dot{q}_{loss,II}''$ is the heat loss by thin condensed phase coating to the solid propellant particle by conduction. This term is given by heat flux balance at the interface of region I and II as shown by Eq. (2.32).

$$\dot{q}_{loss,II}'' = k_p \left. \frac{\partial T_p}{\partial r} \right|_{r=r_{p0}^-} = k_l \left. \frac{\partial T_l}{\partial r} \right|_{r=r_{p0}^+} = k_l \frac{(T_l - T_p)}{\delta_w} \quad (\text{Eq. 2.32})$$

In Eq. (2.32), T_l is the temperature in region II, k_l is thermal conductivity of condensed phase and δ_w is the minimum of thermal wave penetration depth in condensed phase and thickness of coating. The liquid coating thickness (δ_l) can be solved from following equation:

$$\frac{d(4\pi r_{p0}^2 \rho_l \delta_l)}{dt} = \underbrace{\frac{\dot{m}_{FTvhc}}{n_{cp}}}_{\text{rate of liquid mass deposition per particle}} \quad (\text{Eq. 2.33})$$

where n_{cp} is the number of coated particles, and ρ_l the density of liquid coating. In order to solve for T_l , energy balance equation is used for region II as given by Eq. (2.34):

$$\frac{d[c_l \rho_l (4\pi r_{p0}^2 \delta_l) T_l]}{dt} = \underbrace{\frac{\dot{m}_{FTvhc}}{n_{cp}} c_l T_{F,Pellet}}_{\text{Energy input from flash tube}} - \underbrace{4\pi r_{p0}^2 \dot{q}_{loss,II}''}_{\text{Energy loss to propellant}} \quad (\text{Eq. 2.34})$$

In the above equation, $T_{F,Pellet}$ is the temperature of liquid coating at the time of discharge from the flash tube and c_l the specific heat of liquid coating, respectively. The detailed derivation for the explicit form of propellant surface temperature equation is shown in Appendix A.

2.3.8 Method of characteristics formulation

The system of governing equations is a set of six first-order, coupled, non-linear, inhomogeneous partial differential equations, which are hyperbolic in nature. After simplification and manipulation, the governing equations for this problem reduce to following inhomogeneous linear partial differential equations of first order. These equations can be represented by a vector equation shown in Eq. (2.35):

$$\frac{\partial}{\partial t} \begin{bmatrix} U_g & T & P & U_p & \phi \end{bmatrix}^T = \mathbf{M} \frac{\partial}{\partial x} \begin{bmatrix} U_g & T & P & U_p & \phi \end{bmatrix}^T + \mathbf{I}_h \quad (\text{Eq. 2.35})$$

where the coefficient matrix \mathbf{M} and the inhomogeneous terms (\mathbf{I}_h) are defined by Eqs. (2.36)- (2.37):

$$\mathbf{M} \equiv \begin{bmatrix} -U_g & 0 & -\frac{1}{\rho} & 0 & -\frac{P}{\phi\rho} \\ -(\gamma-1)T & -U_g & 0 & 0 & 0 \\ -\gamma P & 0 & -U_g & -\frac{P^2(1-\phi)}{T\phi} & 0 \\ 0 & 0 & 0 & -U_p & \frac{c^2}{(1-\phi)} \\ 0 & 0 & 0 & (1-\phi) & -U_p \end{bmatrix} \quad (\text{Eq. 2.36})$$

$$\mathbf{I}_h \equiv \begin{bmatrix} -\frac{U_g}{\rho\phi} I_1 + \frac{1}{\rho\phi} I_3 \\ \frac{1}{C_v\rho\phi} I_5 - \frac{T}{\rho\phi} I_1 + \frac{U_g^2}{2C_v\rho\phi} I_1 - \frac{U_g}{C_v\rho\phi} I_3 \\ \frac{P}{C_v\rho\phi T} I_5 + \frac{PU_g^2}{2C_v\rho\phi T} I_1 + \frac{P^2}{\phi\rho_p\rho RT} I_2 - \frac{PU_g}{C_v\rho\phi T} I_3 + \frac{P^2}{\rho^2 RT\phi} I_1 - \frac{P}{\rho\phi} I_1 \\ \frac{(I_4 - U_p I_2)}{\rho_p(1-\phi)} \\ -\frac{I_2}{\rho_p} \end{bmatrix} \quad (\text{Eq. 2.37})$$

The eigenvalues of this system of equations are determined by solving the characteristic equation given by Eq. (2.38):

$$\mathbf{M}^T - \lambda_i \mathbf{I} = 0 \quad (\text{Eq. 2.38})$$

In Eq. (2.38), \mathbf{I} is the identity matrix and λ_i the eigenvalues of the system. It is found that the eigenvalues of the system are six distinct real numbers under non-fluidized conditions. The eigenvalues are called the characteristic values indicating the various directions on $x-t$ plot and are given by Eq. (2.39):

$$\begin{aligned} \left(\frac{dx}{dt}\right)_I &= \lambda_1, & \left(\frac{dx}{dt}\right)_{II} &= \lambda_2, & \left(\frac{dx}{dt}\right)_{III} &= \lambda_3 \\ \left(\frac{dx}{dt}\right)_{IV} &= \lambda_4, & \left(\frac{dx}{dt}\right)_V &= \lambda_5, & \left(\frac{dx}{dt}\right)_{VI} &= \lambda_6 \end{aligned} \quad (\text{Eq. 2.39})$$

The subscripts I, II, and III represent the right-running, left-running, and gaseous-path characteristic curves in the gas phase, respectively. The subscripts IV, V, and VI represent the right-running, left-running and particle-path characteristic curves in the solid phase, respectively. These characteristic curves on $x-t$ plane are shown at different spatial locations in Fig. 2-8.

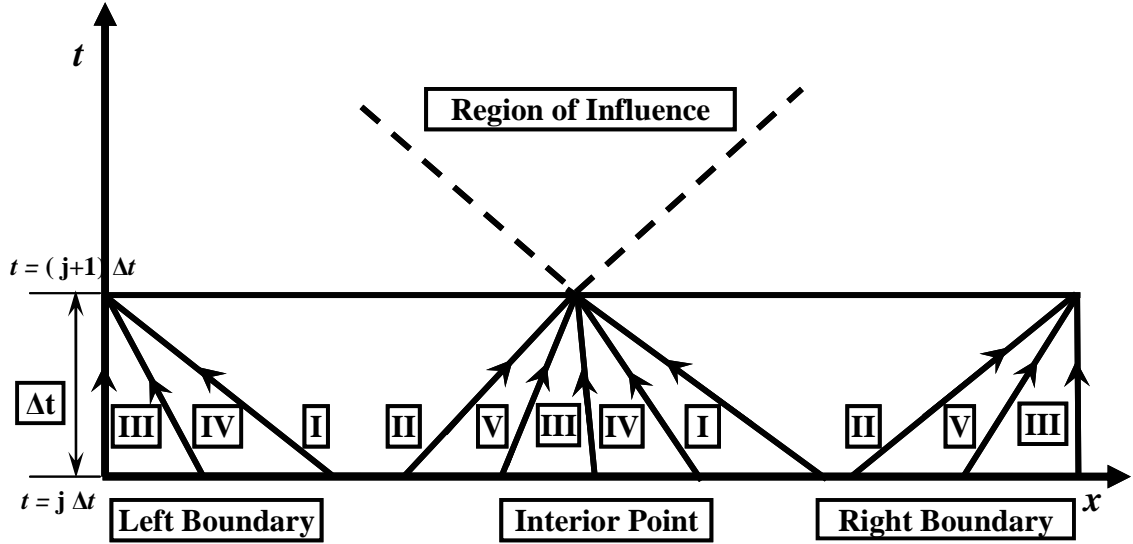


Figure 2-8: Characteristic curves at different locations.

The eigenvalues of the above system of equations are given by Eq. (2.40):

$$\begin{bmatrix} \lambda_1 \\ \lambda_2 \\ \lambda_3 \\ \lambda_4 \\ \lambda_5 \end{bmatrix} = \begin{bmatrix} -(U_g + c_g) \\ -(U_g - c_g) \\ -U_g \\ -(U_p + c) \\ -(U_p - c) \end{bmatrix} \quad (\text{Eq. 2.40})$$

The five adjoint eigenvectors \mathbf{W}_1 , \mathbf{W}_2 , \mathbf{W}_3 , \mathbf{W}_4 , and \mathbf{W}_5 are determined by solving Eq. (2.41):

$$(\mathbf{M}^T - \lambda_i \mathbf{I}) \cdot \mathbf{W}_i = 0 \quad (\text{Eq. 2.41})$$

Here \mathbf{M}^T is the transpose of the coefficient matrix and $i = 1, 2, 3, 4, 5$. Since \mathbf{W}_i 's are linearly independent vectors, the vector differential equation, Eq. (2.41) is multiplied by the transpose of \mathbf{W}_i and five equivalent equations in a new set of dependent variables are

obtained. The eigenvectors can be represented in terms of scalar functions of U_g , T , P , U_p , and ϕ called Z_i . The derivatives of Z_i must satisfy the conditions given by Eq. (2.42):

$$\mathbf{W}_i^T \equiv \left[\frac{\partial Z_i}{\partial U_g} \quad \frac{\partial Z_i}{\partial T} \quad \frac{\partial Z_i}{\partial P} \quad \frac{\partial Z_i}{\partial U_p} \quad \frac{\partial Z_i}{\partial \phi} \right] \quad (\text{Eq. 2.42})$$

By changing the dependent variables U_g , T , P , U_p , and ϕ to new variables Z_i , using the above definition of Z_i and applying chain rule, the Eq. (2.42) becomes:

$$\frac{\partial Z_i}{\partial t} = \lambda_i \frac{\partial Z_i}{\partial x} + \mathbf{W}_i^T \mathbf{I}_h \quad \text{where } i=1, 2, 3, 4, \text{ and } 5 \quad (\text{Eq. 2.43})$$

The characteristic equations shown in Eq. (2.43) can be further reduced to the total differential form by virtue of defined characteristic directions as shown by Eq. (2.44):

$$\left(\frac{dZ_i}{dt} \right)_i \equiv \frac{\partial Z_i}{\partial t} + \left(\frac{dx}{dt} \right)_i \frac{\partial Z_i}{\partial x} = \mathbf{W}_i^T \mathbf{I}_h \quad \text{where } i=1, 2, 3, 4, \text{ and } 5 \quad (\text{Eq. 2.44})$$

The above characteristic equations can be represented by the differentials of U_g , T , P , U_p , and ϕ along the characteristic curves. From the definition given by Eq. (2.42), we have Eq. (2.45):

$$\mathbf{W}_i^T \equiv [W_{i1} \quad W_{i2} \quad W_{i3} \quad W_{i4} \quad W_{i5}] = \left[\frac{\partial Z_i}{\partial U_g} \quad \frac{\partial Z_i}{\partial T} \quad \frac{\partial Z_i}{\partial P} \quad \frac{\partial Z_i}{\partial U_p} \quad \frac{\partial Z_i}{\partial \phi} \right] \quad (\text{Eq. 2.45})$$

Since $Z_i = Z_i(U_g, T, P, U_p, \phi)$, by chain rule we have:

$$dZ_i = \frac{\partial Z_i}{\partial U_g} dU_g + \frac{\partial Z_i}{\partial T} dT + \frac{\partial Z_i}{\partial P} dP + \frac{\partial Z_i}{\partial U_p} dU_p + \frac{\partial Z_i}{\partial \phi} d\phi \quad (\text{Eq. 2.46})$$

Substituting Eq. (2.46) into Eq. (2.44):

$$W_{i1} \left(dU_g \right)_i + W_{i2} \left(dT \right)_i + W_{i3} \left(dP \right)_i + W_{i4} \left(dU_p \right)_i + W_{i5} \left(d\phi \right)_i = \left(\mathbf{W}_i^T \mathbf{I}_h \right) \Delta t \quad (\text{Eq. 2.47})$$

Here the vector product of \mathbf{W}_i with \mathbf{I}_h is given by Eq. (2.48):

$$\mathbf{W}_i^T \mathbf{I}_h \equiv \Omega_i \quad (\text{Eq. 2.48})$$

Substituting Eq. (2.48) into Eq. (2.44), the characteristic equations were then obtained as:

$$W_{i1} (dU_g)_i + W_{i2} (dT)_i + W_{i3} (dP)_i + W_{i4} (dU_p)_i + W_{i5} (d\phi)_i = \Omega_i \Delta t \quad (\text{Eq. 2.49})$$

The sixth characteristic equation was derived from heat equation following the motion of ball propellant particle as shown in Eq. (2.50):

$$W_{61} (dT_{ps})_{VI} + W_{62} (dT)_{VI} = \Omega_6 \Delta t \quad (\text{Eq. 2.50})$$

The components of eigenvector, W_{61} and W_{62} and the source term Ω_6 were determined as function of propellant grain radius (r_{p0}), thermal wave penetration depth (δ) in the ball propellant and heat flux to the ball propellant particle from surroundings gas and condensed phase materials. These eigenvector components and the source term acquire different values depending on whether the thermal wave has penetrated through the particle radius and the relative magnitude of convective to conductive energy transfer rates to the particle.

2.3.9 Linearization of the characteristic equations

For interior points, all six characteristic curves are distinct when the granular bed is non-fluidized and therefore the variables of interest i.e., U_p , ϕ , U_g , P , T , and T_{ps} can be obtained by simultaneously solving the system of six characteristic equations. After

several manipulations of characteristic equations, the algebraic expressions for major variables of interest at all interior points are given by Eqs. (2.51)-(2.56) as following:

$$\begin{aligned}
 U_{p,k}^{j+1} = & \frac{1}{2} \left(U_{p, \text{intsct}, IV}^j + U_{p, \text{intsct}, V}^j \right) \\
 & + \frac{1}{2} \left(\Omega_{4, \text{intsct}}^{j+\frac{1}{2}} + \Omega_{5, \text{intsct}}^{j+\frac{1}{2}} \right) \Delta t \\
 & + \left[\frac{c}{2(1-\phi)} \right]^{j+\frac{1}{2}} \left(-\phi_{\text{intsct}, IV}^j + \phi_{\text{intsct}, V}^j \right)
 \end{aligned} \tag{Eq. 2.51}$$

$$\begin{aligned}
 \phi_k^{j+1} = & \frac{1}{2} \left(\phi_{\text{intsct}, IV}^j + \phi_{\text{intsct}, V}^j \right) \\
 & + \left[\frac{(1-\phi)}{2c} \right]^{j+\frac{1}{2}} \left(\Omega_{5, \text{intsct}}^{j+\frac{1}{2}} - \Omega_{4, \text{intsct}}^{j+\frac{1}{2}} \right) \Delta t \\
 & + \left[\frac{(1-\phi)}{2c} \right]^{j+\frac{1}{2}} \left(U_{p, \text{intsct}, V}^j - U_{p, \text{intsct}, IV}^j \right)
 \end{aligned} \tag{Eq. 2.52}$$

$$\begin{aligned}
 \left(W_{13,k}^{j+\frac{1}{2}} + W_{23,k}^{j+\frac{1}{2}} \right) P_k^{j+1} = & U_{g,k, \text{intsct}, I}^j - U_{g,k, \text{intsct}, II}^j \\
 & + W_{13,k}^{j+\frac{1}{2}} P_{k, \text{intsct}, I}^j + W_{23,k}^{j+\frac{1}{2}} P_{k, \text{intsct}, II}^j \\
 & - W_{14}^{j+\frac{1}{2}} \left(dU_p \right)_{II} - W_{24}^{j+\frac{1}{2}} \left(dU_p \right)_{II} \\
 & - W_{15}^{j+\frac{1}{2}} \left(d\phi \right) - W_{25}^{j+\frac{1}{2}} \left(d\phi \right)_{II} \\
 & + \left(\Omega_{1,k, \text{intsct}, I}^{j+\frac{1}{2}} + \Omega_{2,k, \text{intsct}, II}^{j+\frac{1}{2}} \right) \Delta t
 \end{aligned} \tag{Eq. 2.53}$$

$$\begin{aligned}
 U_{g,k}^{j+1} = & U_{g,k, \text{intsct}, I}^j + W_{13,k}^{j+\frac{1}{2}} P_{k, \text{intsct}, I}^j \\
 & - W_{14,k}^{j+\frac{1}{2}} \left(dU_p \right)_I - W_{15,k}^{j+\frac{1}{2}} \left(d\phi \right)_I \\
 & + \Omega_{1,k, \text{intsct}, I}^{j+\frac{1}{2}} \Delta t - W_{13,k}^{j+\frac{1}{2}} P_k^{j+1}
 \end{aligned} \tag{Eq. 2.54}$$

$$T_k^{j+1} = T_{k, \text{intsct}, III}^j + \frac{1}{W_{32,k}^{j+\frac{1}{2}}} \left[\Omega_{3,k}^{j+\frac{1}{2}} \Delta t - W_{33,k}^{j+\frac{1}{2}} \left(dP \right)_{III} - W_{35,k}^{j+\frac{1}{2}} \left(d\phi \right)_{III} \right] \tag{Eq. 2.55}$$

$$T_{ps,k}^{j+1} = T_{ps, k, \text{intsct}, VI}^j + \Omega_{6, k, \text{intsct}, IV}^{j+\frac{1}{2}} \Delta t - W_{62, k}^{j+\frac{1}{2}} \left(dT \right)_{VI} \tag{Eq. 2.56}$$

For both right and left boundary control volumes, the boundary conditions shown by Eq. (2.57) were used.

$$\begin{aligned} U_g &= 0 \\ U_p &= 0 \end{aligned} \quad (\text{Eq. 2.57})$$

Therefore, the slope of the characteristic lines at these boundaries is given by Eq. (2.58) as following:

$$[\lambda_1 \ \lambda_2 \ \lambda_3 \ \lambda_4 \ \lambda_5]^T = [c_g \ -c_g \ 0 \ c \ -c]^T \quad (\text{Eq. 2.58})$$

The other quantities of interest are determined by using the characteristic equations at the boundaries. The explicit forms for the right boundary are shown in Eqs. (2.59)-(2.62):

$$\phi_k^{j+1} = \phi_{k,\text{intsct},V}^j + \frac{1}{W_{55,k}^{j+1/2}} \left[\Omega_{5,k,\text{intsct}}^{j+1/2} \Delta t - (dU_p)_V \right] \quad (\text{Eq. 2.59})$$

$$P_k^{j+1} = P_{k,\text{intsct},II}^j + \frac{1}{W_{23,k}^{j+1/2}} \left[\begin{aligned} &\Omega_{2,k,\text{intsct},II}^{j+1/2} \Delta t - W_{21,k}^{j+1/2} (dU_g)_{II} \\ &- W_{25,k}^{j+1/2} (d\phi)_{II} - W_{24,k}^{j+1/2} (dU_p)_{II} \end{aligned} \right] \quad (\text{Eq. 2.60})$$

$$T_k^{j+1} = T_{k,\text{intsct},III}^j + \frac{1}{W_{32,k}^{j+1/2}} \left[\Omega_{3,k,\text{intsct},III}^{j+1/2} \Delta t - W_{33,k}^{j+1/2} (dP)_{III} - W_{35,k}^{j+1/2} (d\phi)_{III} \right] \quad (\text{Eq. 2.61})$$

$$T_{ps,k}^{j+1} = T_{ps,k,\text{intsct},VI}^j + \Omega_{6,k,\text{intsct},VI}^{j+1/2} \Delta t - W_{62,k}^{j+1/2} (dT)_{VI} \quad (\text{Eq. 2.62})$$

Similar equations were obtained for left boundary also. The equations were solved along characteristic curves number I, III, and IV at the left boundary.

2.3.10 Validation of calculated results

The ignition cartridge was instrumented with six pressure transducers at different axial and azimuthal locations. The axial locations of these pressure transducers and the

notation used for these pressure transducers is shown in Fig. 2-9. The pressure-time traces were measured from the ignition cartridge using 16 pressure transducers; 4 for each axial location at 90° intervals along the azimuthal direction. Based on these results, it was determined that the physical processes in the ignition cartridge are independent of radial and azimuthal directions. Therefore only 5 pressure transducers were employed in subsequent experimental work and compared with the computational results.

Using the three dimensional mortar interior ballistics (3D-MIB) code, the calculated pressure-time traces at five port locations (port 0 through port 4) on the tail boom of the ignition cartridge are shown in Fig. 2-10. The measured pressure-time traces at these corresponding axial locations are shown in Fig. 2-11. By comparing these two figures, one can notice several similar characteristics. In both figures, pressure at Port 4 location, P_4 starts to rise before Port 1 location, P_1 . This behavior is attributed to stronger discharge of igniter products from the flash tube at P_4 . Once start to rise, P_1 has higher pressurization rate than that of P_4 . This happens due to the generation of pressure wave from P_4 propagating towards P_1 . Along with this pressure wave propagation, gas and particles are driven towards P_1 .

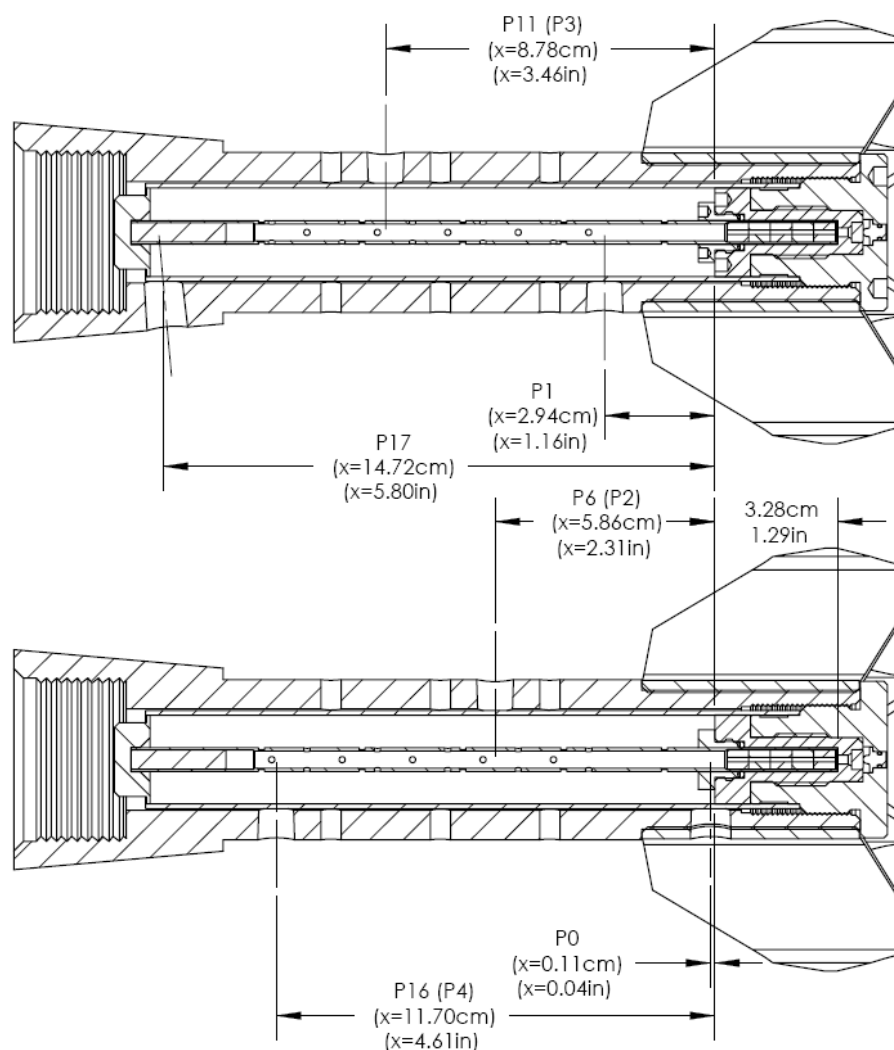


Figure 2-9: Location of pressure transducers on the ignition cartridge.

At a pressure around 41 MPa (6,000 psia), there is a slight drop in pressure at all port locations due to the rupture of the propellant container tube wall and subsequent discharge of combustion products to the surroundings through the vent holes on tail boom. Thereafter, pressure in the granular bed continues to rise due to continued burning. Both calculated and experimental results show that the P_1 takes over that at P_4 before reaching the peak at around 110 MPa (16,000 psia).

At the onset of pressure decay from their peaks, the pressure gradient is higher at P_1 than that at P_4 . Finally, pressure-time traces at all port locations come closer and gradually converge during the later phase of the pressure decay. Both calculated and experimental results show that the event duration of the processes in the tail boom of ignition cartridge is close to 3 ms. In order to explain the flow property variations with respect to time and axial coordinate in the granular bed, it is beneficial to focus on a P-t trace at axial location P_0 . Near the stagnation region, closest to the primer end, pressure reached a substantially higher peak level than P_1 . In this region, there are no nearby vent holes to discharge the combustion products. The burned products can only leave this region by moving in the positive axial direction. Similarly, near the projectile end, P-t traces showed higher-pressure levels than that of P_4 . In view of the existence of the pressure gradients at these two ends, the burned gas and particles are driven towards the middle section of the granular bed where vent holes are accessible. The close similarity of the predicted P-t results with the experimental data partly validates the theoretical model. It is useful to note that the predicted maximum pressure occurred in the axial location ($x = 0.48$ cm) significantly below the P_1 transducer location, which was not measured in the earlier set of experiments. After the numerical results were known, a pressure transducer port called P_0 was added to the tail-boom section. The recorded P_0 -t traces were indeed much higher than the P_1 -t traces as predicted by the computer code. A more detailed comparison at each of the five port locations is shown in Figs. **2-12-2-17**.

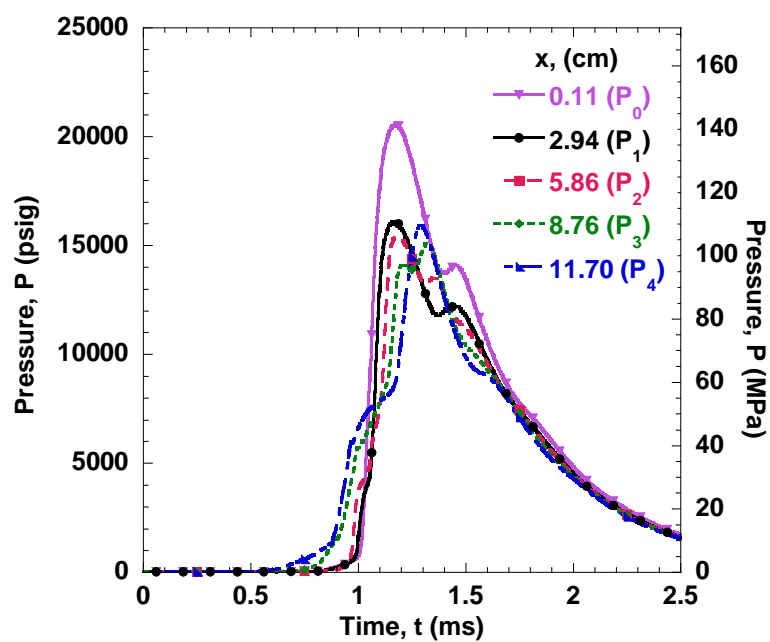


Figure 2-10: Computed pressure-time traces for ignition cartridge at five port locations.

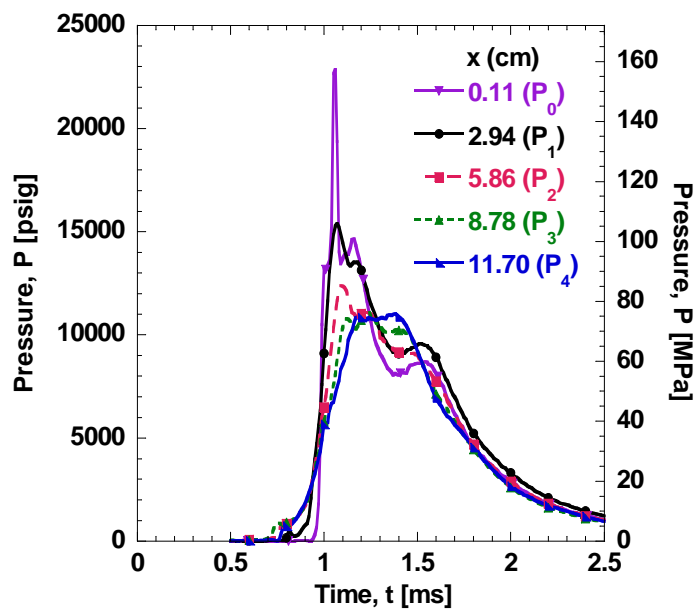


Figure 2-11: Measured pressure-time traces for ignition cartridge at five port locations.

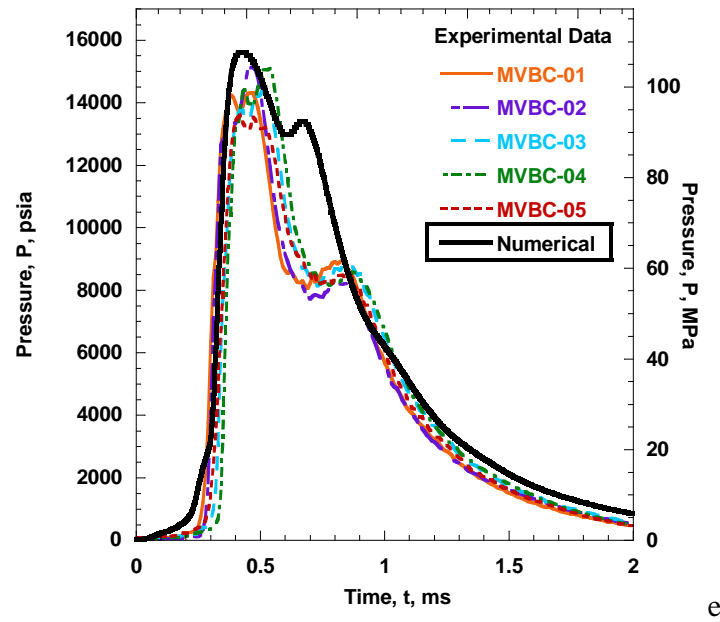


Figure 2-12: Comparison of 5 experimental pressure-time traces with the calculated pressure-time traces at port 0 location ($x=0.11$ cm).

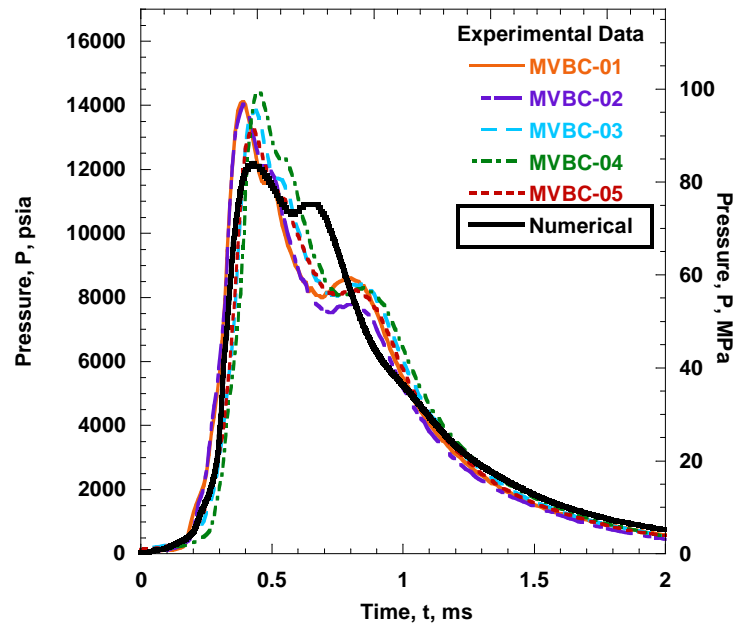


Figure 2-13: Comparison of 5 experimental pressure-time traces with the calculated pressure-time traces at port 1 location ($x=2.94$ cm).

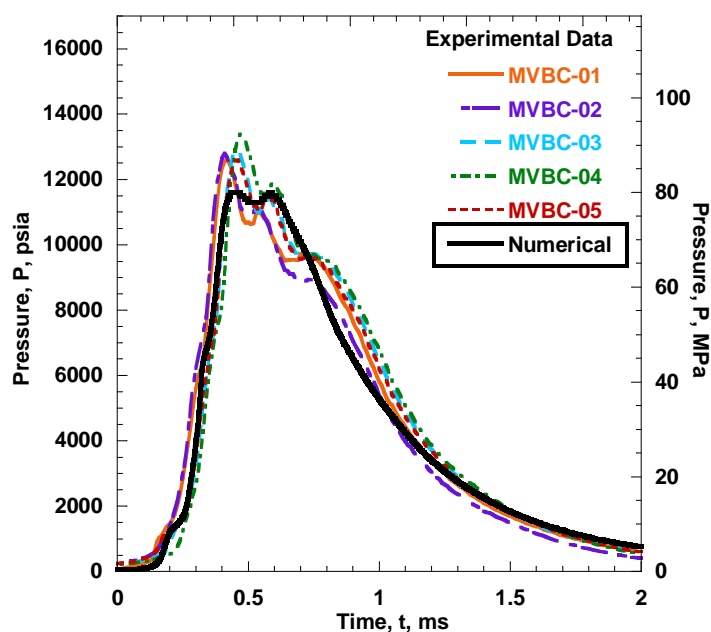


Figure 2-14: Comparison of 5 experimental pressure-time traces with the calculated pressure-time traces at port 2 location ($x=5.86$ cm).

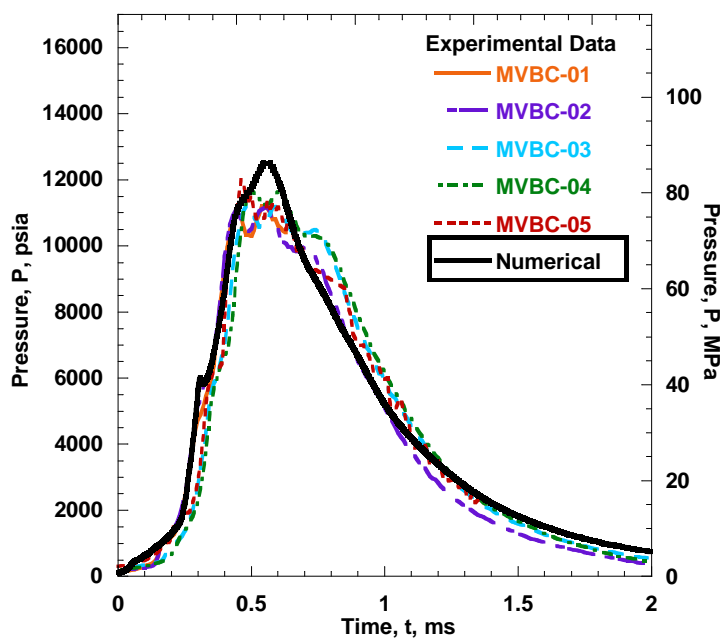


Figure 2-15: Comparison of 5 experimental pressure-time traces with the calculated pressure-time traces at port 3 location ($x=8.76$ cm).

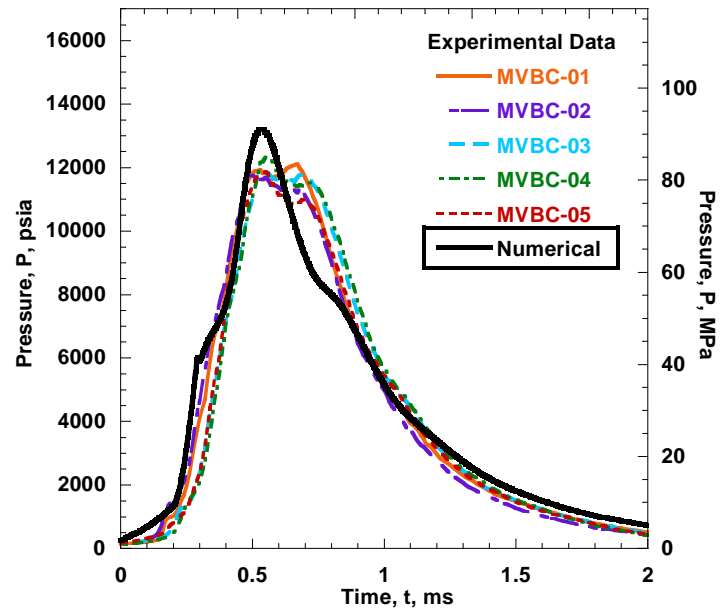


Figure 2-16: Comparison of 5 experimental pressure-time traces with the calculated pressure-time traces at port 4 location ($x=8.78$ cm).

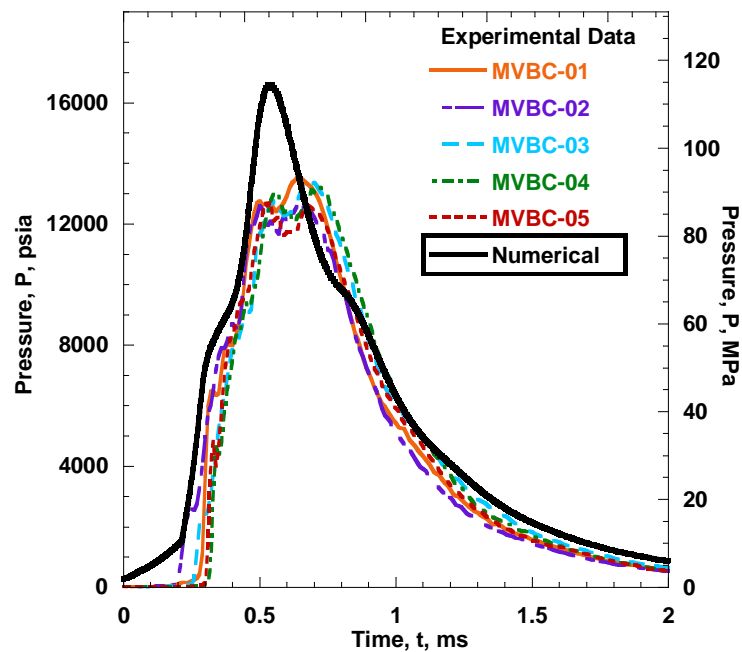


Figure 2-17: Comparison of 5 experimental pressure-time traces with the calculated pressure-time traces at port 5 location ($x=11.70$ cm).

In the interior ballistic studies, it is useful to show the pressure wave phenomenon by plotting ΔP versus time. The calculated time variations of ΔP are shown in Fig. 2-18 and the comparison with the experimental data is shown in Figs. 2-19- 2-20. The ΔP rises first since the pressure at the P_4 and P_5 locations is significantly greater than P_1 and P_0 location due to earlier ignition of propellants there. This trend was reversed in the later phase of ballistic cycle since violent combustion near the primer end produced enormous amount of pressure rise in the stagnation region. The amplitudes of the peak ΔP are close to the experimentally observed values from many test firings.

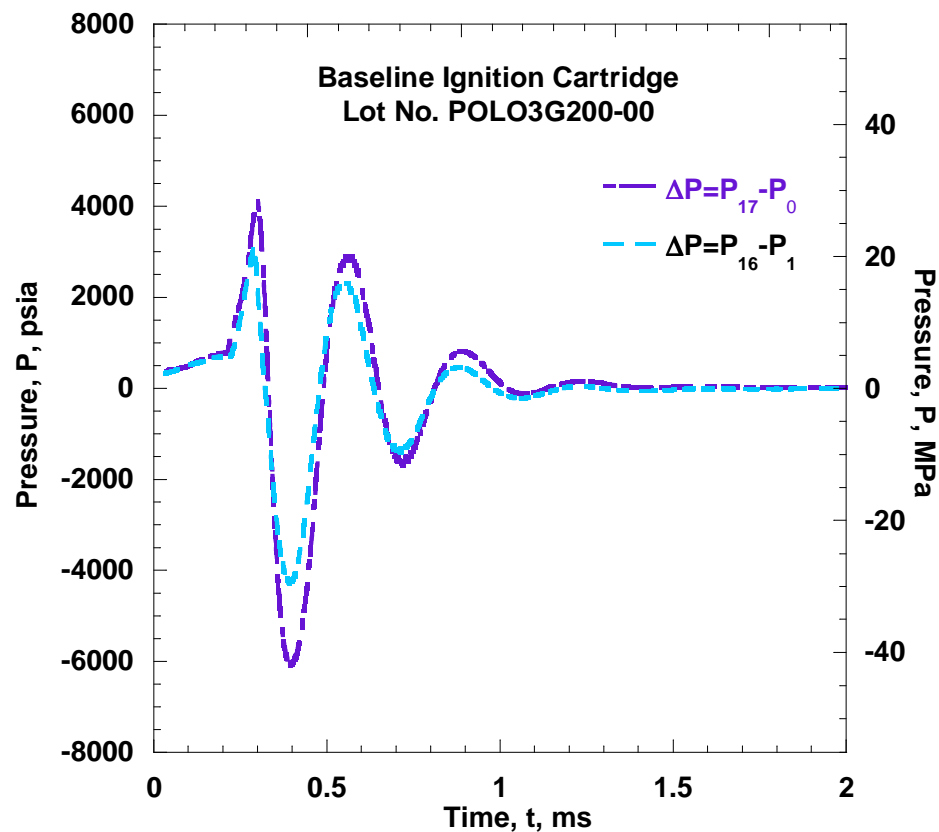


Figure 2-18: Comparison of calculated pressure difference-time traces.

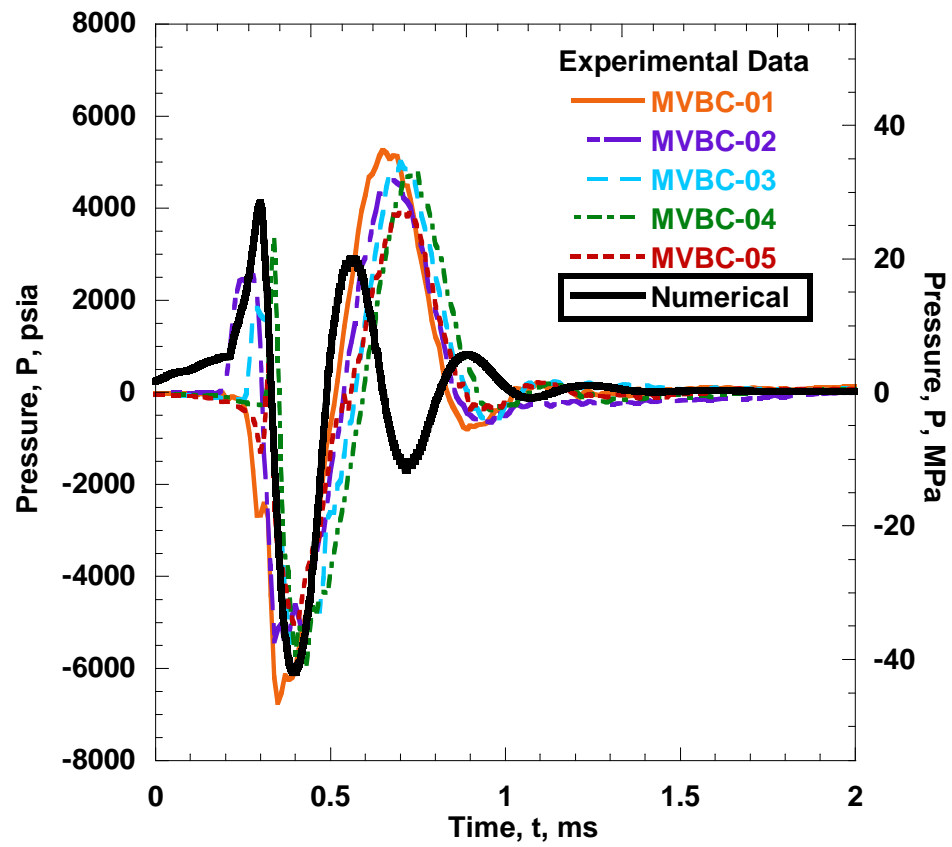


Figure 2-19: Comparison of experimental pressure difference-time traces with the calculated pressure difference-time traces for $\Delta P = P_5 - P_0$.

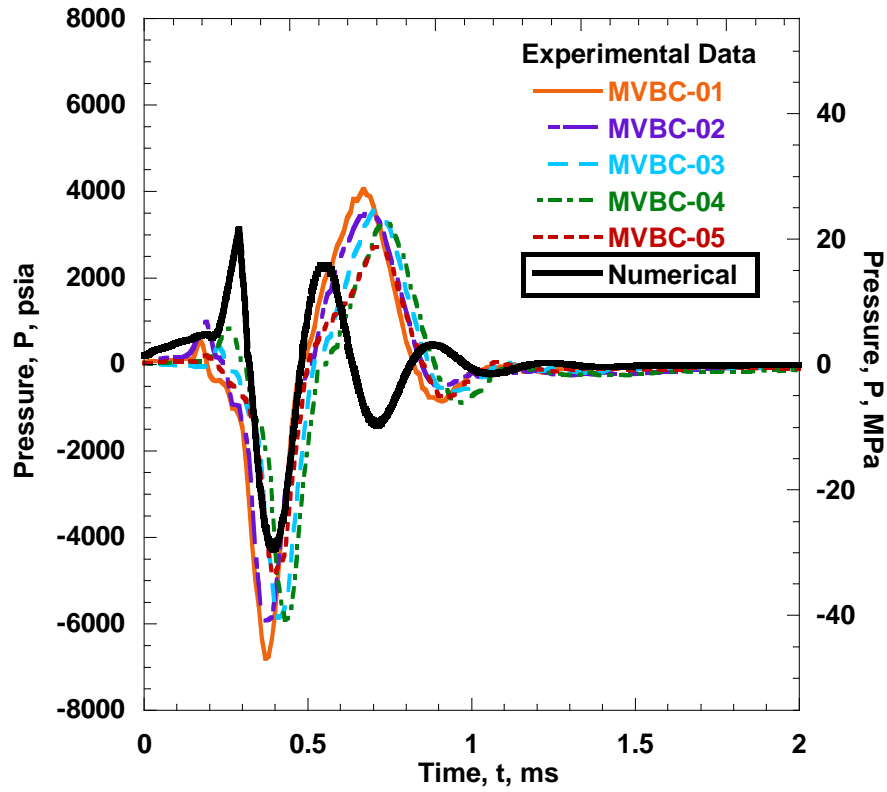


Figure 2-20: Comparison of experimental pressure difference-time traces with the calculated pressure difference-time traces for $\Delta P = P_4 - P_1$.

These phenomena can also be observed from the calculated gas velocity-time traces at five port locations shown in Fig. 2-21. Prior to reaching the peak pressure, the gas velocity in the granular bed is strongly affected by the non-uniform ignition of ball propellants, pressure wave propagation processes, and the discharging of combustion products through vent holes. The order of onset of ignition at the five port locations can be examined from the plot of propellant surface temperature (T_{ps}) variations with respect to time as shown in Fig. 2-22.

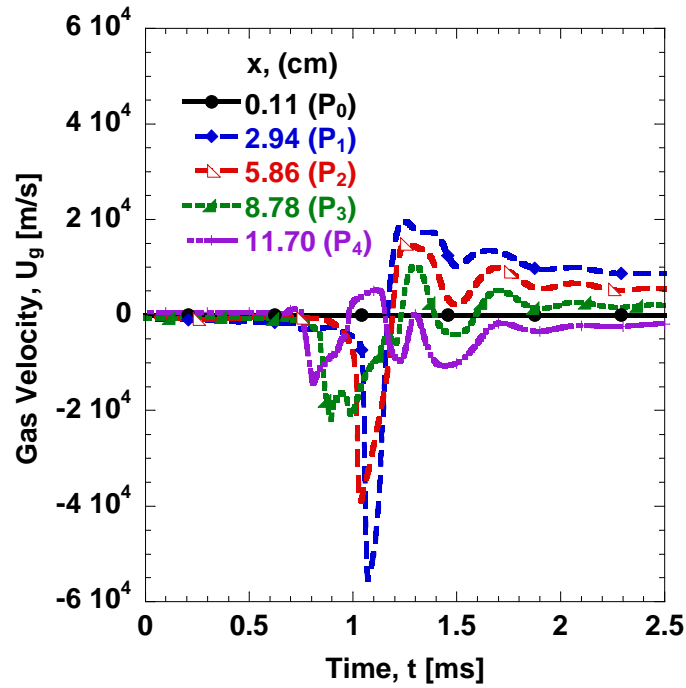


Figure 2-21: Comparison of gas velocity variation in the ignition cartridge at different axial locations.

In the numerical calculations, a ball propellant is considered to reach an ablation condition at 525 K and full ignition condition is attained when the surface temperature reached 600 K. Once the particle is fully ignited, the energy equation for the ball propellant was no longer solved and it was assumed that the surface temperature remains at the ignition temperature. It can be seen that T_{ps} increases first at P_4 and last at P_2 due to the profile and order of igniter products from the flash tube.

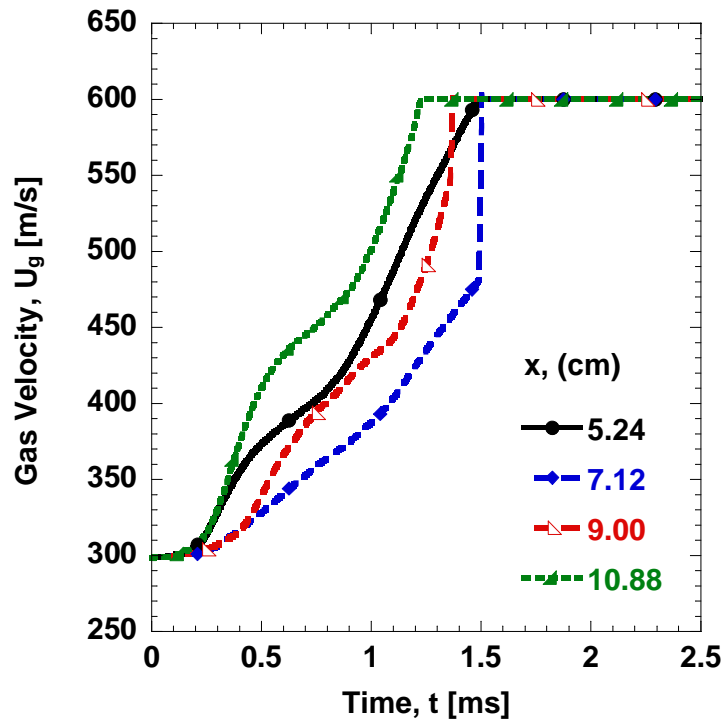


Figure 2-22: Comparison of surface temperature increase of propellant grain in the ignition cartridge.

The calculated gas temperature-time traces at the four port locations are shown in Fig. 2-23. The adiabatic flame temperature of M48 solid propellant is 2,831 K under constant-pressure combustion conditions. The calculated results for gas temperature in granular bed showed that during certain period of the ballistic cycle, the gas temperature at several port locations can exceed the constant-pressure adiabatic flame temperature value. This could be due to the reason that the combustion process is not at constant-pressure but it was close to constant-volume process. The gas temperature rises abruptly during the initial portion of the ballistic cycle following the order of ignition of ball propellants. During the final decay period, all gas temperature-time traces gradually reach the same rate of decay.

The calculated porosity-time traces at the five port locations are shown in Fig. 2-24. The porosity of the granular bed starts to increase first at P_4 where first ignition and ball propellant combustion starts. Burning of ball propellant grains produces gas-phase products while reducing the solid phase material at the same time. Hence the porosity, which is the fraction of gas-phase material in a two-phase mixture, increases. Porosity starts to increase later at P_1 and P_2 locations. During the whole ballistic cycle, the porosity increases monotonically. However, there was a period when the rate of increase was significantly reduced. The reason for this reduction is the influx of particle from adjacent high-pressure zone. This pressure gradient can be seen from Fig 2-26 between 1.2 to 1.6 ms. During this interval, the porosity variations at P_4 is insignificant due to presence of large pressure gradient which drove the particles into the local area and balanced with the particle leaving through the vent holes and to the neighboring regions. Near the later phase of the pressure decay period, the porosity magnitudes at various port locations approach each other and asymptotically increase to the level of unity.

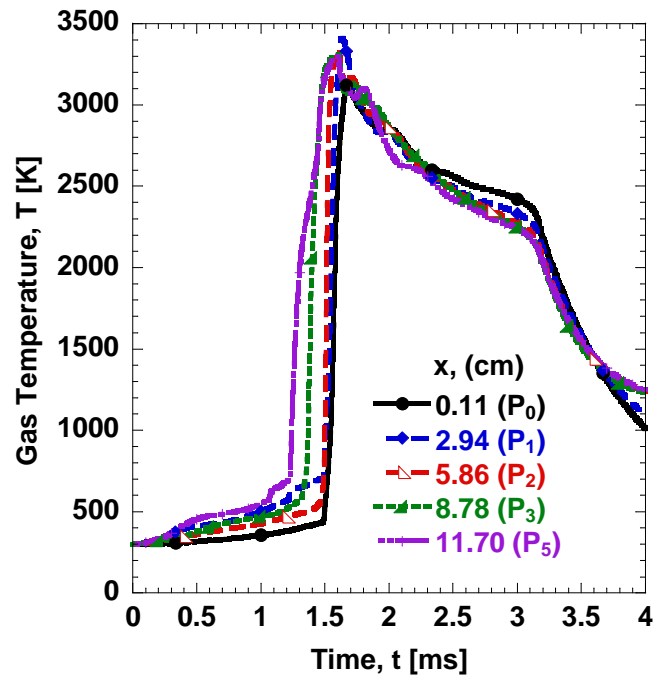


Figure 2-23: Comparison of gas temperature variation in the ignition cartridge at different axial locations.

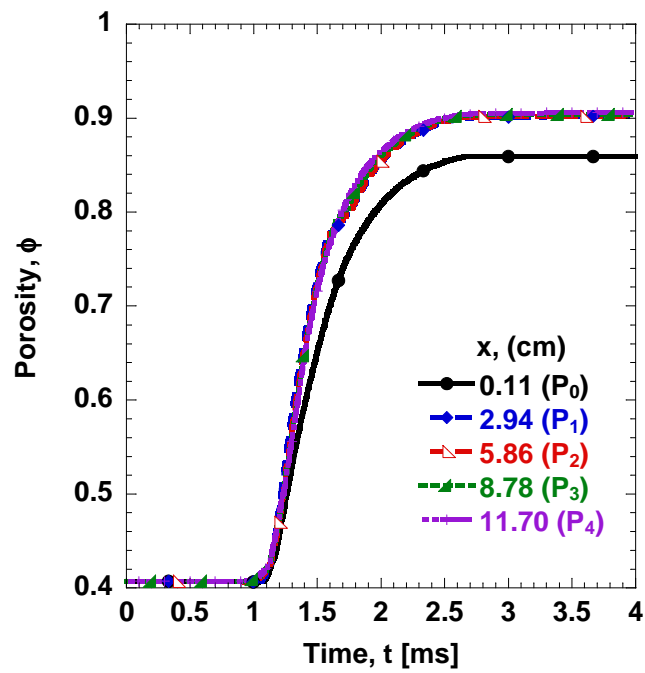


Figure 2-24: Comparison of porosity variations in the ignition cartridge at different axial locations.

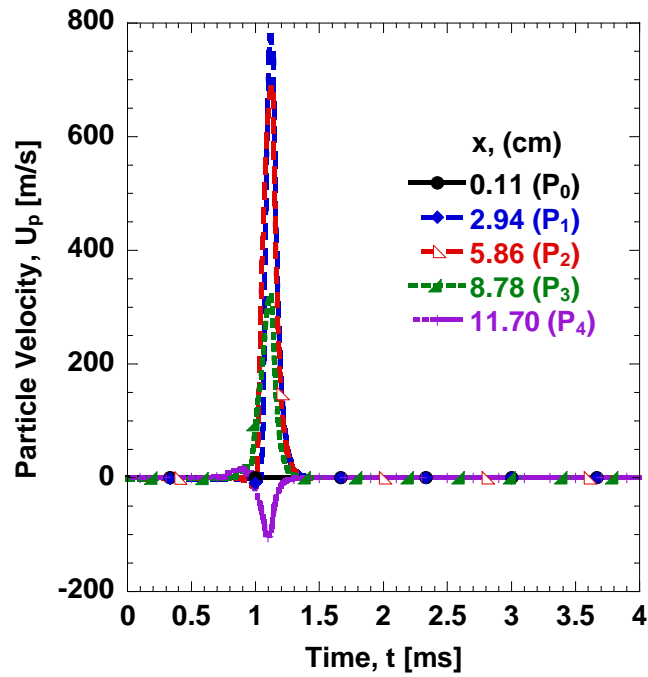


Figure 2-25: Comparison of particle velocity variation in the ignition cartridge at different axial locations.

Additional model validation was performed by comparing the diameter of M48 ball propellants with the experimental data. The experimental data was obtained by collecting over 100 M48 ball propellants at the end of ignition cartridge firing and taking their average diameter. The comparisons of calculated particle diameter with the experimental measurement are shown in Fig. 2-26 and Fig. 2-27 for two separate experiments. The calculations match with the experimental data within the error limits, which is another indication of the robustness of ignition cartridge sub-model.

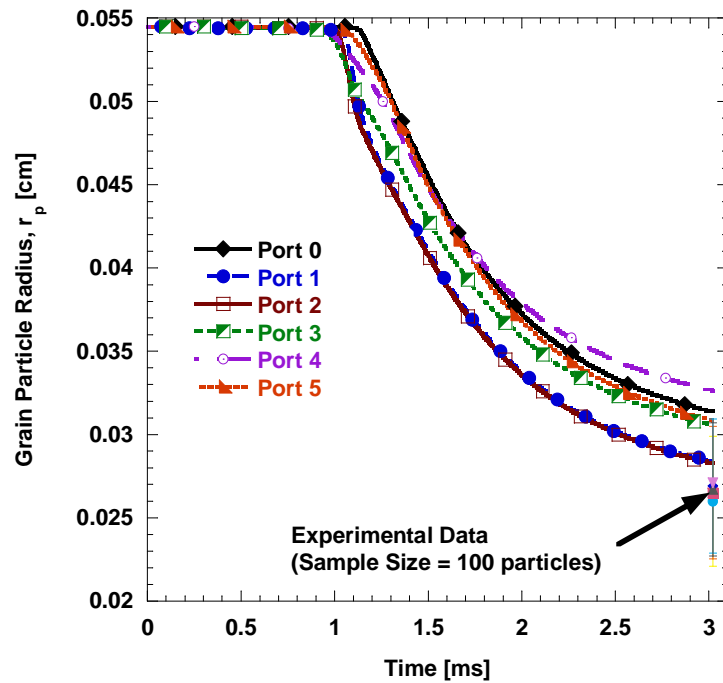


Figure 2-26: Comparison of calculated and measured particle diameter in the ignition cartridge at different axial locations at the end of ballistic event (Test 1).

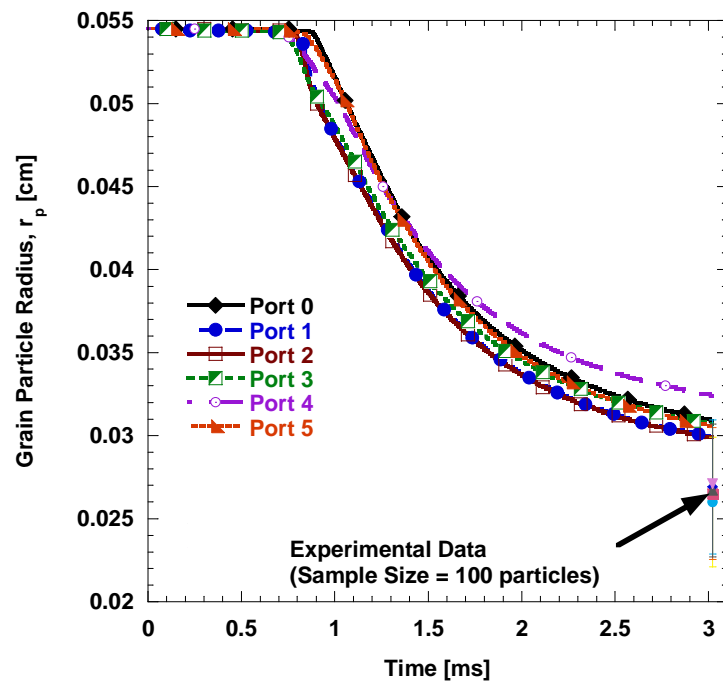


Figure 2-27: Comparison of calculated and measured particle diameter in the ignition cartridge at different axial locations at the end of ballistic event (Test 2).

2.4 Summary of the ignition cartridge sub-model

The ballistic processes in the ignition cartridge are highly non-uniform. The burning starts in the projectile end of the ignition cartridge and it propagates toward the primer end of the ignition cartridge. The ball propellants in the projectile end ignited first due to earlier and higher mass flow from flash tube in this region. In the beginning of the combustion process, pressure is highest at the projectile end of the ignition cartridge and it decreases towards the primer-end. Due to the presence of this pressure gradient, a pressure wave develops in the ignition cartridge, which moves from projectile end (high-pressure end) towards the primer end (low-pressure end). The pressure wave starts to diminish once the vent holes on the ignition cartridge open and combustion products start to discharge from these vent holes. Due to this phenomenon and vigorous burning of ball propellants in the stagnation region near the primer end, the pressure in the primer end becomes highest and it decreases towards the projectile end. After this, a second pressure wave travels from primer end (high pressure end) towards the projectile end (low-pressure end).

The method of characteristics with stagnation boundary conditions proves to be an adequate analysis technique for solving the complicated combustion problem addressed in this chapter. The mortar interior ballistic model is partially validated by the excellent agreement obtained between the calculated and measured P-t traces at various axial locations along the ignition cartridge. The main reason for the generation of pressure waves in the granular bed of the ignition cartridge is due to the non-uniform discharge of combustion products from the flash tube mounted at the center of the cartridge.

Chapter 3

APPLICATION OF IGNITION CARTRIDGE SUB-MODEL FOR PERFORMANCE IMPROVEMENT

The theoretical sub-model and numerical code developed for ignition cartridge performance prediction was used to predict the effect of design changes on the axial pressure gradients in the tail-boom section of the 120mm mortar propulsion system. In addition, the ignition cartridge sub-model was also used to predict the effect of primer material on the gas-dynamical processes in the tail-boom section.

3.1 Background

In the existing design of the flash tube, all vent holes on the flash tube were equal in diameter and were distributed evenly on the tube wall. However, the black powder (BP) pellets are located at the primer-end of the flash tube; such that after ignition, the combustion products travel from the primer-end toward the projectile-end of the flash tube. From the computational study described previously in chapter 1, it was concluded that the pressurization processes at various axial locations in the flash tube are highly non-uniform. This observation was also supported by the experimental study conducted by Moore et al. [49] by using a windowed flash tube test rig, where it was observed that there was a continuous compression of gaseous products toward the projectile-end of the flash tube. The mass discharge rate from a given vent hole is governed by the instantaneous local pressure and the discharge area of the vent hole by the choked flow

equation, if the condensed-phase products are considered to be fully entrained in the discharging flow and the particle sizes are much smaller than the vent hole port area. Therefore, this non-uniformity of local pressure coupled with the even distribution of vent holes (i.e., all vent holes having same diameter) on the flash tube outer surface results in significant differences between the instantaneous mass discharge rates from the flash tube at various axial locations.

The tail-boom section contains closely-packed ball propellants (called M48) in the annular region between the flash tube and the wall of the tail boom. This region is called granular bed. The ball propellants in this granular bed are contained in a paper tube, which fits the inner surface of the tail-boom and blocks the vent holes on the surface of tail-boom until the pressure reaches a threshold rupture pressure. The granular bed section receives the discharge of high-pressure and high-temperature combustion products from the flash tube. These combustion products contain both the gas-phase and condensed-phase species, which heat the ball propellants in the tail-boom section to their ignition temperature. In chapter 2, it was discussed that significant axial non-uniformity in the instantaneous mass discharge rates of combustion products from the flash tube to the granular bed results in significant differences in ignition delay time at these locations. As a consequence, this process generates strong axial pressure gradients and resulting pressure waves in the original ignition cartridge. The existence of strong pressure waves can contribute to higher standard deviations in the overall ballistic performance of the 120mm mortar system during firings. Therefore, the primary focus of the work shown in this chapter is to use the ignition cartridge sub-model to examine that the effect of change in flash tube vent-hole patterns on the reduction in the strength of pressure waves in the

ignition cartridge. The predicted results were validated with the experimental pressure-time traces. The design modification(s) could also increase the reliability and reproducibility of 120mm mortar systems.

It was also observed that the black powder igniter pellets that are used in the flash tube produce highly non-repeatable pressure-time traces. Therefore, a substitute called moisture resistant black powder (MRBPS) was sought to remedy this problem. The ignition cartridge sub-model was utilized to compute the interior ballistics of the M1020 ignition cartridge with MRBPS as an igniter material and the results were compared with the experimental data. The comparison of two pyrotechnic materials also facilitates model validation and increases the robustness of the code. Therefore, there are two specific objectives of the work shown in this chapter:

- (i) Simulation of interior ballistic processes in the granular bed by using modified flash tube(s) with various vent-hole patterns and the comparison of these predicted results with the available experimental data,
- (ii) Comparison of the interior ballistic processes in the granular bed of M1020 ignition cartridge by using black powder (BP) and moisture resistant black powder substitute (MRBPS) as two different pyrotechnic materials.

The secondary objective of this chapter is to partially demonstrate the usefulness of this model and code as a tool for analysis of interior ballistic processes in the 120mm mortar propulsion system.

3.2 Effect of vent hole pattern modification on the flash tube

As a part of this study, simulation of ignition cartridge combustion behavior was conducted through a systematic variation of the flash tube vent-hole pattern to achieve a more uniform venting of combustion products into the ignition cartridge. The mass flow rates of discharged gas and condensed-phase products from the flash tube vent holes to the granular bed were deduced from the flash tube sub-model, which was integrated with the ignition cartridge sub-model for the determination of pressurization rates at various axial locations in the granular bed. In order to examine the effect of vent-hole patterns on the interior ballistic processes in the ignition cartridge, five cases were considered:

1. Original design (baseline or case 0): All vent holes are equal in diameter and their location on the flash tube is uniform in both longitudinal and azimuthal directions.
2. First modification (case 1): The vent holes close to the primer-end are larger in diameter than those close to the projectile-end. The diameter of each vent hole is given in Table 2-1. This modification increased the total vent-hole discharge area by about 14% in comparison with case 0.
3. Second modification (case 2): The vent holes close to the primer-end are even larger in diameter than those in case 1, but vent holes 13 through 20 do not change in diameter. This modification increased the total vent-hole discharge area by 22% in comparison with the baseline case.
4. Third modification (case 3): In this case, the vent-hole diameters of the first twelve are identical to case 2, while the last eight vent holes are made slightly smaller. This

modification increased the total vent-hole discharge area by 19% in comparison with the baseline case.

5. Final modification (final case): In this case, the diameters of the first four vent holes were increased significantly, the vent-hole diameters of subsequent sets decreased with axial distance and the last eight vent holes are made much smaller than the first four vent holes. This modification increased the total vent-hole discharge area by 22% in comparison with the baseline case.

The vent-hole diameter variations for all of the above cases are shown in Table 2-1.

Table 3-1: Distribution of flash tube vent-hole sizes at various axial locations

<u>Case No.</u>	<u>Vent hole numbers and sizes [in]</u>					<u>Total discharge Area [in²]</u>	<u>Percentage increase in area from baseline</u>
	<u>1-4</u>	<u>5-8</u>	<u>9-12</u>	<u>13-16</u>	<u>17-20</u>		
Baseline	0.0650	0.0650	0.0650	0.0650	0.0650	0.0664	0
1	0.0730	0.0730	0.0700	0.0650	0.0650	0.0754	14
2	0.0785	0.0760	0.0729	0.0650	0.0650	0.0807	22
3	0.0785	0.0760	0.0729	0.0625	0.0625	0.0787	19
Final	0.0860	0.0810	0.0760	0.0550	0.0550	0.0787	22

3.2.1 Calculated results

In a parallel experimental study conducted by Moore et al. [50], a set of pressure-time traces from the flash tube were obtained for baseline through the final case. The deduced mass flow rates of the gas-phase combustion products are shown in Figs. 3-1 to 3-9 for original flash tube design (baseline or case 0), 1st, 2nd, 3rd, and final modifications of the flash tube, respectively. For each case of flash tube vent-hole pattern, five tests

were conducted with black powder pellets. The pressure-time traces utilized in this study were obtained from one of these five tests. The detailed procedure for deducing the gaseous mass flow rates from the flash tube vent holes was previously described in chapter 2. The deduced gaseous mass flow rate from the flash-tube vent holes are shown only for the first 3 ms since the later event is not important in the ignition cartridge combustion event. All traces monotonically decay to 0 around 4 ms. A statistical analysis of the 5 tests showed that the total mass flow rates varied as much as 15%, indicating poor reproducibility of BP pellets. Among all 4 flash tube vent-hole pattern modifications, the net mass discharged from all vent holes remained conserved within the limit of experimental error.

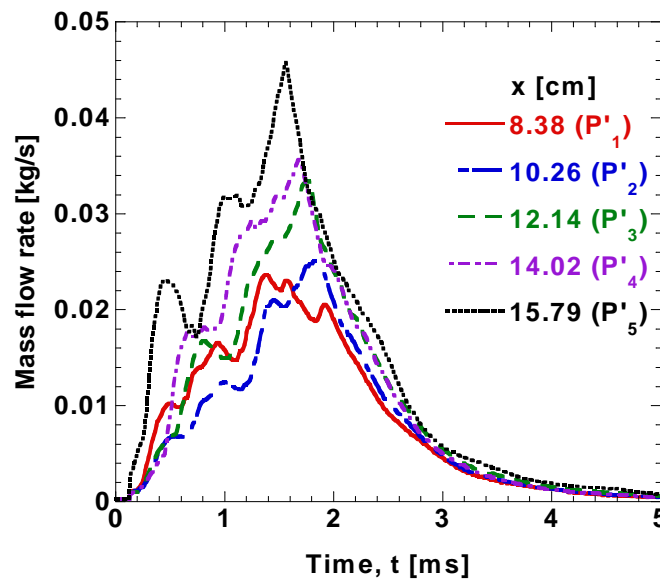


Figure 3-1: Deduced gaseous mass flow rate vs. time traces from one of the P-t traces of five flash tube tests with the original vent-hole pattern (case 0).

The deduced gaseous mass flow rates discharging from the flash tube vent holes for the baseline case is shown in Fig. 3-1. There is significant difference between the mass discharge rate from port 1 and port 5 locations (closer to primer- and projectile-ends, respectively). This difference is most pronounced in first 1.5 ms of the ballistic cycle in the flash tube. The deduced gaseous mass flow rates discharging from the flash tube vent holes for case 1 modification is shown in Fig. 3-2. These mass flow rate-time traces exhibit a different behavior than the baseline case, due to differences in vent-hole diameters at five axial locations.

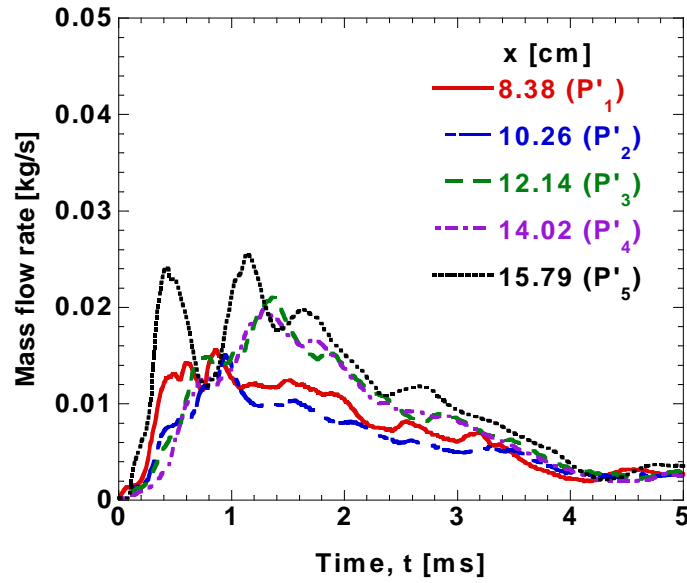


Figure 3-2: Deduced gaseous mass flow rate vs. time traces from one of the P-t traces of five flash tube tests with modified vent-hole pattern (case 1).

For the initial rise time (< 1 ms), the hierarchy of mass discharge rates is similar in nature to that of the baseline tests, though the difference in mass discharge rates between port 5 and port 1 locations is lower than the baseline flash tube design. This period is very important as it is during this period that hot products from the pyrotechnic

pellets spread down the flash tube and exit the vent holes into the granular propellant bed, when the flash tube is actually used in an ignition cartridge. On an average, the difference in mass flow rates between port 5 and port 1 pressure-gauge locations are $40 \pm 15\%$ lower than the baseline flash tube design, which is a significant reduction in the non-uniformity of the venting process.

In keeping with the enlargement of the vent holes, the second modifications to the flash tube (case 2) were conducted by increasing the overall vent-hole area to around 22% compared to the baseline case. Similar to case 1, this was accomplished by taking the original M1020 flash tubes and opening up the first 12 vent holes closest to the primer-end in sets of 4 by using larger drill bits #47 ($d = 0.0785$ inch), #48 ($d = 0.0760$ inch), and #49 ($d = 0.0700$ inch), respectively. It is important to note that by enlarging the first 12 vent holes so that the total vent-hole area increased nearly 22%, the mass flow rate of all 5 measured locations along the flash tube became closer, especially in the initial portion of port 5 and port 1 locations are $73 \pm 15\%$ lower than the baseline flash tube design, which is an even further reduction in the non-uniformity of the venting process than case 1. These results showed that by increasing the vent-hole area close to the primer-end of the flash tube, the local mass discharge rates could be increased even though pressure at these locations were still lower than the port 5 location. This observation was used for the next two modifications of the vent-hole pattern on the flash tube.

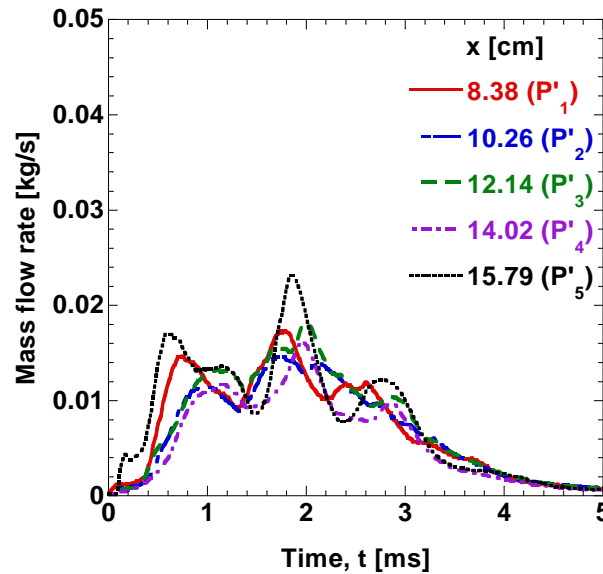


Figure 3-3: Deduced gaseous mass flow rate vs. time traces from one of the P-t traces of five flash tube tests with modified vent-hole pattern (case 2).

For the third modification to the flash tube vent holes (case 3), it was decided to slightly reduce the total flash tube vent hole area from case 2 in order to further reduce the mass flow rate from P_5 location. To accomplish this, it was determined that the first 12 vent holes closest to the primer end would have the same exit hole diameters as that of case 2. However, the diameters of the remaining 8 vent holes near the projectile-end were decreased by drilling 1/16 inch holes ($d = 0.0625$ inch). Selection of this drill size was based on the next smallest drill size from the original flash tube vent hole diameter. The reason for diminishing the vent hole area in this region was to try to reduce the mass flow rate near the end of the flash tube, forcing more gas to discharge via the 12 enlarged vent holes near the primer-end; thus, increasing the mass flow rate at positions P_1 through P_3 , and decreasing the mass flow rate at positions P_4 and P_5 locations. This modification

gave a total vent-hole area 19% higher than the baseline case. Typical deduced mass flow rate results of case 3 can be seen in Fig. 3-3.

With the case 3 design, the overall difference in mass flow rates between P_5 and P_1 locations is $81 \pm 15\%$ lower than the baseline case. However, it should be noted that the mass flow rate at port 5 is lower than that at port 1 location. Also, the mass flow rates at P_2 , P_3 , and P_4 locations show very similar mass flow rates, in some cases overlapping one another, which is a significant improvement compared to the baseline case. Even though the BP pellets have poor reproducibility burning behavior, the vent hole modification for case 3 indeed produced a nearly overlapping mass discharge rates from different vent holes along the flash tube.

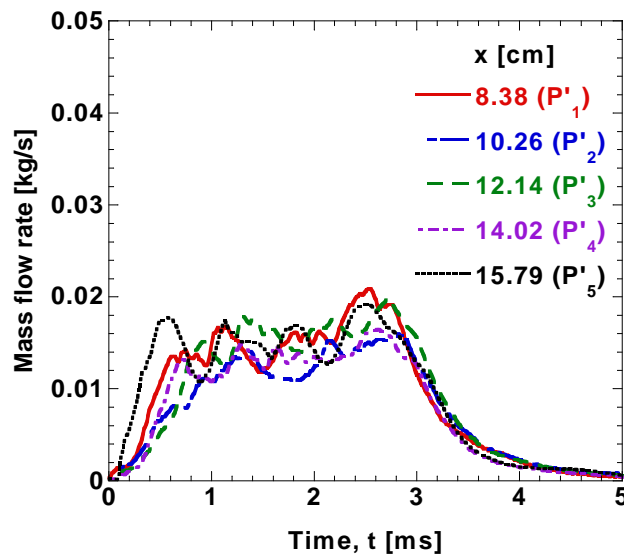


Figure 3-4: Deduced gaseous mass flow rate vs. time traces from one of the P-t traces of five flash tube tests with modified vent-hole pattern (case 3).

In order to examine the effect of modified flash tube designs on the pressurization processes in the M48 granular bed, the flash tube results were coupled with the ignition

cartridge sub-model for each of the three modifications. The interior ballistic processes in the granular bed with original flash tube design have been discussed in chapter 2 in great detail. The calculated pressure-time traces at five port locations (Port 0 through Port 4) on the tail-boom of the ignition cartridge with the original flash tube design are shown in Fig. 2-10. There is noticeable difference in the rise time at various pressure-gage port locations with the original flash tube design. At port 4 location, P_4 starts to rise before port 0 location, P_0 . This behavior is attributed to stronger discharge of igniter products from the flash tube at P_4 . Once start to rise, P_0 has higher pressurization rate than that of P_4 . This happens due to the generation of a pressure wave from P_4 propagating towards P_0 . Along with this pressure wave propagation, gas and particles are driven towards P_0 . At a pressure around 41 MPa (6,000 psia), there is a slight drop in pressure at all port locations due to the rupture of the propellant container tube wall and subsequent discharge of combustion products to the surroundings through the vent holes on the tail-boom. Thereafter, pressure in the granular bed keeps rising due to continued burning. The calculated results show that the pressure at P_0 takes over at P_4 before reaching the peak at around 140 MPa (20,000 psia). Finally, pressure-time traces at all port locations come closer and gradually converge during the later phase of the pressure decay.

The pressure-traces with first modification are shown in Fig. 3-5 and they exhibit a similar behavior to that of original flash tube design. However, it can be observed that during the initial rise time, the differences in pressure at various port locations are smaller than the case with original flash tube design. The calculated pressure-time traces for 2nd flash-tube vent-hole pattern modification (i.e., case 2) are shown in Fig. 3-6.

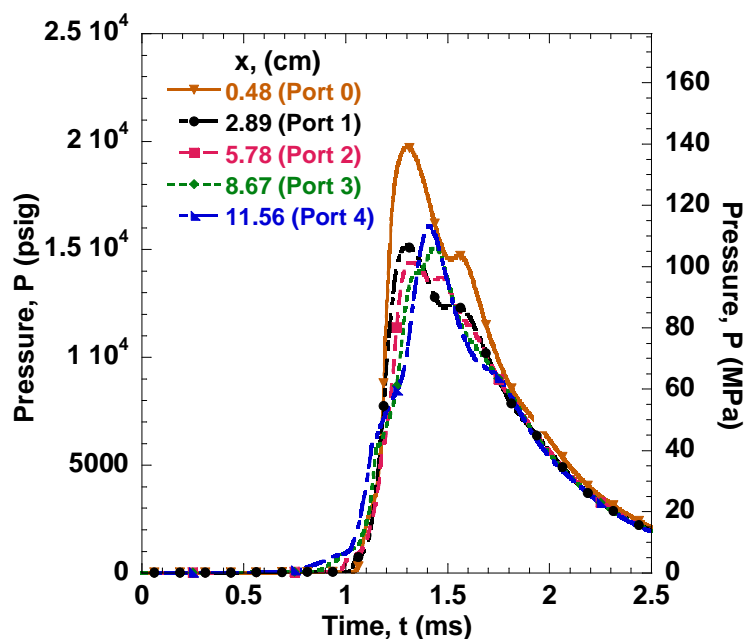


Figure 3-5: Computed pressure-time traces for a M1020 ignition cartridge at various pressure-gage port locations with a modified flash-tube vent-hole pattern (case 1).

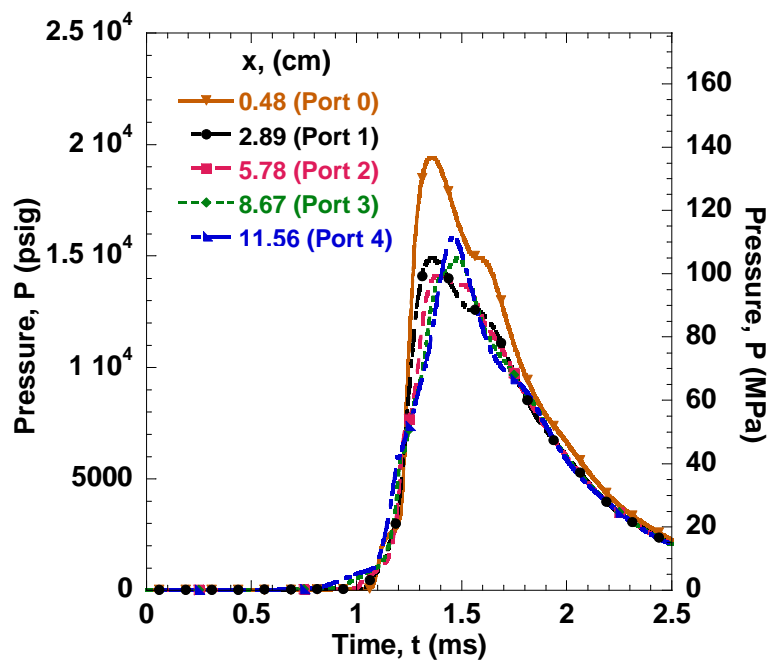


Figure 3-6: Computed pressure-time traces for M1020 ignition cartridge at five pressure-gage port locations with modified flash-tube vent-hole pattern (case 2).

These results show even further reduction of the differences in pressure-time traces at various port locations than the previous two cases during the initial rise time.

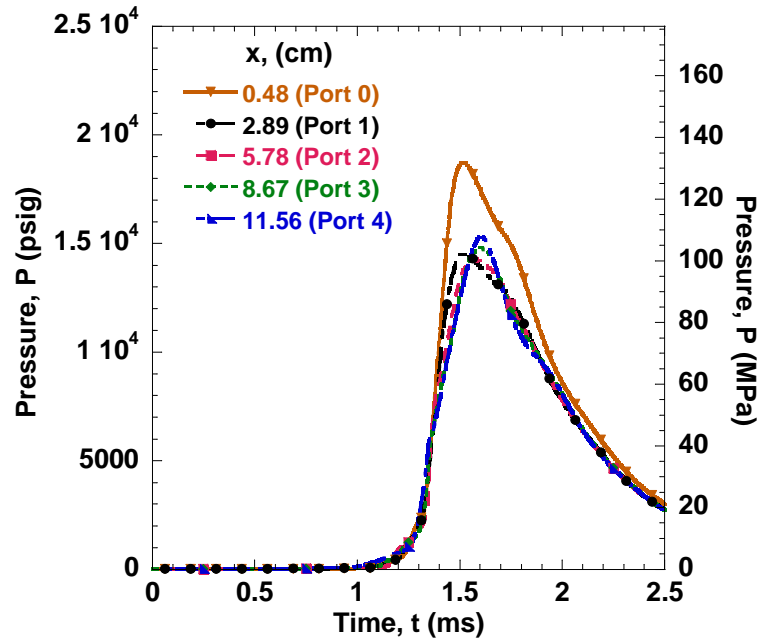


Figure 3-7: Computed pressure-time traces for a M1020 ignition cartridge at five pressure-gage port locations with a modified flash-tube vent-hole pattern (case 3).

In the case with 3rd modification of the flash tube, the pressure-time traces at each of the five port locations almost overlap with each other during the initial rise time as shown in Fig. 3-7. This trend can be explained on the basis of onset of ignition in the granular bed, which strongly depends on the sequence and magnitude of mass discharge events from the flash tube into the granular bed.

In the interior ballistic studies, it is useful to show the existence and intensity of pressure-wave phenomenon by plotting ΔP ($\equiv P_4 - P_0$) versus time. The calculated time variations of ΔP for all four cases in the granular bed are shown in Fig. 3-8. The ΔP -t behavior is very similar between the original flash tube design and the first modification

(case 1). However, a reduction in the amplitude of ΔP can be observed with the first modification of the vent-hole pattern on the flash tube. The second modification (i.e., case 2 with larger vent holes close to the primer-end) results in even greater reduction in the amplitude of ΔP between the projectile and primer ends of the ignition cartridge. The case 3 results show even lower yet significant pressure difference during the initial period ($t \leq 1.2$ ms) of the ballistic cycle that the previous modifications.

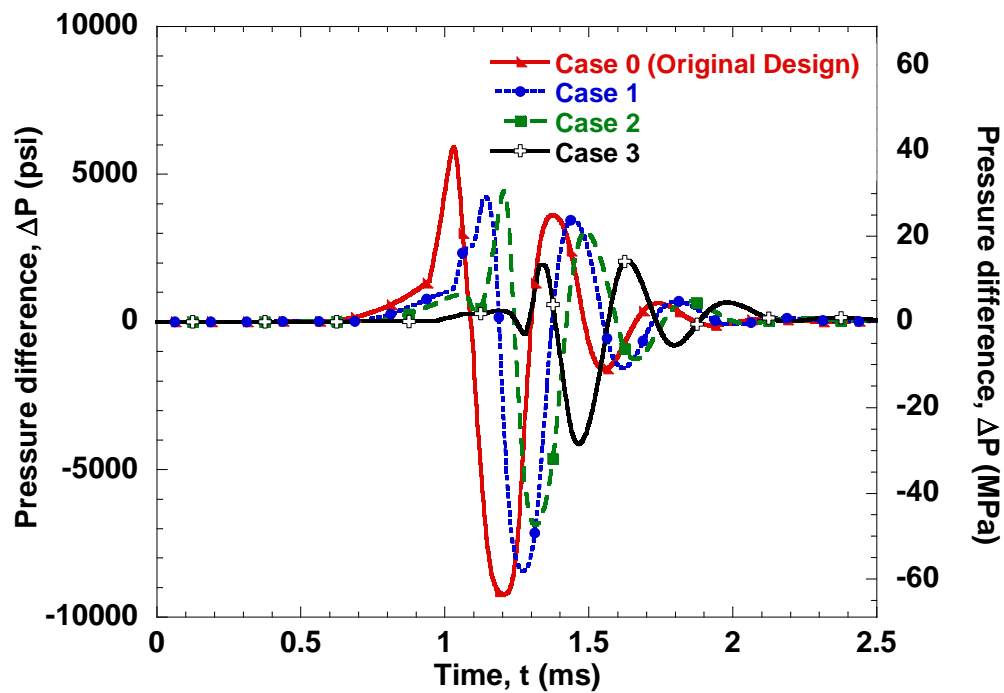


Figure 3-8: A comparison of predicted time variations of ΔP between projectile and primer ends in the granular for various flash-tube vent-hole patterns.

With the above three modifications, the difference in the mass discharge rates relatively reduced from the original design but it still stayed significant. In order to remedy that, a final modification was made with a greater reduction in the diameters of

vent holes no. 13-20. The diameters of vent holes 1-12 were significantly made larger.

The deduced mass discharge rates at five axial locations are shown in Fig. 3-9.

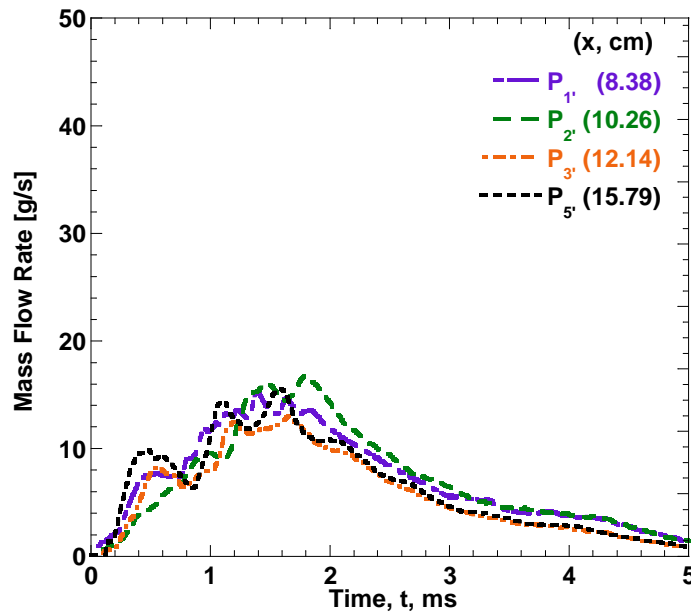


Figure 3-9: Deduced gaseous mass flow rate vs. time traces from one of the P-t traces of five flash tube tests with modified vent-hole pattern (final case).

A comparison of the integrated mass discharge rate difference between vent hole 20 (near the projectile-end) and vent hole 1 (near the primer-end) is shown in Fig. 3-10. It is very clear that the final modification results in a noticeable reduction in the mass discharge rates into the M48 granular bed between the two closed ends, especially during the first 1 ms of the discharging process. The percentage difference of each of these modifications from the original flash tube design (based upon the overall mass difference between vent hole 20 (near the projectile-end) and vent hole 1 (near the primer-end) was $40 \pm 15\%$, $73 \pm 15\%$, 81% , and 130% from the original flash tube design for the 1st, 2nd, 3rd, and final modifications, respectively.

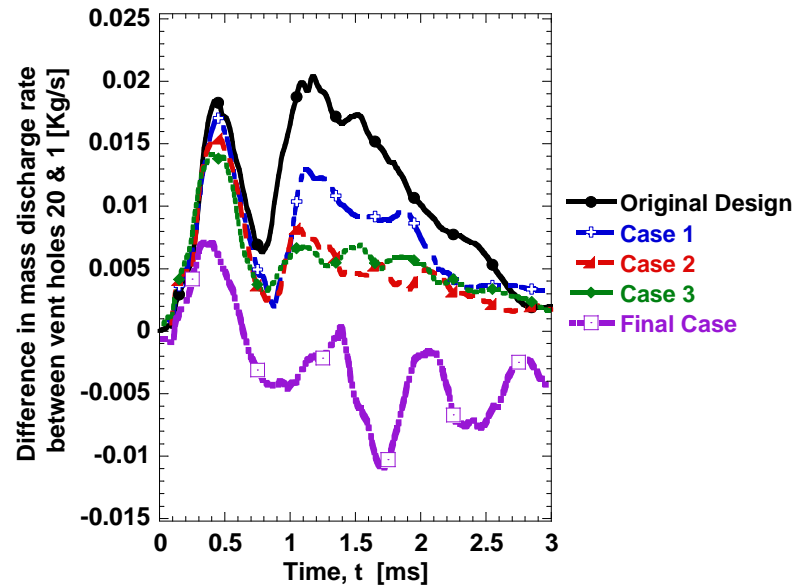


Figure 3-10: Difference in deduced mass flow rate from flash tube with five BP pellets between projectile and primer-ends for various vent-hole designs.

The computed pressure-time traces in the M48 granular bed with the modified flash tube with final modification are shown in Fig. 3-11. The pressure differences between port 17-port 0 and port 16-port 1 with time are shown in Fig. 3-12. The comparison with experimental data is shown in Fig. 3-13 and Fig. 3-14, respectively.

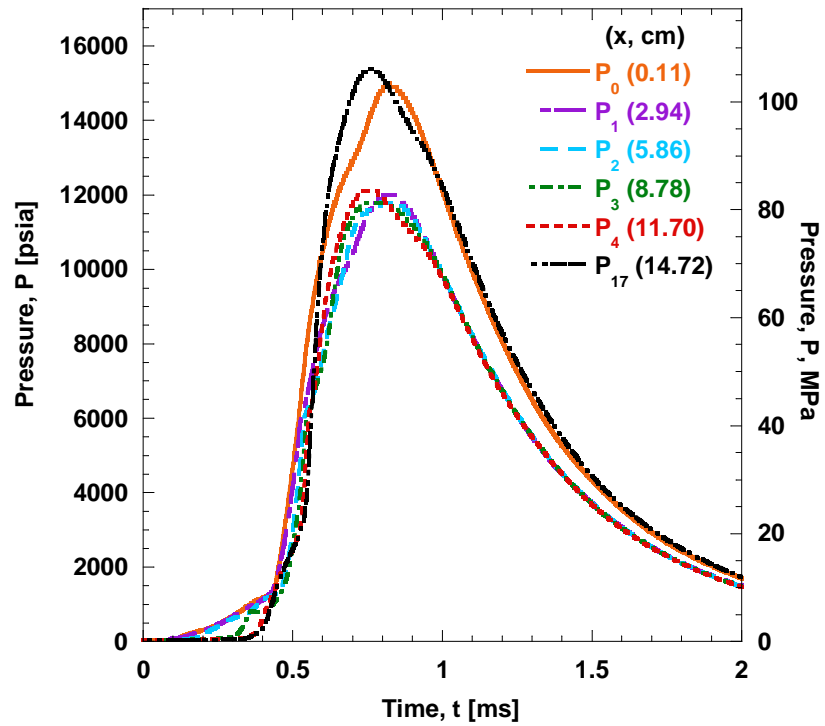


Figure 3-11: Computed pressure-time traces for ignition cartridge at five pressure-gage port locations with a modified flash-tube vent-hole pattern (final case).

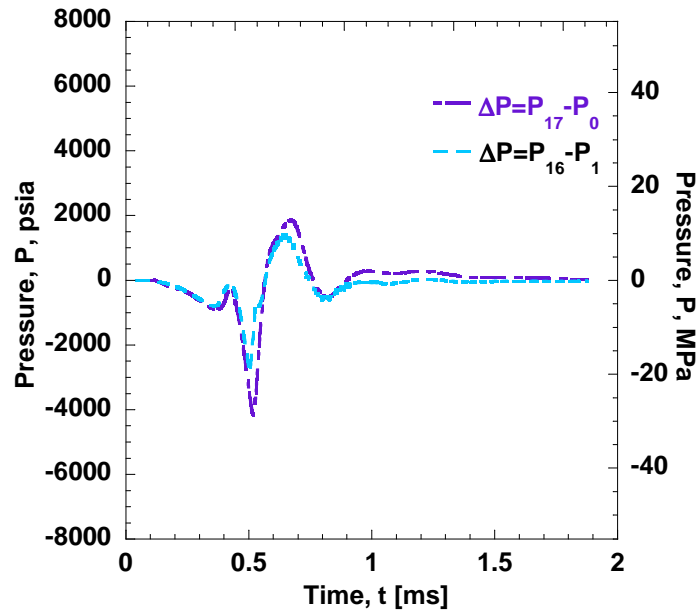


Figure 3-12: Comparison of numerical ΔP ($P_{17}-P_0$)-time traces and with modified ignition cartridge modified ignition cartridge [final modification].

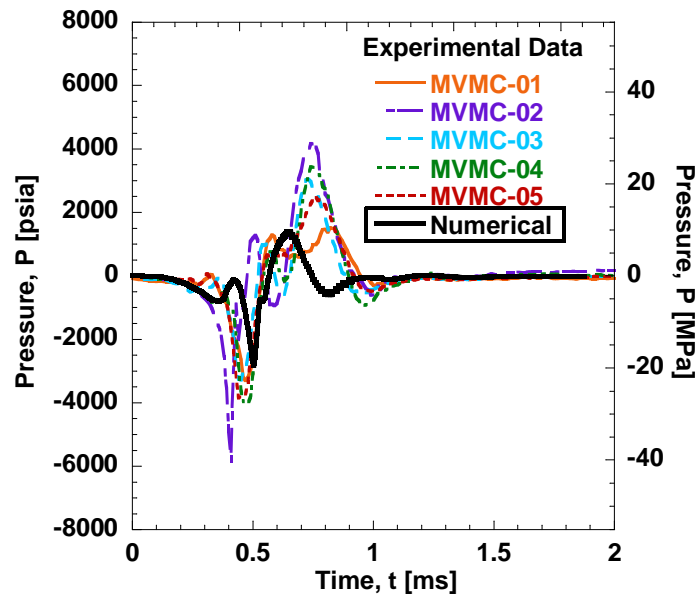


Figure 3-13: Comparison of experimental and numerical ΔP ($P_{16}-P_1$)-time traces and ΔP ($P_{17}-P_0$)-time traces with modified ignition cartridge [final modification].

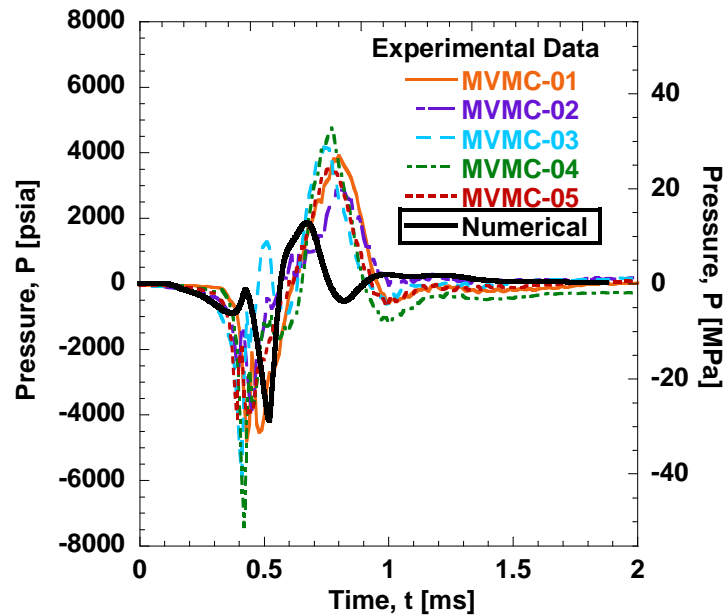


Figure 3-14: Comparison of experimental and numerical ΔP ($P_{17}-P_0$)-time traces with modified ignition cartridge [final modification].

The differences in the magnitudes of mass flow rates from the flash tube vent holes at various axial locations are significantly reduced with the stepwise modifications of the flash tube, thereby reducing the differences in the time of onset of ignition at various axial locations in the granular bed. This phenomenon results in more uniform ignition and pressurization of the granular bed. In case of the final modification, near isochronic ignition of granular propellants occur at all interior axial locations, which results in more uniform mass discharge from flash tube into the granular bed. As a results, there is uniform pressurization during the early phase of the ballistic event, thus the pressure gradient in the granular bed is substantially reduced during this period. This physical phenomenon is narrated by Fig. 3-15.

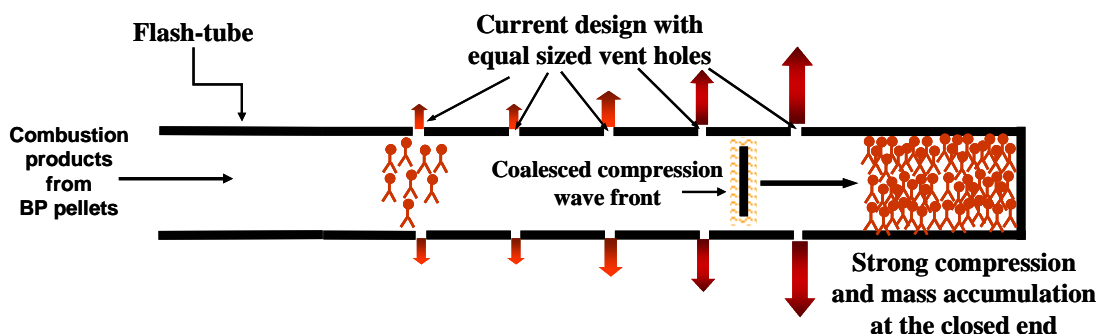


Figure 3-15: Narration of physical processes in the flash tube.

However, in the later period of the ballistic cycle, a pressure difference can still be observed, though it is significantly lower than the original flash-tube design. The generation of pressure difference during this later phase is caused by the presence of two stagnation regions close to the primer and projectile ends, where, there are no nearby vent holes on the tail-boom to discharge the combustion products. The burned products can only leave these regions by moving towards the middle section of the granular bed where vent holes are accessible, thereby resulting in the generation of a weak pressure wave during the later phase of the combustion event. This process is shown in Fig. 3-16.

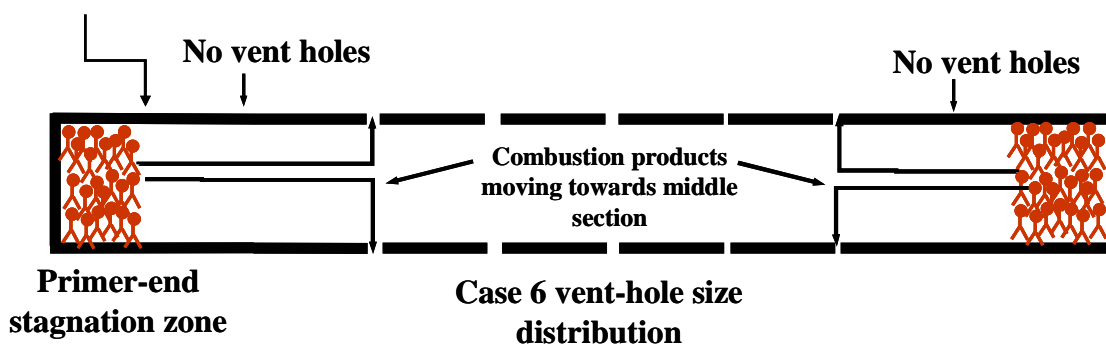


Figure 3-16: Explanation of pressure-time traces behavior in final modification of the flash tube.

The significant reduction in the strength of pressure waves can be further understood by a comparison of the net discharged condensed-phase mass at various axial locations in the M48 granular bed. The net discharged condensed-phase mass at the j^{th} port location on the flash tube is defined by Eq. (3.1).

$$M_{c,j} = \int_0^{t_{final}} \dot{m}_{c,j}(t) dt \quad (\text{Eq. 3.1})$$

The net discharged condensed-phase mass at four axial locations with the original flash tube design is shown in Fig. 3-17 and with the flash tube with final modification is shown in Fig. 3-18. It is useful to note that the accumulated mass of condensed-phase products discharging from different vent holes on the final modification flash tube is much closer in their magnitudes than the baseline case.

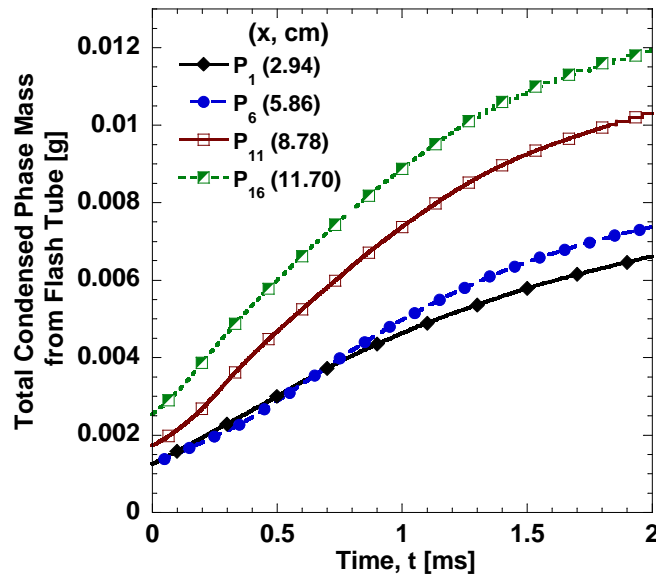


Figure 3-17: Computed accumulated condensed-phase mass from flash tube at various ports (original design).

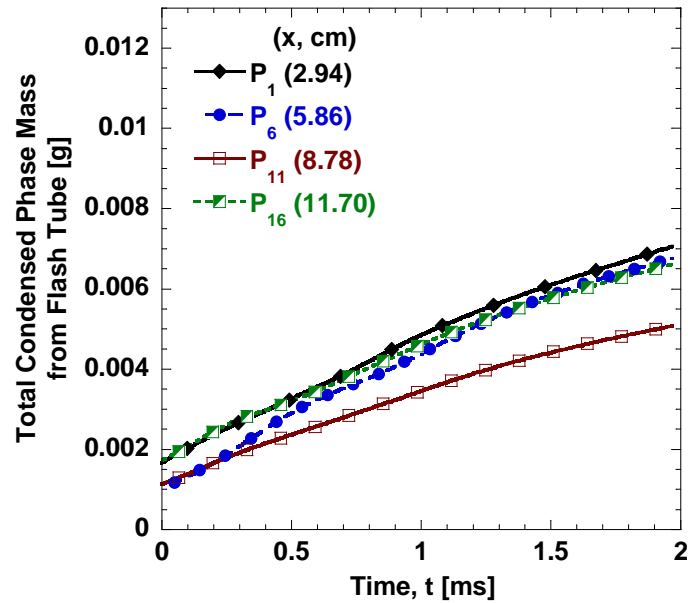


Figure 3-18: Computed accumulated condensed-phase mass from modified flash tube at various ports (final modification).

3.2.2 Discussion of vent-hole pattern analysis

Although the existing flash tube design of the M1020 ignition cartridge has a uniformly distributed vent-hole pattern on its flash tube with equal diameters, there is a significant difference in their pressure-time traces, resulting in substantially different mass discharge rates of the combustion products from the black powder pellets.

- These results show that by changing the vent-hole pattern on the flash tube containing five black powder pellets, more uniform mass discharge rates from these vent holes can be obtained.

- Numerical solution from the ignition cartridge sub-model show that the axial pressure gradient in the granular bed of an M1020 ignition cartridge can be significantly reduced by modifying the vent-hole pattern on the flash tube. Physically, this can be interpreted as the attainment of more uniform ignition (with isochronic ignition as the optimum design) in the granular bed, thus resulting in more uniform combustion of the solid ball propellants. The reproducibility and reliability of the mortar system can be improved with the substantially reduced pressure wave phenomena.

3.3 Effect of pyrotechnic materials in the flash tube

There were two specific reasons to simulate the effect of pyrotechnic materials in the flash tube on the pressurization processes in the ignition cartridge: 1) the flash tube shows a very high variability in overall mass discharge rates with the black powder (BP) igniter pellet, which was thought to be cause for the higher variation in performance of the 120mm mortar system, 2) to examine the robustness of the ignition cartridge sub-model by comparing the calculated pressure-time traces with a different type of igniter pyrotechnic material in the flash tube to the measured pressure-time traces.

Black powder is an important energetic material used in several military applications. However, there are certain limiting characteristics that make it highly unreliable material. The black powder absorbs moisture and its charcoal content varies from lot to lot, which alters its burning rate behavior, thereby resulting in the non-repeatability of the flash tube pressurization processes. In addition, the BP combustion

produces sulfur dioxide that is toxic by inhalation and is an acid rain precursor. The alternative pyrotechnic material is known as moisture resistance black powder substitute (MRBPS). The principle constituent of MRBPS is potassium nitrate (KNO_3), which is same as the black powder. This material is charcoal and sulfur free and phenolphthalein is used as a replacement fuel for charcoal. The heat of explosion of MRBPS (798 kcal/g) is comparable to that of black powder (810 kcal/g). The pressure exponents are somewhat higher for MRBPS (>0.33) than BP ($=0.20$).

3.3.1 Flash tube results

The deduced mass flow rates from the original flash tube design are shown in Fig. 3-1 with the black powder pellets for one experiment. The deduced mass flow rates from the original flash tube design for another experiment are shown in Fig. 2-5. A comparison of these two plots shows that there was poor reproducibility among the flash tube performance with black powder between the two separate tests, even though these BP pellets used for all testing were from the same batch. The other noticeable features of these results are that there are multiple peaks of gas-phase mass flow rates and highest mass flow rate is at the farthest axial location from the black powder pellets and lowest at the closest axial location.

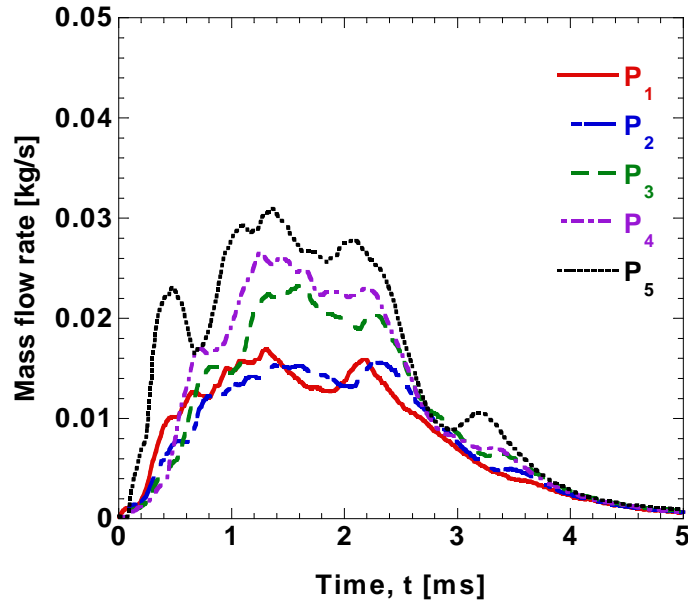


Figure 3-19: Deduced gaseous mass flow rate vs. time traces from a set of P-t traces of five flash tube tests with the original vent-hole pattern.

The deduced mass flow rates from the original flash tube design are shown in Fig. 3-20 with MRBPS pellets for one experiment. The combustion event inside the flash tube differs significantly between the two types of pyrotechnic pellets. Firstly, the magnitudes of gaseous mass discharge rates from the flash tube into the granular bed are significantly higher with the MRBPS pellets. Secondly, a single peak of gas-phase mass flow rates can be observed with the MRBPS pellets whereas the black powder show multiple peaks. However, the combustion products of MRBPS pellets contained a higher percentage of gas-phase products than the black powder pellets.

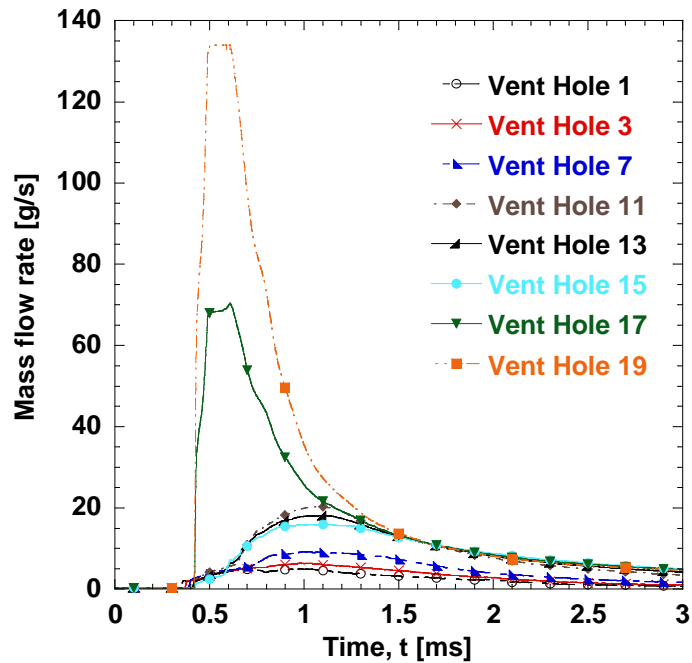


Figure 3-20: Deduced gaseous mass flow rate vs. time traces from the flash tube with MRBPS pellets.

3.3.2 Ignition cartridge results

These gas-phase mass flow rates were deduced from the flash tube sub-model and then used in the granular bed sub-model for the determination of pressurization rates at various axial locations in the granular propellant bed. The calculated pressure-time traces are shown in corresponding to BP and MRBPS pellets, respectively. In both figures, pressure at port 4 location, P_4 starts to rise before port 1 location. This behavior is attributed to stronger discharge of igniter products from the flash tube near P_4 location. The pressure rise starts earlier when MRBPS pellets are used in comparison with BP pellets due to earlier and higher rate of mass discharge. In general, the pressure wave

behavior in the granular bed using MRBPS pellets in the initiator is similar to those using BP pellets as initiator. However, the pressure rise starts earlier when MRBPS pellets are used in comparison with BP pellets due to earlier and higher rate of mass discharge.

The computational results from the numerical code are compared with experimental results for the case with MRBPS pellets as shown in Fig. **3-21**. The predicted pressure-time traces match the pressure wave phenomenon very closely for both BP and MRBPS cases as well as the peak pressure magnitude and rise time. It is useful to note that the predicted maximum pressure occurred in the axial location ($x = 0.11$ cm) significantly below the P_1 transducer location, which was not measured in the earlier set of experiments. After the numerical results were known, a pressure transducer port called P_0 was added to the tail-boom section. The recorded P_0 -t traces were indeed much higher than the P_1 -t traces as predicted by the computer code. This experimental confirmation further verifies the predictability of the numerical code. Similar to BP case, pressure at port 4 location, P_4 starts to rise before port 1 location. This experimental confirmation further verifies the predictability of the numerical code.

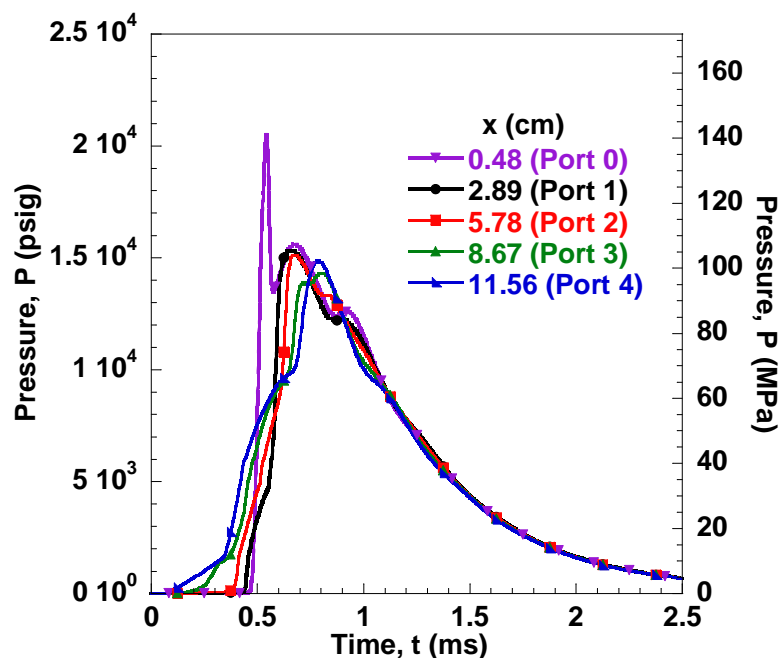


Figure 3-21: Computed P-t traces in ignition cartridge using MRBPS pellets in the flash tube.

The combustion event starts earlier with MRBPS pellets and shows more rapid pressurization rate. In both cases, pressure traces showed significant axial pressure wave phenomena, which were simulated reasonably close to the measured pressure-time traces. The predicted pressure in the igniter-end matched very well with the experimental data that was obtained later, thus affirming the reliability of the numerical code.

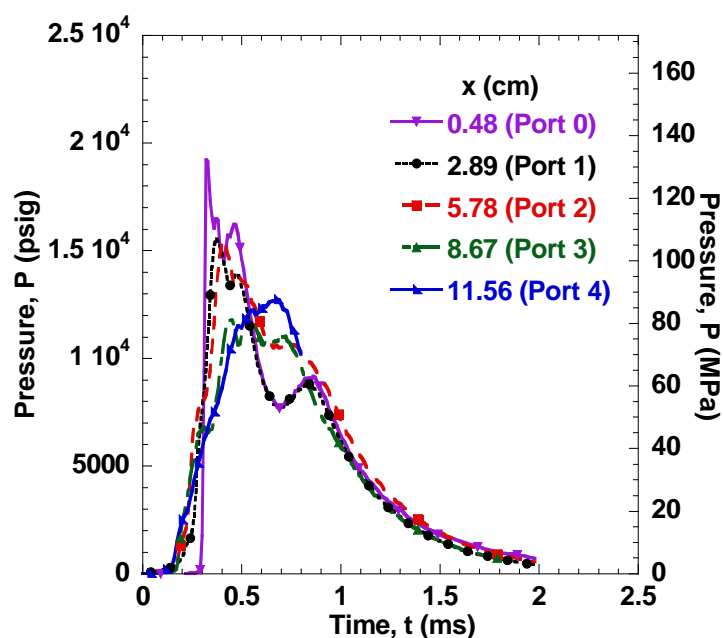


Figure 3-22: Measured P-t traces in ignition cartridge using MRBPS pellets in the flash tube.

3.4 Summary

This work demonstrates the successful implementation of the ignition cartridge sub-model and numerical code for prediction of ignition/combustion, flame spreading, and pressurization processes in the ignition cartridge section of the 120mm mortar propulsion system. The computational results were partially validated by experimental data from ignition cartridge tests. The computed results show the pressure wave generation, propagation, and wave-reflection in ignition cartridge with a number of modified flash tubes and two different igniter materials in the flash tube. In essence, the theoretical model and numerical code developed for ignition cartridge performance

prediction proves to be a useful predictive tool. Two main goals were accomplished with the work described here:

1. The model was successfully tested and validated with a number of design changes in the ignition cartridge, thus showing the robustness of this numerical code;
2. It was demonstrated that a numerical code can be used to provide guidance for performance improvement of complex engineering systems as shown by the in-depth analysis of modified flash tube vent-hole pattern analysis.

Chapter 4

FORMULATION OF MORTAR TUBE COMBUSTION SUB-MODEL

The mortar tube section is the most complex part of the 120mm mortar system. It contains a projectile payload, up to four horseshoe shaped charge increments (called M234) containing granular propellants (called M47), and a fin region. A mathematical model for the simulation of the ignition and combustion of the M47 granular propellants and the resulting two-phase interior ballistic processes was developed. Heating, ignition, flame spreading, combustion, and chamber pressurization processes in the mortar tube in the mortar tube section were coupled with the transient gas dynamic behavior of hot product gas and particles that are discharged into the mortar tube section from the vent holes of the tail-boom section. The mass, momentum, and energy equations for the gas-phase, and the mass, momentum, and heat equations for the granular propellants with the appropriate boundary and initial conditions are described in this chapter.

4.1 Assumptions

There are four basic assumptions considered in the mortar tube sub-model in order to render the model solvable within the scope of the present work. They are listed below:

1. The combustible charge increment cases containing ball-shaped propellant grains are considered to have negligible mechanical resistance to the hot plume jets

issuing from the vent holes on the tail-boom section, after the rupture of the yellow colored propellant cup.

2. The heat of reaction of the combustible cases for the charge increments is considered to be negligibly small. Any heat of reaction due to the burning of the combustible cases can be added at a later stage if necessary.
3. The flow rate associated with the blow-by phenomena at the obturating ring is considered to be negligibly small.
4. Due to the relatively short firing time, the heat loss from the combustion products to the mortar tube wall and the projectile is considered to be negligible.

4.1.1 Governing equations for the mortar tube gas dynamics

The mass, momentum, and energy equations for the gas phase, and the mass and momentum equations for the granular propellants are similar to those described earlier for the tail-boom section. However, the physical processes in the mortar tube section are transient and three-dimensional in nature. Therefore, a three dimensional (3-D) computational model can capture the combustion behavior more efficiently due to the complexity of geometry in this case. The major equations are listed below for the convenience. The governing equations for this system are as follows. The gas-phase mass conservation equation is given by Eq. (4.1) as:

$$\frac{\partial(\rho\phi\zeta)}{\partial t} + \nabla \cdot (\rho\phi\zeta \mathbf{U}_g) = \Sigma_1 \quad (\text{Eq. 4.1})$$

where, $\Sigma_1 \equiv A_{sb}\rho_p r_b \zeta + \alpha_g f(r) \dot{m}_{b,tb-in} + \alpha_g f(r) \dot{m}_{g,tb}$

The mass conservation equation for the solid phase (i.e., granular propellants) is given by Eq. (4.2):

$$\frac{\partial[(1-\phi)\rho_p\zeta]}{\partial t} + \nabla \cdot [(1-\phi)\rho_p\zeta\mathbf{U}_p] = \Sigma_2$$

(Eq. 4.2)

where, $\Sigma_2 \equiv -A_{sb}\rho_p r_b \zeta - \alpha_p f(r)\dot{m}_{b,tb-in} + \alpha_p f(r)\dot{m}_{c,tb}$

The parameter α_g is introduced to account for the presence of vent hole at an axial location. It is equal to 1 if a tail-boom vent hole is located on the surface of this element, and 0 otherwise since there is no direct source term from the tail-boom boundary surface.

$$\alpha_g = \begin{cases} 1 & \text{if vent hole present} \\ 0 & \text{otherwise} \end{cases}$$

The parameter α_p is similar to the parameter α_g and it also accounts for the presence of vent hole at an axial location. It is equal to 1 if a tail-boom vent hole is located on the surface of this element, and 0 otherwise since there is no direct source term from the tail-boom boundary surface.

$$\alpha_p = \begin{cases} 1 & \text{if vent hole present} \\ 0 & \text{otherwise} \end{cases}$$

The function $f(r)$ represents the radial distribution function for deposition of ejected gas and particle from the tail-boom. So, as the radial distance from the surface of tail-boom section, r increases, value of $f(r)$ may decrease slightly depending upon the strength of the ejected gas and particle from the tail-boom vent hole. For the current version of calculations, the radial dependency is considered uniform. Thus, the

function $f(r)$ has been treated as a constant. For example, if there are five radial intervals in the mortar tube then the value of $f(r)$ would be 1/5.

The source terms in the above two equations contain three terms; the first term represents gas generation due to burning of M47 granular propellant, the second term represents the gas-generation due to burning of M48 granular propellants that are injected into the mortar tube from tail-boom, and the third term represents the gas-phase mass addition from the tail-boom. Similarly, the source term in the condensed-phase mass conservation equation consists of the three terms, the first term represents condensed-phase mass loss due to burning of M47 granular propellants, the second term represents the condensed-phase mass loss due to burning of M48 granular propellants that are injected into the mortar tube from tail-boom, and the third term represents the condensed-phase mass addition from the tail-boom. In the above equations, subscript “*tb*” means “tail-boom” and “*tb-in*” means incoming from the tail boom. In Eq. (4.2), ρ_p is the density of M48 ball propellants that are incoming from the tail-boom section and r_b is the burning rate of particles ejected from tail-boom sect M48 ball propellants calculated based on the local pressure. The term \dot{m}_{tb-in} in Eq. (4.1) and Eq. (4.2) Eq. (4.3) is given as following:

$$\dot{m}_{tb-in} = \left(A_{sb} \rho_p r_b [P_{local}] \right)_{tb-in} \quad (\text{Eq. 4.3})$$

The gas-phase momentum equations are given by Eq. (4.4) as:

$$\begin{aligned}
& \frac{\partial \rho \phi \zeta \mathbf{U}_g}{\partial t} + \nabla \rho \phi \zeta \mathbf{U}_g \cdot \mathbf{U}_g + \nabla \phi \zeta P = \mathbf{I}_g \\
\text{where, } & \mathbf{I}_g = \alpha_g f(r) \dot{m}_{g,tb} \mathbf{U}_{g,i} + A_{sb} r_b \rho_p \zeta (\mathbf{U}_{p,i} - \mathbf{U}_{g,i}) - A_s \zeta \mathbf{D}_{v,i} \\
& + \alpha_g f(r) \dot{m}_{b,tb-in} \zeta (\mathbf{U}_{p,i} - \mathbf{U}_{g,i}) - \zeta A_{s,tb-in} \mathbf{D}_{v,i}
\end{aligned} \tag{Eq. 4.4}$$

$$\text{and } \mathbf{I}_g(\mathbf{Q}) \equiv \begin{bmatrix} \Sigma_3(\mathbf{Q}) \\ \Sigma_4(\mathbf{Q}) \\ \Sigma_5(\mathbf{Q}) \end{bmatrix}$$

Even though the viscous stress effects between the gas molecules are present, their effect to the overall momentum balance is believed to be negligible in comparison with the drag force between the solid particles and gas-phase. The latter is approximated by an empirical correlation; thus, there is no need to retain the higher order derivative terms in the governing momentum equations. It is important to note that the total drag force between the gas and particle phases \mathbf{D}_b is equal to the sum of the drag force due to the presence of relative velocity between the gas and particle phases and the drag force induced by change of flow area due to particle size variation in a given plane. The latter effect can also be interpreted as the porosity gradient, i.e. Eq. (4.5).

$$\mathbf{D}_t = \mathbf{D}_v + \mathbf{D}_p = \mathbf{D}_v - \frac{P}{A_s} \nabla \phi \tag{Eq. 4.5}$$

The particle-phase momentum equations are derived in the similar manner as the gas-phase and it is shown in Eq. (4.6).

$$\frac{\partial}{\partial t} [\rho_p (1-\phi) \zeta \mathbf{U}_p] + \nabla \rho_p (1-\phi) \zeta \mathbf{U}_p \cdot \mathbf{U}_p - \nabla \zeta (1-\phi) \tau_p = \mathbf{I}_p$$

$$\text{where, } \mathbf{I}_p = \alpha_p f(r) \dot{m}_{c,TB} \mathbf{U}_p - \alpha_p f(r) \dot{m}_{b,tb-ej} (\mathbf{U}_p - \mathbf{U}_g) \\ + A_s \zeta \mathbf{D}_t - A_{sb} r_b \rho_p \zeta \mathbf{U}_p$$

(Eq. 4.6)

$$\mathbf{I}_p(\mathbf{Q}) \equiv \begin{bmatrix} \Sigma_6(\mathbf{Q}) \\ \Sigma_7(\mathbf{Q}) \\ \Sigma_8(\mathbf{Q}) \end{bmatrix}$$

The energy equation for gas-phase is given by Eq. (4.7):

$$\frac{\partial(\rho \phi \zeta e_t)}{\partial t} + \nabla \cdot (\rho \phi \zeta e_t \mathbf{U}_g) + \nabla \cdot (\phi \zeta P \mathbf{U}_g) = \Sigma_9$$

where,

$$\Sigma_9 = A_{sb} \rho_p r_b \zeta c_{p,T_f} (T_f - T_{ref}) - (A_s - A_{sb}) h_t (T - T_{ps}) \zeta + \alpha_g f(r) \dot{m}_{g,tb} h_{g,tb} \\ + \alpha_g f(r) \dot{m}_{b,tb-ej} c_{p,T_f} (T_f - T_{ref}) - A_s \zeta \mathbf{U}_p \cdot \mathbf{D}_t \\ - P \frac{\partial \phi}{\partial t} - \zeta (A_s \mathbf{U}_p \cdot \mathbf{D}_t)_{tb-ej}$$

(Eq. 4.7)

In the above equations, e_t is the total energy per unit mass and it is defined by Eq. (4.8) as following:

$$e_t \equiv e + \frac{1}{2} \mathbf{U}_g \cdot \mathbf{U}_g = c_v (T - T_{ref}) + \frac{1}{2} \mathbf{U}_g \cdot \mathbf{U}_g$$

(Eq. 4.8)

In the given model, the constant-pressure specific heat has been taken to be a known function of pressure and temperature as in its conventional form. The energy equation for spherical particles in the charge increment would be same as that used for the tail-boom section. The surface temperature equation for the ball propellants is given by Eq. (4.9).

Unlike ignition cartridge, there is no condensed-phase coating on the M47 ball propellants and therefore, the ball propellants in the mortar tube are heated by convection heat transfer. The combustion products of M48 propellants do not contain any liquid-phase products.

$$\begin{aligned} \frac{\partial T_{ps}}{\partial t} + \mathbf{U}_p \cdot \nabla T_{ps} = & \frac{\frac{12\alpha_p}{\delta r_p} \left[(T_{ps} - T_0) + \frac{r_{p0} h_t}{k_p} (T - T_{ps}) \right]}{\left[\frac{6r_{p0} - \delta}{r_{p0}} + \frac{h_t \delta}{k_p} \right]} \\ & + \frac{\frac{\delta h_t}{k_p}}{\left[\frac{6r_{p0} - \delta}{r_{p0}} + \frac{h_t \delta}{k_p} \right]} \left(\frac{\partial T}{\partial t} + \mathbf{U}_p \cdot \nabla T \right) \end{aligned} \quad (\text{Eq. 4.9})$$

4.2 Initial conditions

4.2.1 Initial condition for velocity

In the mortar tube, both the gas-phase and solid particles are stationary at $t = 0$, which is defined as the time before the primer was actuated. Therefore, the initial conditions for both gas-phase velocity and particle velocity are given by Eq. (4.10) and Eq. (4.11) as following:

$$\mathbf{U}_g(\mathbf{x}, t = 0) = 0 \quad (\text{Eq. 4.10})$$

$$\mathbf{U}_p(\mathbf{x}, t = 0) = 0 \quad (\text{Eq. 4.11})$$

4.2.2 Initial condition for porosity

The initial condition for porosity is given by the positioning of charge increments in the mortar tube. The charge increments are horse-shoe shaped. There are four such charge increments in the mortar tube and they are alternatively positioned (*see* Fig. **4-1**). Therefore, the initial condition for porosity reflects this arrangement and it is given by Eq. (4.12) and Eq. (4.13):

For $z_1 \leq z \leq z_2$ and $z_3 < z \leq z_4$

$$\phi(t=0, \mathbf{x}) = \begin{cases} 1 & \text{if } 0 \leq \theta \leq \theta_{empt} \\ \phi_{o,CI} & \text{otherwise} \end{cases} \quad (\text{Eq. 4.12})$$

For $z_2 \leq z \leq z_3$ and $z_4 < z \leq z_5$

$$\phi(t=0, \mathbf{x}) = \begin{cases} \phi_{o,CI} & \text{if } 0 \leq \theta \leq (\pi - \theta_{empt}) \\ 1 & \text{otherwise} \end{cases} \quad (\text{Eq. 4.13})$$

where, $\phi_{o,CI}$ is the initial porosity in the mortar tube charge increments and, θ_{empt} is the half angle between the ends of the horse-shoe shaped charge increments. If the loading of charge increments is changed from alternate to aligned arrangement then the above initial condition must be modified to reflect the actual loading condition.

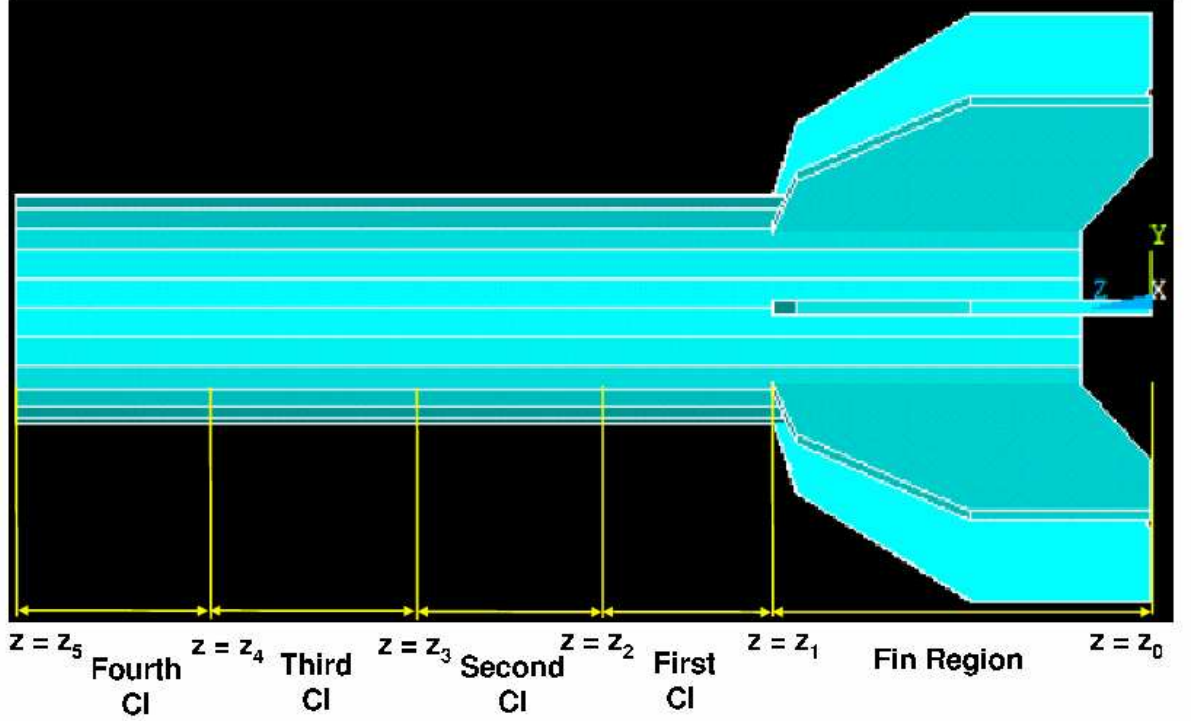


Figure 4-1: Fin region of the 120mm mortar projectile.

4.2.3 Initial condition for temperature and pressure

In the mortar tube, the temperature and pressure at $t = 0$, which is defined as the time before the primer was actuated are given by Eq. (4.14) and Eq. (4.15):

$$T(\mathbf{x}, t = 0) = T_{amb} \quad (\text{Eq. 4.14})$$

$$P(\mathbf{x}, t = 0) = P_{atm} \quad (\text{Eq. 4.15})$$

In the above expressions, subscript *amb* represents the ambient or pre-specified conditions.

4.3 Boundary conditions

In general, solid wall boundary conditions are used for most of the variables in radial, axial, and tangential directions. The boundary conditions for the gas-phase velocity and condensed-phase velocity were complex. These boundary conditions were defined based on the geometry of the mortar tube and projectile.

4.3.1 On ignition cartridge surface in the vent hole region

The boundary conditions on the projectile surface for gas-phase velocity and particle velocity are given by Eq. (4.16) and Eq. (4.17) as:

$$\left. \begin{aligned} U_{g,r} \Big|_{(r=r_i, \theta, z, t)} &= U_{g,tb-in} \\ U_{p,r} \Big|_{(r=r_i, \theta, z, t)} &= U_{p,tb-in} \end{aligned} \right\} \quad \vee \quad \alpha = 1 \quad (\text{Eq. 4.16})$$

$$\frac{\partial U_{p,r}}{\partial r} \Big|_{(z, r=r_i, \theta, t)} = 0 \quad \vee \quad \alpha = 0 \quad (\text{Eq. 4.17})$$

Due to very short duration of the ballistic cycle in the mortar tube, the energy transfer through tail-boom outer surface, projectile surface, and mortar tube surface are assumed to be negligible. Therefore, the solid wall boundary condition was applied for gas density, porosity, and gas-phase temperature. This means that the gradients of these variables in the direction of surface normal were taken as zero, implying that there is no mass or energy transport through the wall.

4.3.2 In the fin region

Fin region is the part of tail-boom where fins are located as shown in Fig. 4-1. If fins are assigned a number (n) from 1 to 8 then the boundary conditions for the gas-phase and particle at the surface of fin are given by Eq. (4.18) as:

$$\left. \begin{aligned} U_{g,\theta} \Big|_{(r,\theta=(n-1)\pi/4,z,t)} &= 0 \\ U_{p,\theta} \Big|_{(r,\theta=(n-1)\pi/4,z,t)} &= 0 \end{aligned} \right\} \text{for } z_0 \leq z \leq z_1 \quad (\text{Eq. 4.18})$$

The above boundary conditions imply that the “average” tangential velocity of numerous particles at the fin surface is zero, even though particles can bounce at the wall upon impact. Similarly, gas cannot penetrate the fin surface, the average $U_g = 0$.

4.3.3 The z-direction boundary conditions

Since the primer end of mortar tube is closed, there can not be any penetration through the wall. Therefore, the average gas-phase velocity in z -direction will be zero at the primer-end location. The gas-phase at the obturating ring location moves along the projectile. Therefore, the gas-phase velocity in z -direction at this axial location is same as the projectile velocity. These boundary conditions are given by Eq. (4.19) as:

$$\left. \begin{aligned} U_{g,z} \Big|_{(z=0,r,\theta,t)} &= 0 \\ U_{g,z} \Big|_{(z=z_6,r,\theta,t)} &= V_{\text{Projectile}} \end{aligned} \right\} \quad (\text{Eq. 4.19})$$

The solid wall boundary condition was applied for gas density, porosity, and gas-phase temperature. This means that the gradients of these variables in the direction of surface normal were taken as zero, implying that there is no mass or energy transport through the walls.

4.4 Summary of mortar tube sub-model

The interior ballistic processes in the mortar tube section are modeled by the governing equations, initial conditions, and the boundary conditions described in this chapter. The governing equations are strongly coupled. In order to have direct temporal derivatives of major unknowns, those equations have been simplified using mathematical manipulations. In order to solve this system of equations, an efficient numerical technique is necessary. Two approaches for solving this system of equations were considered; one by using a finite element method (FEM) based numerical approach and another by using a finite volume method based Riemann solver approach. The results obtained from these two different approaches and issues related to them are described in following chapters.

Chapter 5

FORMULATION OF PROJECTILE DYNAMICS SUB-MODEL

5.1 Basic assumptions

Several basic assumptions have been considered in this analysis as a part of the 3D Mortar Interior Ballistics (3D-MIB) model in order to render the equations solvable within the scope of the present work. These assumptions are listed below:

1. Particles striking the projectile surface have elastic collision with the surface, which means that particles striking the surface return with the same velocity magnitude; thus they do not lose kinetic energy as a result of collision.
2. The solid surface of projectile is considered to be non-permeable except through vent holes on the fin-boom section.
3. The pressure force acting on the projectile is mainly due to gas-phase pressure. Since the porosity will be very close to 1, the force exerted on projectile surface by condensed-phase particles is assumed to be negligible with respect to gas-phase pressure force.
4. The shear stress on projectile surface due to boundary layer is neglected.
5. There are no body forces except gravity acting on projectile.

5.2 Net force and pressure distribution

The net force on the projectile and the force distribution on projectile surface in all three dimensions are formulated in this section. The vector sum of all axial forces (due to gas-pressure, tube-projectile wall friction, and gravity) acting on the projectile is defined as net rate of change of momentum of the projectile in axial direction. Change of projectile momentum is partly due to ejection of partially burned ball propellant and the gas jet through the vent holes on fin-boom section.

$$\frac{d}{dt}(M_{\text{Proj}} U_{\text{Proj}}) = F_{\text{Pressure}} - F_{\text{Friction}} - M_{\text{Proj}} g \cos \beta \quad (\text{Eq. 5.1})$$

In Eq. (5.1), β is the angle of elevation of the mortar tube and g is gravitational acceleration and M_{Proj} is the instantaneous mass of the projectile. The instantaneous mass of projectile is given by Eq. (5.2) as:

$$M_{\text{Proj}}(t) = M_{\text{proj}}(t=0) - \sum_{k=1}^{N_{\text{vh}}} \int_0^t (\dot{m}_{\text{TBvhg}} + \dot{m}_{\text{TBvhc}})_k dt' \quad (\text{Eq. 5.2})$$

Here N_{vh} is the total number of vent holes on the fin-boom section. The terms \dot{m}_{TBvhg} and \dot{m}_{TBvhc} are the rate of gas-phase and condensed-phase mass flowing out of the vent holes on the tail-boom section.

The gas pressure is computed from the gas-phase conservation equations and it is always perpendicular to the surface. Therefore, net force on projectile due to gas pressure is vector sum of the product of pressure and area of all the control volume attached to the projectile surface. Force on projectile surface in z-direction due to gas-phase is given by Eq. (5.3):

$$\mathbf{F}_{\text{Pressure}} = \oint_{A_{\text{Proj}}} P \mathbf{n} \cdot \sin \alpha d\mathbf{A}_{\text{Proj}} \quad (\text{Eq. 5.3})$$

The area \mathbf{A}_{Proj} is a vector and it is defined by Eq. (5.4) as following:

$$d\mathbf{A}_{\text{Proj}} = dA_{\text{Proj}} \mathbf{n} \quad (\text{Eq. 5.4})$$

where α is the local angle between the z-axis and tangent plane to the projectile surface as shown in Fig. 5-1 and \mathbf{n} is the outward normal vector to local projectile surface.

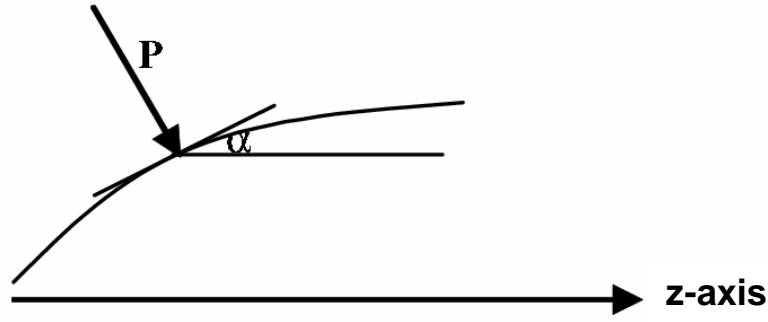


Figure 5-1: Pressure acting on a local projectile surface at angle α .

Therefore, the projectile dynamics is governed by Eq. (5.5):

$$\frac{d}{dt} (M_{\text{Proj}} U_{\text{Proj}}) = \oint_{A_{\text{Proj}}} P \mathbf{n} \cdot \sin \alpha d\mathbf{A}_{\text{Proj}} - F_{\text{Friction}} - M_{\text{Proj}} g \cos \beta \quad (\text{Eq. 5.5})$$

The control volumes attached to the projectile surface are shown as grey colored regions in Fig. 5-2.

In general, force is a vector with three components in r -, θ -, and z - directions. For the desired operation of projectile, the scalar sum of force component in r - and θ -

directions should be zero when summed over the entire surface area of projectile exposed to the high-pressure region. Therefore,

$$\sum_j F_r = 0 \quad (\text{Eq. 5.6})$$

$$\sum_j F_\theta = 0 \quad (\text{Eq. 5.7})$$

The detailed vibrational and rotational motions of the projectile payload were not treated in the present analysis due to the scope limitation.

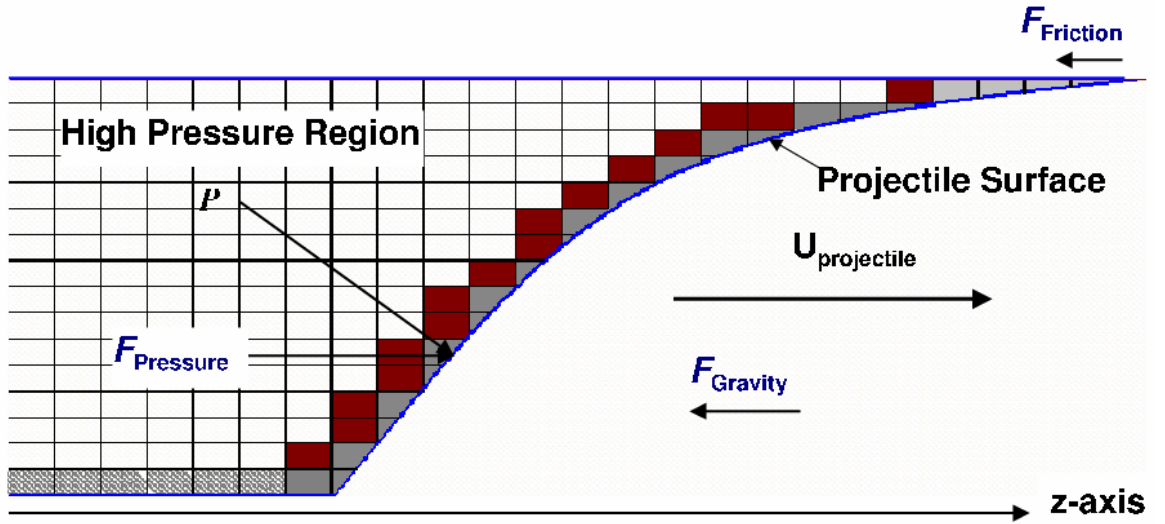


Figure 5-2: Cartoon of a portion of projectile surface profile and control volumes attached to the surface.

5.3 Mesh generation with the moving projectile

In order to simplify the numerical procedure in handling the moving projectile case, it was proposed that the finite difference grid in the region between projectile and the mortar tube moves with the projectile. Therefore, the solution for pressure from gas-

phase conservation equations can be used in Eq. (5.5) for solving the projectile velocity. It is shown in Fig. 5-3 and Fig. 5-4 that the finite difference grid in the region between projectile and the mortar tube moves along the projectile at the same velocity as the projectile and thus these control volumes do not change while the projectile is in motion. The space generated between the base of the projectile and the closed-end of the mortar tube is occupied by several control volumes, which are expanded along the axial direction at the rate governed by the instantaneous projectile velocity. The alternative to the cylindrical grid is to use triangular grid in order to accommodate the curved surface of the projectile.

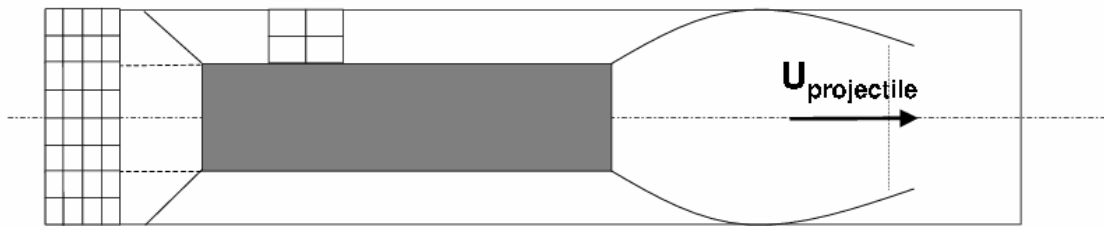


Figure 5-3: Schematic of projectile motion and axial expansion of the gas-phase region near the base of the projectile in an earlier phase.

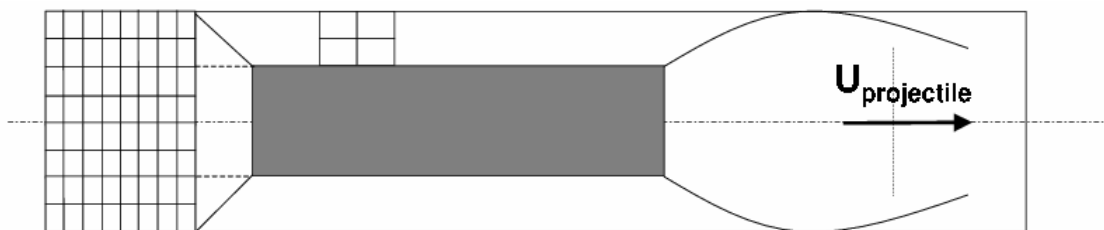


Figure 5-4: Schematic of projectile motion and axial expansion of the gas-phase region near the base of the projectile at a later time.

5.4 Summary of projectile dynamics sub-model

The above analysis is to determine the motion of projectile body under dynamic loading conditions. The instantaneous velocity of the projectile was used to determine the grid size in axial direction.

Chapter 6

FINITE ELEMENT SOLUTION FOR MORTAR TUBE SUB-MODEL

Theoretically, the finite element method should offer greater accuracy and higher flexibility in simulating the flow-field distributions in a complex geometry [8]. A finite element based numerical scheme can also prove to be more suitable for coupling the flow solution with the structural mechanics of the mortar systems. Keeping these issues in mind, an attempt to formulate a finite-element based numerical scheme for the two-phase compressible flow was initiated, which is described in this chapter. The governing partial differential equations were converted into a set of linear algebraic equations using the Taylor-Galerkin method based on finite element analysis. This numerical method was applied on the mortar tube sub-model to give the solution for the stationary mortar tube condition when the projectile motion was not allowed. The purpose of this effort was to predict the pressure-time traces at various locations in the mortar tube. It was also to predict the pressure wave phenomena, and time variations of flow property distributions in the combustion zone.

6.1 Finite element model for two-phase governing equations

The selected numerical method is described below:

6.1.1 Galerkin method

In order to solve the set of governing equations within an element, the Galerkin method has been selected. This method is a weighted residual method, which converts the set of governing equations into an integral form. The weighted residual method sets the residual to zero relative to a weighting function. The residual represents the difference between exact solution and approximate or numerical solution. For the differential equation $Lu=P$, where L is operating on u , the exact solution needs to satisfy governing equation at every point in space. If \bar{u} is an approximate solution and it introduces an error $e(x)$ called the residual, then the residual is given by Eq. (6.1)

$$e(x) = L\bar{u} - P \quad (\text{Eq. 6.1})$$

The approximate methods revolve around setting the residual relative to a weighting function ζ to zero. Therefore, the Eq. (6.1) becomes Eq. (6.2):

$$\int_{\Omega_v} \zeta \cdot (L\bar{u} - P) d\mathbf{V} = 0 \quad (\text{Eq. 6.2})$$

where, Ω_v is the domain of a particular element. In the Galerkin method, the weighting functions are chosen from the basis functions in order to construct the unknown variable in the equation. Weighing functions can be a linear combination of basis (shape) functions. Let \bar{u} be represented by Eq. (6.3):

$$\bar{u} = \sum_{i=1}^n Q_i G_i, \text{ where, } G_i \text{ are basis functions (usually functions of local coordinates).} \quad (\text{Eq. 6.3})$$

Weighting functions are then represented by Eq. (6.4):

$$\zeta = \sum_{i=1}^n \zeta_i G_i \quad (\text{Eq. 6.4})$$

where the coefficient ζ_i are arbitrary except for the requirement that ζ_i satisfy homogeneous boundary conditions where \bar{u} is prescribed.

6.1.2 Leap-Frog Taylor-Galerkin finite element scheme

Let us consider a scalar convection equation shown by Eq. (6.5) :

$$\frac{\partial u}{\partial t} = a \frac{\partial u}{\partial x} \quad (\text{Eq. 6.5})$$

The time derivative can be written as follows using leap-frog discretization:

$$\frac{u^{n+1} - u^{n-1}}{2\Delta t} = a \left. \frac{\partial u}{\partial x} \right|^n \quad (\text{Eq. 6.6})$$

As it is well known that use of center-difference method to discretized the left-hand side of Eq. (6.6) produces a method which is second-order accurate in time [11] [12]. For the case when $a = \text{constant}$ and Courant number $c \leq 1$, the leap-frog method is marginally stable. Using a standard Galerkin discretization method on a uniform mesh, the method becomes fourth-order accurate in space, but remains indeed second-order accurate in the time. The Eq. (6.6) represents a generalized leap-frog discretization of the convection equation. The associated Galerkin equation is given by Eq. (6.7).

$$\int_{\Omega} \zeta \left[\left(\bar{u}^{n+1} - \bar{u}^{n-1} \right) - 2a\Delta t \left. \frac{\partial \bar{u}}{\partial x} \right|^n \right] dx = 0 \quad (\text{Eq. 6.7})$$

The above formulation offers the basis for leap-frog-Taylor-Galerkin (LFTG) finite element schemes, which is used in this numerical simulation.

6.1.3 Reduction of governing equations using LFTG method

The leap-frog finite difference scheme for marching in time using Taylor series expansion gives second-order accuracy in time. The Galerkin method gives fourth-order accuracy in space. Therefore, the difference equations for the above set of governing equations can be derived as following:

Porosity

$$\frac{\phi^{n+1} - \phi^{n-1}}{2\Delta t} = \frac{1}{\zeta} \nabla \cdot (1 - \phi) \zeta \mathbf{U}_p \Big|_n + \Omega_1 \Big|_n \quad (\text{Eq. 6.8})$$

where, $\Omega_1 \equiv -\frac{\Sigma_2}{\rho_p \zeta}$

Pressure

$$\frac{P^{n+1} - P^{n-1}}{2\Delta t} = \left(-\frac{1}{\zeta} \mathbf{U}_g \nabla \zeta P - \frac{\rho c_v}{\eta} \nabla \cdot (\phi \zeta \mathbf{U}_g) - \frac{\rho c_p}{\eta} \nabla \cdot (1 - \phi) \zeta \mathbf{U}_p + \frac{\Omega_2}{\eta} \right) \Big|_n \quad (\text{Eq. 6.9})$$

where,

$$\eta \equiv \frac{\rho \phi R}{P} \left(\frac{\rho c_p T}{P} - 1 \right) \quad (\text{Eq. 6.10})$$

and

$$\Omega_2 \equiv \frac{1}{\zeta} \left[\frac{\rho R}{P} (\Sigma_g - h \Sigma_1) + c_p \left(\Sigma_1 + \frac{\rho \Sigma_2}{\rho_p} \right) - \frac{\rho^2 \phi R T}{P} \left(\frac{\partial c_p}{\partial t} + \mathbf{U}_g \cdot \nabla c_p \right) \right] \quad (\text{Eq. 6.11})$$

Gas-velocity

$$\frac{\mathbf{U}_g^{n+1} - \mathbf{U}_g^{n-1}}{2\Delta t} = -\frac{1}{(\rho \phi \zeta)^n} \left[\left(\rho \phi \zeta \mathbf{U}_g \cdot \nabla \mathbf{U}_g \right) \Big|_n + \left(\phi \zeta \nabla P \right) \Big|_n - \mathbf{I}_g \Big|_n \right] \quad (\text{Eq. 6.12})$$

Particle-velocity

$$\left(\frac{\mathbf{U}_p^{n+1} - \mathbf{U}_p^{n-1}}{2\Delta t} \right) = -\frac{1}{(1-\phi)\zeta|^n} \left[\left((1-\phi)\zeta \mathbf{U}_p \cdot \nabla \mathbf{U}_p \right)^n + \left(c_{ref}^2 \left(\frac{\phi_c}{\phi} \right)^2 \zeta \nabla \phi \right)^n - \frac{\mathbf{I}_p}{\rho_p} \right]^n \quad (\text{Eq. 6.13})$$

Gas-temperature

$$\frac{T^{n+1} - T^{n-1}}{2\Delta t} = -\frac{1}{\xi_1^n} \left[\left(\xi_1 \mathbf{U}_g \cdot \nabla T \right)^n + \xi_2 \nabla \cdot (\phi \mathbf{U}_g)^n + \left(\rho \nabla \cdot [(1-\phi) \mathbf{U}_p] \right)^n - \Omega_9 \right]^n \quad (\text{Eq. 6.14})$$

where,

$$\Omega_9 \equiv \frac{\rho^2 RT}{P^2} (\Sigma_9 - h \Sigma_1) + \Sigma_1 + \frac{\rho}{\rho_p} \Sigma_2 - \frac{\rho^3 \phi RT^2}{P^2} \left(\frac{\partial c_p}{\partial t} + \mathbf{U}_g \cdot \nabla c_p \right) \quad (\text{Eq. 6.15})$$

$$\xi_1 \equiv \frac{\rho^2 \phi R}{P} \left(\frac{\rho c_p T}{P} - 1 \right), \quad \xi_2 \equiv \rho \left(1 - \frac{\rho RT}{P} \right) \quad (\text{Eq. 6.16})$$

Particle Surface Temperature

$$\begin{aligned} & \frac{T_{ps}^{n+1} - T_{ps}^{n-1}}{2\Delta t} + \mathbf{U}_p \cdot \nabla T_{ps} \Big|^n + N_3^n (\mathbf{U}_g^n - \mathbf{U}_p^n) \cdot \nabla T \Big|^n + \frac{N_3^n \xi_2^n}{\xi_1^n} \mathbf{U}_g^n \cdot \nabla \phi \Big|^n \\ & + \frac{N_3^n \xi_2^n}{\xi_1^n} \phi^n \nabla \cdot \mathbf{U}_g \Big|^n - \frac{N_3^n \rho^n}{\xi_1^n} \mathbf{U}_p^n \cdot \nabla \phi \Big|^n \\ & + \frac{N_3^n \rho^n}{\xi_1^n} (1 - \phi^n) \nabla \cdot \mathbf{U}_p \Big|^n - \Omega_{10}^n = 0 \end{aligned} \quad (\text{Eq. 6.17})$$

where,

$$\begin{aligned}
N_1 &\equiv \frac{\frac{12\alpha_p}{\delta r_p}}{\left[\frac{6r_{p0} - \delta}{r_{p0}} + \frac{h_t \delta}{k_p} \right]}, \\
N_2 &\equiv \frac{\frac{12\alpha_p}{\delta r_p} \frac{r_{p0} h_t}{k_p}}{\left[\frac{6r_{p0} - \delta}{r_{p0}} + \frac{h_t \delta}{k_p} \right]}, \\
N_3 &\equiv \frac{\frac{\delta h_t}{k_p}}{\left[\frac{6r_{p0} - \delta}{r_{p0}} + \frac{h_t \delta}{k_p} \right]}
\end{aligned} \tag{Eq. 6.18}$$

and

$$\Omega_{10} \equiv N_1 (T_{ps} - T_0) + N_2 (T - T_{ps}) + N_3 \frac{\Omega_9}{\xi_1} \tag{Eq. 6.19}$$

6.1.4 Weight functions

Several weight functions for different equations are defined below:

Π : weight function for porosity equation

Γ : weight function for pressure equation

W : $\{W_1, W_2, W_3\}$: weight function for gas-phase velocity equation

Λ : $\{\Lambda_1, \Lambda_2, \Lambda_3\}$: weight function for condensed-phase velocity equation

Θ : weight function for gas-phase temperature equation,

Φ : weight function for particle surface temperature equation

6.1.5 Formulated finite element equations

Using the Galerkin method described earlier, the governing equations can be transformed into integral form from their partial differential equation form using weighting functions for minimizing the error over each element. Mathematically, it can be written in following form of equations. To simplify the notation, the overhead bar as mentioned before has not been used here even though all the quantities solved are numerical solutions, which are not the exact solutions.

Porosity

$$\int_{\Omega_e} \Pi \left(\frac{\phi^{n+1} - \phi^{n-1}}{2\Delta t} - \frac{1}{\zeta} \nabla \cdot (1 - \phi) \zeta \mathbf{U}_p \right)^n - \Omega_1 \Big|^n dV_e = 0 \quad (\text{Eq. 6.20})$$

Pressure

$$\int_{\Omega_e} \Gamma \left(\frac{P^{n+1} - P^{n-1}}{2\Delta t} + \left(\mathbf{U}_g \cdot \nabla \zeta P \right)^n + \left(\frac{\rho c_v}{\eta} \nabla \cdot (\zeta \phi \mathbf{U}_g) \right)^n \right)^n + \left(\frac{\rho c_p}{\eta} \nabla \cdot (1 - \phi) \mathbf{U}_p \right)^n - \frac{\Omega_2}{\eta} \Big|^n dV_e = 0 \quad (\text{Eq. 6.21})$$

Gas-velocity

$$\int_{\Omega_e} \mathbf{W}_i \cdot \left(\left(\frac{\mathbf{U}_g^{n+1} - \mathbf{U}_g^{n-1}}{2\Delta t} \right) + \frac{1}{(\rho \phi \zeta)^n} \left[(\rho \phi \zeta \mathbf{U}_g \cdot \nabla \mathbf{U}_g)^n + (\phi \zeta \nabla P)^n - \mathbf{I}_g \right]^n \right) dV_e = 0 \quad (\text{Eq. 6.22})$$

Particle-velocity

$$\int_{\Omega_e} \Lambda_i \cdot \left(\frac{\mathbf{U}_p^{n+1} - \mathbf{U}_p^{n-1}}{2\Delta t} + \frac{1}{(1-\phi)\zeta|^n} \left[\left((1-\phi)\zeta \mathbf{U}_p \cdot \nabla \mathbf{U}_p \right)^n + \left(c_{ref}^2 \left(\frac{\phi_c}{\phi} \right)^2 \zeta \nabla \phi \right)^n - \frac{\mathbf{I}_p}{\rho_p} \right] \right) dV_e = 0 \quad (\text{Eq. 6.23})$$

Gas-temperature

$$\int_{\Omega_e} \Theta \left(\frac{T^{n+1} - T^{n-1}}{2\Delta t} + \frac{1}{\xi_1^n} \left[\left(\xi_1 \mathbf{U}_g \cdot \nabla T \right)^n + \left(\xi_2 \nabla \cdot (\phi \mathbf{U}_g) \right)^n + \left(\rho \nabla \cdot [(1-\phi) \mathbf{U}_p] \right)^n - \Omega_9 \right] \right) dV_e = 0 \quad (\text{Eq. 6.24})$$

Particle Surface Temperature

$$\int_{\Omega_e} \Sigma \left(\frac{T_{ps}^{n+1} - T_{ps}^{n-1}}{2\Delta t} + \mathbf{U}_p^n \cdot \nabla T_{ps} \right)^n + N_3^n (\mathbf{U}_g^n - \mathbf{U}_p^n) \cdot \nabla T \right)^n + \frac{N_3^n \xi_2^n}{\xi_1^n} \mathbf{U}_g^n \cdot \nabla \phi \right)^n + \frac{N_3^n \xi_2^n}{\xi_1^n} \phi^n \nabla \cdot \mathbf{U}_g \right)^n - \frac{N_3^n \rho^n}{\xi_1^n} \mathbf{U}_p^n \cdot \nabla \phi \right)^n + \frac{N_3^n \rho^n}{\xi_1^n} (1 - \phi^n) \nabla \cdot \mathbf{U}_p \right)^n - \Omega_{10} \right)^n dV_e = 0 \quad (\text{Eq. 6.25})$$

The shape functions used in the above equations are described in Appendix A.

6.1.6 The Ritz-Galerkin finite element models

The unknown variables within each element are interpolated by a linear distribution. This approximation becomes increasingly accurate as more elements are considered in the model. Shape functions are introduced to implement this linear interpolation. If both the unknown variable and the coordinate are interpolated using the same shape function within the element, then it is called isoparameteric formulation. This is also a weak-form finite element model. In this work, isoparameteric formulation has been adopted. The interpolation functions for major unknowns are given as following:

$$\phi(\mathbf{x}, t) = \sum_{m=1}^M \lambda_m(\mathbf{x}) \phi^m(t) = \boldsymbol{\lambda}^T \boldsymbol{\phi} \quad (\text{Eq. 6.26})$$

$$P(\mathbf{x}, t) = \sum_{m=1}^M \psi_m(\mathbf{x}) P^m(t) = \boldsymbol{\psi}^T \mathbf{P} \quad (\text{Eq. 6.27})$$

$$U_{g,i}(\mathbf{x}, t) = \sum_{m=1}^M \alpha_{m,i}(\mathbf{x}) U_{g,i}^m(t) = \boldsymbol{\alpha}_i^T \mathbf{U}_{g,i} \quad (\text{Eq. 6.28})$$

$$U_{p,i}(\mathbf{x}, t) = \sum_{m=1}^M \beta_{m,i}(\mathbf{x}) U_{p,i}^m(t) = \boldsymbol{\beta}_i^T \mathbf{U}_{p,i} \quad (\text{Eq. 6.29})$$

$$T(\mathbf{x}, t) = \sum_{m=1}^M \chi_m(\mathbf{x}) T^m(t) = \boldsymbol{\chi}^T \mathbf{T} \quad (\text{Eq. 6.30})$$

$$T_{ps}(\mathbf{x}, t) = \sum_{m=1}^M \sigma_m(\mathbf{x}) T_{ps}^m(t) = \boldsymbol{\sigma}^T \mathbf{T}_{ps} \quad (\text{Eq. 6.31})$$

The vectors $(\boldsymbol{\phi}, \mathbf{P}, \mathbf{U}_{g,i}, \mathbf{U}_{p,i}, \mathbf{T}, \mathbf{T}_{ps})$ in Eq. (6.26)-Eq. (6.31) contain the nodal values of the respective quantities in each element and similarly vectors $(\boldsymbol{\lambda}, \boldsymbol{\psi}, \boldsymbol{\alpha}_i, \boldsymbol{\beta}_i, \boldsymbol{\chi}, \boldsymbol{\sigma})$ contain the nodal values of shape functions corresponding to the major unknowns in each element. Since isoparameteric formulation is used, the weight functions will be same as the interpolation functions. Therefore,

$$\mathbf{\Pi} = \boldsymbol{\lambda} \quad (\text{Eq. 6.32})$$

$$\mathbf{W}_i = \boldsymbol{\alpha}_i \quad (\text{Eq. 6.33})$$

$$\mathbf{\Gamma} = \boldsymbol{\psi} \quad (\text{Eq. 6.34})$$

$$\mathbf{\Lambda}_i = \boldsymbol{\beta}_i \quad (\text{Eq. 6.35})$$

$$\mathbf{\Theta} = \boldsymbol{\chi} \quad (\text{Eq. 6.36})$$

$$\mathbf{\Sigma} = \boldsymbol{\sigma} \quad (\text{Eq. 6.37})$$

The vectors $(\mathbf{\Pi}, \mathbf{\Gamma}, \mathbf{W}_i, \mathbf{\Lambda}_i, \mathbf{\Theta}, \mathbf{\Phi})$ in Eq. (6.32)-Eq. (6.37) contain the nodal values of the respective quantities in each element and similarly vectors $(\boldsymbol{\lambda}, \boldsymbol{\psi}, \boldsymbol{\alpha}_i, \boldsymbol{\beta}_i, \boldsymbol{\chi}, \boldsymbol{\sigma})$ contain the nodal shape functions corresponding to the major unknowns in each element. Using leap-frog Taylor-Galerkin scheme for the time derivative and substituting the weak formulation in Eqs. (4.14)- (4.18), following equations are obtained:

Porosity

$$\begin{aligned} & \left(\int_{\Omega_e} \boldsymbol{\lambda} \boldsymbol{\lambda}^T dV_e \right) (\boldsymbol{\Phi}^{n+1} - \boldsymbol{\Phi}^{n-1}) + 2\Delta t \left(\int_{\Omega_e} \boldsymbol{\lambda} \boldsymbol{\beta}_j^T \mathbf{U}_{p,j}^n \frac{\partial \boldsymbol{\lambda}^T}{\partial x_j} dV_e \right) \boldsymbol{\Phi}^n \\ & - 2\Delta t \left(\int_{\Omega_e} \boldsymbol{\lambda} (1 - \boldsymbol{\lambda}^T \boldsymbol{\Phi}^n) \frac{\partial \boldsymbol{\beta}_i^T}{\partial x_i} dV_e \right) \mathbf{U}_{p,i}^n - 2\Delta t \int_{\Omega_e} \boldsymbol{\lambda} \boldsymbol{\Omega}_1^n dV_e = 0 \end{aligned} \quad (\text{Eq. 6.38})$$

Pressure

$$\int_{\Omega_e} \Psi \left(\begin{aligned} & \Psi^T \frac{\mathbf{P}^{n+1} - \mathbf{P}^{n-1}}{2\Delta t} + \left(\boldsymbol{\alpha}_j^T \mathbf{U}_{g,j}^n \frac{\partial \Psi^T}{\partial x_j} \mathbf{P}^n \right) \\ & + \frac{\rho^n c_v^n}{\eta^n} \left(\boldsymbol{\lambda}^T \boldsymbol{\varphi}^n \frac{\partial \boldsymbol{\alpha}_j^T}{\partial x_j} \mathbf{U}_{g,j}^n + \boldsymbol{\alpha}_j^T \mathbf{U}_{g,j}^n \frac{\partial \boldsymbol{\lambda}^T}{\partial x_j} \boldsymbol{\varphi}^n \right) \\ & + \frac{\rho^n c_p^n}{\eta^n} \left[\left(1 - \boldsymbol{\lambda}^T \boldsymbol{\varphi}^n \right) \frac{\partial \boldsymbol{\beta}_j^T}{\partial x_j} \mathbf{U}_{p,j}^n \right] - \frac{\Omega_2^n}{\eta^n} \end{aligned} \right) dV_e = 0 \quad (\text{Eq. 6.39})$$

Gas-velocity

$$\begin{aligned} & \left(\int_{\Omega_e} \boldsymbol{\alpha}_i \boldsymbol{\alpha}_i^T dV_e \right) (\mathbf{U}_{g,i}^{n+1} - \mathbf{U}_{g,i}^{n-1}) + 2\Delta t \left(\int_{\Omega_e} \boldsymbol{\alpha}_i \boldsymbol{\alpha}_i^T \mathbf{U}_{g,j}^n \frac{\partial \boldsymbol{\alpha}_i^T}{\partial x_j} dV_e \right) \mathbf{U}_{g,i}^n \\ & + 2\Delta t \left(\int_{\Omega_e} \boldsymbol{\alpha}_i \frac{R\boldsymbol{\chi}^T \mathbf{T}^n + b\Psi^T \mathbf{P}^n}{\Psi^T \mathbf{P}^n} \frac{\partial \Psi^T}{\partial x_i} dV_e \right) \mathbf{P}^n \\ & - 2\Delta t \left(\int_{\Omega_e} \boldsymbol{\alpha}_i \frac{R\boldsymbol{\chi}^T \mathbf{T}^n + b\Psi^T \mathbf{P}^n}{\Psi^T \mathbf{P}^n \boldsymbol{\lambda}^T \boldsymbol{\varphi}^n} \boldsymbol{\varepsilon}_{ip2}^T dV_e \right) \mathbf{I}_s^n = 0 \end{aligned} \quad (\text{Eq. 6.40})$$

Particle-velocity

$$\begin{aligned} & \left(\int_{\Omega_e} \boldsymbol{\beta}_i \boldsymbol{\beta}_i^T dV_e \right) \Lambda_i^T (\mathbf{U}_{p,i}^{n+1} - \mathbf{U}_{p,i}^{n-1}) + 2\Delta t \left(\int_{\Omega_e} \boldsymbol{\beta}_i \boldsymbol{\beta}_i^T \mathbf{U}_{p,j}^n \frac{\partial \boldsymbol{\beta}_i^T}{\partial x_j} dV_e \right) \mathbf{U}_{p,i}^n \\ & + 2\Delta t \left(\int_{\Omega_e} \boldsymbol{\beta}_i \frac{c_{ref}^2 \phi_c^2}{(\boldsymbol{\lambda}^T \boldsymbol{\varphi}^n)^2 (1 - \boldsymbol{\lambda}^T \boldsymbol{\varphi}^n)} \frac{\partial \boldsymbol{\lambda}^T}{\partial x_i} dV_e \right) \boldsymbol{\varphi}^n - 2\Delta t \left(\int_{\Omega_e} \frac{\boldsymbol{\beta}_i \boldsymbol{\varepsilon}_{ip5}^T}{\rho_p (1 - \boldsymbol{\lambda}^T \boldsymbol{\varphi}^n)} dV_e \right) \mathbf{I}_p^n = 0 \end{aligned} \quad (\text{Eq. 6.41})$$

Gas-temperature

$$\begin{aligned}
& \left(\int_{\Omega_e} \chi \chi^T dV_e \right) (\mathbf{T}^{n+1} - \mathbf{T}^{n-1}) + 2\Delta t \left(\int_{\Omega_e} \chi \mathbf{a}_j^T \mathbf{U}_{g,j}^n \frac{\partial \chi^T}{\partial x_j} dV_e \right) \mathbf{T}^n \\
& + 2\Delta t \left(\int_{\Omega_e} \chi \frac{b \psi^T \mathbf{P}^n (R \chi^T \mathbf{T}^n + \psi^T \mathbf{P}^n b)}{\lambda^T \boldsymbol{\phi}^n R (c_v \chi^T \mathbf{T}^n - \psi^T \mathbf{P}^n b)} \lambda^T \boldsymbol{\phi}^n \frac{\partial \mathbf{a}_j^T}{\partial x_j} dV_e \right) \mathbf{U}_{g,j}^n \\
& + 2\Delta t \left(\int_{\Omega_e} \chi \frac{(R \chi^T \mathbf{T}^n + \psi^T \mathbf{P}^n b)}{\lambda^T \boldsymbol{\phi}^n R (c_v \chi^T \mathbf{T}^n - \psi^T \mathbf{P}^n b)} \left\{ \begin{aligned} & b \psi^T \mathbf{P}^n \mathbf{a}_j^T \mathbf{U}_{g,j}^n \\ & - \left(R \chi^T \mathbf{T}^n \right) \boldsymbol{\beta}_j^T \mathbf{U}_{p,j}^n \end{aligned} \right\} \frac{\partial \lambda^T}{\partial x_j} dV_e \right) \boldsymbol{\phi}^n \quad (\text{Eq. 6.42}) \\
& + 2\Delta t \left(\int_{\Omega_e} \chi \frac{(R \chi^T \mathbf{T}^n + \psi^T \mathbf{P}^n b)^2}{\lambda^T \boldsymbol{\phi}^n R (c_v \chi^T \mathbf{T}^n - \psi^T \mathbf{P}^n b)} (1 - \lambda^T \boldsymbol{\phi}^n) \frac{\partial \boldsymbol{\beta}_j^T}{\partial x_j} dV_e \right) \mathbf{U}_{p,j}^n \\
& - 2\Delta t \left(\int_{\Omega_e} \chi \frac{(R \chi^T \mathbf{T} + \psi^T \mathbf{P} b)^3}{\psi^T \mathbf{P} \lambda^T \boldsymbol{\phi} R (c_v \chi^T \mathbf{T} - \psi^T \mathbf{P} b)} \boldsymbol{\varepsilon}_9^T dV_e \right) \Omega_9^n = 0
\end{aligned}$$

Particle Surface Temperature

$$\begin{aligned}
& \left(\int_{\Omega_e} \boldsymbol{\sigma} \boldsymbol{\sigma}^T dV_e \right) \frac{\mathbf{T}_{ps}^{n+1} - \mathbf{T}_{ps}^{n-1}}{2\Delta t} + \left(\int_{\Omega_e} \boldsymbol{\sigma} \boldsymbol{\beta}_j^T \mathbf{U}_{p,j}^n \frac{\partial \boldsymbol{\sigma}^T}{\partial x_j} dV_e \right) \mathbf{T}_{ps}^n \\
& + \left(\int_{\Omega_e} \boldsymbol{\sigma} N_3^n (\mathbf{a}_j^T \mathbf{U}_{g,j}^n - \boldsymbol{\beta}_j^T \mathbf{U}_{p,j}^n) \frac{\partial \chi^T}{\partial x_j} dV_e \right) \mathbf{T}^n \\
& + \left(\int_{\Omega_e} \boldsymbol{\sigma} \frac{N_3^n \xi_2^n}{\xi_1^n} \mathbf{a}_j^T \mathbf{U}_{g,j}^n \frac{\partial \lambda^T}{\partial x_j} dV_e \right) \boldsymbol{\phi}^n + \left(\int_{\Omega_e} \boldsymbol{\sigma} \frac{N_3^n \xi_2^n}{\xi_1^n} \lambda^T \boldsymbol{\phi}^n \frac{\partial \mathbf{a}_j^T}{\partial x_j} dV_e \right) \mathbf{U}_{g,j}^n \quad (\text{Eq. 6.43}) \\
& + \left(\int_{\Omega_e} \boldsymbol{\sigma} \frac{N_3^n \rho^n}{\xi_1^n} (1 - \lambda \boldsymbol{\phi}^{nT}) \frac{\partial \boldsymbol{\beta}_j^T}{\partial x_j} dV_e \right) \mathbf{U}_{p,j}^n - \left(\int_{\Omega_e} \boldsymbol{\sigma} \frac{N_3^n \rho^n}{\xi_1^n} \boldsymbol{\beta}_j^T \mathbf{U}_{p,j}^n \frac{\partial \lambda^T}{\partial x_j} dV_e \right) \boldsymbol{\phi}^n \\
& - \left(\int_{\Omega_e} \boldsymbol{\sigma} \boldsymbol{\varepsilon}_{10}^T dV_e \right) \Omega_{10}^n = 0
\end{aligned}$$

6.1.7 Mesh generation

The finite element code mesh was created using the mesh generation software package, “Gambit”, developed and distributed by Fluent Inc. The geometry of the 120mm mortar system was also generated using this software. The dimensions were taken using the drawing of 120mm mortar system and these dimensions were used to create a geometry shown in Fig. 6-3. In the calculations shown here, only a 1/8 section of the 120mm mortar system was simulated because this region could represent the entire space between the tail-boom and the mortar tube. This section is shown as the meshed region in Fig. 6-3. The four regions are identified in this geometry as i) fin-blade region, ii) vent-hole region, iii) conical region, and iv) projectile-payload region. The vent-hole region is the uniform cylindrical section of ignition cartridge where all vent holes are located. The ignition cartridge has a conical section ahead of this cylindrical region, which does not have any vent holes and connects with the projectile-payload region. This section is called conical region. The section where a portion of the explosive charge is loaded is called the projectile-payload region. This is the section before the obturating ring in the mortar system.

There are several mesh generation software packages available for finite element mesh generation and these were considered for use in this work. These include FEAP, Triangulation, DISTMESH, FEMLAB, ANSYS, and Gambit. These software packages are all very good options. However, in this work the geometry is meshed using mesh generation software Gambit, developed by Fluent Inc. Gambit mesh generation program was used, since it was readily available to us through the Mechanical Engineering

departmental license at PSU. In the current work, hexahedral, wedge and tetrahedral elements were used. The general shape and node locations for these two types of elements are shown in Fig. 6-4. A hexahedral element with uniformly distributed propellant grains is shown in Fig. 6-2.

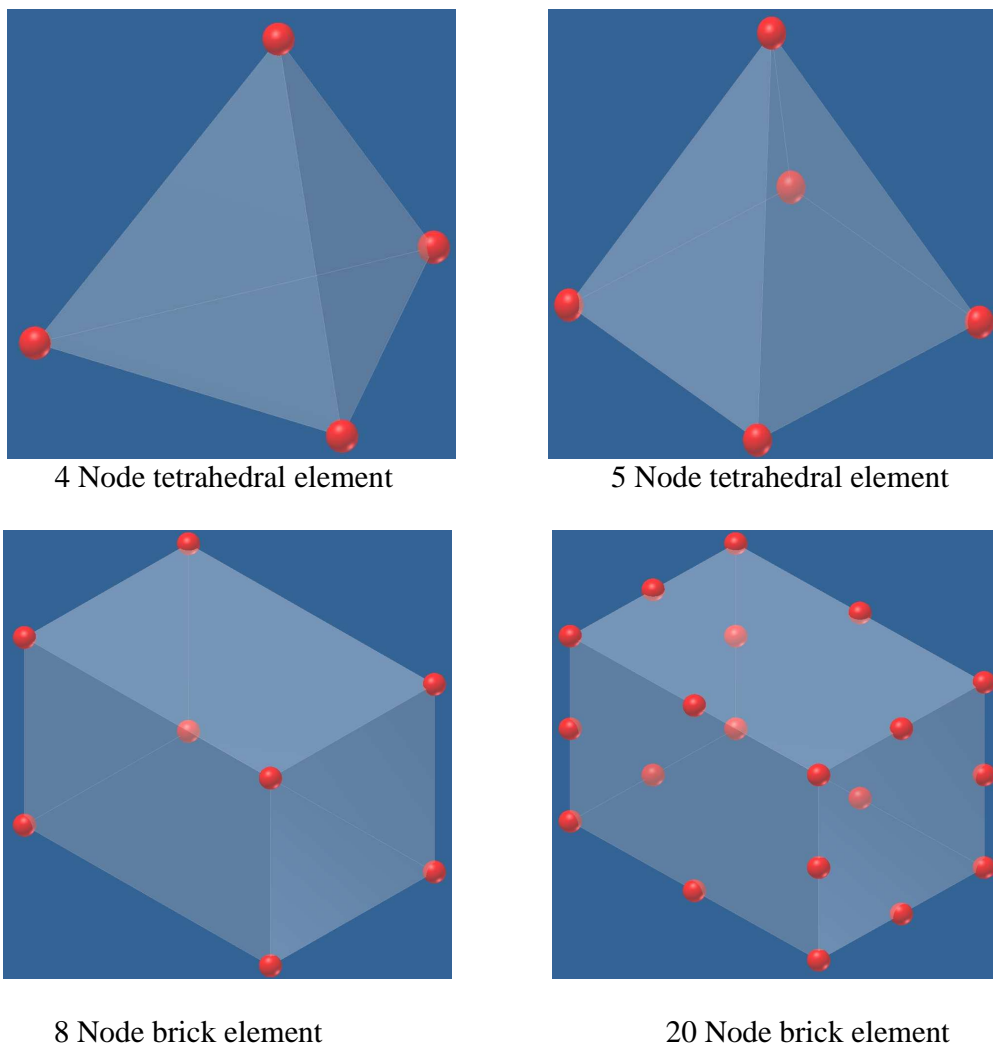


Figure 6-1: Several types of elements and node locations.

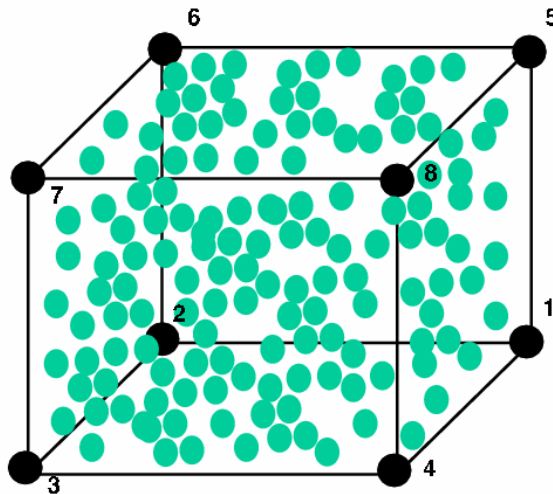


Figure 6-2: Hexahedral element with uniform distribution of ball propellants.

There are total 28 vent holes on the cylindrical surface of the tail-boom and combustion products (both in gas-phase and condensed-phase) are discharged from these vent holes into the mortar tube section. The mass flux of these discharges was computed from the ignition cartridge sub-model, which was explained in chapter 2. In the mortar tube sub-model, these outputs were used for the gas and condensed-phase velocity boundary conditions, and source terms in the governing equations. The vent-hole region has 14 axial divisions, 5 radial divisions, and 5 angular divisions for a $1/8$ portion of the full cross-section of the mortar projectile. Hence, there are a total of 350 elements in the $1/8$ portion of the vent-hole region of mortar tube. The axial meshing ensures that each axial division in $1/8$ portion received mass flow discharge from tail-boom equivalent of 25% of a vent hole. The fin-blade region, conical region, and the projectile-payload region are divided in 5 axial, 5 radial, and 5 angular divisions each for the $1/8$ portion of the projectile. Therefore, the $1/8$ section of the mortar projectile is meshed into total of

725 elements. These meshed sections are displayed in Fig. 6-4 for oblique and y-z views respectively. The hexahedral finite element geometries are used for fin region and vent-hole region. However, both the conical region and the projectile region are converging regions; therefore a combination of hexahedral elements and wedge elements has been utilized for these regions. The wedge finite element is similar to the hexahedral element but all faces are not necessarily perpendicular to each other. The finite element formulation does not change for wedge elements and therein lays one of the advantages of finite element method for this complex geometry.

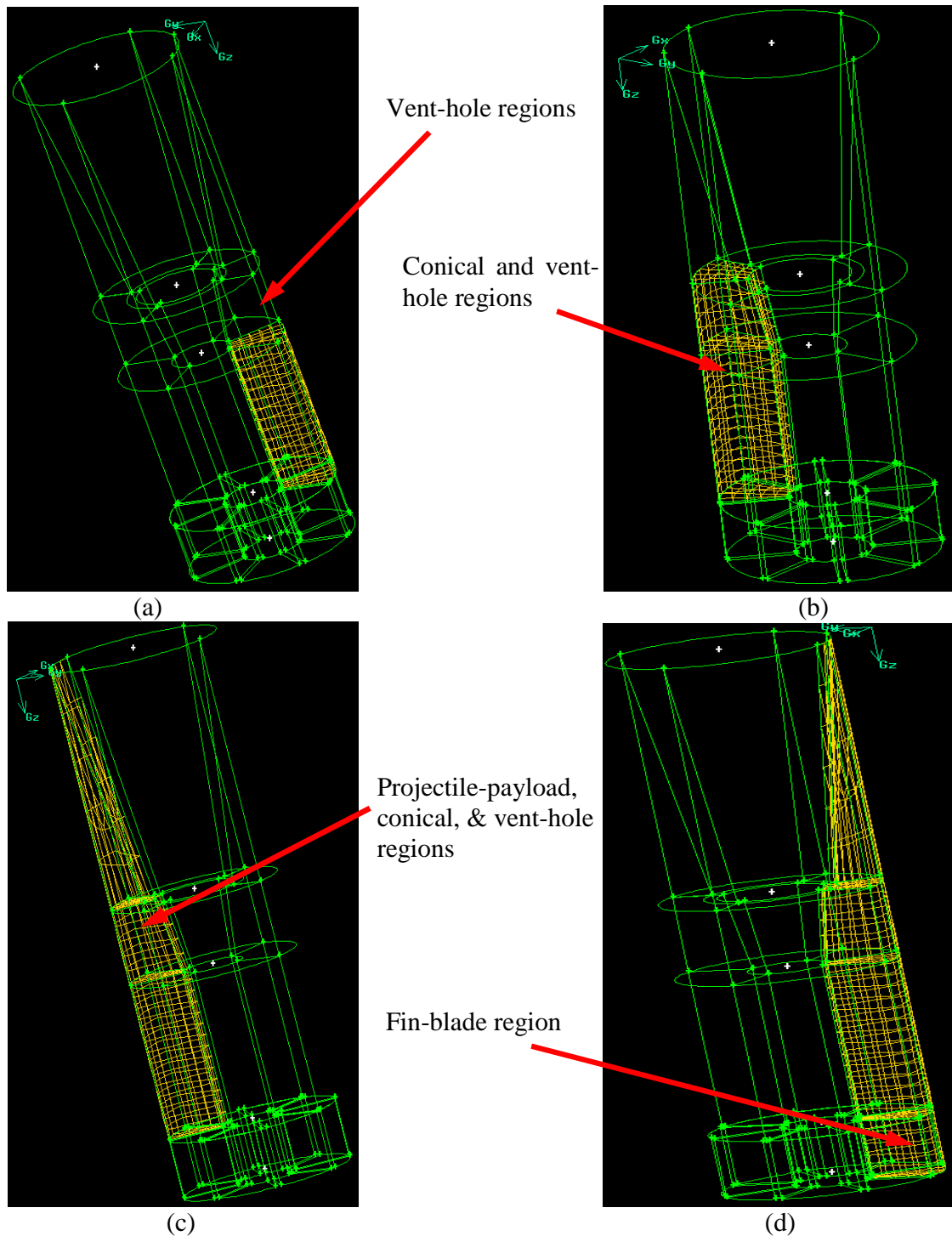


Figure 6-3: Finite element mesh generated in a section of mortar tube: (a) vent-hole region meshed, (b) vent-hole and conical regions meshed, (c) all regions meshed except fin-blade region, (d) all regions meshed.

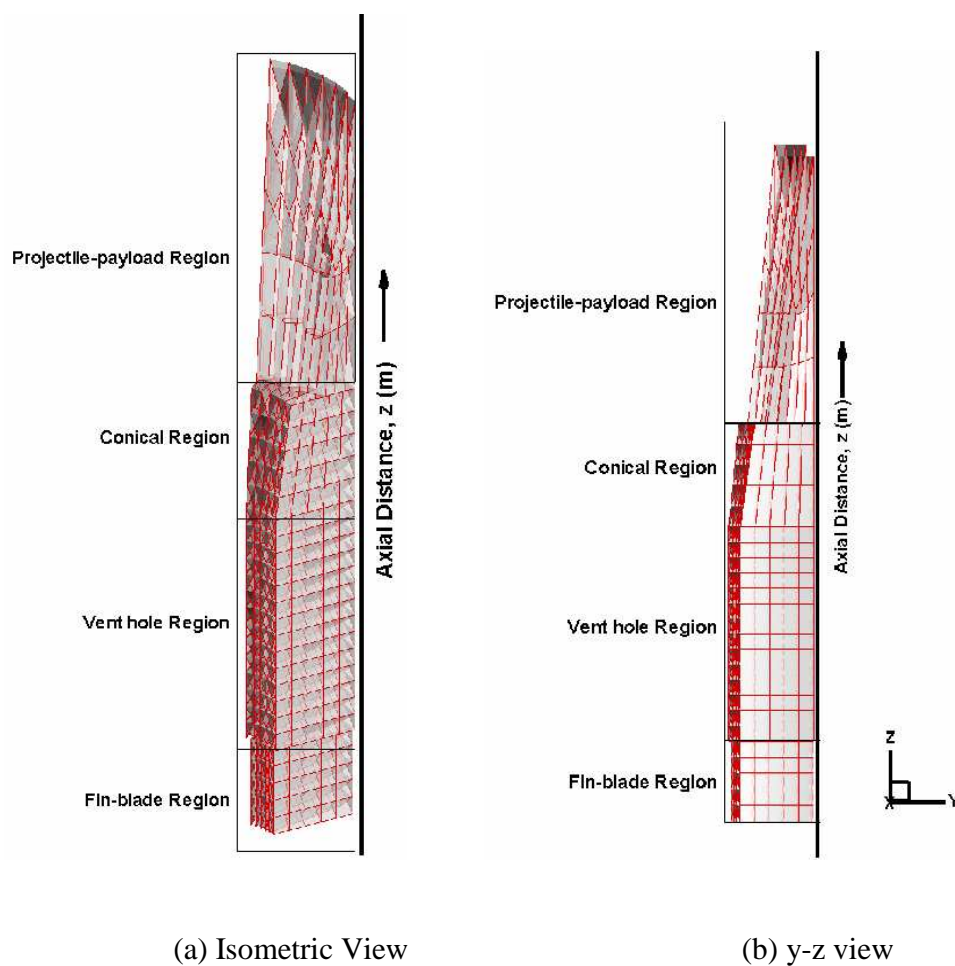


Figure 6-4 A section of mortar tube region with finite element mesh.

6.1.8 Computed results and discussions

The solution of mortar tube sub-model starts with calculation of mass fluxes of gas-phase and condensed-phase combustion products from the ignition cartridge into the vent hole region of mortar tube. In addition, the diameter of M48 particles that are ejected

from the ignition cartridge through the vent holes and the porosity of the two-phase flow from ignition cartridge into the mortar tube are also used as input to the mortar tube sub-model. The computed mass fluxes of combustion products (both gas-phase and condensed-phase) from the ignition cartridge sub-model were further converted into per unit volume for each element in the mortar tube section. This was done because the volume of ignition cartridge is different than the volume of elements in the mortar tube. These volumetric mass flow rates into the mortar tube section at various axial locations are shown in Fig. 6-5.

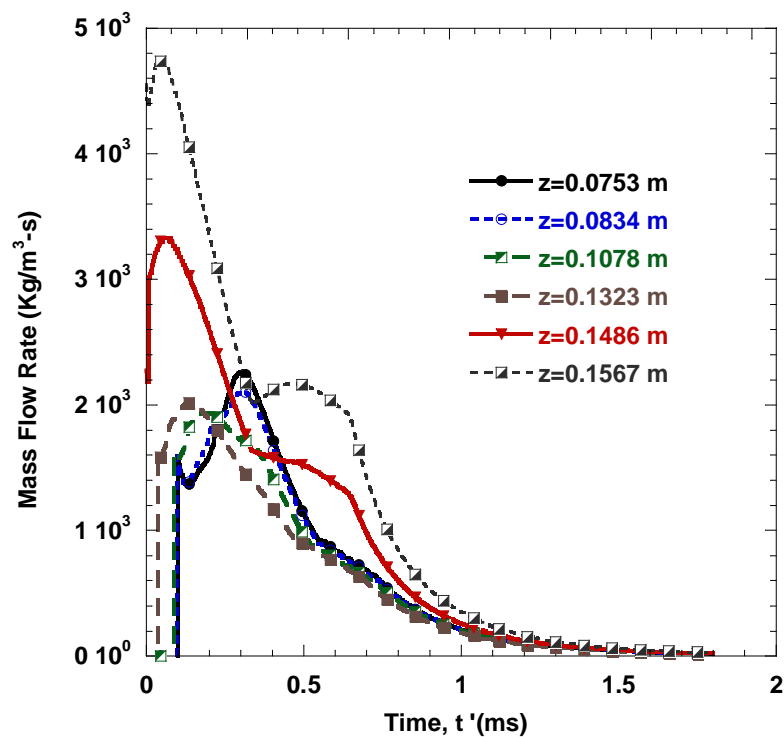


Figure 6-5: Computed mass flow rates from tail-boom into mortar tube at various axial locations.

The computed pressure-time traces at 5 representative axial locations are shown in Fig. 6-6. The non-uniform axial variation of the discharging combustion products from the ignition cartridge causes the sequential pressurization event in the mortar tube, resulting in non-uniform pressurization in the mortar tube. Since the uppermost vent-holes at $z = 15.67$ cm started discharging first, the M47 ball propellants in the charge increment located at this axial position are ignited earlier than the other charge increments.

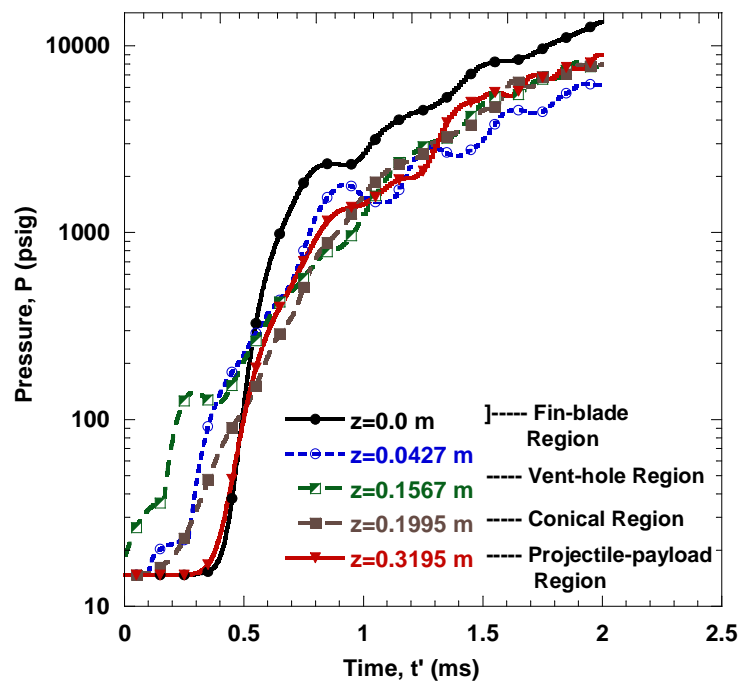


Figure 6-6: Computed P-t traces in the mortar tube at various axial locations.

Following the rapid combustion of M47 granular propellant grains at this location (i.e., $z=15.67$ cm), the pressure-waves are generated and they propagate in both directions toward fin-blade and conical regions (located at $z = 19.95$ cm and $z = 31.95$ cm) and projectile-payload region (located at $z = 0.0$ cm and $z = 4.27$ cm), which do not contain

any propellant at the beginning. The pressurization processes in these regions occur later; the pressure in the fin-blade region rises faster than the other regions and later exceeds those at other regions. This phenomenon occurs due to the downward motion of propellant grains, which were driven by the pressure wave.

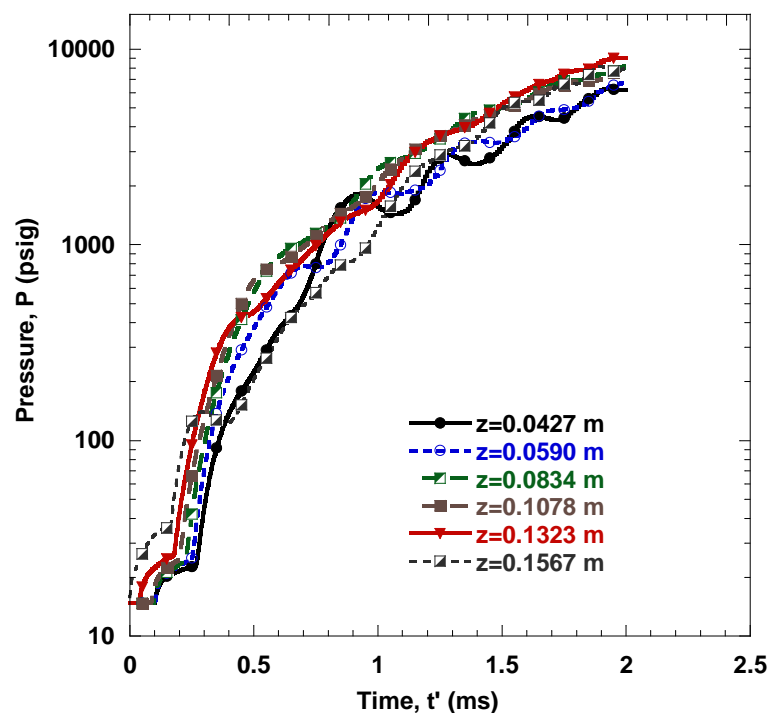


Figure 6-7: Computed P-t traces in the vent-hole region of mortar tube at various axial locations.

The detailed pressure-time traces in the vent-hole region are shown in Fig. 6-7 , which shows that the pressurization event starts at $z = 15.67$ cm and continues toward the projectile-payload region, starting last at $z = 4.27$ cm, although the time delay between the pressurization processes at these various axial locations in the vent-hole region are less than the time delay between vent-hole region and other regions. This observation is

consistent with the postulation that the order of hot combustion products discharge from the ignition cartridge governs the initiation of pressurization in the mortar tube.

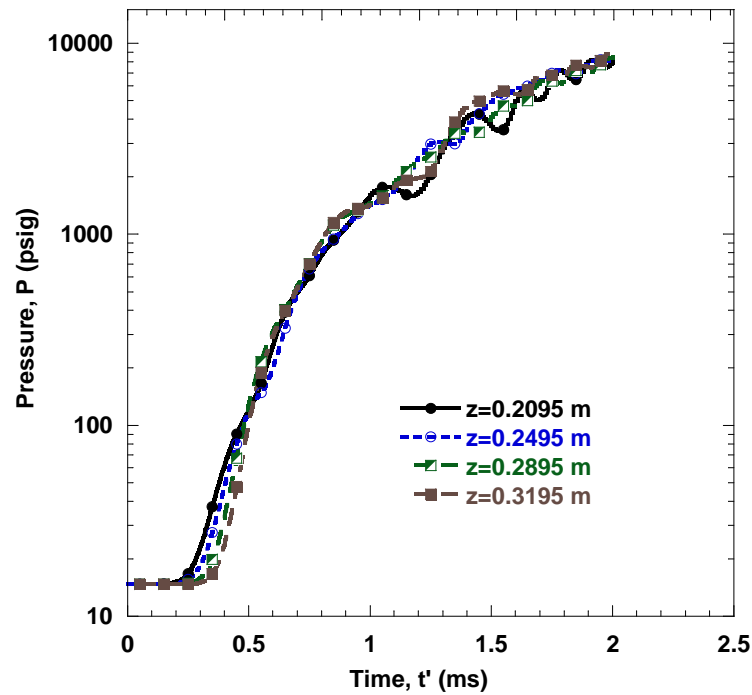


Figure 6-8: Computed P-t traces in the projectile-payload region of mortar tube at various axial locations.

The detailed pressure-time traces in the projectile-payload region and the conical region are shown in Fig. 6-8 and Fig. 6-9. In addition to the sequential pressurization, these results also show a pressure-wave phenomenon, which means that the location for the highest pressure alternates between various axial positions. The pressure-wave phenomenon is a typical characteristic of ballistic behavior in such systems.

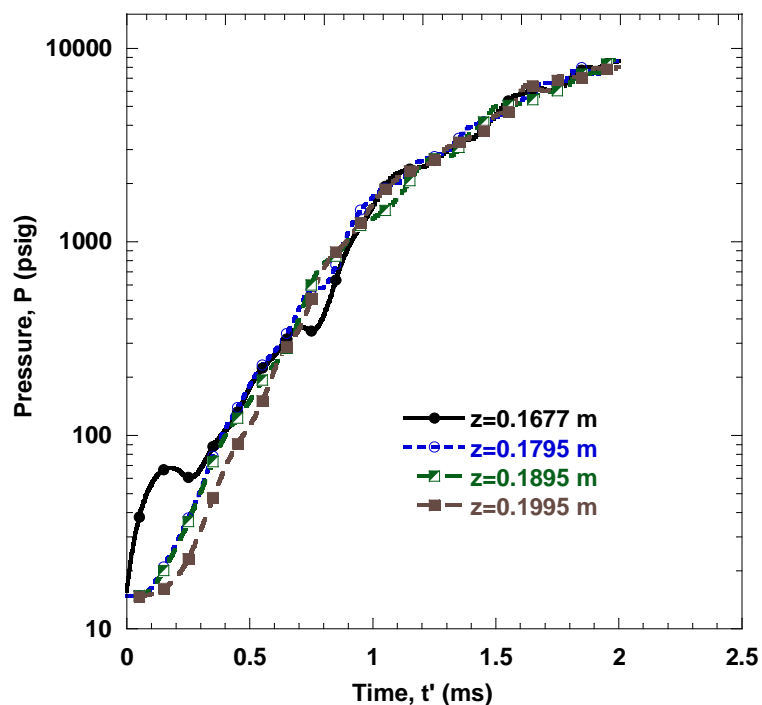


Figure 6-9: Computed P-t traces in the conical region of mortar tube at various axial locations.

The computed pressure-time traces in the fin-blade region are shown in Fig. 6-10. In general, the calculated results at the fin-blade region are in the same peak pressure range and rise time of a measured pressure-time trace obtained from the base area of an actual mortar firing performed at Yuma Proving Ground, AZ as shown in Fig. 6-11.

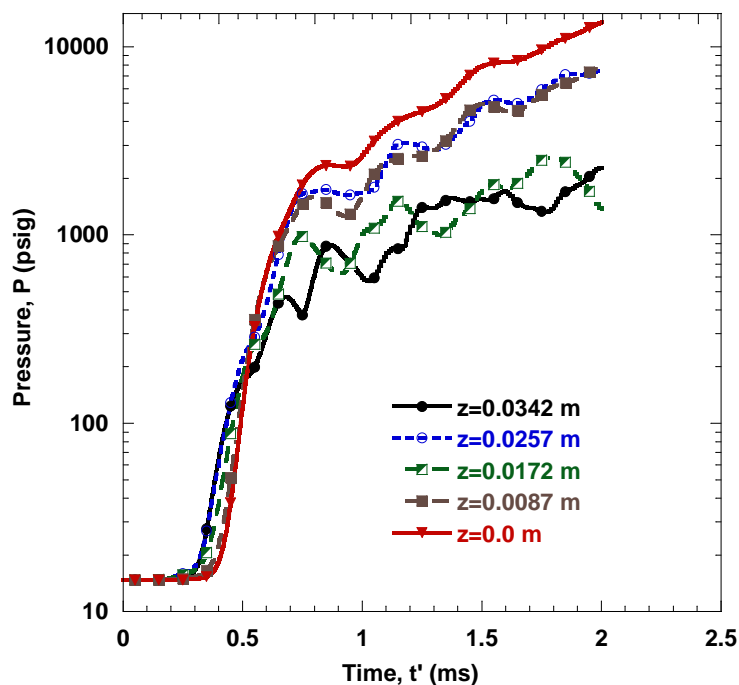


Figure 6-10: Computed P-t traces in the fin-blade region of mortar tube at various axial locations.

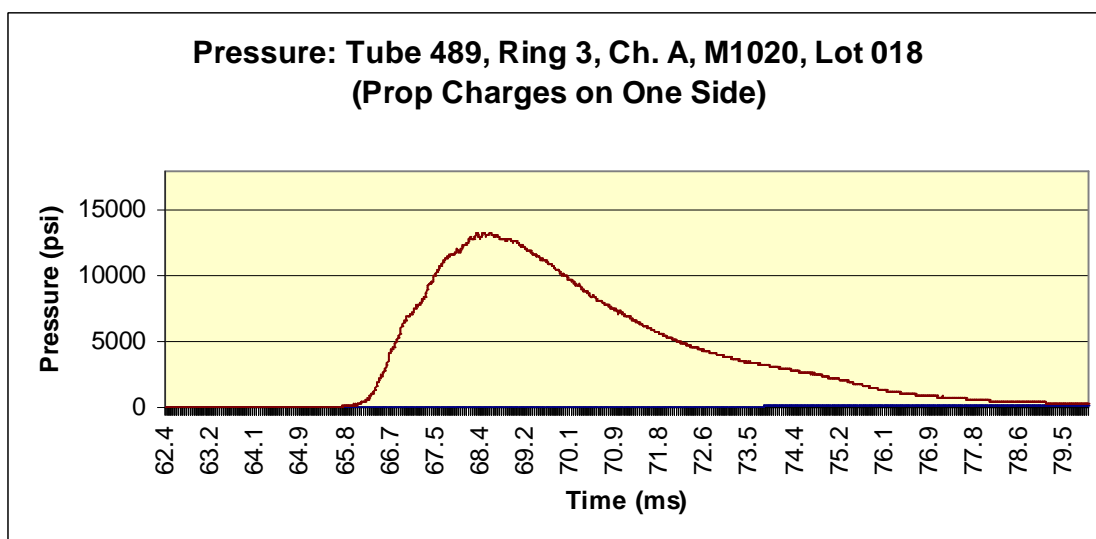


Figure 6-11: Measured P-t traces of projectile firing (P~13,000 psig, rise time ~ 2.6 ms).

The calculated temperature-time traces are shown in Fig. 6-12. These traces indicate the earlier temperature rise in the vent-hole region since the discharge of combustion products from the tail-boom takes place in this area. Also the charge increments are located in this section therefore, the gas-mixture temperature rises earlier in this region in comparison with other regions, however, the rate of temperature rise is faster in the fin-blade region once it starts to pressurize quickly. The axial temperature variations in the fin-blade region are relatively small as shown by the results given in Fig. 6-13. This is partly caused by the relatively uniform distribution of M47 ball propellants that enter in this region with the gas flow from the vent-hole region.

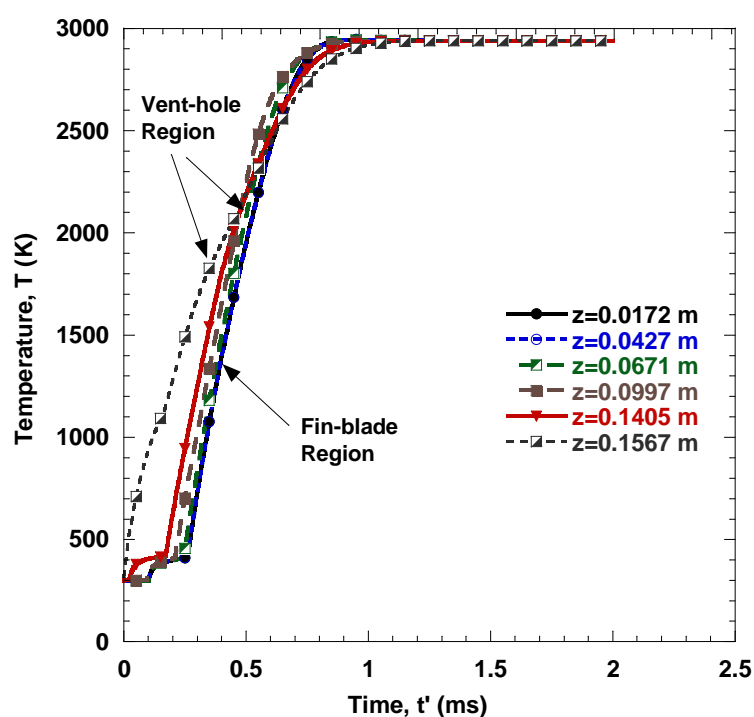


Figure 6-12: Computed temperature-t traces in the mortar tube at various axial locations.

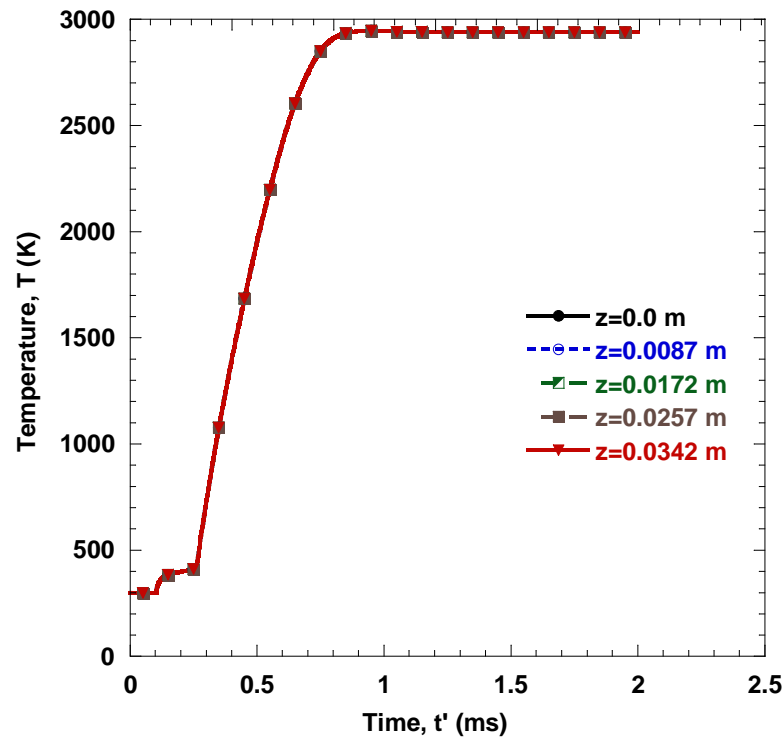


Figure 6-13: Computed temperature- t traces in the fin-blade region of mortar tube.

The calculated propellant surface temperature-time traces are shown in Fig. 6-14. From this figure, one can see that the propellant grains are ignited first in the upper portion of the vent-hole region and then the flame spreads downwards to the fin-blade region. This behavior is similar to that inside the tail-boom section due early discharge of hot combustion products out of the vent holes at the uppermost axial location in the vent-hole region near the projectile end. The computed axial gas velocity-time traces for various axial locations in the mortar projectile also showed that the combustion products flow downward from vent-hole region to fin-blade region and upward into the conical

and projectile-payload regions. In each of these regions, there are oscillations in the axial gas-velocity component due to localized axial pressure gradients. The oscillations are most pronounced in the fin-blade region due to higher pressure gradients.

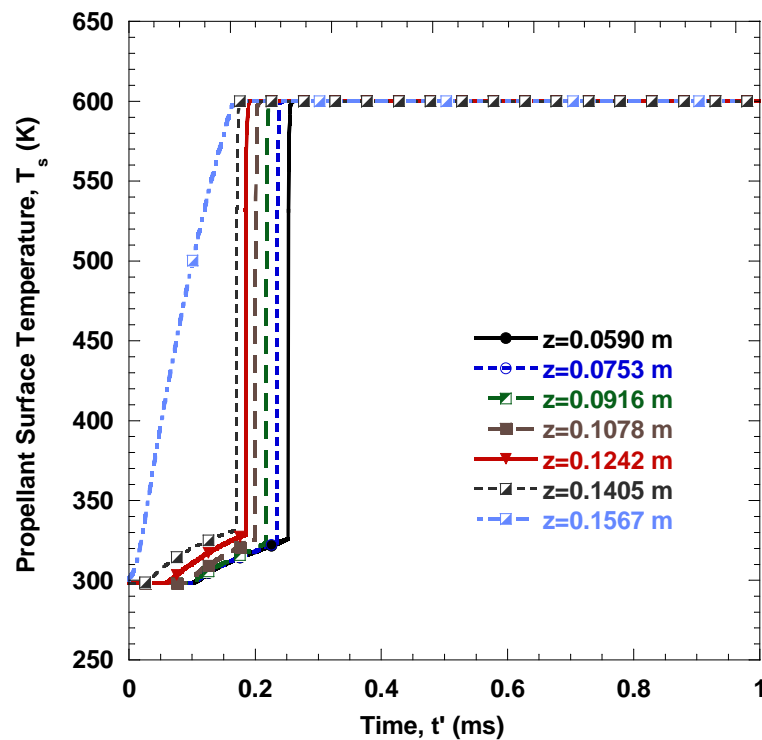


Figure 6-14: Computed particle surface temperature- t traces in the mortar tube at various axial locations.

The calculated linear regression rate of granular propellants in the mortar tube section is shown in Fig. 6-15. Even though there are limited variations in the magnitude of the burning rates at various axial locations, the granular propellant near the fin-blade region rises to a higher level than those in the other locations in the vent-hole region in the first millisecond interval of the ballistic event. The burning rate was then taken over by those near the conical region in the later period of the event. This behavior is dictated

by the pressure wave phenomena in the vent-hole region of the mortar tube as shown in Fig. 6-10.

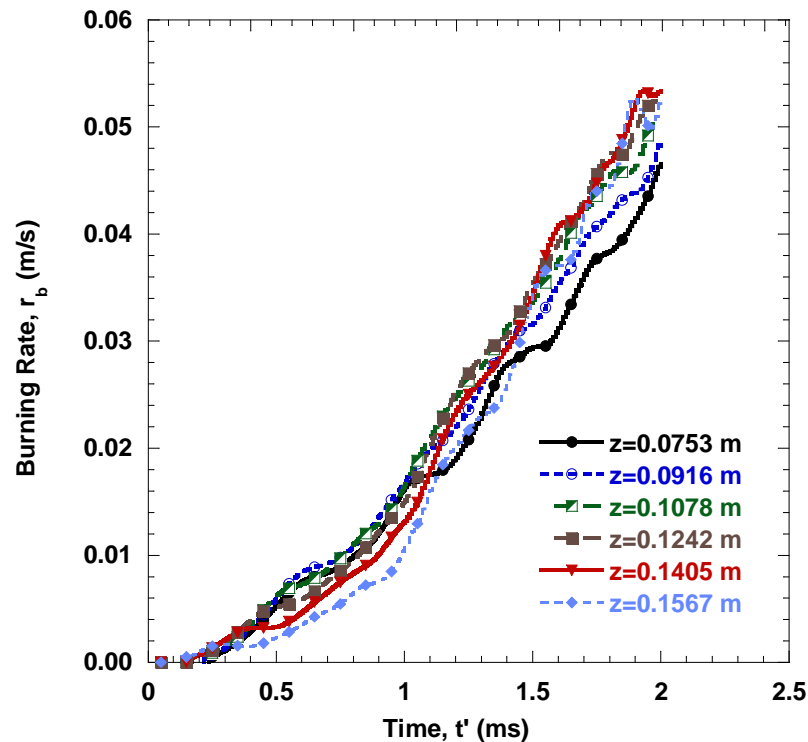


Figure 6-15: Computed burn rate-t trace in the vent-hole region of the mortar tube at various axial locations.

The pressure wave phenomena in the mortar tube are further illustrated in the computed solution by the expansion of the red-colored region from the top-row of the vent holes towards both upward and downward directions in Fig. 6-16. It can be clearly seen from these plots that pressure wave is stronger towards the fin-blade region than the projectile-payload region. This is due to the burning of propellant grains in the charge increments that are located unevenly in the lower portion of the vent-hole region.

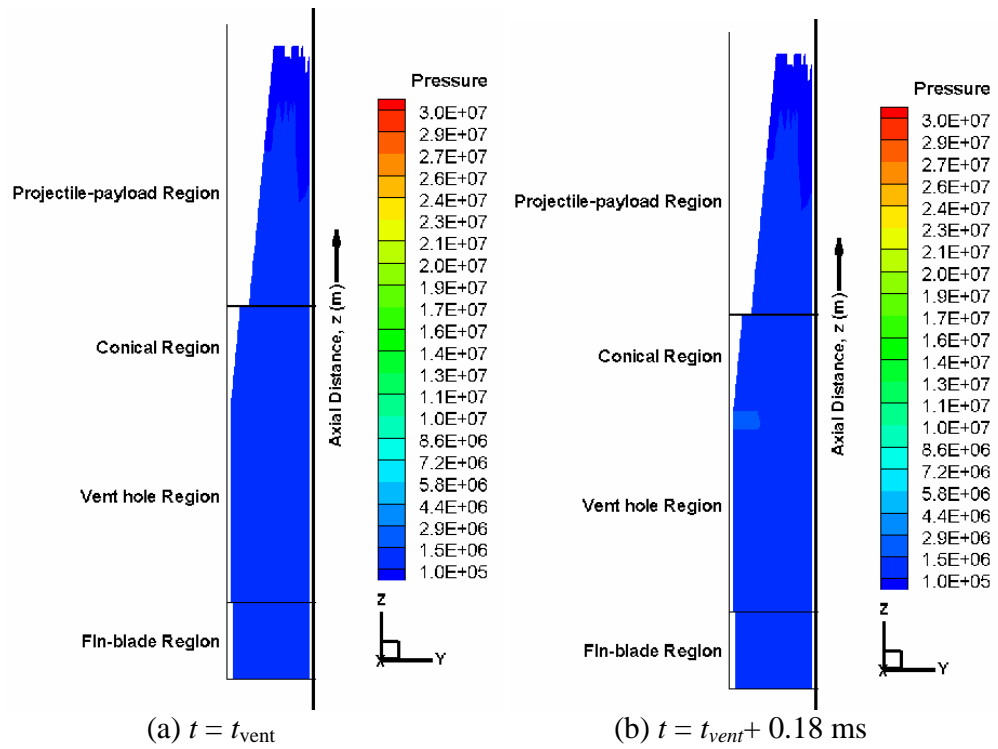


Figure 6-16: Computed pressure contours in the mortar tube at the beginning of ballistic cycle.

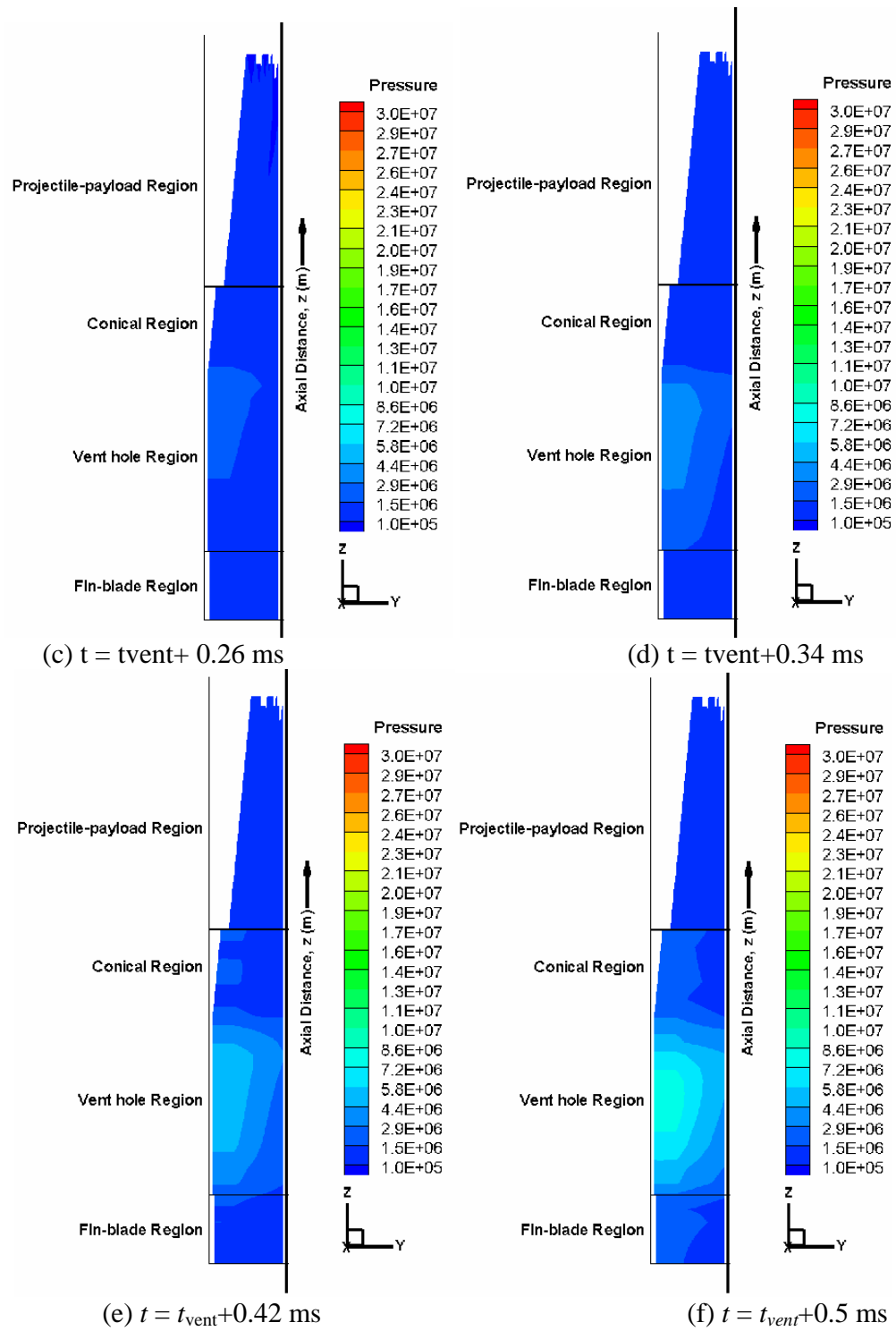


Figure 6-17: Computed pressure contours in the mortar tube at various time instances.

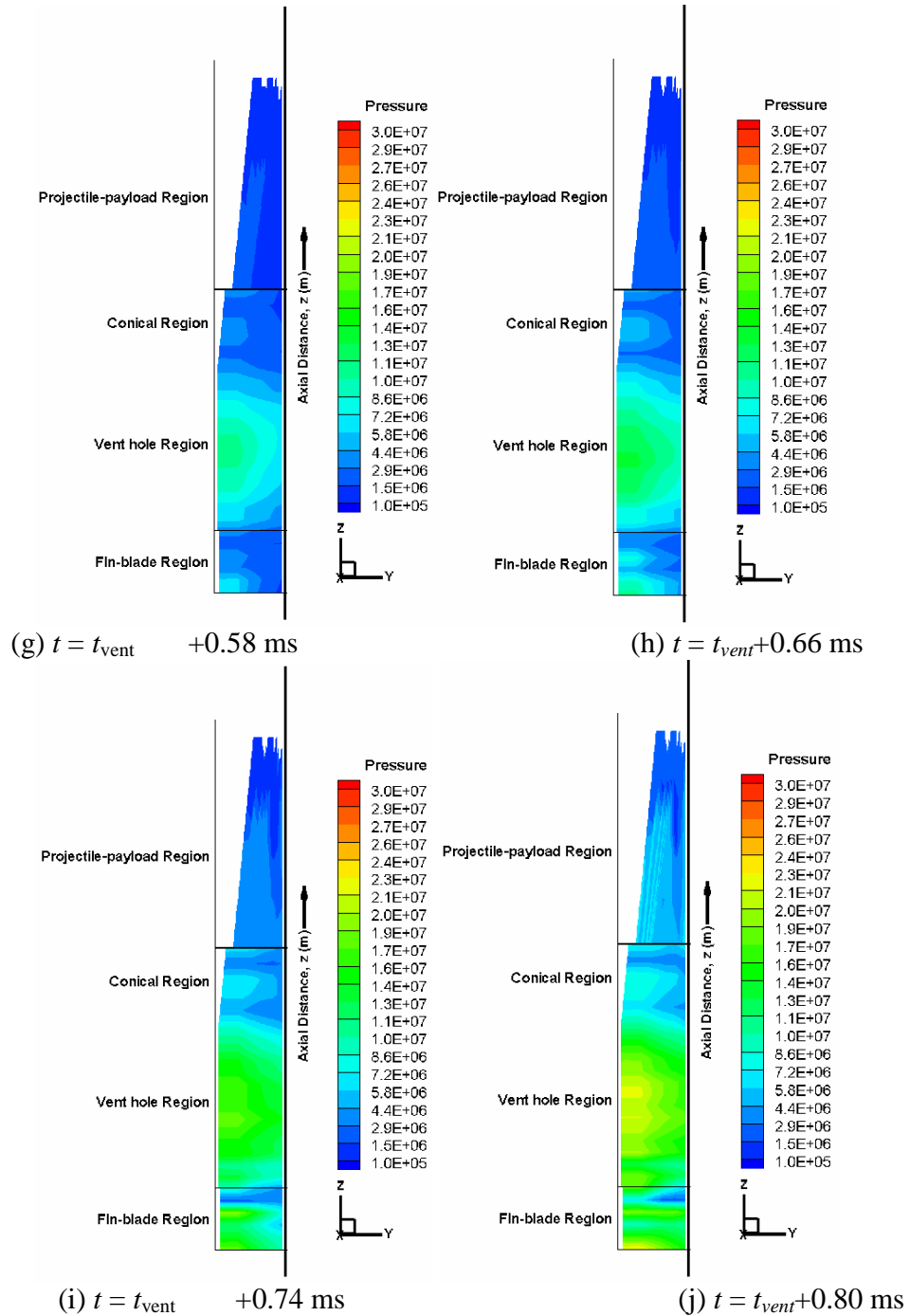


Figure 6-18: Computed pressure contours in the mortar tube at various time instances.

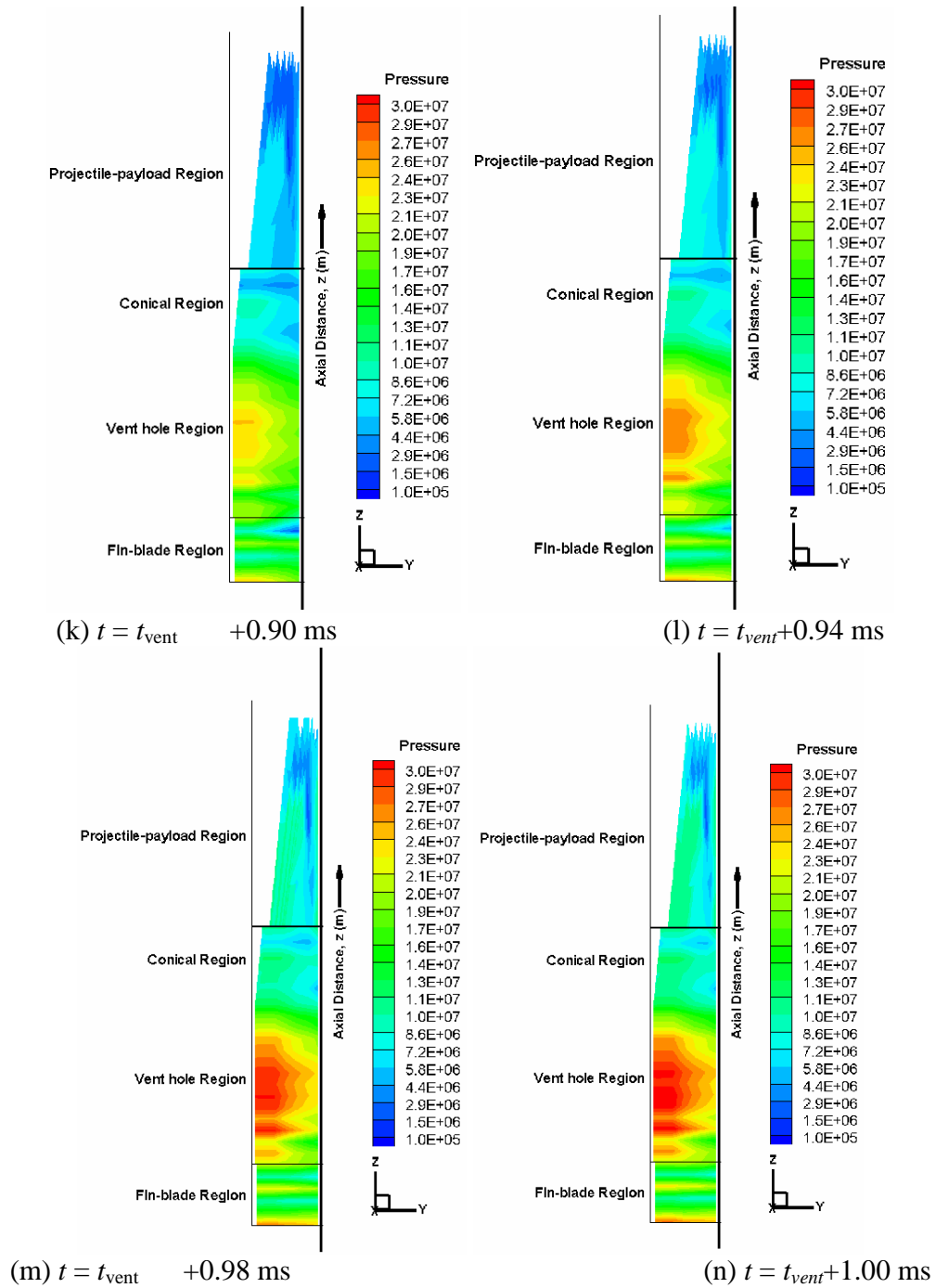


Figure 6-19: Computed pressure contours in the mortar tube at various time instances.

6.2 Remarks on calculated results from mortar tube sub-model

This work demonstrates the successful development of a 3D theoretical model and implementation of a numerical code for prediction of ignition/combustion, flame spreading, and pressurization processes in both the ignition cartridge and the mortar tube sections of the 120mm mortar propulsion system before the onset of projectile motion. The computational results are partially validated by experimental data from both ignition cartridge and mortar tests. The computed results show the pressure wave generation, propagation, and wave-reflection in both ignition cartridge and mortar tube sections. The pressure wave in the ignition cartridge is mainly due to the uneven discharge of combustion products from the flash tube. The discharge of combustion products from the tail-boom vent-holes also occurs in the same sequence as the flash tube. The non-uniform burning in the ignition cartridge combined with the uneven loading of M47 propellant grains in the mortar tube can result in a strong pressure-wave generation in the mortar. The overall combustion process in the existing configuration is strongly influenced by the non-uniformity of mass and energy discharge from flash tube. The fluid state may jump across shock waves or contact surfaces, and it may have discontinuous derivatives across any characteristic.

Chapter 7

MORTAR TUBE SUB MODEL SOLUTION WITH TWO-PHASE APPROXIMATE RIEMANN SOLVER

In the development and implementation of the final portion of this work, i.e., the mortar tube sub-model, a high-resolution Godunov-type shock-capturing approach was used where the discretization is done directly on the integral formulation of the conservation laws. All the schemes available here share the following key ingredients:

1. A linearized approximate Riemann Solver to compute fully non-linear wave interactions and to directly provide upwinding properties in the scheme,
2. An entropy fix based on Harten-Heyman method,
3. A van Leer flux limiter for total variation diminishing,
4. A three dimensional wave propagation method,
5. An explicit four stage fourth order Runge-Kutta time-marching scheme for time-integration of the source terms.

The projectile motion is accounted for by using the mesh generation scheme proposed in chapter 5. The calculated is verified by the exact Riemann solution. The computed solutions are validated extensively by detailed experimental data obtained from instrumented mortar simulator firings.

7.1 General approach

The non-linear coupled conservation equations in the mortar tube sub-model pose an initial value problem with discontinuous initial conditions for conservative variables. For example, the initial conditions for condensed-phase mass are discontinuous in the axial and radial directions (based on the porosity distribution). Similarly, the initial conditions for gas-phase velocity and condensed phase velocity components in radial and tangential directions are also discontinuous owing to the non-uniform flow of combustion products from the ignition cartridge into the mortar tube, as shown by Eq. (4.1) and Eq. (4.2) in chapter 4. This situation poses a very complex problem for obtaining the numerical solution of the sub-model. Based on these observations, it can be concluded that the conservation equations for the mortar tube sub-model possess characteristics of the Riemann problem, although the conservation equations are two-phase and contain non-homogeneity in form of the source terms. First, it is important to address the problem of solving the conservation equations without the source terms.

A Riemann problem is an initial value problem, which in its simplest form is defined by a single linear advection equation and initial condition with a single discontinuity (as shown in Fig. 7-1).

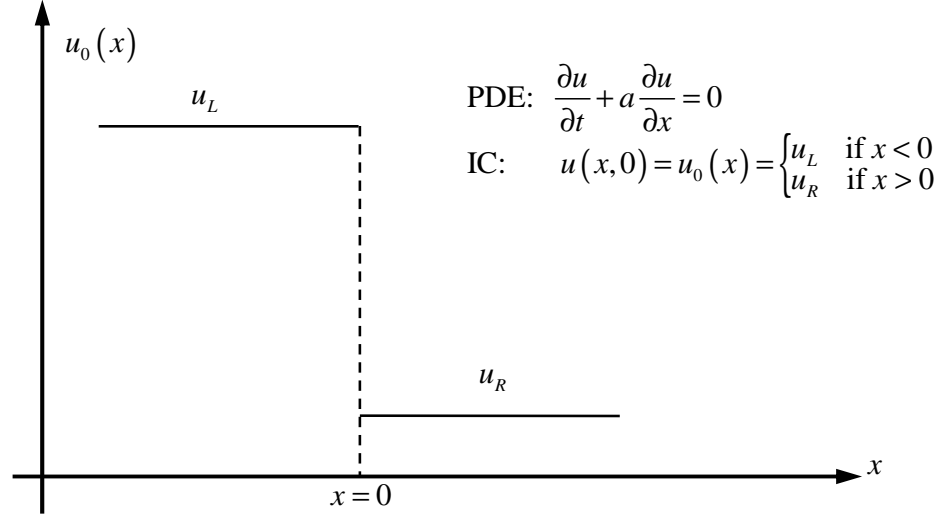


Figure 7-1: Illustration of the initial data for the Riemann problem. At the initial time the data consists of two constant states separated by a discontinuity at $x = 0$.

Physically, the Riemann problem can be interpreted as a flow field in a tube of infinite length, containing two gases separated by a diaphragm at $x = 0$, which has a gas with density u_L at the left hand side and another gas of density u_R at the right hand side, where L and R mean left and right of the discontinuity respectively. The rupture of the diaphragm generates a nearly centered wave system that could consist of a shock wave a contact discontinuity, and a rarefaction wave. Any numerical method used to solve the Riemann problem should be capable of addressing the formation of flow structure such as shock formation, contact discontinuities, and rarefactions. The accurate representation of these flow discontinuities determines the overall accuracy of such numerical method. Therefore, an ingenious approach to solve a system of hyperbolic equations that are initial value problems would be to account for the flow field structure through the non-linear superposition of the solutions of the local Riemann problems. This approach was first proposed by Godunov [15].

7.2 Godunov methods

The conservation equation for a one-dimensional generalized initial boundary value problem (IVBP) is shown in Eq. (7.1):

$$\frac{\partial u}{\partial t} + \frac{\partial f(u)}{\partial x} = 0 \quad (\text{Eq. 7.1})$$

In the above equation, f is the flux vector and u is the conservative variable vector. The choice of flux $f(u) = au$ reproduces the linear advection equation shown earlier in Fig. 7-1. A conservative scheme for the scalar conservation law Eq. (7.1) is a numerical method of the following form given by Eq. (7.2):

$$u_i^{n+1} = u_i^n + \frac{\Delta t}{\Delta x} [f_{i-\frac{1}{2}} - f_{i+\frac{1}{2}}] \quad (\text{Eq. 7.2})$$

The numerical intercell flux $f_{i+\frac{1}{2}}$ is given by Eq. (7.3):

$$f_{i+\frac{1}{2}} = f_{i+\frac{1}{2}}(u_{i-l_L}^n, \dots, u_{i+l_R}^n) \quad (\text{Eq. 7.3})$$

In Eq. (7.3), l_L and l_R are two non-negative integers. It can be proved that choice of 0 and 1 for these two numbers gives a stable solution to the linear advection equation. Thus, the intercell numerical flux can be represented by the following Eq. (7.4):

$$f_{i+\frac{1}{2}} = f_{i+\frac{1}{2}}(u_i^n, u_{i+1}^n) \quad (\text{Eq. 7.4})$$

Godunov's first-order upwind method is a conservative method of the form Eq. (7.2), where the intercell numerical fluxes $f_{i+\frac{1}{2}}$ are computed by using solutions of local Riemann problems. A basic assumption of the method is that at a given time level n the data has a piece-wise constant distribution, as depicted in Fig. 7-2.

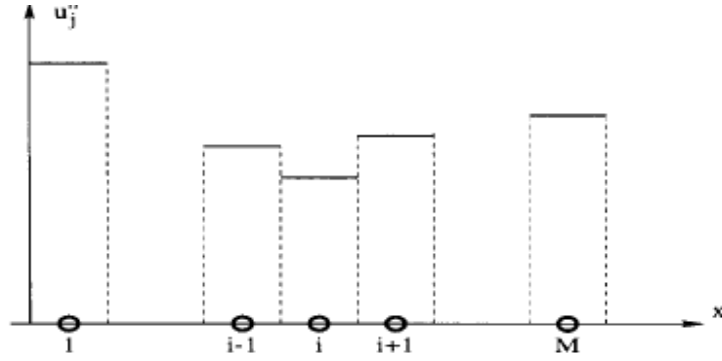


Figure 7-2: Piece-wise constant distribution of data at time level n [71].

The data at time level n may be seen as pairs of constant states, (u_i^n, u_{i+1}^n) separated by a discontinuity at the intercell boundary, $x_{i+1/2}$. Then, one can define a local Riemann problem by Eq. (7.5):

$$\begin{aligned} \text{PDE: } & \frac{\partial u}{\partial t} + \frac{\partial f(u)}{\partial x} = 0 \\ \text{IC: } & u(x, 0) = u_0(x) = \begin{cases} u_i^n & \text{if } x < 0 \\ u_{i+1}^n & \text{if } x > 0 \end{cases} \end{aligned} \quad (\text{Eq. 7.5})$$

This local Riemann problem may be solved analytically, if desired. Thus, at a given time level n , at each intercell boundary, $x_{i+1/2}$ we have the local Riemann problem $\text{RP}(u_i^n, u_{i+1}^n)$ with initial data (u_i^n, u_{i+1}^n) . The time-averaged intercell fluxes $f_{i+1/2}$ and $f_{i-1/2}$ are given as Eq. (7.6) and Eq. (7.7):

$$f_{i+1/2} = \frac{1}{\Delta t} \int_0^{\Delta t} f[\tilde{u}(x_{i+1/2}, t)] dt \quad (\text{Eq. 7.6})$$

$$f_{i-1/2} = \frac{1}{\Delta t} \int_0^{\Delta t} f[\tilde{u}(x_{i-1/2}, t)] dt \quad (\text{Eq. 7.7})$$

The integrand $f[\tilde{u}(x, t)]$ at each cell interface depends on the exact solution $\tilde{u}(x, t)$ of the Riemann problem along the t -axis (local coordinates); this is given by Eq. (7.8) and Eq. (7.9):

$$\tilde{u}(x_{i+1/2}, t) = u_{i+1/2}^n(0) \quad (\text{Eq. 7.8})$$

$$\tilde{u}(x_{i-1/2}, t) = u_{i-1/2}^n(0) \quad (\text{Eq. 7.9})$$

The intercell fluxes $f_{i+1/2}$ and $f_{i-1/2}$ become Eq. (7.10) and Eq. (7.11):

$$f_{i+1/2} = f(u_{i+1/2}^n(0)) \quad (\text{Eq. 7.10})$$

$$f_{i-1/2} = f(u_{i-1/2}^n(0)) \quad (\text{Eq. 7.11})$$

In general, the Godunov intercell numerical flux is represented as following Eq. (7.12):

$$f_{i+1/2} = f(u_{i+1/2}^n(0)) \quad (\text{Eq. 7.12})$$

where $u_{i+1/2}^n$ is the exact solution $u_{i+1/2}^n(x/t)$ of the Riemann problem $RP(u_i^n, u_{i+1}^n)$ evaluated at $x/t=0$, i.e. the solution is evaluated along the intercell boundary, which coincides with the t -axis in the local frame of the Riemann problem solution. The structure of Riemann solution is shown in Fig. 7-3.

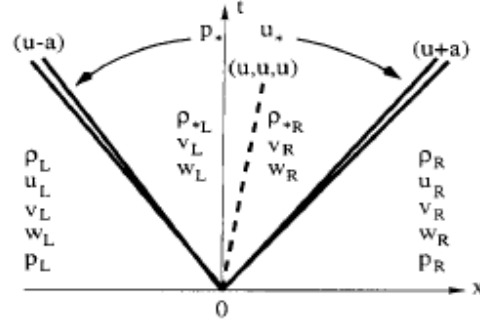


Figure 7-3: Structure of Riemann problem solution for the x-split three dimensional Euler equations [71].

7.3 Issues with Gudonov's method

The method of Godunov and its high-order extensions require the solution of the Riemann problem, which is an iterative procedure. Thus, the computational cost of such numerical method for practical problems is extremely high and poses a hurdle in successful implementation of Gudonov's method. The issue of computational cost is further complicated by equations of state of complicated algebraic form or by the complexity of the particular system of equations being solved, or both. Thus, a non-iterative approach was introduced by approximate solutions of the Riemann problem. There are essentially two ways of extracting approximate information from the solution of the Riemann problem to be used in Godunov-type methods: 1) to find an *approximation to the numerical flux* employed in the numerical method, directly or 2) to find an *approximation to a state* and then evaluate the physical flux function at this state. The latter route was used in this work. The approximate Riemann solvers do not need an iteration process. An approximate solution for the state is used to evaluate the Godunov

flux at cell boundaries. Some of the approximations presented are exceedingly simple but not accurate enough to produce robust numerical methods. This difficulty is resolved by designing hybrid schemes that combine various approximate solvers in an adaptive fashion.

7.4 Approximate Riemann solver: Roe-Pike method

The generalized conservation equations for the three-dimensional problem can be expressed in a very compact notation by defining a column vector \mathbf{Q} of conserved variables and flux vectors $\mathbf{F}(\mathbf{Q})$, $\mathbf{G}(\mathbf{Q})$, $\mathbf{H}(\mathbf{Q})$ in the three directions, respectively. This form is shown in Eq. (7.13).

$$\frac{\partial \mathbf{Q}}{\partial t} + \frac{\partial \mathbf{F}(\mathbf{Q})}{\partial x} + \frac{\partial \mathbf{G}(\mathbf{Q})}{\partial y} + \frac{\partial \mathbf{H}(\mathbf{Q})}{\partial z} = \mathbf{\Xi}(\mathbf{Q}) \quad (\text{Eq. 7.13})$$

Recall that the conserved variables in the mortar tube sub-model are gas-phase mass, condensed-phase mass, gas-phase momentum, condensed-phase momentum, and total energy. The conservation equations for these variables were discussed in chapter 4 with considerable details. For convenience, they are repeated here and the conservation equation for gas-phase mass is shown by Eq. (7.14), for condensed-phase mass is shown by Eq. (7.15), for gas-phase momentum is shown Eq. (7.16), for condensed-phase mass is shown Eq. (7.17), and for gas-phase energy is shown Eq. (7.18).

$$\frac{\partial(\rho\phi\zeta)}{\partial t} + \nabla \cdot (\rho\phi\zeta \mathbf{U}_g) = \Sigma_1 \quad (\text{Eq. 7.14})$$

$$\frac{\partial[(1-\phi)\rho_p\zeta]}{\partial t} + \nabla \cdot [(1-\phi)\rho_p\zeta \mathbf{U}_p] = \Sigma_2 \quad (\text{Eq. 7.15})$$

$$\frac{\partial\rho\phi\zeta\mathbf{U}_g}{\partial t} + \nabla\rho\phi\zeta\mathbf{U}_g \cdot \mathbf{U}_g + \nabla\phi\zeta P = \mathbf{I}_g \quad (\text{Eq. 7.16})$$

$$\frac{\partial}{\partial t}[\rho_p(1-\phi)\zeta\mathbf{U}_p] + \nabla\rho_p(1-\phi)\zeta\mathbf{U}_p \cdot \mathbf{U}_p - \nabla\zeta(1-\phi)\tau_p = \mathbf{I}_p \quad (\text{Eq. 7.17})$$

$$\frac{\partial(\rho\phi\zeta e_t)}{\partial t} + \nabla \cdot (\rho\phi\zeta e_t \mathbf{U}_g) + \nabla \cdot (\phi\zeta P \mathbf{U}_g) = \Sigma_9 \quad (\text{Eq. 7.18})$$

Therefore, the column vector \mathbf{Q} consisting of conserved variables is shown in Eq. (7.19).

$$\mathbf{Q} \equiv \begin{bmatrix} q_1 \\ q_2 \\ q_3 \\ q_4 \\ q_5 \\ q_6 \\ q_7 \\ q_8 \\ q_9 \end{bmatrix} = \begin{bmatrix} \rho\phi\zeta \\ (1-\phi)\rho_p\zeta \\ \rho\phi\zeta U_{g_1} \\ \rho\phi\zeta U_{g_2} \\ \rho\phi\zeta U_{g_3} \\ \rho_p(1-\phi)\zeta U_{p_1} \\ \rho_p(1-\phi)\zeta U_{p_2} \\ \rho_p(1-\phi)\zeta U_{p_3} \\ \rho\phi\zeta e_t \end{bmatrix} \quad (\text{Eq. 7.19})$$

The flux vectors $\mathbf{F}(\mathbf{Q})$ in x -direction, $\mathbf{G}(\mathbf{Q})$ in y -direction and $\mathbf{H}(\mathbf{Q})$ in the z -directions are shown by Eqs. (7.20)- (7.22), respectively.

$$\mathbf{F}(\mathbf{Q}) \equiv \begin{bmatrix} f_1 \\ f_2 \\ f_3 \\ f_4 \\ f_5 \\ f_6 \\ f_7 \\ f_8 \\ f_9 \end{bmatrix} = \begin{bmatrix} \rho\phi\zeta U_{g_1} \\ (1-\phi)\rho_p\zeta U_{p_1} \\ \rho\phi\zeta U_{g_1} U_{g_1} + \phi\zeta P \\ \rho\phi\zeta U_{g_2} U_{g_1} \\ \rho\phi\zeta U_{g_3} U_{g_1} \\ \rho_p(1-\phi)\zeta U_{p_1} U_{p_1} - \zeta(1-\phi)\tau_p \\ \rho_p(1-\phi)\zeta U_{p_1} U_{p_2} \\ \rho_p(1-\phi)\zeta U_{p_1} U_{p_3} \\ \rho\phi\zeta e_t U_{g_1} + P\phi\zeta U_{g_1} \end{bmatrix} \quad (\text{Eq. 7.20})$$

$$\mathbf{G}(\mathbf{Q}) \equiv \begin{bmatrix} g_1 \\ g_2 \\ g_3 \\ g_4 \\ g_5 \\ g_6 \\ g_7 \\ g_8 \\ g_9 \end{bmatrix} = \begin{bmatrix} \rho\phi\zeta U_{g_2} \\ (1-\phi)\rho_p\zeta U_{p_2} \\ \rho\phi\zeta U_{g_2} U_{g_1} \\ \rho\phi\zeta U_{g_2} U_{g_2} + \phi\zeta P \\ \rho\phi\zeta U_{g_2} U_{g_3} \\ \rho_p(1-\phi)\zeta U_{p_2} U_{p_1} \\ \rho_p(1-\phi)\zeta U_{p_2} U_{p_2} - \zeta(1-\phi)\tau_p \\ \rho_p(1-\phi)\zeta U_{p_2} U_{p_3} \\ \rho\phi\zeta e_t U_{g_2} + P\phi\zeta U_{g_2} \end{bmatrix} \quad (\text{Eq. 7.21})$$

$$\mathbf{H}(\mathbf{Q}) \equiv \begin{bmatrix} h_1 \\ h_2 \\ h_3 \\ h_4 \\ h_5 \\ h_6 \\ h_7 \\ h_8 \\ h_9 \end{bmatrix} = \begin{bmatrix} \rho\phi\zeta U_{g_3} \\ (1-\phi)\rho_p\zeta U_{p_3} \\ \rho\phi\zeta U_{g_1} U_{g_3} \\ \rho\phi\zeta U_{g_2} U_{g_3} \\ \rho\phi\zeta U_{g_3} U_{g_3} + \phi\zeta P \\ \rho_p(1-\phi)\zeta U_{p_1} U_{p_3} \\ \rho_p(1-\phi)\zeta U_{p_2} U_{p_3} \\ \rho_p(1-\phi)\zeta U_{p_3} U_{p_3} - \zeta(1-\phi)\tau_p \\ \rho\phi\zeta e_t U_{g_3} + P\phi\zeta U_{g_3} \end{bmatrix} \quad (\text{Eq. 7.22})$$

The source term vector is shown by Eq. (7.23). The components of source term vector were defined in chapter 2.

$$\Xi(\mathbf{Q}) \equiv \begin{bmatrix} \Sigma_1(\mathbf{Q}) \\ \Sigma_2(\mathbf{Q}) \\ \Sigma_3(\mathbf{Q}) \\ \Sigma_4(\mathbf{Q}) \\ \Sigma_5(\mathbf{Q}) \\ \Sigma_6(\mathbf{Q}) \\ \Sigma_7(\mathbf{Q}) \\ \Sigma_8(\mathbf{Q}) \\ \Sigma_9(\mathbf{Q}) \end{bmatrix} \quad (\text{Eq. 7.23})$$

The direct approximation to the flux vector $\mathbf{F}(\mathbf{Q})$ is obtained by introducing the Jacobian of the flux functions, which is defined in Eq. (7.24). This approach was proposed by Roe [59] and Roe and Pike [66]:

$$\mathbf{A}(\mathbf{Q}) \equiv \frac{\partial \mathbf{F}(\mathbf{Q})}{\partial \mathbf{Q}} \quad (\text{Eq. 7.24})$$

Using the chain rule on the conservation equations, the Eq. (7.13) can be written as following:

$$\frac{\partial \mathbf{Q}}{\partial t} + \mathbf{A}(\mathbf{Q}) \frac{\partial \mathbf{Q}}{\partial x} + \mathbf{B}(\mathbf{Q}) \frac{\partial \mathbf{Q}}{\partial y} + \mathbf{C}(\mathbf{Q}) \frac{\partial \mathbf{Q}}{\partial z} = \Xi(\mathbf{Q}) \quad (\text{Eq. 7.25})$$

In order to obtain the Jacobian matrix $\mathbf{A}(\mathbf{Q})$ by using the Eq. (7.24), the flux vector $\mathbf{F}(\mathbf{Q})$ is expressed in terms of conserved variables vector as shown in Eq. (7.26):

$$\begin{aligned}
f_1 &= \rho\phi\zeta U_{g_1} = q_3 \\
f_2 &= (1-\phi)\rho_p\zeta U_{p_1} = q_6 \\
f_3 &= \rho\phi\zeta U_{g_1} U_{g_1} + \phi\zeta P = \frac{q_3^2}{q_1} + (\gamma-1) \left[q_9 - \frac{q_3^2 + q_4^2 + q_5^2}{2q_1} \right] \\
f_4 &= \rho\phi\zeta U_{g_2} U_{g_1} = \frac{q_3 q_4}{q_1} \\
f_5 &= \rho\phi\zeta U_{g_3} U_{g_1} = \frac{q_3 q_5}{q_1} \\
f_6 &= \rho_p (1-\phi) \zeta U_{p_1} U_{p_1} - \zeta (1-\phi) \tau_p = \frac{q_6^2}{q_2} - \rho_p c_{ref}^2 \phi_c \zeta \frac{1-\phi_c - q_2/\zeta\rho_p}{(1-q_2/\zeta\rho_p)} \\
f_7 &= \rho_p (1-\phi) \zeta U_{p_2} U_{p_1} = \frac{q_6 q_7}{q_2} \\
f_8 &= \rho_p (1-\phi) \zeta U_{p_3} U_{p_1} = \frac{q_6 q_8}{q_2} \\
f_9 &= \rho\phi\zeta e_t U_{g_1} + P\phi\zeta U_{g_1} = \frac{q_3 q_9}{q_1} + (\gamma-1) \left[q_9 - \frac{q_3^2 + q_4^2 + q_5^2}{2q_1} \right] \frac{q_3}{q_1}
\end{aligned} \tag{Eq. 7.26}$$

By using the Eq. (7.24), the Jacobian matrix $\mathbf{A}(\mathbf{Q})$ is obtained and it is shown in

Eq. (7.27):

$$\mathbf{A} = \begin{bmatrix}
0 & 0 & 1 & 0 & 0 & 0 & 0 & 0 & 0 \\
0 & 0 & 0 & 1 & 0 & 0 & 0 & 0 & 0 \\
\frac{1}{2}\bar{\gamma} \left(\frac{\mathbf{U}_g \cdot \mathbf{U}_g}{-2U_{g_1}^2} \right) - U_{g_1}^2 & 0 & (3-\gamma)U_{g_1} & -\bar{\gamma}U_{g_3} & -\bar{\gamma}U_{g_2} & 0 & 0 & 0 & \bar{\gamma} \\
-U_{g_1} U_{g_2} & 0 & U_{g_2} & U_{g_1} & 0 & 0 & 0 & 0 & 0 \\
-U_{g_1} U_{g_3} & 0 & U_{g_3} & 0 & U_{g_1} & 0 & 0 & 0 & 0 \\
0 & U_{p_1}^2 - c_p^2 & 0 & 0 & 0 & 2U_{p_1} & 0 & 0 & 0 \\
0 & -U_{p_1} U_{p_2} & 0 & 0 & 0 & U_{p_2} & U_{p_1} & 0 & 0 \\
0 & -U_{p_1} U_{p_3} & 0 & 0 & 0 & U_{p_3} & 0 & U_{p_1} & 0 \\
\frac{\gamma-2}{2} \mathbf{U}_g \cdot \mathbf{U}_g U_{g_3} & 0 & \frac{c_g^2}{\bar{\gamma}} - \frac{3}{2} \bar{\gamma} U_{g_1}^2 & -\bar{\gamma} U_{g_1} U_{g_2} & -\bar{\gamma} U_{g_3} U_{g_1} & 0 & 0 & 0 & \bar{\gamma} U_{g_1} \\
-\frac{c_g^2 U_{g_1}}{\bar{\gamma}} & 0 & + \frac{\bar{\gamma} \mathbf{U}_g \cdot \mathbf{U}_g}{2} & 0 & 0 & 0 & 0 & 0 & 0
\end{bmatrix} \tag{Eq. 7.27}$$

The Eigenvalues of matrix $\mathbf{A}(\mathbf{Q})$ are shown in Eq. (7.28):

$$\begin{aligned}
 \lambda_1 &= U_{g_1} - c_g \\
 \lambda_2 &= \lambda_3 = \lambda_4 = U_{g_1} \\
 \lambda_5 &= U_{g_1} + c_g \\
 \lambda_6 &= U_{p_1} - c_p \\
 \lambda_7 &= \lambda_8 = U_{p_1} \\
 \lambda_9 &= U_{p_1} + c_p
 \end{aligned}
 \tag{Eq. 7.28}$$

The corresponding right eigenvectors of $\mathbf{A}(\mathbf{Q})$ are shown in Eq. (7.29):

$$\begin{aligned}
 \mathbf{K} &= [\mathbf{K}_1 \quad \mathbf{K}_2 \quad \mathbf{K}_3 \quad \mathbf{K}_4 \quad \mathbf{K}_5 \quad \mathbf{K}_6 \quad \mathbf{K}_7 \quad \mathbf{K}_8 \quad \mathbf{K}_9] \\
 &= \begin{bmatrix} 1 & & & & 0 & 0 & 1 & & 0 & 0 & 0 & 0 \\ U_{g_1} - c_g & U_{g_1} & & & 0 & 0 & U_{g_1} + c_g & & 0 & 0 & 0 & 0 \\ U_{g_2} & U_{g_2} & 1 & 0 & U_{g_2} & & 0 & & 0 & 0 & 0 & 0 \\ U_{g_3} & U_{g_3} & 0 & 1 & U_{g_3} & & 0 & & 0 & 0 & 0 & 0 \\ H - U_{g_1} c_g & \frac{1}{2} \mathbf{U}_g \cdot \mathbf{U}_g & U_{g_2} & U_{g_3} & H + U_{g_1} c_g & & 0 & & 0 & 0 & 0 & 0 \\ 0 & 0 & 0 & 0 & 0 & & 1 & 1 & 0 & 0 & 0 & 0 \\ 0 & 0 & 0 & 0 & 0 & & U_{p_1} - c_p & U_{p_1} + c_p & 0 & 0 & 0 & 0 \\ 0 & 0 & 0 & 0 & 0 & & U_{p_2} & U_{p_2} & 0 & 1 & 0 & 0 \\ 0 & 0 & 0 & 0 & 0 & & U_{p_3} & U_{p_3} & 1 & 0 & 0 & 0 \end{bmatrix}
 \end{aligned}
 \tag{Eq. 7.29}$$

Similarly, the Jacobian matrices of flux vectors \mathbf{G} and \mathbf{H} are defined as follows:

Eq. (7.30) and Eq. (7.31).

$$\mathbf{B}(\mathbf{Q}) \equiv \frac{\partial \mathbf{G}(\mathbf{Q})}{\partial \mathbf{Q}}
 \tag{Eq. 7.30}$$

$$\mathbf{C}(\mathbf{Q}) \equiv \frac{\partial \mathbf{H}(\mathbf{Q})}{\partial \mathbf{Q}}
 \tag{Eq. 7.31}$$

Again, the flux vector $\mathbf{G}(\mathbf{Q})$ and $\mathbf{H}(\mathbf{Q})$ are expressed in terms of variable vector

\mathbf{Q} as shown in Eq. (7.32) and Eq. (7.33).

$$\begin{aligned}
g_1 &= \rho\phi\zeta U_{g_2} = q_4 \\
g_2 &= (1-\phi)\rho_p\zeta U_{p_2} = q_7 \\
g_3 &= \rho\phi\zeta U_{g_2} U_{g_1} = \frac{q_3 q_4}{q_1} \\
g_4 &= \rho\phi\zeta U_{g_2} U_{g_2} + \phi\zeta P = \frac{q_4^2}{q_1} + (\gamma-1) \left[q_9 - \frac{q_3^2 + q_4^2 + q_5^2}{2q_1} \right] \\
g_5 &= \rho\phi\zeta U_{g_3} U_{g_2} = \frac{q_3 q_5}{q_1} \\
g_6 &= \rho_p (1-\phi) \zeta U_{p_1} U_{p_2} = \frac{q_6 q_7}{q_2} \\
g_7 &= \rho_p (1-\phi) \zeta U_{p_2} U_{p_2} - \zeta (1-\phi) \tau_p = \frac{q_7^2}{q_2} - \rho_p c_{ref}^2 \phi_c \zeta \frac{1-\phi_c - q_2/\zeta\rho_p}{(1-q_2/\zeta\rho_p)} \\
g_8 &= \rho_p (1-\phi) \zeta U_{p_3} U_{p_2} = \frac{q_6 q_8}{q_2} \\
g_9 &= \rho\phi\zeta e_t U_{g_2} + P\phi\zeta U_{g_2} = \frac{\gamma q_4 q_9}{q_1} - (\gamma-1) \left[\frac{q_3^2 + q_4^2 + q_5^2}{2q_1} \right] \frac{q_4}{q_1} \\
h_1 &= \rho\phi\zeta U_{g_3} = q_5 \\
h_2 &= (1-\phi)\rho_p\zeta U_{p_3} = q_8 \\
h_3 &= \rho\phi\zeta U_{g_1} U_{g_3} = \frac{q_3 q_5}{q_1} \\
h_4 &= \rho\phi\zeta U_{g_2} U_{g_3} = \frac{q_4 q_5}{q_1} \\
h_5 &= \rho\phi\zeta U_{g_3} U_{g_3} + \phi\zeta P = \frac{q_5^2}{q_1} + (\gamma-1) \left[q_9 - \frac{q_3^2 + q_4^2 + q_5^2}{2q_1} \right] \\
h_6 &= \rho_p (1-\phi) \zeta U_{p_1} U_{p_3} = \frac{q_6 q_8}{q_2} \\
h_7 &= \rho_p (1-\phi) \zeta U_{p_2} U_{p_3} = \frac{q_7 q_8}{q_2} \\
h_8 &= \rho_p (1-\phi) \zeta U_{p_3} U_{p_3} - \zeta (1-\phi) \tau_p = \frac{q_8^2}{q_2} - \rho_p c_{ref}^2 \phi_c \zeta \frac{1-\phi_c - q_2/\zeta\rho_p}{(1-q_2/\zeta\rho_p)} \\
h_9 &= \rho\phi\zeta e_t U_{g_3} + P\phi\zeta U_{g_3} = \frac{q_4 q_9}{q_1} + (\gamma-1) \left[q_9 - \frac{q_3^2 + q_4^2 + q_5^2}{2q_1} \right] \frac{q_5}{q_1}
\end{aligned}$$

(Eq. 7.32)

(Eq. 7.33)

Thus, the Jacobian matrices B and C are shown by Eq. (7.34) and Eq. (7.35),

respectively.

$$\mathbf{B} = \begin{bmatrix} 0 & 0 & 0 & 1 & 0 & 0 & 0 & 0 & 0 \\ 0 & 0 & 0 & 0 & 0 & 0 & 1 & 0 & 0 \\ -U_{g_1} U_{g_2} & 0 & U_{g_2} & U_{g_1} & 0 & 0 & 0 & 0 & 0 \\ \frac{1}{2} \bar{\gamma} \left(\mathbf{U}_g \cdot \mathbf{U}_g \right) - U_{g_2}^2 & 0 & -\bar{\gamma} U_{g_1} & (3-\gamma) U_{g_2} & -\bar{\gamma} U_{g_3} & 0 & 0 & 0 & \bar{\gamma} \\ -U_{g_3} U_{g_2} & 0 & 0 & U_{g_3} & U_{g_1} & 0 & 0 & 0 & 0 \\ 0 & -U_{p_1} U_{p_2} & 0 & 0 & 0 & U_{p_2} & U_{p_1} & 0 & 0 \\ 0 & c_p^2 - U_{p_1}^2 & 0 & 0 & 0 & 0 & 2U_{p_1} & 0 & 0 \\ 0 & -U_{p_1} U_{p_3} & 0 & 0 & 0 & U_{p_3} & 0 & U_{p_1} & 0 \\ \frac{(\gamma-2)}{2} \mathbf{U}_g \cdot \mathbf{U}_g U_{g_1} & 0 & -\bar{\gamma} U_{g_1} U_{g_2} & \frac{c_g^2}{\bar{\gamma}} - \frac{3\bar{\gamma}}{2} U_{g_2}^2 & -\bar{\gamma} U_{g_3} U_{g_2} & 0 & 0 & 0 & \gamma U_{g_2} \\ -\frac{c_g^2 U_{g_2}}{\bar{\gamma}} & 0 & -\bar{\gamma} U_{g_1} U_{g_2} & +\frac{\gamma}{2} \mathbf{U}_g \cdot \mathbf{U}_g & -\bar{\gamma} U_{g_3} U_{g_2} & 0 & 0 & 0 & \gamma U_{g_2} \end{bmatrix} \quad (\text{Eq. 7.34})$$

$$\mathbf{C} = \begin{bmatrix} 0 & 0 & 0 & 0 & 1 & 0 & 0 & 0 & 0 \\ 0 & 0 & 0 & 0 & 0 & 0 & 0 & 1 & 0 \\ -U_{g_1} U_{g_3} & 0 & U_{g_3} & 0 & U_{g_1} & 0 & 0 & 0 & 0 \\ -U_{g_2} U_{g_3} & 0 & 0 & U_{g_3} & U_{g_2} & 0 & 0 & 0 & 0 \\ \frac{1}{2} \bar{\gamma} \left(\mathbf{U}_g \cdot \mathbf{U}_g \right) - U_{g_3}^2 & 0 & -\bar{\gamma} U_{g_1} & -\bar{\gamma} U_{g_2} & (3-\gamma) U_{g_3} & 0 & 0 & 0 & \bar{\gamma} \\ 0 & -U_{p_3} U_{p_1} & 0 & 0 & 0 & U_{p_3} & 0 & U_{p_1} & 0 \\ 0 & -U_{p_3} U_{p_2} & 0 & 0 & 0 & 0 & U_{p_3} & U_{p_2} & 0 \\ 0 & c_p^2 - U_{p_3}^2 & 0 & 0 & 0 & 2U_{p_3} & 0 & 0 & 0 \\ \frac{(\gamma-2)}{2} \mathbf{U}_g \cdot \mathbf{U}_g U_{g_3} & 0 & -\bar{\gamma} U_{g_1} U_{g_3} & -\bar{\gamma} U_{g_2} U_{g_3} & \frac{c_g^2}{\bar{\gamma}} - \frac{3\bar{\gamma}}{2} U_{g_3}^2 & 0 & 0 & 0 & \gamma U_{g_3} \\ -\frac{c_g^2 U_{g_3}}{\bar{\gamma}} & 0 & -\bar{\gamma} U_{g_1} U_{g_3} & -\bar{\gamma} U_{g_2} U_{g_3} & +\frac{\gamma}{2} \mathbf{U}_g \cdot \mathbf{U}_g & 0 & 0 & 0 & \gamma U_{g_3} \end{bmatrix} \quad (\text{Eq. 7.35})$$

7.4.1 Roe's method

Roe's approach replaces the Jacobian matrices in Eq. (7.25), Eq. (7.30) and Eq. (7.31) by constant Jacobian matrices, which are functions of two data states; represented by $(\mathbf{Q}_L, \mathbf{Q}_R)$. For instance, the Jacobian matrix $\mathbf{A}(\mathbf{Q})$ is replaced by a *constant* Jacobian matrix $\bar{\mathbf{A}}(\mathbf{Q})$ that is a function of data sets $(\mathbf{Q}_L, \mathbf{Q}_R)$. The original Riemann problem is thus replaced by an *approximate linearized Riemann problem with constant coefficients*, which can be solved directly, shown by Eq. (7.36):

$$\begin{aligned} \frac{\partial \mathbf{Q}}{\partial t} + \bar{\mathbf{A}}(\mathbf{Q}) \frac{\partial \mathbf{Q}}{\partial x} + \bar{\mathbf{B}}(\mathbf{Q}) \frac{\partial \mathbf{Q}}{\partial y} + \bar{\mathbf{C}}(\mathbf{Q}) \frac{\partial \mathbf{Q}}{\partial z} &= \Xi(\mathbf{Q}) \\ \mathbf{Q}(\mathbf{x}, t) &= \begin{cases} \mathbf{Q}_L & \text{if } \mathbf{x} < 0 \\ \mathbf{Q}_R & \text{if } \mathbf{x} > 0 \end{cases} \end{aligned} \quad (\text{Eq. 7.36})$$

The *approximate* matrix $\bar{\mathbf{A}}(\mathbf{Q})$ is known as Roe-averaged matrix. The determination of Roe's Jacobian matrix $\bar{\mathbf{A}}(\mathbf{Q})$ requires that this matrix satisfy three important condition, i.e, hyperbolicity of the system, consistency with the exact Jacobian, and continuity with the property jump, i.e., $\mathbf{F}(\mathbf{Q}_L) - \mathbf{F}(\mathbf{Q}_R) = \bar{\mathbf{A}}(\mathbf{Q}_L - \mathbf{Q}_R)$. These conditions make the construction of matrix $\bar{\mathbf{A}}(\mathbf{Q})$ for a generalized problem computationally expensive. For the specific case of Euler equations, this issue was resolved by defining a parameter vector such that both the vectors of conserved variables \mathbf{Q} and the flux vector $\mathbf{F}(\mathbf{Q})$ could be expressed in terms of \mathbf{Q} as shown by Eq. (7.37):

$$\mathbf{Q} = \mathbf{Q}(\mathbf{U}) \quad \mathbf{F} = \mathbf{F}(\mathbf{U}) \quad (\text{Eq. 7.37})$$

Roe's parameter vector is defined in Eq. (7.38).

$$\mathbf{U} \equiv \frac{\mathbf{Q}}{\sqrt{\rho\phi\zeta}} = \begin{bmatrix} \sqrt{\rho\phi\zeta} \\ (1-\phi)\rho_p\zeta \\ \sqrt{\rho\phi\zeta} \\ \sqrt{\rho\phi\zeta}U_{g_1} \\ \sqrt{\rho\phi\zeta}U_{g_2} \\ \sqrt{\rho\phi\zeta}U_{g_3} \\ \rho_p(1-\phi)\zeta U_{p_1} \\ \sqrt{\rho\phi\zeta} \\ \rho_p(1-\phi)\zeta U_{p_2} \\ \sqrt{\rho\phi\zeta} \\ \rho_p(1-\phi)\zeta U_{p_3} \\ \sqrt{\rho\phi\zeta} \\ \sqrt{\rho\phi\zeta}e_t \end{bmatrix} = \begin{bmatrix} u_1 \\ u_2 \\ u_3 \\ u_4 \\ u_5 \\ u_6 \\ u_7 \\ u_8 \\ u_9 \end{bmatrix} \quad (\text{Eq. 7.38})$$

The parameter vector has the property that every component of variable vector \mathbf{Q} and every component flux matrix $\mathbf{F}(\mathbf{Q})$ in Eq. (7.26) is a quadratic in the components \mathbf{Q} . For instance $q_1 = u_1^2$ and $q_3 = u_1u_3$, etc. This property is also valid for the components of the \mathbf{G} and \mathbf{H} fluxes for the full three-dimensional equations. The parameter vector is then used to express the jump in conserved variables $\Delta\mathbf{Q} = \mathbf{Q}_L - \mathbf{Q}_R$ and flux vectors $\Delta\mathbf{F} = \mathbf{F}(\mathbf{Q}_L) - \mathbf{F}(\mathbf{Q}_R)$ in terms of the change $\Delta\mathbf{U} = \mathbf{U}_L - \mathbf{U}_R$ via two matrices $\bar{\mathbf{X}}$ and $\bar{\mathbf{Y}}$. This is shown by Eq. (7.39) and Eq. (7.40):

$$\Delta\mathbf{Q} = \bar{\mathbf{X}}\Delta\mathbf{U} \quad (\text{Eq. 7.39})$$

$$\Delta\mathbf{F} = \bar{\mathbf{Y}}\Delta\mathbf{U} \quad (\text{Eq. 7.40})$$

Using the above two equations, the Roe-averaged matrix is produced as shown in Eq. (7.41).

$$\Delta \mathbf{F} = (\bar{\mathbf{Y}}\bar{\mathbf{X}}^{-1})\Delta \mathbf{Q} = \bar{\mathbf{A}}\Delta \mathbf{Q} \quad (\text{Eq. 7.41})$$

Once the matrix $\bar{\mathbf{A}}$ is known, its eigenvalues $\bar{\lambda}_i$ and the right eigenvectors $\bar{\mathbf{K}}^i$ can be determined. The intercell Godunov flux $\mathbf{F}_{i+\frac{1}{2}}^n$ can be determined by using $\bar{\mathbf{Q}}_{i+\frac{1}{2}}^n(0)$, which is the solution to the local Riemann problem as described in an earlier section. In order to determine $\bar{\mathbf{Q}}_{i+\frac{1}{2}}^n(0)$, the data difference $\Delta \mathbf{Q} = \mathbf{Q}_L - \mathbf{Q}_R$ is projected on the right eigenvectors of matrix $\bar{\mathbf{A}}$ by using Eq. (7.42), where $\bar{\alpha}_i = \bar{\alpha}_i(\mathbf{Q}_L, \mathbf{Q}_R)$ are called wave strengths and can be deduced for a specific problem by using the Roe-average matrix $\bar{\mathbf{A}}$.

$$\Delta \mathbf{Q} = \mathbf{Q}_L - \mathbf{Q}_R = \sum_{i=1}^m \bar{\alpha}_i \bar{\mathbf{K}}^i \quad (\text{Eq. 7.42})$$

Thus, the solution $\bar{\mathbf{Q}}_{i+\frac{1}{2}}^n(0)$ is given by Eq. (7.43):

$$\bar{\mathbf{Q}}_{i+\frac{1}{2}}^n(0) = \begin{cases} \mathbf{Q}_L + \sum_{\bar{\lambda}_i \leq 0} \bar{\alpha}_i \bar{\mathbf{K}}^i \\ \text{or} \\ \mathbf{Q}_R - \sum_{\bar{\lambda}_i \geq 0} \bar{\alpha}_i \bar{\mathbf{K}}^i \end{cases} \quad (\text{Eq. 7.43})$$

By using the definition of intercell Godunov flux and solution of $\bar{\mathbf{Q}}_{i+\frac{1}{2}}^n(0)$ given by Eq. (7.43), it can be concluded that the intercell Godunov flux $\mathbf{F}_{i+\frac{1}{2}}^n$ is given by Eq. (7.44):

$$\mathbf{F}_{i+1/2}^n = \begin{cases} \mathbf{F}_L + \sum_{\lambda_i \leq 0} \bar{\alpha}_i \lambda_i \bar{K}^i \\ \text{or} \\ \mathbf{F}_R - \sum_{\lambda_i \geq 0} \bar{\alpha}_i \lambda_i \bar{K}^i \\ \text{or} \\ \frac{1}{2}(\mathbf{F}_L + \mathbf{F}_R) - \frac{1}{2} \sum_{i=1}^m \bar{\alpha}_i |\lambda_i| \bar{K}^i \end{cases} \quad (\text{Eq. 7.44})$$

7.4.2 Roe-Pike method

In Roe-Pike method, the philosophy for calculation of the intercell Godunov flux is same as that of Roe's method. However, it is a much simpler technique due to elimination of the Roe-averaged matrix $\bar{\mathbf{A}}$ from the calculation procedure. Instead of calculating the matrix $\bar{\mathbf{A}}$ by using the procedure described by Roe's method, an approximate Jacobian matrix $\hat{\mathbf{A}}$ is used, which is evaluated at a reference state \mathbf{W} , a vector consisting of the primary variables. These average primitive variables are also used to determine the eigenvalues, right eigenvectors and wave strengths needed in Eq. (7.44). The components of vector \mathbf{W} are known as Roe averaged primitive variables. Usually, evaluation of the Roe-averaged quantities is done by using gas density ρ as a parameter. Since the mortar tube sub-model is two-phase flow with variable volume, a new parameter was defined. In place of density, gas-phase mass was used as a primitive variable are given by Eq. (7.45):

$$m_g \equiv \rho \phi \zeta \quad (\text{Eq. 7.45})$$

For the case considered in this work, the Roe-averaged values are given by a number of equations. The average density, gas-velocity vector, enthalpy, porosity, condensed-phase velocity vector, speed of sound in gas-phase, and speed of sound in solid particles are given by Eqs. (7.46)- (7.52), respectively.

$$\tilde{\rho} = \frac{\sqrt{\rho_L \phi_L} \rho_L + \sqrt{\rho_R \phi_R} \rho_R}{\sqrt{\rho_L \phi_L} + \sqrt{\rho_R \phi_R}} \quad (\text{Eq. 7.46})$$

$$\tilde{\mathbf{U}}_g = \frac{\sqrt{\rho_L \phi_L} \mathbf{U}_{g,L} + \sqrt{\rho_R \phi_R} \mathbf{U}_{g,R}}{\sqrt{\rho_L \phi_L} + \sqrt{\rho_R \phi_R}} \quad (\text{Eq. 7.47})$$

$$\tilde{H} = \frac{\sqrt{\rho_L \phi_L} H_L + \sqrt{\rho_R \phi_R} H_R}{\sqrt{\rho_L \phi_L} + \sqrt{\rho_R \phi_R}}, \text{ where } H \equiv e_t + P\phi \quad (\text{Eq. 7.48})$$

$$\tilde{\phi} = \frac{\sqrt{\rho_L \phi_L} \phi_L + \sqrt{\rho_R \phi_R} \phi_R}{\sqrt{\rho_L \phi_L} + \sqrt{\rho_R \phi_R}} \quad (\text{Eq. 7.49})$$

$$\tilde{\mathbf{U}}_p = \frac{\sqrt{\rho_L \phi_L} \mathbf{U}_{p,L} + \sqrt{\rho_R \phi_R} \mathbf{U}_{p,R}}{\sqrt{\rho_L \phi_L} + \sqrt{\rho_R \phi_R}} \frac{1}{\rho_p (1 - \tilde{\phi})} \quad (\text{Eq. 7.50})$$

$$\tilde{c}_g = \sqrt{\tilde{\gamma} (\tilde{H} - \frac{1}{2} \tilde{\mathbf{U}}_g \cdot \tilde{\mathbf{U}}_g)} \quad (\text{Eq. 7.51})$$

$$\tilde{c}_p = \frac{c_{ref} \phi_c}{\tilde{\phi}} \quad (\text{Eq. 7.52})$$

7.5 • Entropy condition and entropy fix

The admissible discontinuities in the weak solution of the linearized Riemann problem represented by the speed of such discontinuities S_i ; must obey two conditions, which are known as the Rankine-Hugoniot condition and entropy jump condition (also known as the Lax entropy condition). These are given by Eq. (7.53) and Eq. (7.54), respectively. (For details, please see Appendix E.)

$$\mathbf{F}(\mathbf{Q}_R) - \mathbf{F}(\mathbf{Q}_L) = S_i (\mathbf{Q}_R - \mathbf{Q}_L) \quad (\text{Eq. 7.53})$$

$$\lambda_i(\mathbf{Q}_L) > S_i > \lambda_i(\mathbf{Q}_R) \quad (\text{Eq. 7.54})$$

Roe-Pike method utilizes the weak solution of linearized Riemann problem at the boundary of each cell. These Riemann solutions consist of discontinuous jumps only, which are a good approximation for contact discontinuities and shocks, in that the discontinuous character of the wave is correct, although the size of the jump may not be correctly approximated by the linearized solution. Rarefaction waves, on the other hand, carry a continuous change in flow variables, and as time increases, they tend to spread; that is spatial gradients tend to decay. Quite clearly then, the linearized approximation via discontinuous jumps is grossly incorrect. In a practical computational set up however, it is only in the case in which the rarefaction wave is transonic or sonic where linearized approximations encounter difficulties; these show up in the form of unphysical, entropy violating discontinuous waves, sometimes called rarefaction shocks. Presence of rarefaction shock violates the Lax entropy condition in the Roe-Pike technique. Roe's solver can be modified so as to avoid entropy violating solutions. This is usually referred to as entropy fix. Harten and Hyman [25] suggested an entropy fix for Roe's method, which has widespread use. Other ways of correcting the scheme have been discussed by Roe and Pike [66], Roe [60], Sweby [73], and Dubois and Mehlman [13], amongst others. A Harten-Hyman entropy fix was utilized to make the solution admissible.

7.6 Flux limiter

The Roe-Pike scheme described so far is first order accurate scheme. A higher order scheme could give higher resolution to the discontinuities but it also exhibits spurious oscillations around discontinuities. The problem of spurious oscillations in the vicinity of high gradients is depicted in the sketch of Fig. 7-4 , where the full line denotes the exact solution and the dotted line denotes the numerical solution obtained by some linear method of second or higher order of accuracy [71]. Different methods produce different patterns for the oscillatory profile. For example, the Lax-Wendroff method (second order accurate) will produce spurious oscillations behind the wave, whereas the Warming-Beam method (second order accurate) will produce spurious oscillations ahead of the wave. This is related to the form of the leading term in the local truncation error of the method.

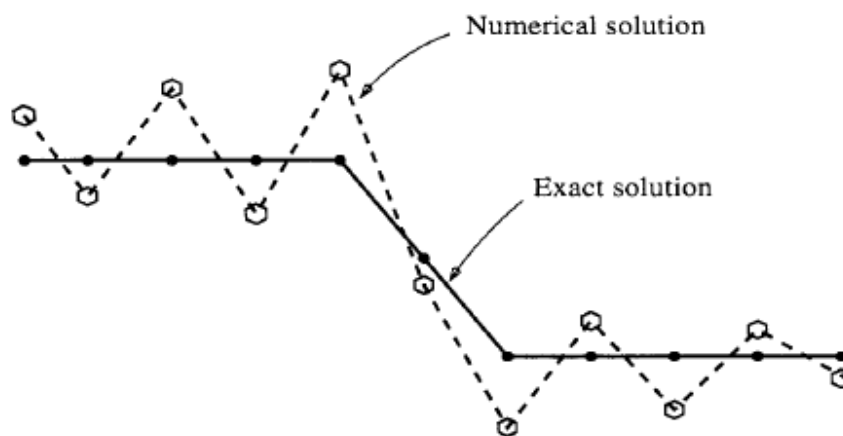


Figure 7-4: Illustration of the numerical phenomenon of spurious oscillations near high gradients [71].

Thus, a middle ground to retain the stability of the solution (known as total variation diminishing or TVD) and get higher resolution was proposed by Harten [25] by using flux limiters with the first order scheme. This is obtained by replacing the right eigenvectors by a corrected right eigenvectors as shown in Eq. (7.55):

$$\tilde{\mathbf{K}}_i^p = \Phi(\theta_i^p) \mathbf{K}_i^p \quad (\text{Eq. 7.55})$$

The term θ_i^p is a measure of the smoothness of the solution. It is determined by considering the ratio of wave strengths α_p in upwind direction as shown in Eq. (7.56):

$$\theta_i^p = \begin{cases} \alpha_{i-1}^p / \alpha_i^p & \lambda_p > 0 \\ \alpha_{i+1}^p / \alpha_i^p & \lambda_p < 0 \end{cases} \quad (\text{Eq. 7.56})$$

van Leer [76] [77] derived a scheme using a flux limiter in his search for the ultimate conservative difference scheme, and Roe [62] utilized flux limiting in his original monotonicity preserving second order scheme. Chakravarthy and Osher [7] have used limiters, as has Harten [24] who also introduced the notion of TVD (total variation diminishing) to characterize oscillation free schemes. In this work, the flux limiter proposed by van Leer was used. The van Leer flux limiter is determined by Eq. (7.57):

$$\Phi(\theta) = \frac{\theta + |\theta|}{1 + \theta} \quad (\text{Eq. 7.57})$$

7.7 Higher order correction

The numerical scheme described above is only first order accurate in space. In order to increase the order of accuracy, second order correction terms were introduced as shown by Eq. (7.58):

$$\bar{\mathbf{Q}} = \mathbf{Q} - \left(\frac{\Delta t}{\Delta x} \mathbf{A} \Delta_x \mathbf{Q} + \frac{\Delta t}{\Delta y} \mathbf{B} \Delta_y \mathbf{Q} + \frac{\Delta t}{\Delta z} \mathbf{C} \Delta_z \mathbf{Q} \right) - \underbrace{\left(\frac{\Delta t}{\Delta x} \Delta \tilde{\mathbf{F}} + \frac{\Delta t}{\Delta y} \Delta \tilde{\mathbf{G}} + \frac{\Delta t}{\Delta z} \Delta \tilde{\mathbf{H}} \right)}_{\text{Second order correction}} \quad (\text{Eq. 7.58})$$

The second order correction term for the x-direction is given by Eq. (7.59). The second order correction terms for the other two coordinate directions follow the same principle and they are shown in Eq. (7.60) for y-direction and in Eq. (7.61) for z-direction. The indices i, j, and k represent x-direction, y-direction, and z-direction respectively.

$$\begin{aligned} \Delta \tilde{\mathbf{F}} &= \mathbf{F}_{i+1} - \mathbf{F}_i \\ \text{where, } \mathbf{F}_i &= \frac{1}{2} \sum_{p=1}^9 |\lambda_p| \left(1 - |\lambda_p| \left(\frac{\Delta t}{\Delta x} \right)_{ave} \right) \alpha_p \mathbf{K}_i^p \\ \text{and } \left(\frac{\Delta t}{\Delta x} \right)_{ave} &= \frac{1}{2} \left(\frac{\Delta t}{\Delta x_{i-1}} + \frac{\Delta t}{\Delta x_i} \right) \end{aligned} \quad (\text{Eq. 7.59})$$

$$\begin{aligned} \Delta \tilde{\mathbf{G}} &= \mathbf{G}_{j+1} - \mathbf{G}_j \\ \text{where, } \mathbf{G}_j &= \frac{1}{2} \sum_{p=1}^9 |\lambda_p| \left(1 - |\lambda_p| \left(\frac{\Delta t}{\Delta y} \right)_{ave} \right) \alpha_p \mathbf{K}_j^p \\ \text{and } \left(\frac{\Delta t}{\Delta y} \right)_{ave} &= \frac{1}{2} \left(\frac{\Delta t}{\Delta y_{j-1}} + \frac{\Delta t}{\Delta y_j} \right) \end{aligned} \quad (\text{Eq. 7.60})$$

$$\begin{aligned} \Delta \tilde{\mathbf{H}} &= \mathbf{H}_{k+1} - \mathbf{H}_k \\ \text{where, } \mathbf{H}_k &= \frac{1}{2} \sum_{p=1}^9 |\lambda_p| \left(1 - |\lambda_p| \left(\frac{\Delta t}{\Delta z} \right)_{ave} \right) \alpha_p \mathbf{K}_k^p \\ \text{and } \left(\frac{\Delta t}{\Delta z} \right)_{ave} &= \frac{1}{2} \left(\frac{\Delta t}{\Delta z_{k-1}} + \frac{\Delta t}{\Delta z_k} \right) \end{aligned} \quad (\text{Eq. 7.61})$$

7.8 Three dimensional wave propagation

A common approach when solving multi-dimensional hyperbolic problems is to use a dimensional splitting method suggested by Gudonov [17]. This means that the three

dimensional conservation equations are divided into three initial value boundary problems with each problem representing one direction. At a time step n , the one-dimensional approach is used in each of the three dimensions sequentially. For instance, first the IVBP is solved in x-direction. This step is called the x-sweep. The solution obtained from this first step is used as an initial condition for the next step in y-direction or y-sweep. Then the solution of the second step is used as the initial condition for the final step in z-direction or the z-sweep. This process is demonstrated by Eq. (7.62). The above algorithm is very popular because it produces good results and it is very simple. Basically, any one-dimensional Riemann solver can be easily extended to the multi-dimensional case by using this approach. However, this method only allows flow of fluxes in the three coordinate directions, which means that the discontinuities traveling in directions oblique to the grid orientation will have more smearing than those traveling along the coordinate directions. The implementation of complex boundary conditions may also be complicated using this strategy. Therefore, another approach was utilized that does not require dimensional splitting. Such methods are known as the unsplit methods.

$$\begin{aligned}
&\text{PDE: } \frac{\partial \mathbf{Q}}{\partial t} + \mathbf{A}(\mathbf{Q}) \frac{\partial \mathbf{Q}}{\partial x} + \mathbf{B}(\mathbf{Q}) \frac{\partial \mathbf{Q}}{\partial y} + \mathbf{C}(\mathbf{Q}) \frac{\partial \mathbf{Q}}{\partial z} = 0 \\
&\text{IC: } \mathbf{Q}(x, y, z, t^n) = \mathbf{Q}_0(x, y, z) \\
&\text{x-sweep} \\
&\text{PDE: } \frac{\partial \mathbf{Q}}{\partial t} + \mathbf{A}(\mathbf{Q}) \frac{\partial \mathbf{Q}}{\partial x} = 0 \\
&\text{IC: } \mathbf{Q}(x, y, z, t^n) = \mathbf{Q}_0(x, y, z) \\
&\text{Solution: } \mathbf{Q}^*(x, y, z) \\
&\text{y-sweep} \\
&\text{PDE: } \frac{\partial \mathbf{Q}}{\partial t} \mathbf{C}(\mathbf{Q}) \frac{\partial \mathbf{Q}}{\partial z} = 0 \tag{Eq. 7.62} \\
&\text{IC: } \mathbf{Q}(x, y, z, t^n) = \mathbf{Q}^*(x, y, z) \\
&\text{Solution: } \mathbf{Q}^{**}(x, y, z) \\
&\text{z-sweep} \\
&\text{PDE: } \frac{\partial \mathbf{Q}}{\partial t} + \mathbf{C}(\mathbf{Q}) \frac{\partial \mathbf{Q}}{\partial z} = 0 \\
&\text{IC: } \mathbf{Q}(x, y, z, t^n) = \mathbf{Q}^{**}(x, y, z) \\
&\text{Solution: } \mathbf{Q}(x, y, z, t^{n+1})
\end{aligned}$$

In unsplit methods, information is propagated in a multi-dimensional way. The unsplit scheme used in this work was first described in an unfinished form in [42]. As shown in Eq. (7.44), the flux term can be expressed in terms of wave strengths, eigenvalues, and right eigenvectors and as left-going and right-going parts. Since the flux terms act like increments to the variable vectors, they are also called the increment waves. The second order terms also have wave like expressions and thus, they are called the correction waves. The unsplit method used in this work, both the increment waves and correction waves are split into parts propagating in both the direction normal to the interface between two spatial locations and the transverse direction by solving Riemann problems in coordinate directions tangential to the interfaces.

This models cross-derivative terms necessary for obtaining both a stable and formally second order scheme. One-dimensional Riemann problems are solved at the interfaces. Limiter functions are applied to suppress spurious oscillations arising from second derivative terms. The scheme extends the approach used for two space-dimensions and the advection scheme for three-dimensional problems considered in [31].

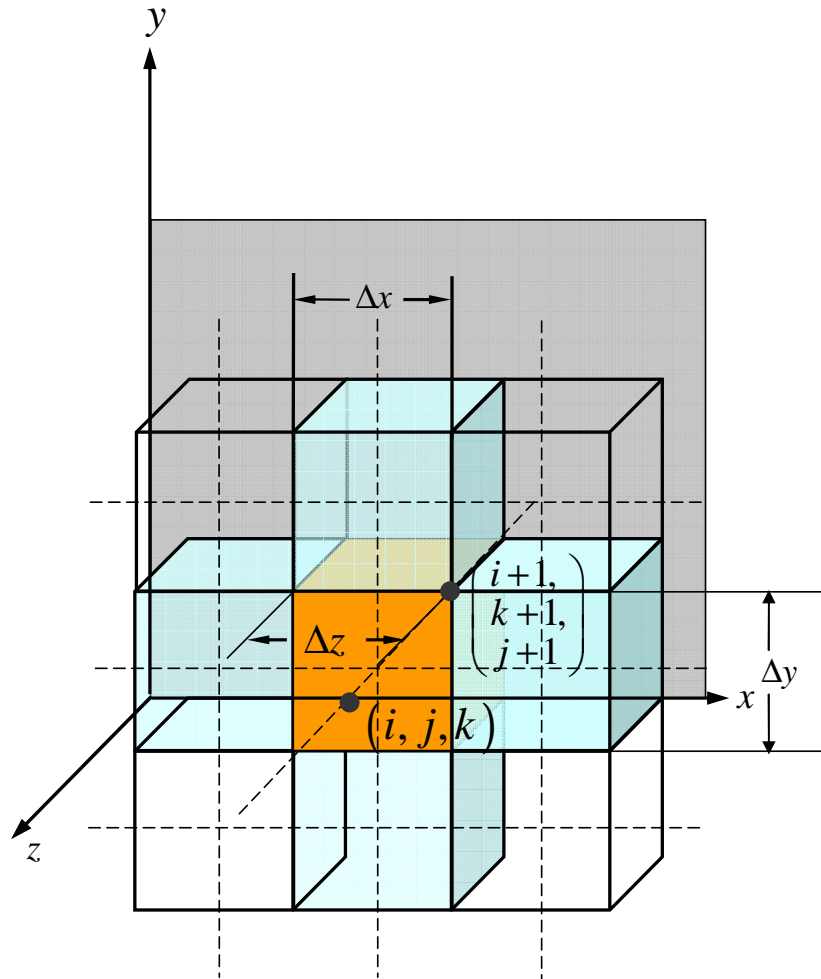


Figure 7-5: Discretization of a three-dimensional Cartesian domain into finite volumes of volume $\Delta x \Delta y \Delta z$.

7.9 Runge-Kutta method

The conservation equations in the mortar tube sub-model contain source terms. The general equation for the problem in the mortar tube sub-model is defined by Eq. (7.13). A split approach was used to handle the advection and source terms of this equation. With this approach, the Eq. (7.13) was split into an advection problem and a source problem. The two-step procedure is shown by Eq. (7.63) and Eq. (7.64):

$$\left. \begin{array}{l} \text{PDE: } \frac{\partial \mathbf{Q}}{\partial t} + \frac{\partial \mathbf{F}(\mathbf{Q})}{\partial x} + \frac{\partial \mathbf{G}(\mathbf{Q})}{\partial y} + \frac{\partial \mathbf{H}(\mathbf{Q})}{\partial z} = 0 \\ \text{IC: } \mathbf{Q}(x, y, z, t^n) = \mathbf{Q}_0(x, y, z) \end{array} \right\} \Rightarrow \bar{\mathbf{Q}}(x, y, z, t^n) \quad (\text{Eq. 7.63})$$

$$\left. \begin{array}{l} \text{ODE: } \frac{D\mathbf{Q}}{Dt} = \Xi(\mathbf{Q}) \\ \text{IC: } \mathbf{Q}(x, y, z, t^n) = \bar{\mathbf{Q}}(x, y, z, t^n) \end{array} \right\} \Rightarrow \mathbf{Q}(x, y, z, t^{n+1}) \quad (\text{Eq. 7.64})$$

The advection part of the problem described by Eq. (7.63) was solved using the approximate Riemann solver. The solution obtained from this method was used as an initial condition for the second step in which the problem was defined as an ordinary differential equation (ODE). In order to integrate these source terms for solving the ODE described by Eq. (7.64), a fourth order and four-stage Runge-Kutta method was used. This is an explicit method and it is considered a very accurate method for solving ODEs. The four stages of the fourth order Runge-Kutta method are shown in Eq. (7.65)

$$\begin{aligned} \mathbf{S}_1 &= \Delta t \, \Xi(t^n, \mathbf{Q}^n) \\ \mathbf{S}_2 &= \Delta t \, \Xi\left(t^n + \frac{1}{2}\Delta t, \mathbf{Q}^n + \frac{1}{2}\mathbf{S}_1\right) \\ \mathbf{S}_3 &= \Delta t \, \Xi\left(t^n + \frac{1}{2}\Delta t, \mathbf{Q}^n + \frac{1}{2}\mathbf{S}_2\right) \\ \mathbf{S}_4 &= \Delta t \, \Xi\left(t^n + \Delta t, \mathbf{Q}^n + \mathbf{S}_3\right) \\ \mathbf{Q}^{n+1} &= \mathbf{Q}^n + \frac{1}{6}[\mathbf{S}_1 + 2\mathbf{S}_2 + 2\mathbf{S}_3 + \mathbf{S}_4] \end{aligned} \quad (\text{Eq. 7.65})$$

7.10 Boundary conditions

The boundary conditions were implemented by extending the computational grid. Two cells were used outside the physical domain in each dimension. These cells are known as the “ghost cells.” The ghost cells were assigned values at the beginning of each time step. Only one cell is needed outside the physical domain in order to compute the flux difference splitting, the right eigenvectors, and the associated eigenvalues. However, a flux limiter was used in this work and therefore an additional block of ghost cells were needed. The limiting is based on comparing waves from the same family emanating from neighboring cells. This comparison is done in the upwind direction. Hence, if the boundary condition models a general inflow situation, two ghost cells are needed outside the boundary. The reflective boundary conditions were used for all variables except gas-phase and condensed-phase velocities. For the gas-phase velocity and condensed-phase velocity, a wall boundary condition was used if it wasn’t specified otherwise.

7.11 Calculated results and discussions

The numerical method described above was used on the coupled mortar tube sub-model and the projectile dynamics sub-model. The calculations were performed in following order:

- Comparison with the exact solution of a Riemann problem: the numerical code was reduced to gas-phase only since the exact solution is known for that condition.

- Comparison of three-dimensional calculations with the experimental data (including pressure-time traces at multiple locations, projectile displacement, and muzzle velocity) obtained from instrumented mortar tube firings.

7.11.1 Exact solution versus calculated solution

A test problems for the one-dimensional, time dependent Euler equations for ideal gases with $\gamma = 1.4$; which has exact solutions. In all chosen tests, data consists of two constant states $\mathbf{Q}_L = \{\rho_L, U_L, P_L\}$ and $\mathbf{Q}_R = \{\rho_R, U_R, P_R\}$ separated by a discontinuity at an axial position $x = 2$. The states \mathbf{Q}_L and \mathbf{Q}_R are given in Table 7-1. The exact and numerical solutions were found in the spatial domain $0 < x < 5$. The numerical solution was computed with reflective boundaries and CFL number was close to 0.7. The comparisons of exact solution for density and velocity at time = 0.25 s with numerical results are shown in Fig. 7-6 and Fig. 7-7. The numerical results without flux limiter are also shown in these plots and the oscillatory behavior of numerical method without the flux limiter near discontinuity is clearly visible, which is smoothed out when a flux limiter is used. Also, the numerical results with flux limiter match very well with the exact solution of this Riemann problem.

Table 7-1: Data for test problem with exact solution for the time-dependent. one dimensional Euler equations

$\underline{\rho}_L$	\underline{U}_L	\underline{P}_L	$\underline{\rho}_R$	\underline{U}_R	\underline{P}_R
10	0	100	1.0	0	1.0

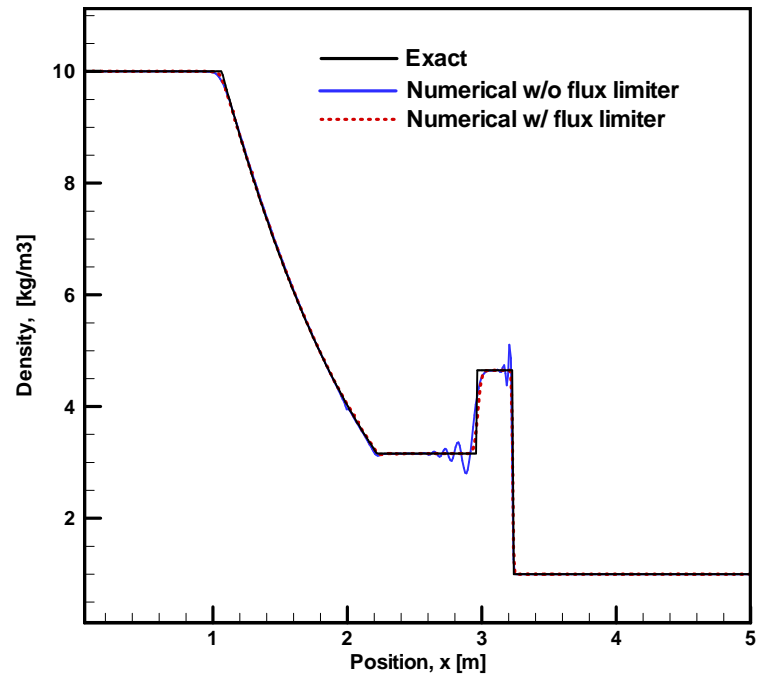


Figure 7-6: Comparison of exact density profile with calculated results at time 0.25 s.

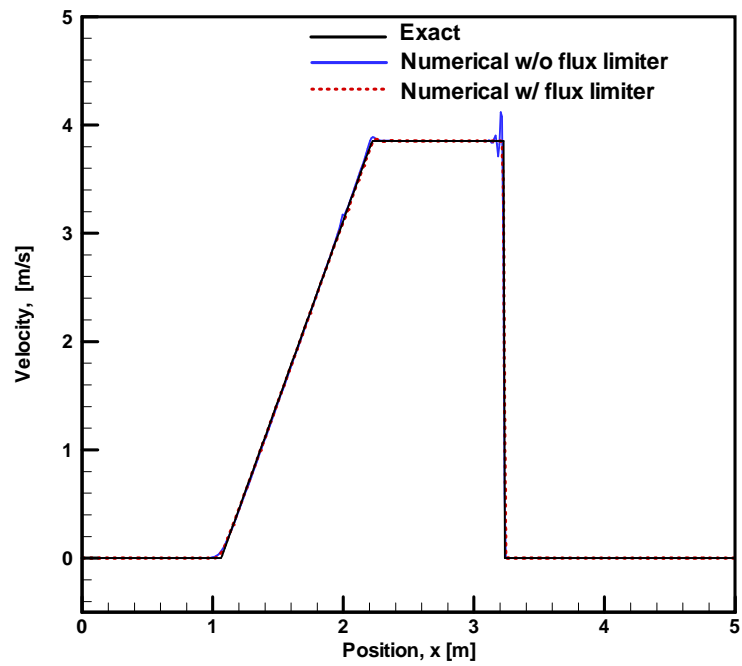


Figure 7-7: Comparison of exact velocity profile with calculated results at time 0.25 s.

7.11.2 Validation of calculated results by experimental data

The mortar tube is the outermost cylindrical portion of the 120mm mortar system, which has a fin-blade region, a vent-hole cylindrical region, and a projectile-payload region. The vent-hole region contains charge increments loaded with the M47 ball propellants. The number of charge increments can vary from 0 to 4. Thereafter, predicted results were obtained for the mortar tube with 0, 2, and 4 charge increments and results are validated with the experimental data for breech pressure from the instrumented mortar tube (IMS) test firings at Aberdeen Test Center (ATC). A total of 38 pressure transducers were installed along a 1.5 m long mortar tube at 6 different axial locations. The schematic of IMS test stand is shown in Fig. 7-8.

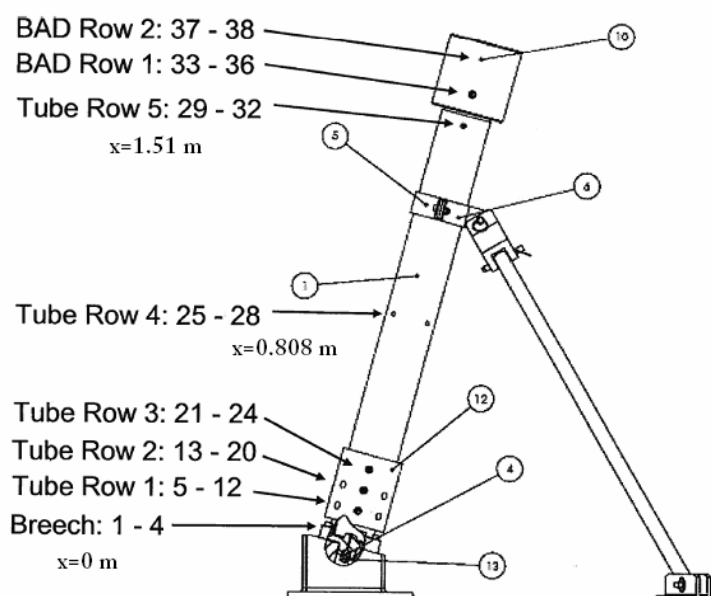


Figure 7-8: Schematic of instrumented mortar simulation and pressure transducer locations.

The three major axial locations are at 0, 8.08 m, and 1.5 m distance from the breech plug. The comparison of calculated and measured pressure-time traces as well as the projectile travel was made at these three axial locations. The pressure variations in the azimuthal directions were not significant.

The non-uniform axial variation of the discharging combustion products from tail-boom causes the sequential pressurization event in the mortar tube. The pressure-waves are generated and they propagate in both directions toward fin-blade region and projectile-payload region. These waves subside with the projectile motion as shown in $x-t$ diagrams for pressure, axial gas velocity, particle velocities, and porosity with 0 charge increments loading (see Figs. **7-9**-. **7-14**). The $x-t$ diagrams for porosity and particle velocity show the initial downward motion of propellant grains towards breech and later movement towards the projectile driven by the gas motion. The $x-t$ diagram for early-phase pressure variations are shown in Fig. **7-10**, which demonstrates strong compression and rarefaction waves in the mortar tube. The comparison of calculated breech pressure-time trace with the experimental data shows agreement in Fig. **7-15**. The predicted projectile trajectory and velocity are shown in Fig. **7-16**.

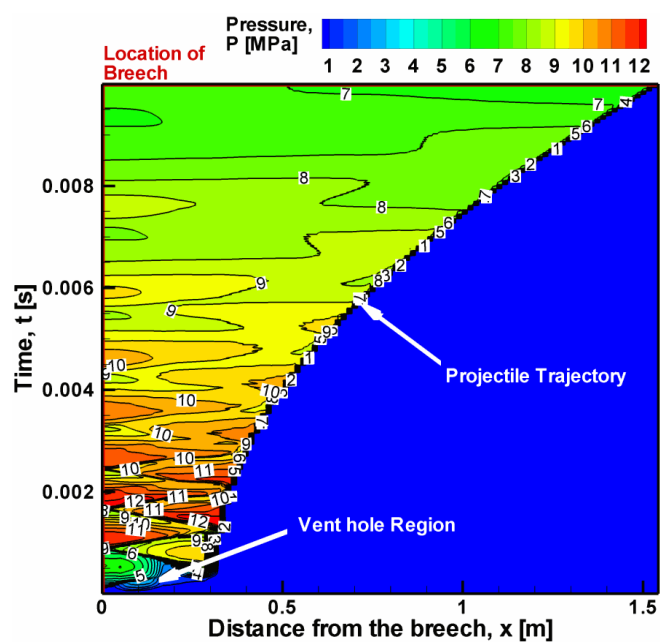


Figure 7-9: Calculated pressure variation in the mortar tube with projectile motion (with 0 charge increments).

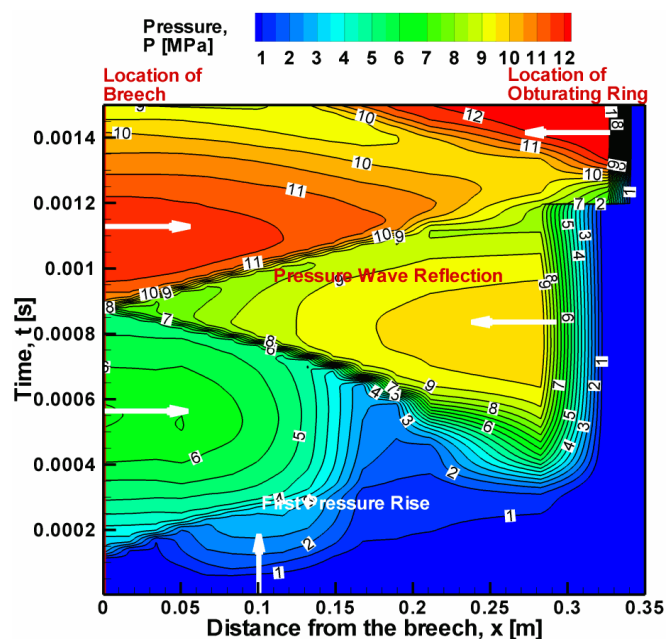


Figure 7-10: Early phase pressure wave phenomena in the mortar tube before projectile motion (with 0 charge increments).

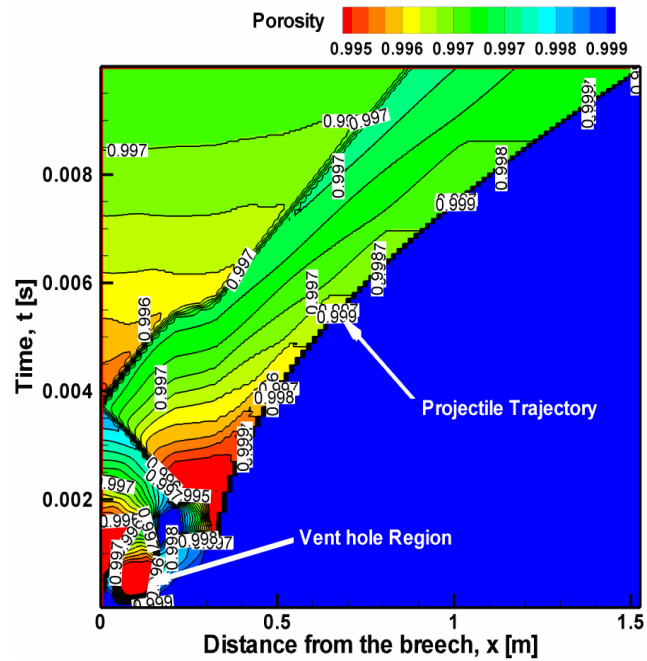


Figure 7-11: Calculated porosity variation in the mortar tube with projectile motion (with 0 charge increments).

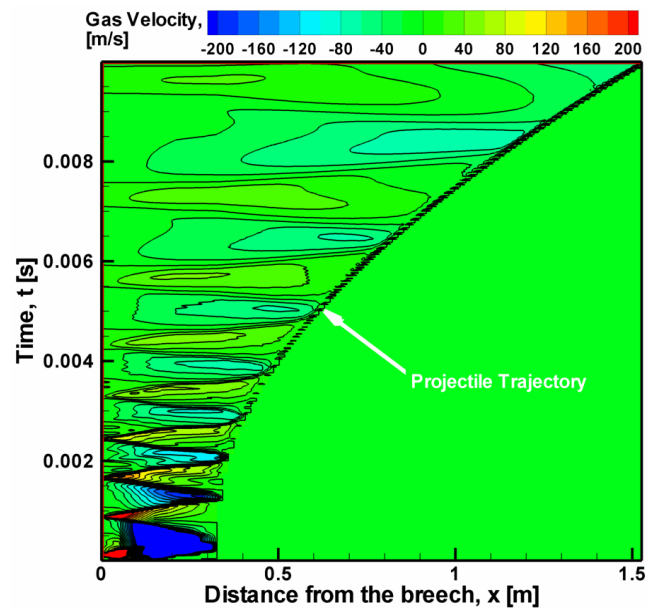


Figure 7-12: Calculated axial gas-velocity variation in the mortar tube with projectile motion (with 0 charge increments).

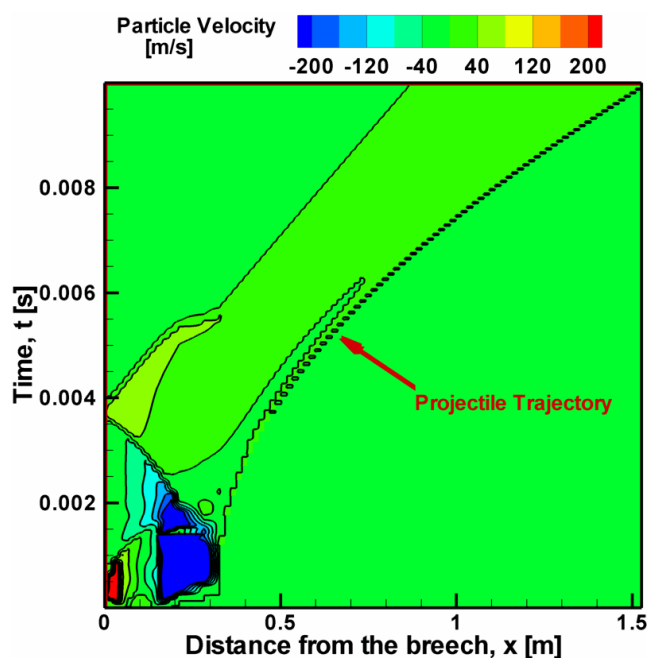


Figure 7-13: Calculated axial particle velocity variation in the mortar tube with projectile motion (with 0 charge increments).

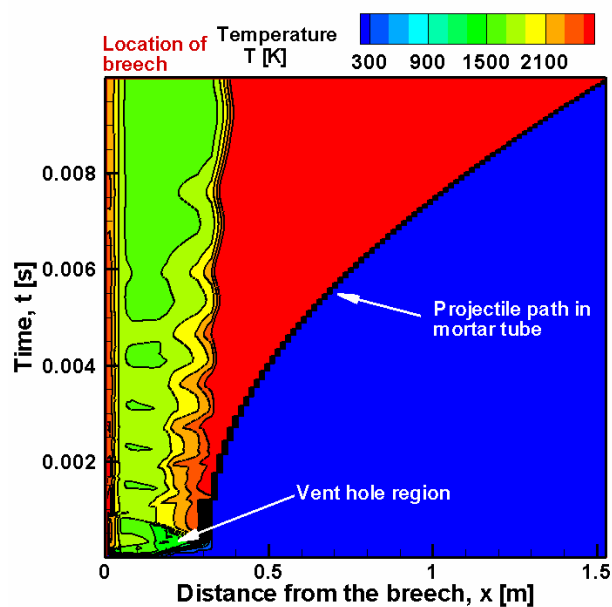


Figure 7-14: Calculated gas temperature variation in the mortar tube with projectile motion (with 0 charge increments).

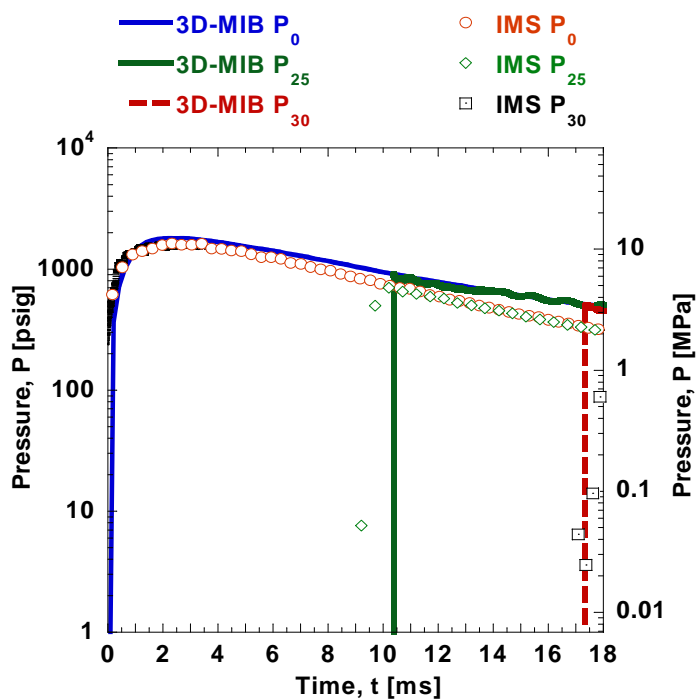


Figure 7-15: Comparison of 3D-MIB predictions for pressure-time traces at 3 port locations along the mortar tube with measured data.

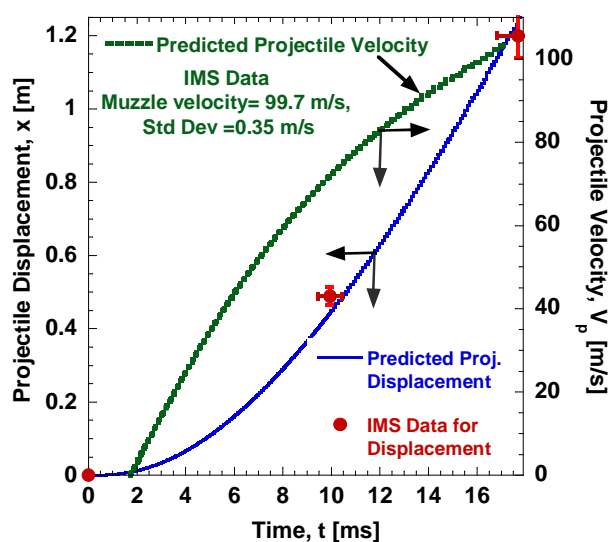


Figure 7-16: Comparison of 3D-MIB predictions for projectile dynamics with measured data for 0 charge increments loading

The detailed results for pressure, porosity, gas temperature, axial gas velocity, and axial particle velocity in the mortar tube with 2 charge increments are shown in Figs. **7-17- 7-22**. Like the 0 charge increments case, here also, the non-uniform axial variation of the discharging combustion products from tail-boom causes the sequential pressurization event in the mortar tube. The pressurization rate is higher due to additional M47 propellants. The $x-t$ diagrams for porosity (Fig. **7-19**) and the particle velocity (Fig. **7-22**) show the initial downward motion of propellant grains towards breech and later movement towards the projectile driven by the gas motion, which is similar to the case with no charge increments. These plots also show that the propellants burn quickly within the first 4 milliseconds of the ballistic event and the later phase phenomena contains only the gas-phase. The early-phase pressurization process in the mortar tube before the projectile motion is initiated is shown in Fig. **7-18**. This process shows similar behavior to the case with zero charge increments. The comparison of calculated pressure-time traces with the experimental data at three axial locations in the mortar tube is shown Fig. **7-23**. The calculated results show agreement with the measured data including the rise time at all three axial locations and magnitude of pressure. However, the pressure decay profile during the last few milliseconds shows some departure from the calculated pressure-time traces. This is believed to be due to a process called “blow-by”, which means that the obturating ring allows some gas leakage, resulting in faster pressure decay. This phenomenon depends on the manufacturing quality of the ring and is regarded as an experimental error. The calculated projectile velocity and displacement profiles show good agreement with the measurements as shown in Fig. **7-24**. Muzzle velocity is defined as projectile velocity at the end of the mortar tube.

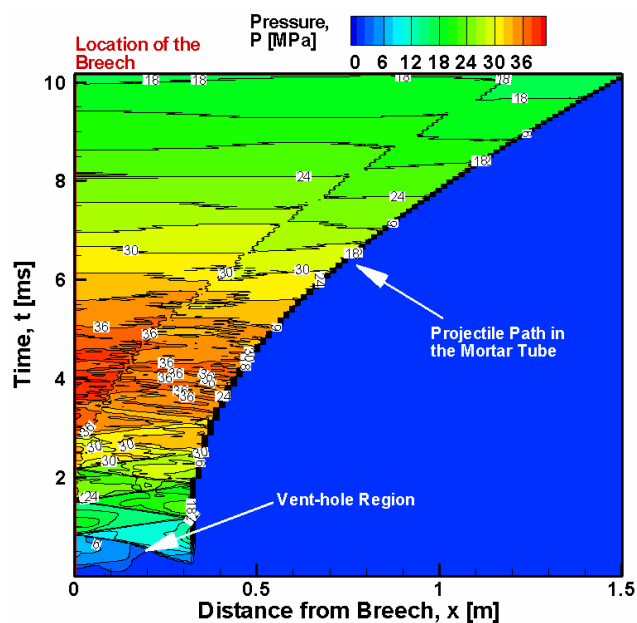


Figure 7-17: Calculated pressure variation in the mortar tube with projectile motion (with 2 charge increments).

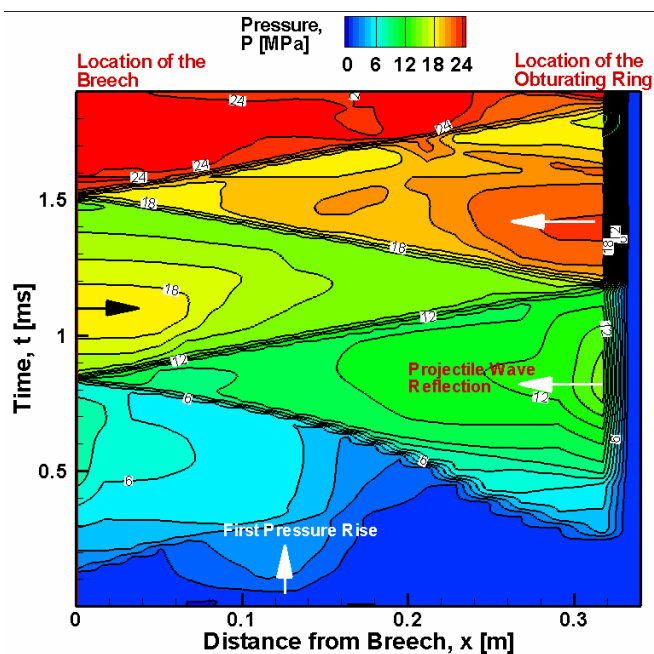


Figure 7-18: Early phase pressure wave phenomena in the mortar tube before projectile motion (with 2 charge increments).

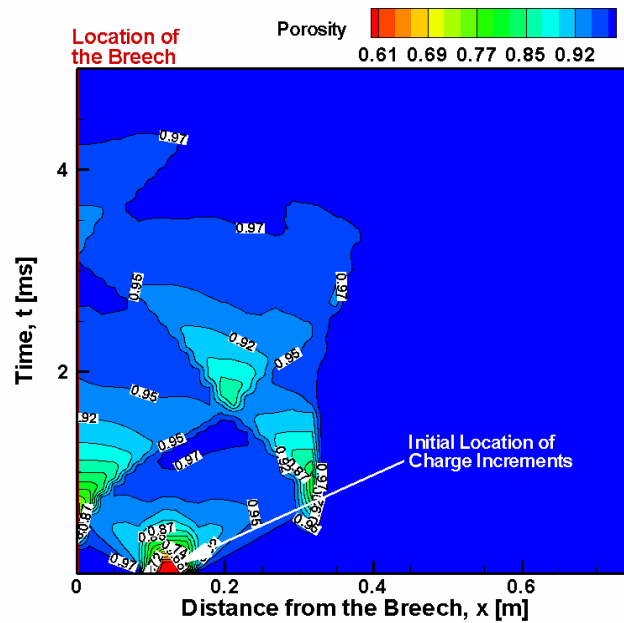


Figure 7-19: Calculated porosity variation in the mortar tube with projectile motion (with 2 charge increments).

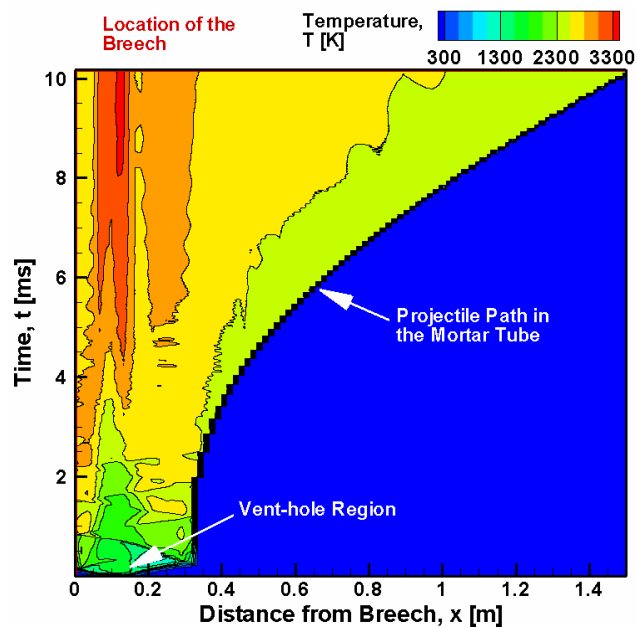


Figure 7-20: Calculated gas temperature variation in the mortar tube with projectile motion (with 2 charge increments).

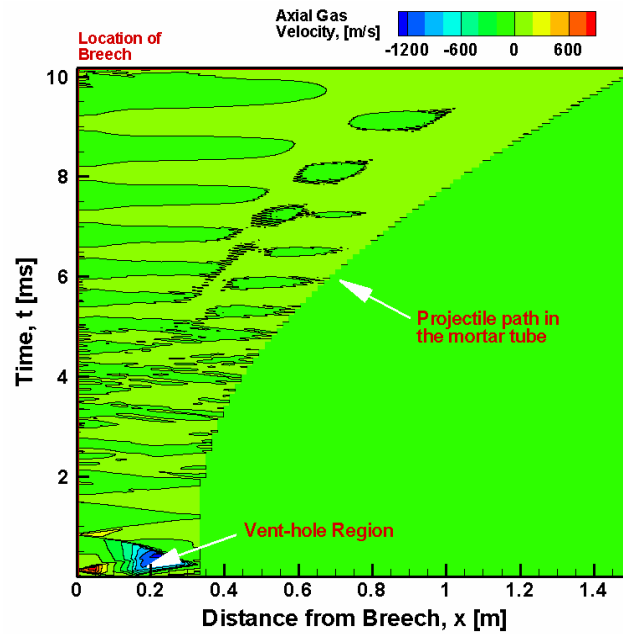


Figure 7-21: Calculated axial gas velocity variation in the mortar tube with projectile motion (with 2 charge increments).

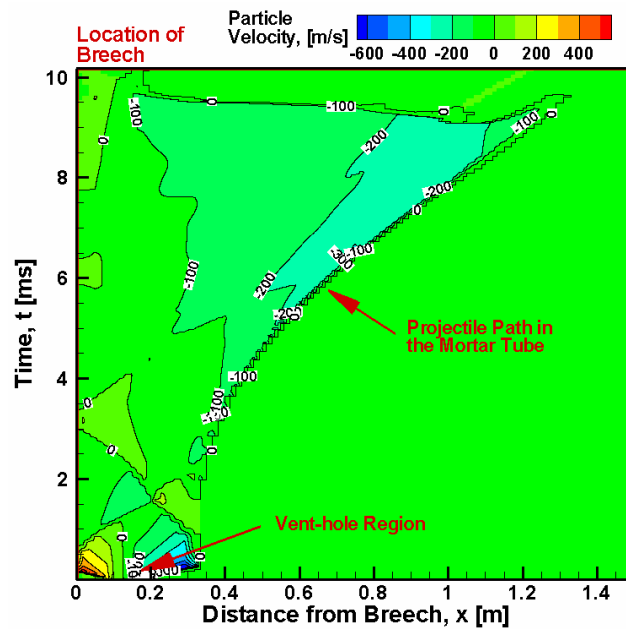


Figure 7-22: Calculated axial particle velocity variation in the mortar tube with projectile motion (with 2 charge increments).

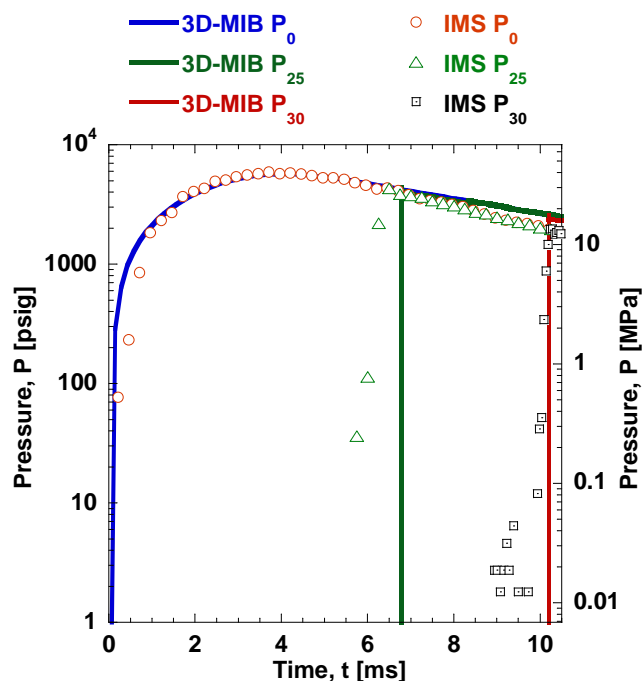


Figure 7-23: Comparison of 3D-MIB predictions for pressure-time traces at 3 port locations along the mortar tube with measured data for 2 charge increments loading.

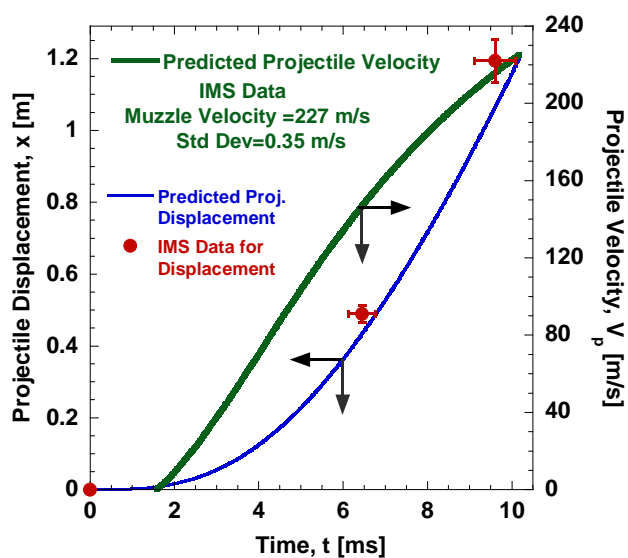


Figure 7-24: Comparison of 3D-MIB predictions for projectile dynamics with measured data for 2 charge increments loading.

The detailed results for pressure, porosity, gas temperature, axial gas velocity, and axial particle velocity in the mortar tube with 4 charge increments are shown in Figs **7-25**-. **7-30**. Like the 0 and 2 charge increments cases, once again, the pressure wave phenomena during the early phase of the ballistic even is visible. This process is also aided by the non-uniform axial distribution of M47 ball propellants in the mortar tube. The early-phase pressurization process in the mortar tube before the projectile motion is initiated is shown in Fig. **7-18**. The M47 ball propellants contained in the charge increments are initially located in the vent-hole region. The pressurization rate with 4 charge increments is higher than both 0 charge increments and 2 charge increments case due to additional M47 propellants. The $x-t$ diagrams for porosity (Fig. **7-27**) and the particle velocity (Fig. **7-30**) show the first the ball propellants move towards breech and later towards the projectile driven by the gas motion. These plots also show that the propellants burn even faster than the 2 charge increments case. This phenomenon is due to dependency of propellant burning rate on pressure. The mortar tube pressure with 4 charge increments is significantly higher than the 2 charge increments case.

The comparison of calculated pressure-time traces with the experimental data at three axial locations in the mortar tube is shown Fig. **7-31**. The calculated results show agreement with the measured data including the rise time at all three axial locations and magnitude of pressure. However, the pressure decay profile during the last few milliseconds shows some departure from the calculated pressure-time traces, which is similar to the earlier cases with 0 charge increments and 2 charge increments. The calculated projectile velocity and displacement profiles show good agreement with the measurements as shown in Fig. **7-32**.

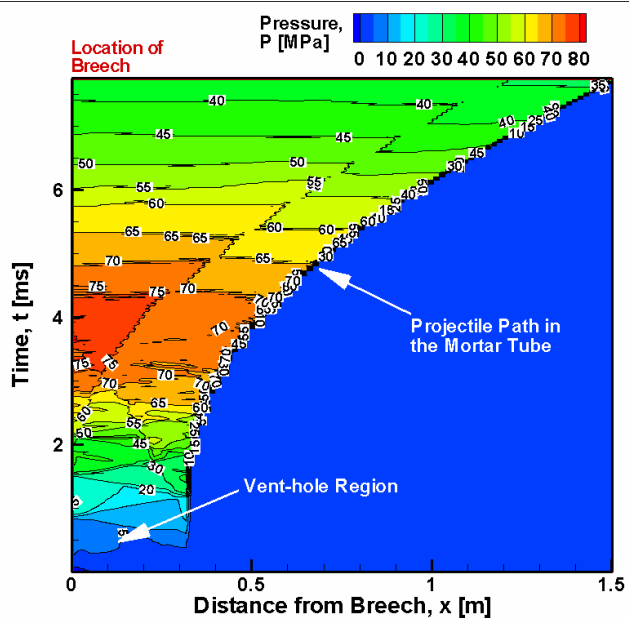


Figure 7-25: Calculated pressure variation in the mortar tube with projectile motion (with 4 charge increments).

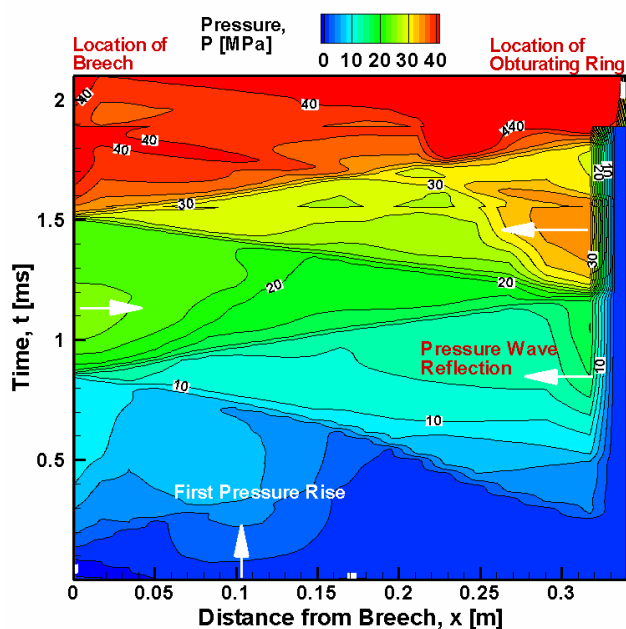


Figure 7-26: Early phase pressure wave phenomena in the mortar tube before projectile motion (with 4 charge increments).

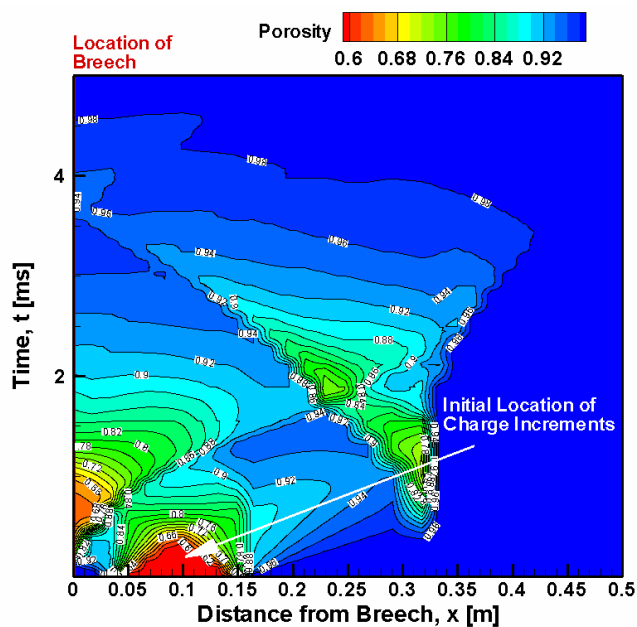


Figure 7-27: Calculated porosity variation in the mortar tube with projectile motion (with 4 charge increments).

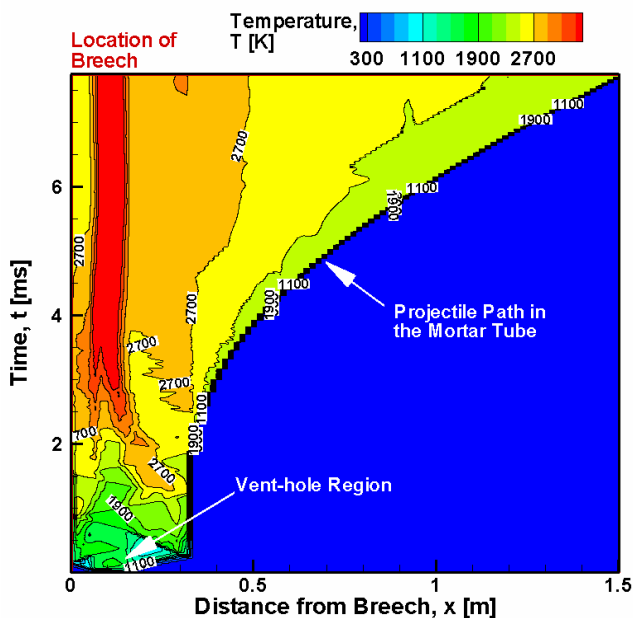


Figure 7-28: Calculated gas temperature variation in the mortar tube with projectile motion (with 4 charge increments).

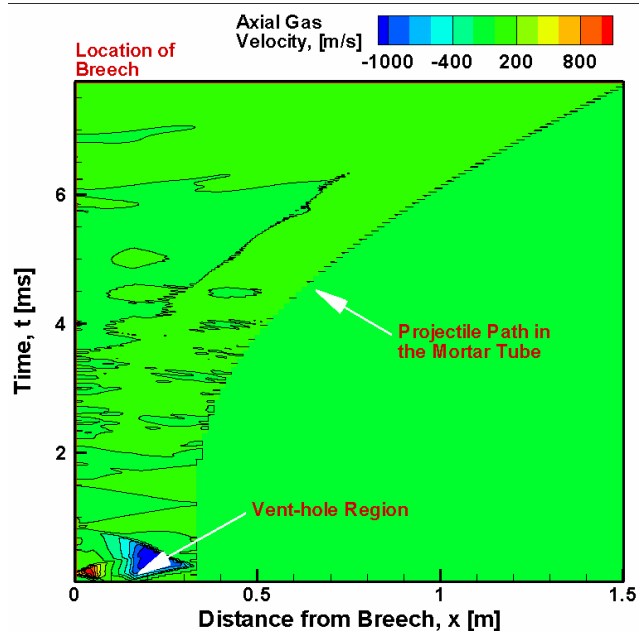


Figure 7-29: Calculated axial gas velocity variation in the mortar tube with projectile motion (with 4 charge increments).

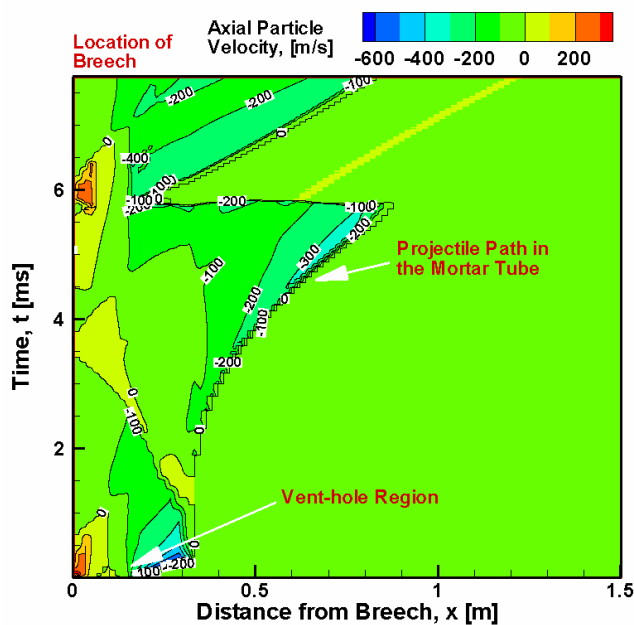


Figure 7-30: Calculated axial particle velocity variation in the mortar tube with projectile motion (with 4 charge increments).

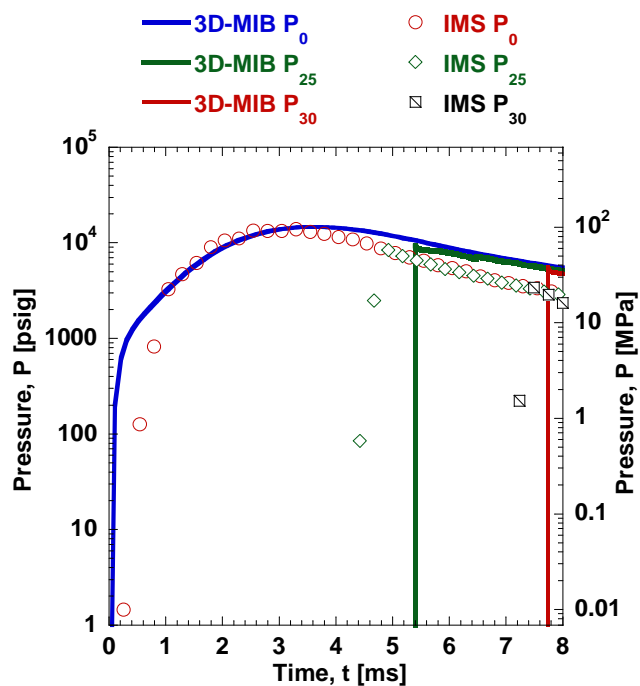


Figure 7-31: Comparison of 3D-MIB predictions for pressure-time traces at 3 port locations along the mortar tube with measured data for 4 charge increments loading.

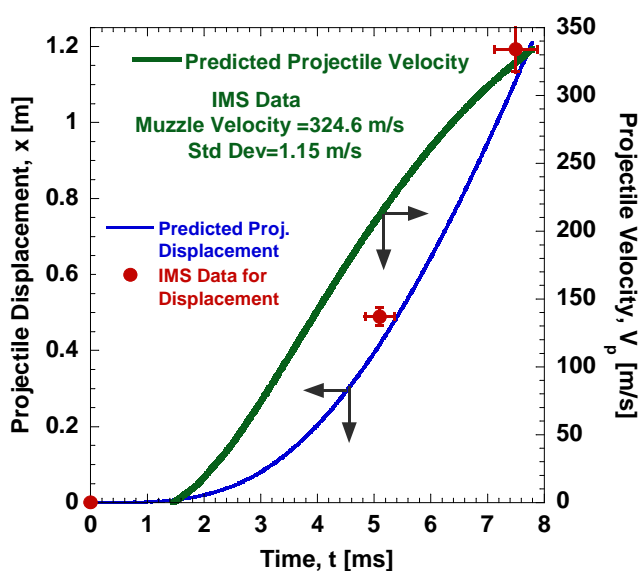


Figure 7-32: Comparison of 3D-MIB predictions for projectile dynamics with measured data for 4 charge increments loading.

7.12 Summary of mortar tube sub-model simulation

The simulation of flow field in mortar tube with a moving projectile is a complex problem. The flow is three dimensional, compressible, two-phase, and the physical domain expands due to projectile motion. The initial porosity distribution is non-uniform depending on the number of charge increments loaded in the mortar tube. In addition, the ignition of ball propellants in the mortar tube is strongly coupled with the discharging of hot combustion products from the ignition cartridge. Due to these reasons, the finite element solver described in chapter 6 could not make very accurate predictions of wave propagation velocities. The approximate Riemann solvers are known to work very well for the gas-phase compressible flows. The results presented in this chapter show that these solvers can be successfully applied to the two-phase flows with the modifications shown in this work. A comparison of 3D-MIB predictions for muzzle velocities with the IMS data is shown in Table 7-2.

Table 7-2: Comparison of 3D-MIB calculations for the muzzle velocity with the IMS data

<u>Muzzle velocity [m/s]</u>	<u>3D-MIB calculations</u>	<u>IMS data</u>
Charge 0	103.2	99.7±0.35
Charge 2	225.2	227±0.35
Charge 4	332.6	324.6±1.15

Although the comparison seems extremely close, the difference can be further improved by addition certain empirical relations (i.e., blow-by phenomena, friction on the obturating ring) in the 3D-MIB model and code.

Chapter 8

CONCLUSIONS AND FUTURE WORK

In this work, the development and validation of a three dimensional mortar interior ballistic code (3D-MIB) for prediction of two-phase interior ballistic processes in the 120mm mortar system was achieved. A stepwise approach was adopted to solve the various processes in the system and three separate but inter-linked sub-models were developed. The granular bed combustion sub-model is transient quasi one-dimensional. Six coupled quasi-linear inhomogeneous hyperbolic partial differential equations (PDEs) were solved by using the method of characteristics (MOC) approach. The presence of pressure waves was found in the ignition cartridge and based on the analysis of this sub-model; it was determined to be the non-uniform discharge of mass and energy of the combustion products from the vent holes of the flash tube.

Based on this analysis, it was found that this pressure-wave phenomenon depends strongly upon the hierarchy and magnitudes of mass discharge rates of hot combustion products exiting through the 20 circular vent holes on the flash tube, which varied significantly along axial direction even though the vent-holes were distributed evenly. The highly non-uniform discharge of combustion products from the flash tube into the granular bed is believed to be the main reason for generating strong pressure waves in the existing 120mm ignition cartridge. The vent-hole pattern on the flash tube was systematically modified to achieve a more uniform discharge of igniter products into the granular bed. Numerical results showed that significant reduction in axial pressure

gradients can be obtained by modifying the flash tube vent-hole sizes such that the igniter products are discharged more evenly at various axial locations in the granular bed. The reduction of the axial pressure gradient in the ignition cartridge can improve the reliability and reproducibility of the 120mm mortar propulsion system. In addition, it was also noted that the black powder produces highly non-repeatable pressure-time traces and a substitute called moisture resistant black powder (MRBPS) was sought to remedy this problem. The ignition cartridge sub-model was also utilized to compute the interior ballistics of the M1020 ignition cartridge with MRBPS as an igniter material and the results were compared with the experimental data. The comparison of two pyrotechnic materials also facilitates model validation and increases the robustness of the code.

Two different numerical approaches were adopted for solving the mortar tube sub-model, i.e., a finite-element method based Leap Frog Taylor-Galerkin (LFTG) approach and an approximate Riemann solver approach. It is common to use a finite volume based numerical approach to solve compressible flow problems. The numerical code based on Finite element method showed strong promise for application in two-phase and multi-phase problems such as one discussed in this work. However, presence of discontinuities is a major stumbling block in application of such methods. In order to resolve these issues, the second approach was later adopted to solve the mortar tube sub-model. Approximate Riemann solver such as Roe-Pike method with Rankine-Hugoniot conditions, flux limiters, and second order corrections worked successfully for this problem. It was shown that such approach can be applied to two-phase problems with modified equations presented in this work.

8.1 Major contributions

There is only a limited body of work available in the development of interior ballistic codes as noted in the literature review section of this work. NGEN3 developed by Army Research Laboratory is the only major code available for numerical simulation of interior ballistic processes. The NGEN3 code is based on an Eulerian/Lagrangian approach and is extremely comprehensive. The work done here for the development of the 3D-MIB code offers an alternative approach in the area of interior ballistic simulation. This code is also very comprehensive; however, it offers a very different approach for simulation of interior ballistic processes in the 120mm mortar system.

The overall 3D-MIB code has been designed to have many independent subprograms for each physical component of the mortar system. Each subprogram was validated by specially designed experiments. This approach is effective since some subsystems can be tested and simulated easily. The modular design of 3D-MIB code enables the users to apply the code without any major modification when one or more physical components are upgraded or changed in their design. Stable and efficient numerical techniques have been adopted, which permit the code to be executed on a personal computer or single processor or a multiple processor machine with shared memory. The 3D-MIB code can also be used to provide the guidance for design and performance improvements of the mortar projectile.

- Effect of different primer material, flash tube geometry, pellet configurations, granular bed loading densities, vent-hole distributions can be studied as demonstrated by this work.

- The numerical code can be helpful to acquire deeper understanding of the ballistic processes of mortar systems.
- 3D-MIB code can provide predicted pressure-time traces and many other physical parameter variations at multiple axial locations. These physical parameter variations are useful for reducing the pressure wave phenomena during the interior ballistic cycle in the mortar firing.
- The knowledge gained from the simulation of these processes can help to reduce the possibilities for critical failures during operation in the field by better understanding the combustion process and the resulting peak pressures and pressure waves.
- The 3D-MIB code can also be used as an analytical tool for studying any abnormal behavior of the mortar projectile during operation. For example, the local region overpressure generated by aligning all charge increments in one orientation or the effect of out of spec flash holes.
- The numerical simulation with the code can be used to replace or reduce the need for expensive ballistic test firing throughout the lifecycle of the program.

Overall, the 3D-MIB code should be an extremely useful tool for advancing the state-of-the-art for both mortar and gun systems.

8.2 Future work

As mentioned in chapter 7, the predictions from 3D-MIB as it is show excellent comparisons with the experimental data for each of the three stages, i.e., flash tube, ignition cartridge, mortar tube, and projectile dynamics. However, there is still scope of improvements in this work. The major area of future work can be both experimental and numerical directions. Experimentally, a better understanding of flame spreading mechanism in the granular bed could enable the 3D-MIB code to provide more accurate information. Also, some physical processes like losses due to friction in ignition cartridge and mortar tube, blow-by phenomena are extremely hard to quantify. It would be helpful to gather some information in these areas.

Although, the robustness of the 3D-MIB code was tested to a certain extent by using the ignition cartridge sub-model for studying the effect of flash tube vent-hole pattern modification, there are wide range of applications where an interior ballistic code such as 3D-MIB can be applied. One such major area would be the 60mm mortar system and 81mm mortar systems. Another interesting area could be to further improve the finite-element approach for such problems, which has shown some promise for the interior ballistic applications as shown by the present work.

Bibliography

1. Andersson, K.E.B., "Pressure drop in ideal fluidization," *Chem. Eng. Sci.*, Vol. 15, 1961, pp. 276–297.
2. Asay, B.W., Son, S.F., and Bdzil, J.B., "The role of gas permeation in convective burning," *International Journal of Multiphase Flow*, Vol. 22, Issue 5, 1995, pp. 923–952.
3. Baer, M.R., Nunziato, J.W., and Embid, P. F., "*Deflagration-to-Detonation Transition in Reactive Granular Materials*," *Progress in Astronautics and Aeronautics Series*, Vol. 66, 1979, pp. 481–512.
4. Baer, M.R., and Nunziato, J.W., "A two-phase mixture theory for the deflagration-to-detonation transition (DDT) in reactive granular materials," *International Journal of Multiphase Flow*, Vol. 12, Issue 6, 1986, pp. 861–889.
5. Bdzil, J.B., Menikoff, R., Son, S.F., Kapila, A.K., and Stewart, D. S., "Two-phase modeling of deflagration-to-detonation transition in granular materials: A critical examination of modeling issues," *Phys. Fluids*, Vol. 11, Issue 2, 1999, pp. 378–402.
6. Boyer, J. E., Risha, G. A., and Kuo, K. K., "Characterization and analysis of percussion primers and a black powder initiation system," *Proceedings of 21st International Ballistics Symposium*, 2004, pp. 638–644.
7. Chakravarty, S.R. and Osher, S., "Numerical Experiments with the Osher Upwind Scheme for the Euler Equations," *AIAA Journal*, Vol. 21, No. 11, 1983, pp. 1241–1248.
8. Chandrapatula, T. R., and Belegundu, A. D., "Introduction to Finite Elements in Engineering," Second Edition, Prentice-Hall of India, New Delhi, 1999.
9. Courant, R., Isaacson, E., and Rees, M., "On the Solution of Nonlinear Hyperbolic Differential Equations by Finite Differences," *Comm. Pure. Appl. Math.*, Vol. 5, 1952, pp.243–255.
10. Denton, W. H., "General Discussion on Heat Transfer," *Institute of Mechanical Engineers and American Society of Mechanical Engineers*, London, 1951, pp. 370.

11. Donea, J., and Giuliani, S., "A Simple Method to Generate High-Order Accurate Convection Operators for Explicit Schemes Based on Linear Finite Elements," *International Journal of Numerical Methods in Fluids*, Vol. 1, 1981, pp. 63-79.
12. Donea, J., "A Taylor-Galerkin Method for Convective Transport Problem," *International Journal for Numerical Methods in Engineering*, Vol. 20, 1984, pp. 101-119.
13. Dubois, F., and Mehlman, G., "A Non-Parameterized Entropy Fix for Roe's Method," *AIAA Journal*, Vol. 31, Issue 1, 1993, pp.199-200.
14. Fromm, J. E., "A Method for Reducing Dispersion in Convective Difference Schemes," *J. Comput. Phys.*, Vol. 3, 1968, pp.176-189.
15. Godunov, S. K., "A Finite Difference Method for the Computation of Discontinuous Solutions of the Equations of Fluid Dynamics," *Mat. Sb.*, Vol. 47, 1959, pp.357-393.
16. Godunov, S. K., Zabrodin, A. V., and Prokopov, G. P., -. *J. Comp. Math. Phys. USSR*, Vol. 1, 1962, pp. 1187-1962.
17. Godunov, S. K., Numerical Solution of Multi-Dimensional Problems in Gas Dynamics, Nauka Press, Moscow, 1976.
18. Gough, P. S., "The XNOVAKTC Code Final report," Oct 1985-Mar 1985
19. Gough, P. S., and Zwarts, F. J., "Modeling Heterogeneous Two-Phase Reacting Flow," *AIAA Journal*, Vol. 17, No. 1, 1979, pp. 17-25.
20. Gough, P. S., "Modeling Two-Phase Flow in Guns," Interior Ballistics of Guns, Edited by H. Krier, American Institute of Aeronautics and Astronautics, New York, 1979.
21. Gough, P. S., "Formulation of a Next-Generation Interior Ballistic Code," ARL-CR-68; U.S. Army Research Laboratory: Aberdeen Proving Ground, MD, September 1993.
22. Gough, P. S., "Modeling Arbitrarily Packaged Multi-Increment Solid Propellant Charges of Various Propellant Configurations," Proceedings of the 33rd JANNAF Combustion Meeting, CPIA Publication 653, Vol. 1, 1996, pp 421-435.
23. Gough, P. S., "Interior Ballistics Modeling: Extensions to the XKTC Code and Analytical Studies of Pressure Gradient for Lumped Parameter Codes," ARL-CR-460; U.S. Army Research Laboratory: Aberdeen Proving Ground, MD, February 2001.

24. Harten, A., "High Resolution Schemes for Hyperbolic Conservation Laws," *J. Comput. Phys.*, Vol. 49, 1983, pp. 357-393.
25. Harten, A. and Hyman, J. M., "Self Adjusting Grid Methods for One-Dimensional Hyperbolic Conservation Laws," *J. Comput. Phys.*, Vol. 50, 1983, pp. 235-269.
26. Hirsch, C., *Numerical Computation of Internal and External Flows, Vol. I: Fundamentals of Numerical Discretization*. Wiley, 1988.
27. Hirsch, C., *Numerical Computation of Internal and External Flows, Vol. II: Computational Methods for Inviscid and Viscous Flows*. Wiley, 1990.
28. Horst, A. W., Keller, G. E., and Gough, P.S., "New directions in multiphase flow interior ballistic modeling," Technical Report BRL-TR-3102, Ballistics Research Laboratory, Aberdeen Proving Ground, MD, 1990.
29. Kuo, K. K. and Nydegger, C. C., "Flow Resistance Measurement and Correlation in Packed Beds of WC 870 Ball Propellants," *Journal of Ballistics*, Vol. 2, No.1, 1978, pp. 1-26.
30. Kuo, K. K., Moore, J. D., Boyer, J. E., Risha, G. A., Ferrara, P. J., Rand, R., and Travaille, J., "Characterization of the M1020 ignition cartridge under simulated mortar firing conditions," Proceedings of 21st International Ballistics Symposium, 2004, pp. 582-588.
31. Langseth, J. O., and LeVeque, R. J., "A wave-propagation method for three-dimensional hyperbolic conservation laws," *J. Comput. Phys.*, Vol. 165, 2000, pp.126-166.
32. Lax, P. D., "Weak Solutions of Nonlinear Hyperbolic Equations and Their Numerical Computation," *Comm. Pure. Appl. Math.*, Vol 11, 1954, pp.159-193.
33. Lax, P. D., and Wendroff, B., "Systems of Conservation Laws," *Comm. Pure. Appl. Math.*, Vol. 13, 1960, p. 217.
34. Lax, P. D., and Wendroff, B., "On the Stability of Difference Scheme" *Comm. Pure. Appl. Math.*, Vol. 15, 1962, p. 363.
35. Lax, P. D., and Wendroff, B., "Difference Schemes for Hyperbolic Equations with High Order of Accuracy," *Comm. Pure. Appl. Math.*, Vol. 17, 1964, p. 381.
36. Lax, P. D., "The Formation and Decay of Shock Waves," *American Mathematical Monthly*, Vol. 79, 1972, pp.227-241.
37. Lax, P. D., and Wendroff, B., "Systems of Conservation Laws," *Comm. Pure Appl. Math.*, Vol. 13, 1960, pp.217-237.

38. Lax, P. D., and Wendroff, B., "Difference Schemes for Hyperbolic Equations with High Order Accuracy," *Comm. Pure Appl. Math.*, Vol. XVII, 1964, pp.381-393.
39. Lenoir, J. M., and Robillard, G., "A Mathematical Method to Predict the Effects of Erosive Burning in Solid-Propellant Rockets," 6th International Symposium on Combustion, Reinhold, New York, 1957, pp. 663-667.
40. LeVeque, R. J., Numerical Methods for Conservation Laws. Birkhauser Verlag, 1992.
41. LeVeque, R. J., "Balancing Source Terms and Flux Gradients in High-Resolution Godunov Methods," *J. Comput. Phys.*, Vol. 146, 1998, pp.346-365.
42. LeVeque, R. J., "Wave propagation algorithms for multi-dimensional hyperbolic systems," *J. Comput. Phys.*, Vol. 131, 1997, pp. 327-353.
43. LeVeque, R. J., Mihalas, D., Dorfi, E. A., and Muller, E., Computational Methods for Astrophysical Flow, Springer-Verlag, 1998.
44. Lowe, C.A., and Clarke, J.F., "Aspects of solid propellant combustion," Philosophical Transactions of the Royal Society, Combustion Science Thematic Vol. 357, 1999, pp. 3639–3654.
45. Lowe, C.A., "Two-phase shock-tube problems and numerical methods of solution," *Journal of Computational Physics*, Vol. 204, 2005, pp. 598–632.
46. Miura, H., and Matsuo, A., "Numerical Simulation of Projectile Accelerator Using Solid Propellant," AIAA Paper No. 2006-1439, 2006.
47. Miura, H., and Matsuo, A., "Numerical Simulation of Solid Propellant Combustion in a Gun Chamber," AIAA Paper No. 2006-4955, July 2006.
48. Miura, H., Matsuo, A., and Nakamura, Y., "Interior Ballistics Simulation of Projectile Launch System Utilizing Tubular Solid Propellant," AIAA 2008-4972, July 2008.
49. Moore, J.D., Ferrara, P.J., and Kuo, K.K. (2007) Characterization of Combustion Processes in a Windowed Flash Tube of M1020 Ignition Cartridge for 120-mm Mortar System, Proceedings of the 23rd International Symposium on Ballistics, Tarragona, Spain, 16-20 April, 2007, F. Galvez and V. Sanchez-Galvez (eds.).
50. Moore, J.D., Acharya, R., Ferrara, P.J., and Kuo, K.K., "Characterization Combustion Processes and Different Vent-Hole Patterns in a Flash Tube of M1020 Ignition Cartridge for 120mm Mortar," presented at the 7-International

Symposium on Special Topics in Chemical Propulsion, Kyoto, Japan, September 8-11, 2007.

51. Nusca, M. J., "Application of the NGEN Interior Ballistics Code to the Modular Artillery Charge System," Proc. 34th JANNAF Combustion Meeting, CPIA Pub. 662, Vol. 3, Oct. 1997, pp. 247-263.
52. Nusca, M. J., and Gough, P. S., "Numerical Model of Multiphase Flows Applied to Solid Propellant Combustion in Gun Systems," AIAA Paper No. 1998-3695, July 1998.
53. Nusca, M. J., "Computational Fluid Dynamics Model of Multiphase Flows Applied to Solid Propellant Combustion in Gun Systems," Proceedings of the 18th International Symposium on Ballistics, San Antonio, TX, 1999, pp. 252-261.
54. Nusca, M. J., "Investigation of Ignition and Flame spreading Dynamics in the Modular Charge Artillery System Using the NGEN Multiphase CFD Code," Proc. of the 36th JANNAF Combustion Subcommittee Meeting, CPIA Pub. No.691, Vol. 3, October 1999, pp. 137-154.
55. Nusca, M. J., and Conroy, P. J., "Multiphase CFD Simulations of Solid Propellant Combustion in Gun Systems," AIAA Paper No. 2002-1091, January 2002.
56. Nusca, M. J., and Horst, A. W., "Progress in Multidimensional, Two-Phase Simulations of Notional Telescoped-Ammunition Propelling Charge," Proceedings of the 39th JANNAF Combustion Subcommittee Meeting, Colorado Springs, CO, CPIA Publication JSC CD-25, December 2003.
57. Oleinik, O. A., "Discontinuous solutions of non-linear differential equations," *UMN*, Vol. 12, Issue 3, 1957, pp. 3-73.
58. Roache, P. J., "Computational Fluid Dynamics," Hermosa Publishers, 1982.
59. Roe, P. L., "Approximate Riemann Solvers, Parameter Vectors, and Difference Schemes," *Journal of Computational Physics*, Vol. 43, 1981, pp. 357-372.
60. Roe, P. L., "Numerical Algorithms for the Linear Wave Equation," Technical Report 81047, Royal Aircraft Establishment, Bedford, UK, 1981
61. Roe, P. L., "Some Contributions to the Modeling of Discontinuous Flows," Proceedings of the SIAM/AMS Seminar, San Diego, 1983.
62. Roe, P. L., "Generalized Formulation of TVD Lax-Wendroff Schemes," Technical Report ICASE 84-53, NASA Langley Research Center, Hampton, US, 1984

63. Roe, P. L., "Discrete Models for the Numerical Analysis of Time-Dependent Multidimensional Gas Dynamics," *Journal of Computational Physics*, Vol. 63, 1986, pp. 458-476.
64. Roe, P. L., "Upwind Differencing Schemes for Hyperbolic Conservation Laws with Source Terms," Proc. First International Conference on Hyperbolic Problems, Edited by Carasso, Raviart and Serre, Springer, 1986, pp. 41-51.
65. Roe, P. L., "Sonic Flux Formulae," *SIAM J. Sei. Stat. Comput.*, Vol. 13, Issue 2, 1992, pp. 611-630.
66. Roe, P. L., and Pike, J., "Efficient Construction and Utilization of Approximate Riemann Solutions," *Computing Methods in Applied Science and Engineering*. North-Holland, 1984.
67. Rowe, P. N., and Claxton, K. T., "Heat and Mass Transfer from a Single Sphere to Fluid Flowing through an Array," *Trans. Instr. Chem. Engrs.*, Vol. 43, 1965, pp. 321-331.
68. Shapiro, A. H., "The Dynamics and Thermodynamics of Compressible Fluid Flow Volumes 1 and 2," The Ronald Press Company, New York, 1953.
69. Sod, G. A., *Numerical Methods in Fluid Dynamics*. Cambridge University Press, 1985.
70. Toro, E.F., "Riemann-problem based techniques for computing reactive two-phase flows," *Lecture Notes in Physics, Numerical combustion*, Dervieux, Larrouturou (Eds.) Vol. 351, Springer, Berlin, 1989.
71. Toro, E.F., "Riemann Solvers and Numerical Methods for Fluid Dynamics," First edition, Springer, Heidelberg, 1997.
72. Toro, E.F., and Billet, S. J., "A unified Riemann-problem-based extension of the Warming-Beam and Lax-Wendroff schemes," *IMA Journal of Numerical Analysis*, Vol. 17, Issue 1, 1997, pp. 61-102.
73. Sweby, P. K., "Shock Capturing Schemes," PhD thesis, Department of Mathematics, University of Reading, UK, 1982.
74. Toro, E.F., and Sviglia, A., "PRICE: Primitive centered schemes for hyperbolic systems," *International Journal for Numerical Methods in Fluids*, Vol. 42, 2003, pp. 1263-1291.
75. Trohanowsky, R., "120mm Mortar System Accuracy Analysis," International Infantry & Joint Services Small Arms Systems Annual Symposium, Exhibition & Firing Demonstration, May 17, 2005

76. van Leer, B., "Progress in Multi-Dimensional Upwind Differencing," Technical Report CR-189708/ICASE 92-43, NASA, Sept. 1992.
77. van Leer, B., Thomas, L., and Roe, P. L., "A Comparison of Numerical Flux Formulas for the Euler and Navier-Stokes Equations," AIAA 8th Computational Fluid Dynamics Conference, June 9-11, 1987, Honolulu, Hawaii, AIAA Paper No. 87-1104-CP.
78. Warming, R. F., Beam, R. M., and Hyett, B. J., "Diagonalization and Simultaneous Symmetrization of the Gas-Dynamic Matrices" *Math. Comp.*, Vol. 29, No. 132, 1975, pp. 1037-1045.

Appendix A

Formulation of Heat Equation for Ball Propellants

The ignition cartridge and mortar tube charge increments contain ball propellants. The ball propellants are assumed to be spherical in shape. The heat equation for a single spherical propellant particle is given by Eq. (A.1) in spherical coordinates as:

$$\frac{\partial}{\partial t}(\rho_p c_p T_p) = \frac{1}{r^2} \frac{\partial}{\partial r} \left(r^2 k_p \frac{\partial T_p}{\partial r} \right) \quad (\text{Eq. A.1})$$

In the above equation, ρ_p is the mass density of the ball propellants, c_p is the heat capacity of the ball propellants, k_p is the thermal conductivity of the ball propellants, and T_p is the temperature in the ball propellant as a function of radial coordinate r and time t . If the properties of ball propellants (ρ_p , c_p , and k_p) are independent of radius then Eq. (A.1) can be written as following:

$$\frac{\partial T_p}{\partial t} = \frac{\alpha_p}{r} \frac{\partial^2}{\partial r^2} (r T_p) \quad (\text{Eq. A.2})$$

In the above equation, α_p is the thermal diffusivity of ball propellants. The initial condition for Eq. (A.2) is given as following:

$$T_p(t=0, r) = T_{amb} \quad (\text{Eq. A.3})$$

The boundary conditions for Eq. (A.2) are given as following:

$$\frac{\partial T_p(t, 0)}{\partial r} = 0 \quad (\text{Eq. A.4})$$

$$\frac{\partial T_p(t, r_{p0})}{\partial r} = \frac{\dot{q}_{loss}''(t)|_s}{k_p} = Z(t) \quad (\text{Eq. A.5})$$

The heat flux loss from the propellant particle (\dot{q}_{loss}'') could be conductive if there is a coating of condensed-phase material on its outer surface. If that is the case (for example, some ball propellants in ignition cartridge), then the heat flux loss at the propellant surface is given by Eq. (A.6):

$$\dot{q}_{loss}''|_s = k_p \frac{\partial T_p}{\partial r} \Big|_{r=r_{p0}^-} = k_l \frac{\partial T_l}{\partial r} \Big|_{r=r_{p0}^+} = k_l \frac{(T_l - T_{ps})}{\delta_w} \quad (\text{Eq. A.6})$$

Here, k_l is the thermal conductivity of condensed phase, T_l is the temperature of liquid phase, T_{ps} is the temperature of the ball propellant at the outer surface, and δ_w is the minimum of thermal wave penetration depth in condensed phase and thickness of coating. If there is no condensed-phase coating on the ball propellant, then the heat flux loss is given by Eq. (A.7)

$$\dot{q}_{loss}''|_s = h_t (T - T_{ps}) \quad (\text{Eq. A.7})$$

In the above equation, h_t is the sum of convective and radiation heat transfer coefficient given by Eq. (A.8):

$$h_t = h_c + \varepsilon_p \sigma (T + T_{ps}) (T^2 + T_{ps}^2) \quad (\text{Eq. A.8})$$

The heat equation can be transformed into a Fourier heat equation by following transformation:

$$T_p^* \equiv T_p - T_0 \quad (\text{Eq. A.9})$$

where T_0 = ambient temperature. Substituting Eq. (A.9) in Eq. (A.1):

$$\frac{\partial T_p^*}{\partial t} = \frac{\alpha_p}{r} \frac{\partial^2}{\partial r^2} (r T_p^*) \quad (\text{Eq. A.10})$$

The initial condition for Eq. (A.2) is given as following:

$$T_p^*(t=0, r) = 0 \quad (\text{Eq. A.11})$$

The boundary conditions for Eq. (A.2) are given as following:

$$\frac{\partial T_p^*(t, 0)}{\partial r} = 0 \quad (\text{Eq. A.12})$$

$$\frac{\partial T_p^*(t, r_{p0})}{\partial r} = \frac{\dot{q}_{loss}''(t)|_s}{k_p} \quad (\text{Eq. A.13})$$

A function for T_p^* is proposed as following:

$$T_p^*(t, r) = \frac{c_0 + c_1 r + c_2 r^2 + c_3 r^3}{r} \quad (\text{Eq. A.14})$$

As the ball propellants are heated, a radial temperature profile is developed, which is known as thermal wave. Before the thermal wave penetrates to the centre of the sphere, these four constants can be determined by following four conditions:

$$\frac{\partial T_p^*(t, r_{p0} - \delta)}{\partial r} = 0 \quad (\text{Eq. A.15})$$

$$T_p^*(t, r_{p0} - \delta) = 0 \quad (\text{Eq. A.16})$$

$$\frac{\partial T_p^*(t, r_{p0})}{\partial r} = \frac{\dot{q}_{loss}''(t)}{k_p} = Z(t) \quad (\text{Eq. A.17})$$

$$\frac{\partial^2 T_p^*(t, r_{p0} - \delta)}{\partial r^2} = 0 \quad (\text{Eq. A.18})$$

In the above equations, δ is called the thermal wave thickness or wave penetration depth. The boundary condition specified by Eq. (A.18) is a smoothing condition that tends to make the temperature profile go smoothly into the initial temperature. Using the above conditions for solving Eq. (A.14), the expressions for constants used in the polynomial are as following:

$$c_0 = \frac{-r_\delta^3 r_{p0}^2 Z}{2r_{p0}^3 + r_\delta^3 - 3r_{p0}^2 r_\delta} \quad (\text{Eq. A.19})$$

$$c_1 = \frac{3r_\delta^2 r_{p0}^2 Z}{2r_{p0}^3 + r_\delta^3 - 3r_{p0}^2 r_\delta} \quad (\text{Eq. A.20})$$

$$c_2 = \frac{-3r_\delta r_{p0}^2 Z}{2r_{p0}^3 + r_\delta^3 - 3r_{p0}^2 r_\delta} \quad (\text{Eq. A.21})$$

$$c_3 = \frac{r_{p0}^2 Z}{2r_{p0}^3 + r_\delta^3 - 3r_{p0}^2 r_\delta} \quad (\text{Eq. A.22})$$

In the above equations, the term $r_\delta \equiv r_{p0} - \delta$. Substituting above in Eq. (A.14), following profile is obtained for temperature as a function of radial coordinate in the ball propellants:

$$T_p^* = \frac{r_{p0}^2 Z(t)}{(2r_{p0}^3 - 3r_{p0}^2 r_\delta + r_\delta^3)} \frac{(r - r_\delta)^3}{r} \quad \forall r > \delta \quad (\text{Eq. A.23})$$

Differentiating Eq. (A.23) with respect to r :

$$\frac{\partial T_p^*}{\partial r} = Z \frac{r_{p0}^2}{r} \frac{(2r + r_\delta)(r - r_\delta)^2}{(2r_{p0} + r_\delta)(r_{p0} - r_\delta)} \quad (\text{Eq. A.24})$$

$$\frac{\partial^2 T_p^*}{\partial r^2} = \frac{2r_{p0}^2 Z}{(2r_{p0}^3 - 3r_{p0}^2 r_\delta + r_\delta^3)} \frac{(r^2 - r_\delta^3)}{r^3} \quad (\text{Eq. A.25})$$

At $r = r_{p0}$, $T_p^* = T_{ps}^*$ and substituting this into Eq. (A.23):

$$T_{ps}^* = \frac{r_{p0}(r_{p0} - r_\delta)Z(t)}{(2r_{p0} + r_\delta)} \quad (\text{Eq. A.26})$$

By substituting r_δ by $r - \delta$ in Eq. (A.26), the analytical expression for the surface temperature is obtained as:

$$T_{ps}^* = \frac{r_{p0}\delta}{(3r_{p0} - \delta)}Z(t) \quad (\text{Eq. A.27})$$

The equation Eq. (A.27) expresses a relationship between the particle surface temperature and the wave penetration distance r_δ . As a result, there is really only one unknown (i.e., either T_{ps}^* or δ) in Eq. (A.27). This unknown can be obtained by integrating the heat balance equation Eq. (A.10).

Assuming that the thermal properties of propellant are constant and then integrating the heat equation between wave penetration distance and outer radius, we get the following form:

$$\int_{r_\delta}^{r_{p0}} r \frac{\partial T_p^*}{\partial t} dr = \alpha_p \int_{r_\delta}^{r_{p0}} \frac{\partial^2 (rT_p^*)}{\partial r^2} dr \quad (\text{Eq. A.28})$$

The RHS of Eq. (A.28) can be expressed as following:

$$\alpha_p \int_{r_\delta}^{r_{p0}} \frac{\partial^2 (rT_p^*)}{\partial r^2} dr = \alpha_p \left[\frac{\partial (rT_p^*)}{\partial r} \right]_{r_\delta}^{r_{p0}} = \alpha_p [T_{ps}^* + r_{p0}Z(t)] \quad (\text{Eq. A.29})$$

The LHS of Eq. (A.28) can be expressed as following:

$$\int_{r_\delta}^{r_{p0}} r \frac{\partial T_p^*}{\partial t} dr = \frac{r_{p0}^2}{4} \frac{d}{dt} \left[\frac{(r_{p0} - r_\delta)^2 Z(t)}{(2r_{p0} + r_\delta)} \right] \quad (\text{Eq. A.30})$$

After substituting Eq. (A.29) & Eq. (A.30) into Eq. (A.28), and some rearranging of terms, following integral equation is obtained:

$$\frac{(3r_{p0} - \delta)\delta^2 \frac{dZ}{dt} + (6r_{p0} - \delta)Z\delta \frac{d\delta}{dt}}{(3r_{p0} - \delta)^2} = \frac{4\alpha_{pr}}{r_{p0}^2} [T_{ps}^* + r_{p0}Z(t)] \quad (\text{Eq. A.31})$$

Differentiating Eq. (A.27) with respect to time, we get the following:

$$\frac{d\delta}{dt} = \frac{(3r_{p0} - \delta)^2}{3Zr_{p0}^2} \left[\frac{dT_{ps}^*}{dt} - \frac{r_{p0}\delta}{(3r_{p0} - \delta)} \frac{dZ}{dt} \right] \quad (\text{Eq. A.32})$$

Substituting Eq. (A.32) into Eq. (A.31) and by using the definitions of Z and T_{ps}^* , we finally get the following equation:

$$\frac{dT_{ps}}{dt} = \frac{\frac{12\alpha_{pr}}{\delta r_{p0}} [T_{ps} - T_0 + r_{p0}Z(t)] + \delta \frac{dZ}{dt}}{\frac{(6r_{p0} - \delta)}{r_{p0}}} \quad (\text{Eq. A.33})$$

The thermal wave penetration depth δ is obtained from Eq. (A.27) as following:

$$\delta = \frac{3r_{p0}(T_{ps} - T_0)}{(T_{ps} - T_0) + r_{p0}Z} \quad (\text{Eq. A.34})$$

Appendix B

Shape Functions

In a finite element model, the unknown variables within each element are interpolated by a linear distribution. This approximation becomes increasingly accurate as more elements are considered in the model. Shape functions have been introduced to implement this linear interpolation. If both the unknown variables (ρ , ϕ , u , v , w , T , and p) and the coordinates (r , θ , and z) are interpolated using the same shape function within the element, then it is called isoparametric formulation.

B.1 Master element

In two- and three-dimensional problems, the integrations required by the finite element method can become intractable if carried out in the physical (or global) coordinates, i.e., r , θ , and z . But since the method is an integral one, these calculations can instead be carried out in a local (or natural) coordinate system on the master element, where it is relatively easy to integrate. In fact, the concept of the master element is one of the keys for understanding the power of the finite element method, because it is possible to use this integral approach on problems with complex geometries by mapping the difficult actual physical geometry into a collection of well-arranged master elements. The master element also represents a "common denominator" for element calculations, so calculations common to a large number of elements can be performed once and for all at

the master element level, and the cost (or computational time) of these calculations can be decreased by the large number of elements found in the finite element mesh. Both of these characteristics enable the finite-element method to be used on a wide variety of difficult problems that would be intractable or excessively expensive by any other means.

Fig. **B-1** shows transformation of an actual element in the physical coordinate system(x_1 , x_2 , x_3 system) into a master element in the natural coordinate system (ξ , η , ζ system).

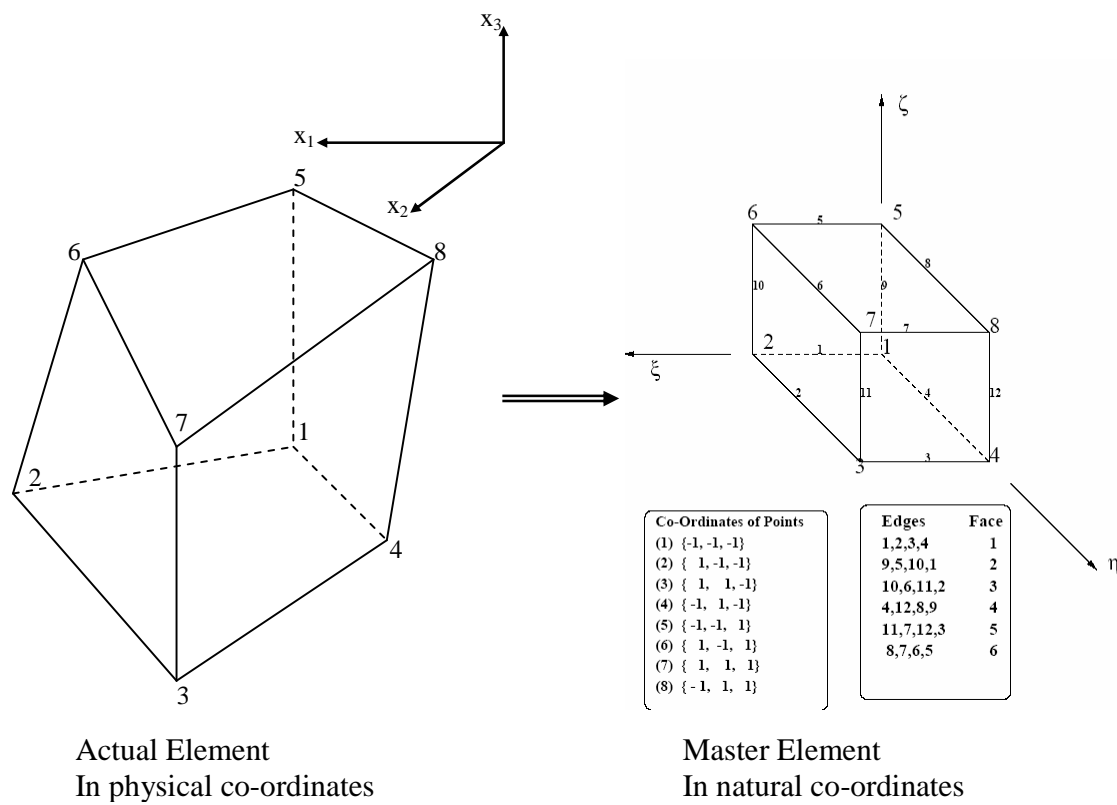


Figure **B-1**: Transformation of an actual element into a master element.

The transformation of physical coordinates (x_1, x_2, x_3) into natural coordinates (ξ, η, ζ) is also given by the shape functions that are used to interpolate other variables in the element. Therefore,

$$x_i(\xi, \eta, \zeta) = \sum_{m=1}^M N_m(\xi, \eta, \zeta) x_{n_i, m} \quad (\text{Eq. B.1})$$

Here, N_m is the nodal shape function and M is the number of nodes in n^{th} single element. For a 8-node hexahedral element, M is equal to 8. The shape function has the following property as demonstrated by Eq. (B.2):

$$N_m(\xi, \eta, \zeta) = \begin{cases} 1 & \text{at node } m \\ 0 & \text{at any node other than } m \end{cases} \quad (\text{Eq. B.2})$$

Taking the derivatives of x_i with respect to the natural (or local) co-ordinates, a Jacobian can be calculated as shown in Eq. (B.3):

$$J = \begin{bmatrix} \frac{\partial x_1}{\partial \xi} & \frac{\partial x_1}{\partial \eta} & \frac{\partial x_1}{\partial \zeta} \\ \frac{\partial x_2}{\partial \xi} & \frac{\partial x_2}{\partial \eta} & \frac{\partial x_2}{\partial \zeta} \\ \frac{\partial x_3}{\partial \xi} & \frac{\partial x_3}{\partial \eta} & \frac{\partial x_3}{\partial \zeta} \end{bmatrix} = \begin{bmatrix} \sum_{m=1}^M x_{n_1, m} \frac{\partial N_m}{\partial \xi} & \sum_{m=1}^M x_{n_1, m} \frac{\partial N_m}{\partial \eta} & \sum_{m=1}^M x_{n_1, m} \frac{\partial N_m}{\partial \zeta} \\ \sum_{m=1}^M x_{n_2, m} \frac{\partial N_m}{\partial \xi} & \sum_{m=1}^M x_{n_2, m} \frac{\partial N_m}{\partial \eta} & \sum_{m=1}^M x_{n_2, m} \frac{\partial N_m}{\partial \zeta} \\ \sum_{m=1}^M x_{n_3, m} \frac{\partial N_m}{\partial \xi} & \sum_{m=1}^M x_{n_3, m} \frac{\partial N_m}{\partial \eta} & \sum_{m=1}^M x_{n_3, m} \frac{\partial N_m}{\partial \zeta} \end{bmatrix} \quad (\text{Eq. B.3})$$

The above formulation is used in order to solve the finite element model. The elements of the Jacobian matrix given in Eq. (B.3) can be easily evaluated since the nodal coordinates are known, and the derivatives of the shape function are equally simple to calculate as described in next section.

B.2 Lagrange polynomials

Lagrange isoparametric elements are perhaps the most commonly used quadrilateral (2D) and hexahedral (3D) elements. Interpolation functions obtained using

the dependent unknown (not its derivatives) are Lagrange interpolation functions known as Lagrange polynomials. The one-dimensional linear element and the two-dimensional quadratic element are examples of elements constructed from Lagrange linear interpolation functions, and their shape functions are given by Eq. (B.4) for 1-dimensional element and by Eq. (B.5) for 2-dimensional element.

$$1D: \quad N_1(\xi) = \frac{1}{2}(1-\xi) \quad N_2(\xi) = \frac{1}{2}(1+\xi) \quad (\text{Eq. B.4})$$

$$\begin{aligned} 2D: \quad N_1(\xi, \eta) &= \frac{1}{4}(1+\xi)(1+\eta) & N_2(\xi, \eta) &= \frac{1}{4}(1-\xi)(1+\eta) \\ N_3(\xi, \eta) &= \frac{1}{4}(1-\xi)(1-\eta) & N_4(\xi, \eta) &= \frac{1}{4}(1+\xi)(1-\eta) \end{aligned} \quad (\text{Eq. B.5})$$

It should be noted that the so-called “linear” interpolation functions are linear with respect to each independent parameter only, and not as a whole. For example, the shape function $N_3(\xi, \eta)$ for 2D element is linear with respect to ξ or η but not to both of them.

The local node numbering for the quadrilateral or hexahedral element follows the convention for the counterclockwise numbering as shown in Fig. B-1. The three-dimensional shape functions are constructed from products of one-dimensional interpolation functions in the three independent coordinates ξ , η and ζ . For 8-node hexahedral element, the shape functions are given by Eq. (B.6):

$$\begin{aligned}
N_1 &= \frac{1}{8}(1-\xi)(1-\eta)(1-\varsigma), & N_2 &= \frac{1}{8}(1+\xi)(1-\eta)(1-\varsigma) \\
N_3 &= \frac{1}{8}(1+\xi)(1+\eta)(1-\varsigma), & N_4 &= \frac{1}{8}(1-\xi)(1+\eta)(1-\varsigma) \\
N_5 &= \frac{1}{8}(1-\xi)(1-\eta)(1+\varsigma), & N_6 &= \frac{1}{8}(1+\xi)(1-\eta)(1+\varsigma) \\
N_7 &= \frac{1}{8}(1+\xi)(1+\eta)(1+\varsigma), & N_8 &= \frac{1}{8}(1-\xi)(1+\eta)(1+\varsigma)
\end{aligned} \tag{Eq. B.6}$$

This process can easily be generalized for higher-order elements. In the present version of the numerical code, an 8-node hexahedral element is used with the option of adding more nodes (upto 20) to the element if needed. The general form of shape functions for hexahedral element with 8-20 nodes is given as shown by Eq. (B.7):

$$\begin{aligned}
N_1 &= g_1 - (g_9 + g_{12} + g_{17})/2 & N_2 &= g_2 - (g_9 + g_{10} + g_{18})/2 \\
N_3 &= g_3 - (g_{10} + g_{11} + g_{19})/2 & N_4 &= g_4 - (g_{11} + g_{12} + g_{20})/2 \\
N_5 &= g_5 - (g_{13} + g_{16} + g_{17})/2 & N_6 &= g_6 - (g_{13} + g_{14} + g_{18})/2 \\
N_7 &= g_7 - (g_{14} + g_{15} + g_{19})/2 & N_8 &= g_8 - (g_{15} + g_{16} + g_{20})/2 \\
N_j &= g_j \text{ for } j = 9, \dots, 20
\end{aligned} \tag{Eq. B.7}$$

where, g_j and G are defined by Eq. (B.8) and Eq. (B.9), respectively.

$$g_j = \begin{cases} 0 & \text{if node } j \text{ is not included} \\ G(\xi, \xi_j)G(\eta, \eta_j)G(\varsigma, \varsigma_j) & \text{otherwise} \end{cases} \tag{Eq. B.8}$$

$$G(\alpha, \alpha_j) = \begin{cases} \frac{1}{2}(1 + \alpha_j \alpha) & \text{for } \alpha_j = \pm 1 \\ (1 - \alpha^2) & \text{for } \alpha_j = 0 \end{cases} \tag{Eq. B.9}$$

Appendix C

Numerical Integration on the Master Element

The basic formula for a change of integration variables is given by Eq. (C.1):

$$\iiint_{V_{Arbitrary\ Element}} f(x_1, x_2, x_3) dx_1 dx_2 dx_3 = \iiint_{V_{Master\ Element}} f(\xi, \eta, \varsigma) |J| d\xi d\eta d\varsigma \quad (\text{Eq. C.1})$$

where, $|J|$ is the determinant of Jacobian for the co-ordinate transformation given by Eq. (C.2):

$$|J| \equiv \frac{\text{Volume of actual element}}{\text{Volume of Master element}} = \frac{\text{Volume of actual element}}{1/8} \quad (\text{Eq. C.2})$$

Note that this expression implicitly defines the element volume V_n in terms of the global coordinates of the corner nodes.

The element integrals are not evaluated by analytic integration (i.e., computing the integrals in closed form), because in general, the integrands are very complicated nonlinear functions of the local coordinates (recall that the determinant of the Jacobian and of its inverse appears throughout the integrands). Instead, a numerical integration scheme involving NSP integration points with corresponding weights w_p ($p = 1, 2, \dots, NP$) is employed. In schematic terms, the process looks like:

$$\iiint_{V_{Master\ Element}} f(\xi, \eta, \varsigma) |J| d\xi d\eta d\varsigma = \sum_{p=1}^{NSP} w_p f(\xi_p, \eta_p, \varsigma_p) |J(\xi_p, \eta_p, \varsigma_p)| \quad (\text{Eq. C.3})$$

Generally, a Gaussian Integration scheme (*Gauss Quadrature*) is employed, but there are notable exceptions (such as the use of Simpson's Rule in certain specialized cases). In this work, Gaussian Quadrature is used with the option of using upto 10 point

integration in 3-dimensions. These points and corresponding weights are given in Table C-1. Note that this scheme will integrate *exactly* any polynomial of degree 3 or less (i.e. an arbitrary cubic). In general, a one-dimensional Gauss-Legendre numerical integration scheme (such as this one) with NSP sampling points will integrate any polynomial of degree $2*NSP-1$ exactly on the interval $[-1,1]$. In three dimensions, separate one-dimensional schemes for numerical integration in the three master element coordinate directions are composed to obtain appropriate approximations for calculation of the element matrices. The sampling points are merely the combination of three independent one-dimensional sampling. The weights are simply the *product* of the weights in the three directions, and in this case of 2-point scheme, remain as unity. This four-point scheme is capable of exact integration of functions that are cubic in x_1 , x_2 , and x_3 .

Table C-1: Gauss-Legendre abscissae and weights

<u>No. of points</u>	<u>Value of points</u>	<u>Weights</u>	<u>Maximum polynomial order</u>
2	± 0.57735	1.0	3.0
3	0.0	0.888888889	5.0
	± 0.77459	0.555555559	
4	± 0.33998104	0.65214515	7.0
	± 0.86113631	0.34785485	
5	0.0	0.56888889	9.0
	± 0.53846931	0.47862867	
	± 0.90617985	0.23692689	
6	± 0.23861918	0.46791393	11.0
	± 0.66120939	0.36076157	
	± 0.93246951	0.17132449	
7	0.0	0.41795918	13.0
	± 0.40584515	0.38183005	
	± 0.74153119	0.27970539	
	± 0.94910791	0.12948497	
8	± 0.18343464	0.36268378	15
	± 0.52553241	0.31370665	
	± 0.79666648	0.22238103	
	± 0.96028986	0.10122854	
10	± 0.14887434	0.29552422	19
	± 0.43339539	0.26926672	
	± 0.67940957	0.21908636	
	± 0.86506337	0.14945135	
	± 0.97390653	0.06667134	

Appendix D

Hyperbolic Systems

The conservation equations for problems in gas dynamics can be written in form of first order partial differential equations (PDE) as shown by Eq. (D.1):

$$\frac{d\mathbf{Q}}{dt} = \frac{\partial \mathbf{Q}}{\partial t} + \frac{\partial \mathbf{Q}}{\partial x} \frac{dx}{dt} = \mathbf{B}(\mathbf{Q}) \quad (\text{Eq. D.1})$$

In the above equations, the vector \mathbf{Q} contains variables like mass, momentum, energy etc. These variables are known as conserved variables. The primary variables like density, pressure, velocity etc. are known as the primitive variables. The vector $\mathbf{F}(\mathbf{Q})$ is called the flux vector and its components is a function of vector \mathbf{Q} . The vector $\mathbf{B}(\mathbf{Q})$ contains the source terms. If the vector $\mathbf{B}(\mathbf{Q})$ is zero then the PDE are called *homogeneous*. Generally, the components of matrix $\mathbf{A}(\mathbf{Q})$ are functions of conserved variables \mathbf{Q} and the source vector $\mathbf{B}(\mathbf{Q})$ is not zero. Such equations are known as inhomogeneous non-linear (or quasi-linear) partial differential equations. For convenience, the source term vector is ignored here since it does not change the fundamental behavior of hyperbolic equations.

The governing equations written in terms of conserved variables are called “conservative” equations. By applying the chain rule on the derivative of the flux vector it can be written in terms of a Jacobian and a derivative of vector \mathbf{Q} as following:

$$\frac{\partial \mathbf{F}(\mathbf{Q})}{\partial x_i} \approx \frac{\partial \mathbf{F}(\mathbf{Q})}{\partial \mathbf{Q}} \frac{\partial \mathbf{Q}}{\partial x_i} = \mathbf{A}(\mathbf{Q}) \frac{\partial \mathbf{Q}}{\partial x_i} \quad (\text{Eq. D.2})$$

By substituting above in Eq. (D.1), it becomes Eq. (D.3) as shown below:

$$\frac{\partial \mathbf{Q}}{\partial t} + \mathbf{A}(\mathbf{Q}) \frac{\partial \mathbf{Q}}{\partial x_i} = 0 \quad (\text{Eq. D.3})$$

If the components of matrix $\mathbf{A}(\mathbf{Q})$ are constant values then the system of equations Eq. (D.3) is called *linear with constant coefficients*. If the components of matrix $\mathbf{A}(\mathbf{Q})$ are variable but functions of spatial variable x_i and t only then the system of equations Eq. (D.3) is called *linear with variable coefficients*.

The general behavior of the system of equations mentioned above can be understood by two major parameters called eigenvalues and eigenvectors. Sometimes, they are combined together and jointly called the eigensystem. The eigenvalues of matrix $\mathbf{A}(\mathbf{Q})$ are determined by solving the characteristic polynomial $|\mathbf{A} - \lambda_i \mathbf{I}| = 0$, where \mathbf{I} is the identity matrix. Physically, the eigenvalues λ_i represent speeds of propagation of information in the x - t space. The speeds are measured positive in the direction of increasing x and negative otherwise. The other important parameter is eigenvectors of matrix $\mathbf{A}(\mathbf{Q})$, which are further divided into two categories of right eigenvectors and left eigenvectors. The right eigenvectors \mathbf{K}^i of matrix $\mathbf{A}(\mathbf{Q})$ corresponding to eigenvalues λ_i are determined by solving equation $\mathbf{A} \mathbf{K}^i = \lambda_i \mathbf{K}^i$. Similarly, the left eigenvectors \mathbf{L}^i of matrix $\mathbf{A}(\mathbf{Q})$ corresponding to eigenvalues λ_i are determined by solving equation $\mathbf{L}^i \mathbf{A} = \lambda_i \mathbf{L}^i$.

A system of equations shown by Eq. (D.1) is said to be hyperbolic at a point (x, t) if matrix $\mathbf{A}(\mathbf{Q})$ has m real eigenvalues λ_i , and a corresponding set of m linearly

independent right eigenvectors \mathbf{K}^i . The system is said to be strictly hyperbolic if the eigenvalues λ_i are all *distinct*. Strict hyperbolicity implies hyperbolicity, because real and distinct eigenvalues ensure the existence of a set of linearly independent eigenvectors. If the effects of viscosity and heat conduction are neglected (which is very often the case in gas dynamics) then the conservation equations shown by Eq. (D.1) reduce to hyperbolic equations.

The partial differential equations Eq. (D.3) can be transformed into ordinary differential equations (ODE) by using chain rule:

$$\frac{d\mathbf{Q}}{dt} = \frac{\partial \mathbf{Q}}{\partial t} + \frac{\partial \mathbf{Q}}{\partial x} \frac{dx}{dt} \quad (\text{Eq. D.4})$$

The curves in x-t space that have slopes dx/dt are called characteristic curve. Along the characteristic curve, the PDEs become ODEs. By comparing Eq. (D.4) with Eq. (D.3), it becomes evident that the eigenvalues of the Jacobian $\mathbf{A}(\mathbf{Q})$ are the slopes of characteristic curves, $dx/dt = \lambda_i$ and that for a strict hyperbolic system; the number of characteristic curves is equal to the number of eigenvalues of the system. The slope of characteristic curves is sometimes called characteristic speeds.

By using this information, the characteristic curve can be defined by an ODE given by Eq. (D.5)

$$\frac{dx}{dt} = \lambda_i \text{ with IC: } x = x_0 \quad (\text{Eq. D.5})$$

The solution of above ODE is given by Eq. (D.6):

$$x = x_0 + \lambda_i t \quad (\text{Eq. D.6})$$

If the source term in Eq. (D.4) is zero then this equation implies that the rate of change of vector \mathbf{Q} is zero along a characteristic curve defined by Eq. (D.6). Therefore, if vector \mathbf{Q} is given an initial value at time $t = 0$ then along the whole characteristic curve $x(t) = x_0 + \lambda_i t$ that passes through the initial point x_0 on the x -axis, the solution is equal to its values at point x_0 , i.e.,

$$\mathbf{Q} = \mathbf{Q}_0(x_0) = \mathbf{Q}_0(x - \lambda_i t) \quad (\text{Eq. D.7})$$

The Eq. (D.7) means that the hyperbolic differential equations can be transformed into ordinary differential equations with a specified initial condition and that is why they are often called the initial value problems, indicating that the solution depends on the initial condition of the problem. The solution of initial value problem at a given point in $x-t$ space depends solely on the initial data at points $x_0 + \lambda_i t$ on the x -axis. These points are obtained by tracing back the characteristic curves passing through the point x .

The interval between the points $x_0 + \max|\lambda_i|t$ and $x_0 + \min|\lambda_i|t$ is known as domain of dependence. The solution obtained at time t at position x_1 can only affect the solution at point between $x_1 + \max|\lambda_i|t$ and $x_1 + \min|\lambda_i|t$ in future. The interval between these two points is known as region of influence.

D.1 Wave formation

One of the distinguishing features of non-linear hyperbolic PDEs is wave steepening, shock formation, and rarefaction wave formation. This can be explained by

studying the behavior of characteristic curves in x - t space. In the non-linear PDEs, the Jacobian $\mathbf{A}(\mathbf{Q})$ is a function of vector \mathbf{Q} ; thereby the eigenvalues λ_i of Jacobian $\mathbf{A}(\mathbf{Q})$ are also functions of \mathbf{Q} . Thus, slopes of characteristic curves, which in fact are the eigenvalues λ_i depend on the solution itself, which results in distortions. This can be explained by considering the initial data shown in Fig. D-1

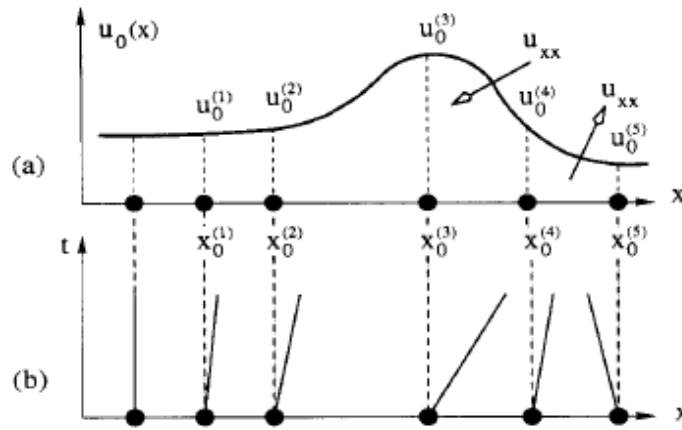


Figure D-1: Wave steepening in a convex , non-linear hyperbolic conservation law, (a) Initial condition, (b) Slopes of characteristic curves

For convenience, the system is assumed to be one-dimensional. A smooth initial profile is shown in Fig xx along with five initial points and their corresponding initial data values. If the flux function is convex, i.e., $\mathbf{F}'(\mathbf{Q}) > 0$ then $\lambda' > 0$ meaning that the characteristic speeds will be an increasing function of \mathbf{Q} . Given this condition, higher value of $\mathbf{Q}_0(x_0)$ travel faster than the its lower values. There are two intervals on the x -axis where distortions are most evident. These are the intervals $\text{IE} = [x_{01}, x_{03}]$ and $\text{IC} = [x_{03}, x_{05}]$. In the interval IE , $\mathbf{Q}_0(x_0)$ is increasing with x , therefore the slope of characteristic curves increases with x . This results in a broader IE at a later time. This

phenomenon is called expansion or rarefaction wave. In the interval IC, the gradient of λ is negative; the value Q_{03} will propagate faster than the value Q_{05} . The interval IC is called compressive and it will get narrower and steeper as the time evolves. Eventually, the wave steepening mechanism in the compressive interval will produce an anomalous condition with corresponding crossing over of the characteristic curves and three values of the solution at one point. This condition implies that the ODE solution cannot be used at this point of intersection. The locus of this point is known as shock wave. It can also be concluded from this analysis that the solution of a non-linear hyperbolic PDE may always contain discontinuities if the initial condition is non-uniform, no matter how smooth it is. This is the most important feature of non-linear hyperbolic equations and an essential difference from linear hyperbolic equations. It is this phenomenon that leads to special difficulties.

D.2 Rankine-Hugoniot condition

The solution of the IVP Eq. (D.3) at the point of shock formation is approximated by mathematical discontinuities. The solution is continuous in the regions left and right of a line $s = s(t)$ on the $x-t$ plane, across which there is a jump discontinuity. The line $s = s(t)$ represents the locus of point of shock formation and the slope of this line is the shock speed S . If a finite region $[x_L, x_R]$ on the $x-t$ plane is considered then $x_L < s(t) < x_R$. By using the integral form of the conservation equation Eq. (D.3) on the control volume $[x_L, x_R]$ we have:

$$\mathbf{F}(\mathbf{Q}_L) - \mathbf{F}(\mathbf{Q}_R) = \frac{d}{dt} \int_{x_L}^{s(t)} \mathbf{Q}(x, t) dx + \frac{d}{dt} \int_{s(t)}^{x_R} \mathbf{Q}(x, t) dx \quad (\text{Eq. D.8})$$

The Eq. (D.8) can be re-written as:

$$\mathbf{F}(\mathbf{Q}_L) - \mathbf{F}(\mathbf{Q}_R) = (\mathbf{Q}_L - \mathbf{Q}_R)S + \int_{x_L}^{s(t)} \frac{d}{dt} \mathbf{Q}(x, t) dx + \int_{s(t)}^{x_R} \frac{d}{dt} \mathbf{Q}(x, t) dx \quad (\text{Eq. D.9})$$

In Eq. (D.9), $\mathbf{Q}_L = \lim_{x_L \rightarrow s(t)} \mathbf{Q}$ from the left and $\mathbf{Q}_R = \lim_{x_R \rightarrow s(t)} \mathbf{Q}$ from the right. The

function \mathbf{Q}_L and \mathbf{Q}_R are bounded, thus the integrals in Eq. (D.9) vanish and we have:

$$\mathbf{F}(\mathbf{Q}_L) - \mathbf{F}(\mathbf{Q}_R) = (\mathbf{Q}_L - \mathbf{Q}_R)S \quad (\text{Eq. D.10})$$

The above algebraic expression relating the jumps $\Delta \mathbf{F}$, $\Delta \mathbf{Q}$ and the speed of shock wave S is called the Rankine-Hugoniot condition and it is usually expressed as:

$$S = \frac{\Delta \mathbf{F}}{\Delta \mathbf{Q}} \quad (\text{Eq. D.11})$$

By the above analysis, it is evident that the shock speed is not same as the characteristic speeds or eigenvalues of Jacobian $\mathbf{A}(\mathbf{Q})$.

D.3 Entropy condition

The solution of the IVP shown by Eq. (D.3) contains discontinuities as explained in the earlier section. In order to ensure the uniqueness of the IVP solution, an additional condition is required to obtain a physically relevant solution. It has been identified that the discontinuity of such acceptable solution must satisfy the following condition [57]:

$$\lambda_L > S > \lambda_R \quad (\text{Eq. 4.12})$$

The above condition is called the entropy condition. Oleinik [57] has shown that the weak solutions satisfying the above conditions are uniquely determined by their initial data. The rarefaction waves violate the entropy condition; therefore isentropic equations are used to determine an entropy-satisfying solution.

Appendix E

Riemann Problem

The Riemann problem is one of the fundamental problems in gas dynamics. The Riemann problem is represented by a set of conservation laws in form of hyperbolic partial differential equations with the simplest and non-trivial initial conditions. The solution of Riemann problem contains the fundamental physics and mathematical character of the conservation laws that were formulated in this work and are generally applied to the compressible flows and various similar problems in gas-dynamics. Thus, a solution of the Riemann problem provides an invaluable reference solution for the numerical schemes applied to the theoretical models in such areas. Due to this reason, it is invariably used to assess the performance and correctness of such numerical methods. In addition, Godunov methods and their high-order extensions use the exact or approximate solutions of the Riemann problem *locally*. The numerical methods used to solve the mortar tube sub-model are Godunov-type methods. Therefore, it is very important to understand the Riemann problem and its solution.

The Riemann problem does not actually have an exact closed-form solution (even for much simpler models such as isentropic or isothermal equations). However, an iterative solution with a practical degree of accuracy has been obtained and refined by many researchers. The key issues in solving Riemann problem are the selected variables (conservative or primitive), the equations used and their number, the technique for the iterative procedure, the initial guess and handling of the unphysical conditions such as

negative pressure. The major work in this direction has been done and refined by many researchers over past several years.

The Riemann problem for transient one-dimensional process is defined by conservation law shown in Eq. (E.1) and initial conditions shown in Eq. (E.2)

$$\text{PDE: } \frac{\partial \mathbf{Q}}{\partial t} + \frac{\partial \mathbf{F}(\mathbf{Q})}{\partial x} = 0 \quad (\text{Eq. E.1})$$

where

$$\mathbf{Q} = [\rho, \rho u, E] \quad \mathbf{F}(\mathbf{Q}) = [\rho u, \rho u^2 + P, u(E + p)]$$

$$\text{IC: } \mathbf{Q}(x, 0) = \mathbf{Q}_0(x) = \begin{cases} \mathbf{Q}_L & \text{if } x < 0 \\ \mathbf{Q}_R & \text{if } x > 0 \end{cases} \quad (\text{Eq. E.2})$$

The domain of interest in the x - t plane are point (x, t) with $-\infty < x < \infty$ and $t > 0$.

In practice, x is varied in a finite interval $[x_L, x_R]$ around the point $x = 0$. The vector \mathbf{Q} is known as vector of conserved variables. The Riemann solution used a vector $\mathbf{W} = [\rho, u, P]$ of primitive variables rather than the vector of conserved variables. Physically, the Riemann problem defined by Eq. (E.1) - Eq. (E.2) is a slight generalization of the so called shock-tube problem: two stationary gases ($u_L = 0$ and $u_R = 0$) in a tube are separated by a diaphragm. The rupture of the diaphragm generates a nearly centered wave system that typically consists of a rarefaction wave, a contact discontinuity and a shock wave. In the Riemann problem the particle speeds u_L and u_R are allowed to be non-zero, but the structure of the solution is the same as that of the shock-tube problem.

The solution of Riemann problem defined by Eq. (E.1) - Eq. (E.2) also consists of three waves (i.e, a shock wave, a rarefaction wave, and a contact discontinuity), which

are associated with the eigenvalues of the system shown by Eq. (E.1). A shock wave is a *discontinuous* wave across which all primitive variables like density, pressure, and velocity change. The shock waves are generated by strong compression, which means that the pressure ahead of discontinuity is higher than the pressure behind it resulting in generation of a compression wave. A contact discontinuity (or contact wave) is also a *discontinuous* wave across which both pressure and velocity are constant but density jumps discontinuously as do such variables that depend on density including specific internal energy, temperature, sound speed, and entropy. A rarefaction wave is a *smooth* wave across which density, velocity, and pressure change. This wave has a fan-like structure and it is enclosed by two bounding characteristics corresponding to the Head and Tail of the wave. Generally, speeds of these waves are not same as the characteristic speeds given by the eigenvalues. The Riemann problem at $t = 0$ can be represented by Fig. E-1. The contact discontinuity is usually in the middle and the right and left waves could be either shock waves or rarefaction waves.

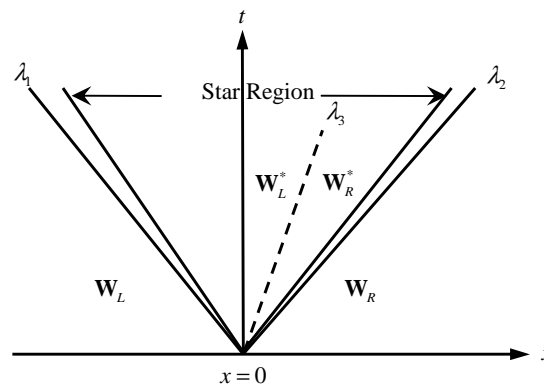


Figure E-1: Structure of the solution of the Riemann problem on the x - t plane for the one-dimensional time-dependent Euler equations [71].

The three waves in this solution separate four constant states namely, \mathbf{W}_L , \mathbf{W}_L^* , \mathbf{W}_R^* , and \mathbf{W}_R . The variables in the region between the states \mathbf{W}_L and \mathbf{W}_R are unknown. This region is typically called the star region and it is divided by the middle wave into two sub-regions star left (\mathbf{W}_L^*) and star right (\mathbf{W}_R^*). The middle wave is always a contact discontinuity and it is shown by a dashed line. The left and right waves could be either rarefaction waves or shock waves. Therefore, according to the type of these non-linear waves, there could be four possible solutions, which are shown in Fig. E-2. There could be two possible variations of these, namely when the left or right non-linear wave is a sonic rarefaction wave. Such condition may exist while using Godunov type methods and an entropy fix is used to modify the Riemann solution.

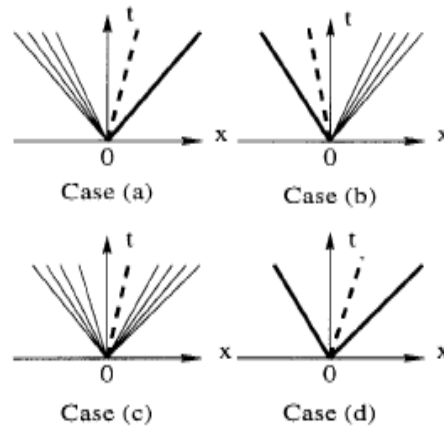


Figure E-2: Possible wave patterns in the solution of the Riemann problem: (a) left rarefaction, contact, right shock (b) left shock, contact, right rarefaction (c) left rarefaction, contact, right rarefaction (d) left shock, contact, right shock [71].

An analysis based on the eigensystem (i.e., eigenvalues and eigenvectors) of the Euler equations reveals that both pressure P^* and velocity u^* in the star region are constant while the density takes on the two constant values ρ_L^* and ρ_R^* across the contact

discontinuity Therefore, the major unknown physical quantities are P^* , u^* , ρ_L^* and ρ_R^* .

By using the constancy of pressure and velocity in the star region, an algebraic non-linear equation for pressure with the ideal gas equation of state is given by Eq. (E.3)

$$f(P^*, \mathbf{W}_L, \mathbf{W}_R) \equiv f_L(P^*, \mathbf{W}_L) + f_R(P^*, \mathbf{W}_R) + \Delta u = 0 \quad (\text{Eq. E.3})$$

where $\Delta u \equiv u_R - u_L$

The functions f_L and f_R can have two algebraic expressions depending on whether the left and right non-linear waves are shock waves or rarefaction waves. If either of the left or right non-linear waves is a shock wave then the functions f_L and f_R are derived by using the Rankine-Hugoniot conditions by using the pre-shock and post-shock values for the primitive variables. The pre-shock values for the left shock wave are (ρ_L, u_L, P_L) and those for the right shock wave are (ρ_R, u_R, P_R) . The post-shock values for the left shock wave are (ρ_L^*, u^*, P^*) and those for the right shock wave are (ρ_R^*, u^*, P^*) . If either of these waves is a rarefaction wave then isentropic relations are used to connect the unknown vectors \mathbf{W}_L^* or \mathbf{W}_R^* with the left or right data state. The functions f_L and f_R obtained by this procedure are shown in Eq. (E.4) and Eq. (E.5) as:

$$f_L(P^*, \mathbf{W}_L) = \begin{cases} (P^* - P_L) \left[\frac{A_L}{P^* + B_L} \right]^{\frac{1}{2}} & \text{if } P^* > P_L \text{ (shock)} \\ \frac{2c_{g,L}}{\gamma-1} \left[\left(\frac{P^*}{P_L} \right)^{\frac{\gamma-1}{2\gamma}} - 1 \right] & \text{if } P^* \leq P_L \text{ (rarefaction)} \end{cases} \quad (\text{Eq. E.4})$$

$$A_L = \frac{2}{(\gamma+1)\rho_L}, B_L = \frac{(\gamma-1)}{(\gamma+1)} P_L$$

$$f_L(P^*, \mathbf{W}_L) = \begin{cases} (P^* - P_L) \left[\frac{A_L}{P^* + B_L} \right]^{\frac{1}{2}} & \text{if } P^* > P_L \text{ (shock)} \\ \frac{2c_{g,L}}{\gamma-1} \left[\left(\frac{P^*}{P_L} \right)^{\frac{\gamma-1}{2\gamma}} - 1 \right] & \text{if } P^* \leq P_L \text{ (rarefaction)} \end{cases} \quad (\text{Eq. E.5})$$

$$A_L = \frac{2}{(\gamma+1)\rho_L}, B_L = \frac{(\gamma-1)}{(\gamma+1)} P_L$$

The algebraic expressions for the unknown velocity u^* in the star region are also obtained using either Rankine-Hugoniot condition or isentropic relations depending on whether there is a shock wave or a rarefaction wave at left and right wave fronts. By combining these expressions, the algebraic equation for the velocity in star region is given by Eq. (E.6) as:

$$u^* = \frac{1}{2}(u_L + u_R) + \frac{1}{2} [f_R(P^*) - f_L(P^*)] \quad (\text{Eq. E.6})$$

As mentioned earlier, unknown pressure P^* in the star region is found by solving the non-linear algebraic Eq. (E.3). This is accomplished by using an iterative procedure. The iterative procedure can be used because the pressure function $f(P^*)$ is differentiable and an analytical expression for its derivative can be obtained. A Newton-Raphson [228]

iterative procedure can be used to find the root of $f(P^*) = 0$. The general procedure is shown by Eq. (E.7) as:

$$P_k^* = P_{k-1}^* - \frac{f(P_{k-1}^*)}{f'(P_{k-1}^*)} \quad (\text{Eq. E.7})$$

In the above equation, index k represents the iteration level. The iteration procedure is stopped whenever the relative pressure change is less than the prescribed tolerance level, which is typically set to $1e-6$. The relative pressure change between two iterations is shown by Eq. (E.8) as:

$$\mathcal{E} = \frac{|P_k^* - P_{k-1}^*|}{\frac{1}{2}(P_k^* + P_{k-1}^*)} \quad (\text{Eq. E.8})$$

The other two unknowns in the star region, i.e., ρ_L^* and ρ_R^* are determined by comparing the pressure p^* to p_l and p_r . The relations used to accomplish this depend on the type of non-linear waves at left and right locations. The analytical expressions for ρ_L^* are given by Eq. (E.9) as:

$$\rho_L^* = \begin{cases} \rho_L \left[\frac{\frac{P^*}{P_L} + \frac{(\gamma-1)}{(\gamma+1)}}{\frac{(\gamma-1)}{(\gamma+1)} \frac{P^*}{P_L} + 1} \right] & \text{if } P^* > P_L \text{ (shock)} \\ \rho_L \left(\frac{P^*}{P_L} \right)^{\frac{1}{\gamma}} & \text{if } P^* \leq P_L \text{ (rarefaction)} \end{cases} \quad (\text{Eq. E.9})$$

The analytical expressions for ρ_R^* are given by Eq. (E.10) as:

$$\rho_R^* = \begin{cases} \rho_R \left[\frac{\frac{P^*}{P_R} + \frac{(\gamma-1)}{(\gamma+1)}}{\frac{(\gamma-1)}{(\gamma+1)} \frac{P^*}{P_R} + 1} \right] & \text{if } P^* > P_R \text{ (shock)} \\ \rho_R \left(\frac{P^*}{P_R} \right)^{\frac{1}{\gamma}} & \text{if } P^* \leq P_R \text{ (rarefaction)} \end{cases} \quad (\text{Eq. E.10})$$

The speeds of shock and rarefaction waves are also parameters of interest. The explicit expression for speed of shock wave S_L or S_R can also be derived by using the Rankine-Hugoniot condition. They are given by Eq. (E.11) and Eq. (E.12) as:

$$S_L = u_L - c_{g,L} \left[\frac{(\gamma+1)}{2\gamma} \frac{P^*}{P_L} + \frac{(\gamma-1)}{2\gamma} \right]^{\frac{1}{2}} \quad (\text{Eq. E.11})$$

$$S_R = u_R + c_{g,R} \left[\frac{(\gamma+1)}{2\gamma} \frac{P^*}{P_R} + \frac{(\gamma-1)}{2\gamma} \right]^{\frac{1}{2}} \quad (\text{Eq. E.12})$$

The rarefaction wave is enclosed by a head and a tail, which are characteristics of speeds given respectively by Eq. (E.13) and Eq. (E.14)

$$S_{HL} = u_L - c_{g,L} \quad (\text{Eq. E.13})$$

$$S_{TL} = u^* - c_{g,L}^* \quad (\text{Eq. E.14})$$

Similarly, the speeds for head and tail of right rarefaction waves are given by Eq. (E.15) and Eq. (E.16)

$$S_{HR} = u_R + c_{g,R} \quad (\text{Eq. E.15})$$

$$S_{TR} = u^* + c_{g,R}^* \quad (\text{Eq. E.16})$$

VITA

Ragini Acharya

Ragini Acharya received her Bachelor of Technology (Honors) in Mechanical engineering degree in 2000 from Institute of Technology, Banaras Hindu University, Varanasi, India. She received her Masters degree from The Pennsylvania State University in Spring 2004. She was an invited speaker in the 9th CLEERS Workshop organized by Oak Ridge National. Three of her co-authored papers have received the Best Paper Awards; two from the Joint Army, Navy, NASA, Air force (JANNAF) Rocket Nozzle Technology Subcommittee (RNTS) Meeting; and third at 7th International Symposium on Special Topics in Chemical Propulsion (7-ISICIP), Kyoto, Japan in 2007. She also served as a Graduate Teaching Fellow at Penn State University for 2006-2007. Some of her publications are:

1. R. Acharya, M. Alam, and A. L. Boehman, "Fuel and System Interaction Effects on Urea-SCR Control of NO_x in Diesel Exhaust Aftertreatment", *Diesel Exhaust*, SP-2022, ISBN Number: 978-0-7680-1757-1, April 2006
2. R. Acharya and K. K. Kuo, "Effect of Chamber Pressure & Propellant Composition on Erosion Rate of Graphite Rocket Nozzle," *Journal of Propulsion and Power*, 23, 6, pp.1242-1254, 2007.
3. R. Acharya and K. K. Kuo, "Finite Element Simulation of Interior Ballistic Processes in 120-mm Mortar Systems," *Proceedings of International Symposium on Ballistics*, Vol. 1, pp. 343-350, 2007.
4. R. Acharya and K. K. Kuo, "Effect of Different Flash-tube Vent-hole Patterns on Interior Ballistic Processes of Ignition Cartridge of 120-mm Mortar System," *Journal of Advancements in Energetic Materials and Chemical Propulsion*, Vol. 1, pp. 387, 2008.
5. R. Acharya and K. K. Kuo, "Graphite Rocket Nozzle Erosion Rate Reduction by Boundary-Layer Control Using Ablative Materials at High Pressures," *Journal of Advancements in Energetic Materials and Chemical Propulsion*, Vol. 1, pp. 402, 2008.